2015

Dual-Band Non-Stationary Channel Modeling for the Air-Ground Channel

Ruoyu Sun
University of South Carolina

DUAL-BAND NON-STATIONARY CHANNEL MODELING FOR THE AIR-GROUND CHANNEL

by

Ruoyu Sun

Bachelor of Science
Tianjin University, 2004

Master of Science
Beijing Jiaotong University, 2007

Submitted in Partial Fulfillment of the Requirements

For the Degree of Doctor of Philosophy in

Electrical Engineering

College of Engineering and Computing

University of South Carolina

2015

Accepted by:

David Matolak, Major Professor

Mohammod Ali, Committee Member

Guoan Wang, Committee Member

Srihari Nelakuditi, Committee Member

Lacy Ford, Senior Vice Provost and Dean of Graduate Studies

DEDICATION

This dissertation is dedicated to my parents Jingqi Sun and Ping Sun, to my wife Jingjing Gao and to my son Hayden Sun. Their unconditional love, unstoppable support and unreserved encouragement gave me unlimited power to move forward, helped me believe in myself and concentrate on my dissertation. I am grateful to them for being a part of my life.

ACKNOWLEDGEMENTS

First, I would like to express my most sincere appreciation and gratitude to my advisor, Dr. David Matolak, for his professional and patient guidance over the course of my Ph.D. studies and job search. I am grateful that he took me from Ohio University to the University of South Carolina. His diligence, enthusiasm, in-depth knowledge of wireless communication and excellent suggestions have been an invaluable asset for me throughout my research. This dissertation would be impossible without his creative ideas and thoughtful advice.

Next, I would like to extend my appreciation to my Ph.D. committee members: Dr. Mohammod Ali, Dr. Srihari Nelakuditi, and Dr. Guoan Wang, for their insightful comments, critical thinking and timely feedback. Many thanks to Dr. Paul Huray from the University of South Carolina and from Ohio University, Dr. Chris Bartone, Dr. Jeffrey Dill, Dr. Wei Lin, Dr. Wouter Pelgrum, Dr. Roger Radcliff and Dr. H. Bryan Riley, for their extremely helpful courses and invaluable discussions.

I would also acknowledge the NASA Glenn Research Center for providing me the opportunity to participate in the UAS integration into the NAS project, and for conducting the AG channel measurements. In particular I extend special thanks to James Griner, Kurt Shalkhauser, Robert Kerczewski and Joseph Ishac.

Many thanks to my colleagues Kai-jen Cheng, Hunter Huang, Hosseinali Jamal, Liu Liu, Pengyu Liu, William Rayess, Qiong Wu, Jingtao Zhang, and Qian Zhang who were always ready to share and help. They provided such a friendly atmosphere with

multi-cultural communications. I have learned so much from all these friends at the University of South Carolina and Ohio University and wish to keep the friendship forever.

ABSTRACT

Multiple air-to-ground (AG) radio propagation channels are experimentally characterized for two frequency bands, C-band and L-band. These characterizations are aimed to support the specification of the control and non-payload communication (CNPC) links being designed for civil unmanned aircraft systems (UAS). The use of UAS is expected to grow dramatically in the coming decades. In the United States, UAS will be monitored and guided in their operation within the national airspace system (NAS) via the CNPC link. The specifications of the CNPC link are being designed by government, industries, academia and standards bodies such as the Radio Technical Commission for Aeronautics (RTCA). Two bands have been allocated for the CNPC applications: from 5030 to 5091 MHz in C-band and a portion of the aeronautical L-band from 960 to 1215 MHz. The project under which this work was conducted is entitled "Unmanned Aircraft Systems Research: The AG Channel, Robust Waveforms, and Aeronautical Network Simulations", and this is a sub-project of a NASA project entitled "Unmanned Aircraft Systems Integration in the National Airspace System."

Measurements and modeling for radio propagation channels play an essential role in wireless communication system design and performance evaluation; such models estimate attenuation, delay dispersion, and antenna diversity in wireless channels. The AG channel differs significantly from classic cellular, ground-to-satellite, and other terrestrial wireless channels, particularly in terms of antenna heights and velocity. The

previous studies about the AG channels are reviewed and the significant gaps are indicated.

NASA Glenn Research Center has conducted an AG channel measurement campaign for multiple ground station local environments, including over sea, over freshwater, desert, suburban, near urban, hilly and mountainous settings. In this campaign, over 316 million power delay profiles (PDPs) or channel impulse responses (CIRs), over 82 flight tracks, have been collected. The measurement equipment was a dual-band single-input multiple-output (SIMO) wideband channel sounding system with bandwidth of 50 MHz in C-band and 5 MHz in L-band.

Given the dynamic nature of the AG environments, the channels are statistically non-stationary, meaning that the channel's statistical parameters change over time/space. We have estimated, via two distinct methods, that the stationarity distance is approximately 15 m—this is the distance over which the channel characteristics can be assumed to be wide sense stationary. The AG channel attenuation is considered as a combination of large scale path loss, small scale fading, and airframe shadowing. The large scale path loss is modeled by both the log-distance model and two-ray models. The theoretical flat earth and curved earth two-ray models are presented, along with their limitations, boundaries and some enhancements. Numerous propagation effects in the AG channels are discussed, and this includes earth spherical divergence, atmospheric refraction, atmospheric gas and hydrometeor attenuations, and ducting. The small scale fading is described by the Ricean distribution, which for unit-energy normalizations are completely characterized by Ricean *K*-factors; these *K*-factors are approximately 28.7 dB in C-band and 13.1 dB in L-band. The line-of-sight (LOS) signal can be obstructed by the

airplane itself in some specific maneuvers, and this is termed airframe shadowing. For the specific flights and NASA aircraft used in our measurements, the shadowing duration was found to be on average 30 seconds, and the shadowing loss can be as large as 40 dB. The statistics, models and simulation algorithm for the airframe shadowing are provided.

The wideband characteristics of the AG channel are quantified using root-mean-square delay spread (RMS-DS), and illustrated by sequences of PDPs. Tapped delay line (TDL) models are also provided. Doppler effects for over water channels are also addressed. Given the sparsity of the diffuse multipath components (MPCs) in the AG channels and generally short lifetime of these MPCs, the CIRs are modeled by the two-ray model plus intermittent 3rd, 4th or 5th "rays." Models for intermittent ray probability of occurrence, duration, relative power, phase, and excess delay are provided.

The channels at C-band and L-band were found to be essentially uncorrelated; this conclusion holds for the specific antenna locations used in our experiments (the aircraft underside), but is not expected to change for arbitrary antenna locations. For the aircraft antenna locations employed, *intra*-band signals are highly correlated, and this is as expected for channels with a dominant LOS component; analytical correlation computations show interesting two-ray effects that also appear in measurements. Multiple aircraft antennas and carefully selected locations are recommended for mitigating airframe shadowing for the CNPC link.

Future work for AG channel modeling includes characterization of L-band delay dispersion and L-band TDL models, estimation of building and/or tree shadowing for small UAS that fly at very low altitudes, evaluation of multiple ground site(s) antenna diversity, and AG channel modeling via geometric techniques, e.g., ray-tracing.

TABLE OF CONTENTS

LIST OF TABLES

LIST OF FIGURES

LIST OF ABBREVIATIONS

ACARS ..... Aircraft Communications Addressing and Reporting System

AFD ..... Average Fade Duration

AFS ..... Airframe Shadowing

AG ..... Air-to-Ground

AMCP ..... Aeronautical Mobile Communications Panel

AOA ..... Angle of Arriving

ATC ..... Air Traffic Control

AWGN ..... Additive White Gaussian Noise

B2B ..... Back-to-Back

B-AMC ..... Broadband Aeronautical Multi-Carrier System

BER ..... Bit Error Ratio

b-LOS ..... Beyond Line of Sight

BPSK ..... Binary Phase-Shift Keying

B-VHF ..... Broadband VHF

BVS ..... Berkeley Varitronics Systems

CCIR ..... Consultative Committee on International Radio

CDF ..... Cumulative Distribution Function

CE2R ..... Curved Earth Two Ray

CIR ..... Channel Impulse Response

CMD ..... Correlation Matrix Distance

CNPC ..... Control and Non-Payload Communications

DOD ..... Department of Defense

DS-SS ..... Direct Sequence Spread Spectrum

ECEF ..... Earth-Centered Earth-Fixed

EIA ..... Electronic Industry Association

ENU ..... East North Up

FAA ..... Federal Aviation Administration

FDTD ..... Finite-Difference Time-Domain

FE2R ..... Flat Earth Two Ray

FP6 ..... European 6th Framework

FT ..... Flight Track

GA ..... Ground-to-Air

GBSBE ..... Geometrically Based Single-Bounce Elliptical

GEV ..... Generalized Extreme Value

GRC ..... Glenn Research Center

GS ..... Ground Site

HPA ..... High Power Amplifier

I ..... In-Phase

ICAO ..... International Civil Aviation Organization

iOS ..... iPhone Operating Systems

ISI ..... Inter-Symbol Interference

ITU ..... International Telecommunications Union

LCR ..... Level Crossing Rate

L-DASC1 ..... L-band Digital Aeronautical Communication System of Type 1

L-DASC2 ..... L-band Digital Aeronautical Communication System of Type 2

LNA ..... Low Noise Amplifier

LOS ..... Line-of-Sight

MANET ..... Mobile AD Hoc Network

MB ..... Moment Based

MC-CDMA ..... Multi-Carrier Code Division Multiple Address

MIMO ..... Multiple-Input Multiple-Output

ML ..... Maximum Likelihood

MLS ..... Microwave Landing System

MPC ..... Multipath Component

NAS ..... National Airspace System

NASA ..... National Aeronautics and Space Administration

NLOS ..... Non-LOS

OFDM ..... Orthogonal Frequency-Division Multiplexing

P34 ..... Project 34

PDF ..... Power Density Function

PDP ..... Power Delay Profile

Q ..... Quadrature

QPSK ..... Quadrature Phase-Shift Keying

RMS-DS ..... Root-Mean-Square Delay Spread

RTCA ..... Radio Technical Commission for Aeronautics

Rx ..... Receiver

SC ..... Special Committee

SD ..... Stationarity Distance

SIMO ..... Single-Input Multiple-Output

SISO ..... Single-Input Single-Output

TDL ..... Tapped Delay Line

TIA ..... Telecommunications Industry Association

TPCC ..... Temporal PDP Correlation Coefficient

Tx ..... Transmitter

UAS ..... Unmanned Aircraft Systems

UAT ..... Universal Access Transceiver

UAV ..... Unmanned (Uninhabited) Aerial Vehicles

US ..... Uncorrelated Scattering

USC ..... University of South Carolina

V2V ..... Vehicle-to-Vehicle

VDL ..... VHF Data (Digital) Link

VHF ..... Very High Frequency

WSS ..... Wide-Sense Stationary

WSS-US ..... Wide-Sense Stationary Uncorrelated Scattering

CHAPTER 1

INTRODUCTION

1.1 BACKGROUND: INTEGRATION OF UAS INTO THE NAS

The use of unmanned aircraft systems (UAS) is expected to grow dramatically in the coming decades [1]. These UAS are also termed uninhabited or unmanned aerial vehicles (UAVs), and in the popular press by the rather inaccurate term "drones." Civilian applications for UAS include law enforcement, communications after disasters, industrial monitoring surveys (e.g., electricity networks in remote areas), agricultural services, public safety and police communications, weather monitoring, earth science remote sensing, film-making, and package delivery. Numerous additional applications, like the rapidly growing applications for smartphones that use iPhone operating systems (iOS) or Android," will surely arise in the near future when UAS are (likely) permitted for public use. At the present time, UAS are only authorized for use by military and specially licensed operators in the United States. The licensed operators have to report detailed specifications of flying locations and be pre-approved.

Several organizations, including the Federal Aviation Administration (FAA), the Department of Defense (DOD), the National Aeronautics and Space Administration (NASA), and many standards bodies, such as the Radio Technical Commission for Aeronautics (RTCA) [2], the International Civil Aviation Organization (ICAO) [3], and the International Telecommunications Union (ITU) [4], are presently working on integrating UAS into the airspace worldwide. In the USA, this is termed the National

Airspace System (NAS). All UAS must follow the standards that are being established in order to fly safely in the NAS. UAS will have to be able to communicate with ground stations in the first phase of their deployment into the NAS; later phases of operation in the NAS will allow the UAS to exchange data with satellites, and may also allow for air-to-air relay. Only communication required for UAS control is addressed by the standards[1], and this part of communications is termed "control and non-payload communications" (CNPC). Two civilian bands were recently allocated for CNPC: the L-band (960-1215 MHz)[2] and C-band (5030-5091 MHz) [5]. The RTCA special committee (SC) 228 is responsible for developing CNPC specifications for UAS in the United States. RTCA recommendations will also likely guide action for the ICAO, which in turn provides inputs to the ITU.

We are collaborating with NASA Glenn Research Center (GRC) on a project (the University of South Carolina, USC, project) entitled "Unmanned Aircraft Systems (UAS) Research: The AG Channel, Robust Waveforms, and Aeronautical Network Simulations." The project is part of a large NASA project entitled "Unmanned Aircraft Systems (UAS) Integration in the National Airspace System (NAS)", which includes detailed investigations of communication system elements (air-to-ground radio channel characteristics, prototype radio evaluation, and full-scale nationwide simulation of UAS networking), as well as system-level topics such as "sense and avoid" interoperability, and human systems integration. Our USC project covers several communication system

[1] This is true for air-ground links, at least initially; it may not be true for satellite links, and will likely not be true for air-air links.
[2] L-band 960-1215 MHz is used for multiple aeronautical and radio navigation applications. RTCA plan to use the cleanest portion 960-977 MHz for CNPC link.

areas, and in this dissertation we focus on quantification of air-to-ground (AG) channel characteristics.

1.2 INTRODUCTION TO WIRELESS CHANNEL MODELING

One of the most serious hindrances to reliable communication is the wireless channel. The narrowband channel model that encompasses path loss, small scale fading and shadowing loss is vital for accurate link budgets and specifying transmitter power requirements. Path loss typically increases with frequency and distance between transmitter (Tx) and receiver (Rx). The line-of-sight (LOS) can be blocked by terrain, buildings, trees, vehicles, etc. Such blockage is often called shadowing. Other than path loss and shadowing loss, the channel is also degraded by small scale fading caused by multipath propagation. An illustration of narrowband channel effects vs. distance is shown in Figure 1.1. The green line indicates an example value of path loss or attenuation above which the radio link is not available (outage). If only average path loss (blue dashed straight line) is considered, the link distance can be up to 45 km. Small scale fading (red curve) makes the path loss vary considerably, and depending upon outage definition, with small scale fading added to path loss, maximum link distance is reduced to less than 20 km. Shadowing may occur at any distance which may also cause an outage for a short duration. Quantitative characteristics of all these effects are essential for radio communication system design.

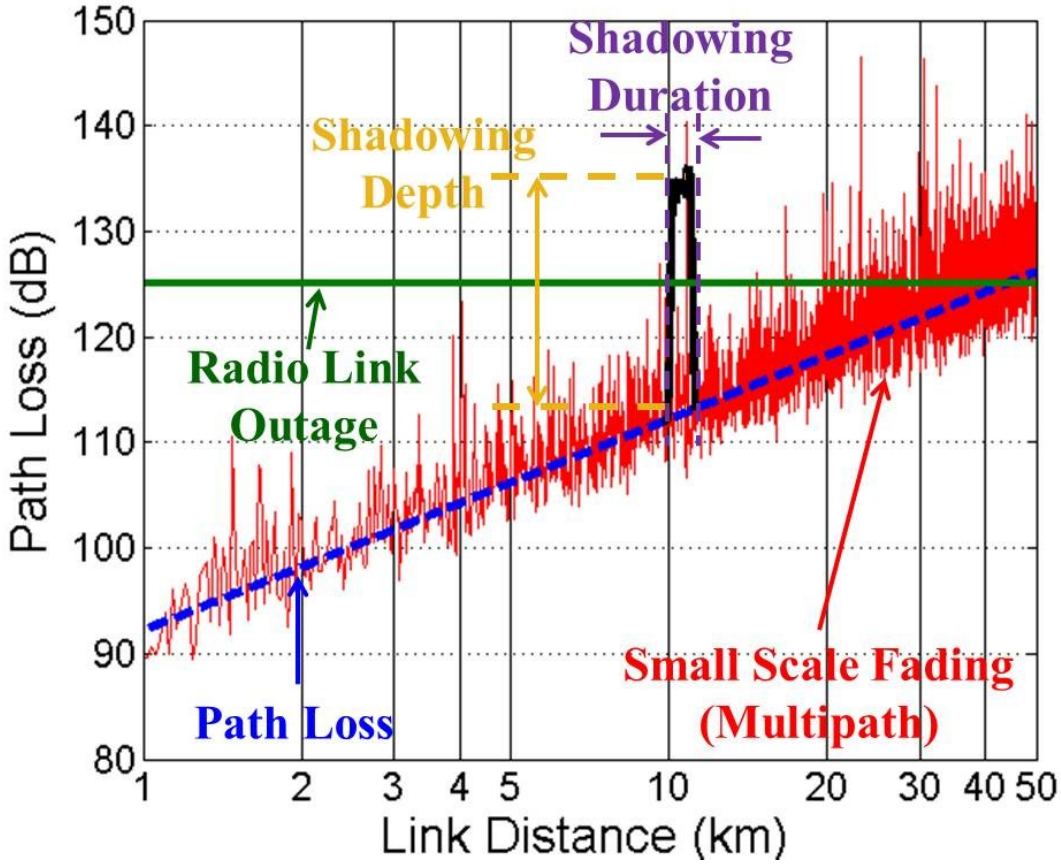

Figure 1.1. Illustration of narrowband channel attenuation vs. distance.

The radio propagation channel generally consists of multipath components (MPCs), and these MPCs can be spread both in delay and spatial angle. The spread in delay can result in frequency selectivity, and for digital communication systems, inter-symbol interference (ISI) can occur, and this becomes more severe as data rate and signal bandwidth increases. In order to develop a high-performance CPNC radio system, all of these channel characteristics, along with some other characteristics such as spatial correlation, inter-band correlation and Doppler spread, must be known—at least in a statistical sense [6].

The existing studies on the AG channel (which is identical to the ground-to-air (GA) channel via reciprocity) are very limited relative to those on terrestrial channels.

Most past research only considered tall ground sites (GSs) in wide open areas, and narrow band signals. Some analytical and measurement results exist for different frequency bands, but very little exists on attenuation caused by the airframe itself (airframe shadowing). For UAS applications, operation may be at very low altitudes, and in cluttered areas, and for these settings, minimal work exists on explicit AG channel characteristics [7] and [8]. The previous studies will be reviewed in Chapter 2.

The AG channel characterization on which we have worked is based on a large amount of empirical data taken in different scenarios, including over sea, over fresh water, hilly terrain, mountainous terrain, near-urban, suburban and desert. Our measurements cover the two UAS bands with one transmitter and two receivers in each band – this is termed a single-input multiple-output (SIMO) channel for each band. More measurements that address GS antenna diversity and different GS antenna heights may also be conducted. From these measurements and from analysis, we have quantied the AG channel's path loss, root-mean-square delay spread (RMS-DS), inter-band and spatial correlation for a specific antenna arrangement, and Doppler shift/spread. From all these channel characteristics, statistical tapped delay line (TDL) models for the AG channels have been generated.

1.3 NON-STATIONARY CHANNELS

The so-called wide-sense stationary (WSS) channel is defined as one for which the fading statistics do not change over a short interval [9] (or equivalently for mobile platforms, over a short distance). An uncorrelated scattering (US) channel is one in which the contributions from primary scatterers with different delays are uncorrelated. The correlation between MPCs is another important channel feature. With the (common)

assumption of a WSS-US channel, Doppler spread can be estimated from the autocorrelation of the channel impulse response (CIR) via time-frequency transform (the Fourier transform).

Mobility causes channel time variation and Doppler shifts. The velocity of a typical aircraft may be a few hundred meters per second, which is much larger than that in terrestrial channels. The relative velocity between aircraft and potential reflectors on the ground can be much slower, depending upon link geometry. The estimation of stationarity intervals (or distances, given a specific velocity) is of interest for the CPNC design. No explicit study on this has been reported as far as we are aware.

1.4 DISSERTATION OBJECTIVES

In this section, a list of the dissertation objectives is presented.

1. [Chapter 2] Perform a literature review of the state of art on characterization of aeronautical radio propagation channels.

   Review typical aeronautical communication systems and their operating frequency, bandwidth, modulation and other physical layer technologies. Review the existing studies on AG channel measurements, simulations and models, and note the main conclusions and findings. Discuss the major gaps that we fill in the dissertation.

2. [Chapter 3] Describe the measurements, initial data processing algorithms and evaluation of stationarity distance.

   Present the NASA AG channel measurement campaign and detailed description of the measurement system including channel sounder, aircraft, ground station and antennas. Describe the algorithms used for “raw” data processing, noise

removal and alignment of power delay profiles (PDP) to GPS data. Describe the performance of the channel sounder in a back-to-back mode. Describe estimation of the stationarity distance (where the channel characteristics are wide sense stationary) based on measured data.

3. [Chapter 4] Develop earth surface reflection based deterministic models and provide their limitations and corrections.

   Generate both flat earth two-ray (FE2R) and curved earth two-ray (CE2R) analytical channel models. Obtain improvements for the CE2R model, including incorporation of spherical earth divergence, atmospheric refraction and earth surface roughness. Indicate the limitations of the CE2R model for AG channels. Discuss other effects for the AG channel, including those from atmospheric gases, hydrometeor attenuation, and ducting.

4. [Chapter 5] Generate narrowband AG channel models that address path loss, small scale fading and airframe shadowing.

   Develop both log-distance and corrected CE2R path loss models based on empirical data for different scenarios. Estimate the small scale fading Ricean *K* factor. Model shadowing by aircraft wings in some special maneuvers.

5. [Chapter 6] Quantify delay dispersion and multipath components.

   Report the measured RMS-DS and illustrate dynamics via example sequences of PDPs. Develop TDL models for the AG channels that quantify MPC probability of presence ("on" probability or "birth" of MPCs), magnitude and fading, phase, delay, and duration.

6. [Chapter 7] Investigate inter-receiver correlations.

Quantify the spatial correlation between two intra-band aircraft antennas via both analytical CE2R method and measured data. Evaluate the relation between C-band and L-band LOS components by estimating their cross correlation.

7. [Chapter 8] Summarize the dissertation and indicate future work.

1.5 DISSERTATION CONTRIBUTIONS

The project "Unmanned Aircraft Systems (UAS) Research: The AG Channel, Robust Waveforms, and Aeronautical Network Simulations" started in August 2012. We have eight project reports submitted to NASA GRC and I co-authored six of them. We have three journal papers and eleven conference papers published or submitted[3].

In addition to the NASA project, I have five journal papers and seven conference papers (some of them are still under review) focusing on indoor propagation channels and vehicle-to-vehicle (V2V) channels.

NASA Reports:

[R1] D. W. Matolak, **R. Sun**, "AG Channel Measurement & Modeling Results for Over-Water & Hilly Terrain Conditions," (Report #7) NASA Grant #NNX12AR56G, 26 September 2014.

[R2] D. W. Matolak, **R. Sun**, "AG Channel Measurement & Modeling Results for Over-Sea Conditions," (Report #6) NASA Grant #NNX12AR56G, 3 December 2013.

[R3] D. W. Matolak, "AG Channel Measurements & Modeling: Year One Results," NASA Grant #NNX12AR56G, 26 July 2013

[R4] D. W. Matolak, **R. Sun**, "AG Channel Measurements & Modeling: BVS Channel Sounder Performance: Measurement Stability," (Report #5) NASA Grant #NNX12AR56G, 19 April 2013.

[3] The notation J denotes journal paper, C denotes conference paper and R denotes technical reports.

[R5] D. W. Matolak, **R. Sun**, "AG Channel Measurements & Modeling: Initial Channel Sounder Laboratory & Flight Tests—Supplementary Report," (Report #4) NASA Grant #NNX12AR56G, 1 March 2013.

[R6] D. W. Matolak, **R. Sun**, "AG Channel Measurements & Modeling: Initial Channel Sounder Laboratory & Flight Tests," (Report #3) NASA Grant # NNX12AR56G, 29 January 2013.

[R7] D. W. Matolak, **R. Sun**, "AG Channel Measurements & Modeling: Initial Analysis & Flight Test Planning," (Report #2) NASA Grant #NNX12AD53G, 8 June 2012.

[R8] D. W. Matolak, "The Air-Ground Channel: Literature Review, and Channel Modeling for UAS Transmission Scheme Design and Evaluation," (Report #1) NASA Grant #NNX12AD53G, 29 June 2011.

Articles from the AG channel project:

[J1] D. W. Matolak, **R. Sun**, "Air-Ground Channel Characterization for Unmanned Aircraft Systems—Part I: Methods, Measurements, and Models for Over-water Settings," *IEEE Transactions on Vehicular Technology*, Submitted, Mar. 2015.

[J2] D. W. Matolak, **R. Sun**, "Unmanned Aircraft Systems: Air-Ground Channel Characterization for Future Applications," *IEEE Vehicular Technology Magazine*, vol. 10, no. 2, pp. 79-85, June 2015.

[J3] D. W. Matolak, **R. Sun**, "Air-Ground Channel Measurements and Modeling for UAS," *IEEE A&E Systems Magazine*, vol. 29, no. 11, pp. 30-35, Nov. 2014 (invited, converted from a conference paper [8]).

[C1] D. W. Matolak, **R. Sun**, "Effects of Stationarity Distance on Small Scale Channel

Statistics in Air-Ground Channels," *2016 IEEE Aerospace Conference*, Submitted, Big Sky, MT, 5-12 March 2016.

[C2] D. W. Matolak, **R. Sun**, "Air-Ground Channel Characterization for Unmanned Aircraft Systems: the Near-Urban Environment," *2015 Military Communications Conference (MILCOM 2015)*, Submitted, Tampa, FL, 26-28 Oct. 2015.

[C3] **R. Sun**, D. W. Matolak, "Air-Ground Channel Characterization for Unmanned Aircraft Systems: the Mountainous Environment," *2015 IEEE/AIAA 34th Digital Avionics Systems Conference (DASC 2015)*, Accepted, Prague, Czech Republic, 13-17 September 2015.

[C4] H. Jamal, D. W. Matolak, **R. Sun**, "Comparison of L-DACS and FBMC Performance in Over-water Air-Ground Channels," *2015 IEEE/AIAA 34th Digital Avionics Systems Conference (DASC 2015)*, Accepted, Prague, Czech Republic, 13-17 September 2015.

[C5] **R. Sun**, D. W. Matolak, "Initial Results for Airframe Shadowing in L- and C-band Air-Ground Channels," *2015 Integrated Communications, Navigation and Surveillance (ICNS) Conference*, pp. , Herndon, VA, 21-23 April 2015. ***(Won the best student paper).***

[C6] **R. Sun**, D. W. Matolak, "Over-Harbor Channel Modeling with Directional Ground Station Antennas for the Air-Ground Channel," *2014 Military Communications Conference (MILCOM 2014)*, pp. 1-6, Baltimore, MD, 6-8 Oct. 2014.

[C7] D. W. Matolak, **R. Sun**, "Antenna and Frequency Diversity in the Unmanned Aircraft Systems Bands for the Over-Sea Setting," *2014 IEEE/AIAA 33rd Digital Avionics Systems Conference (DASC 2014)*, pp. 6A4-1 - 6A4-10, Colorado Springs, CO, 5-9 Oct. 2014.

[C8] D. W. Matolak, **R. Sun**, "Air-Ground Channel Characterization for Unmanned Aircraft Systems: the Hilly Suburban Environment," *2014 IEEE 80th Vehicular Technology Conference (VTC'14 Fall)*, pp. 1-5, Vancouver, Canada, 14-17 Sept. 2014.

[C9] D. W. Matolak, **R. Sun**, "Air-Ground Channel Characterization for Unmanned Aircraft Systems: The Over-Freshwater Setting," *2014 Integrated Communications, Navigation and Surveillance (ICNS) Conference*, pp. 1-9, Herndon, VA, 8-10 April 2014. ***(Won the best session paper).***

[C10] D. W. Matolak, **R. Sun**, "Initial Results for Air-Ground Channel Measurements & Modeling for Unmanned Aircraft Systems: Over-Sea," *2014 IEEE Aerospace Conference*, pp. 1-15, Big Sky, MT, 1-8 March 2014.

[C11] D. W. Matolak, **R. Sun**, "Air-Ground Channel Measurements & Modeling for UAS," *2013 Integrated Communication, Navigation and Surveillance (ICNS) Conference*, pp. 1-9, Herndon, VA, 22-25 April 2013. ***(Won the third place of professional paper).***

Articles outside the AG channel project:

[J1] **R. Sun**, D. W. Matolak, P. Liu, "5-GHz V2V Channel Characteristics for Parking Garages," *IEEE Transactions on Vehicular Technology*, Submitted, May 2015.

[J2] P. Liu, D. W. Matolak, B. Ai, **R. Sun**, Y. Li, "5 GHz Vehicle-to-Vehicle Channel Characterization for Example Overpass Channels" *IEEE Transactions on Vehicular Technology*, Accepted, May 2015.

[J3] **R. Sun**, D. W. Matolak, "Path Loss and Delay Spread for the Stairwell Channel at 5 GHz," *International Journal of Communication Systems*, Early view:

http://onlinelibrary.wiley.com/doi/10.1002/dac.2920/abstract, Jan. 2015.

[J4] P. Liu, D. W. Matolak, B. Ai, **R. Sun**, "Path Loss Modeling for Vehicle-to-Vehicle Communication on a Slope," *IEEE Transactions on Vehicular Technology*, vol. 63, no. 6, pp. 2954-2958, July 2014.

[J5] **R. Sun**, D. W. Matolak, "Characterization of the 5-GHz Elevator Shaft Channel," *IEEE Transactions on Wireless Communications*, vol. 12, no. 10, pp. 5138-5145, Oct. 2013.

[C1] D. W. Matolak, **R. Sun**, P. Liu, "V2V Channel Characteristics and Models for 5 GHz Parking Garage Channels," *9th European Conference on Antennas and Propagation (EuCAP 2015)*, pp. 1-4, Lisbon, Portugal, 12-17 April 2015.

[C2] P. Liu, B. Ai, Y. Li, **R. Sun**, "A Message Broadcast Model for Train-to-Train Communication Network," *Multimedia and Ubiquitous Engineering (MUE 2014)*, vol. 308, pp. 345-352, Zhangjiajie, China, 28-31 May 2014.

[C3] P. Liu, B. Ai, Y. Li, **R. Sun**, "Urban Viaduct Channel Characterization of Train-to-Train Communication at 900 MHz," *Multimedia and Ubiquitous Engineering (MUE 2014)*, vol. 308, pp. 353-360, Zhangjiajie, China, 28-31 May 2014.

[C4] P. Liu, B. Ai, D. W. Matolak, **R. Sun**, "V2V Path Loss Modeling for Example 5 GHz Overpass Channels," *2014 IEEE 79th Vehicular Technology Conference (VTC'14 Spring)*, pp. 1-5, Seoul, South Korea, 18-21 May 2014.

[C5] P. Liu, B. Ai, D. W. Matolak, J. Ding, **R. Sun**, Y. Li, "Wave-Guide Effects in Urban Viaduct Propagation Channels for High-Speed Railway At 930 MHz," *8th European Conference on Antennas and Propagation (EuCAP 2014)*, pp. 3479-3483, Hague, The Netherlands, 6-11 April 2014.

[C6] D. W. Matolak, **R. Sun**, ”Elevator Shaft Channel Characteristics at 5 GHz,” *2013 IEEE Global Communications Conference (GLOBECOM)*, pp. 3931-3935, Atlanta, GA, 9-13 Dec. 2013.

[C7] **R. Sun**, D. W. Matolak, P. Liu, “Parking Garage Channel Characteristics at 5 GHz for V2V Applications,” *2013 IEEE 78th Vehicular Technology Conference (VTC’13 Fall)*, pp. 1-5, Las Vegas, NV, 2-5 Sept. 2013.

CHAPTER 2

LITERATURE REVIEW

2.1 VHF AG CHANNEL

A number of typical civil air-ground aeronautical communications systems are listed in Table 2.1. The Aircraft Communications Addressing and Reporting System (ACARS) may be viewed as a pioneer of modern air-ground communications system. ACARS operates in the very high frequency (VHF) band. It was developed in 1978 and employed analog radio with amplitude modulation [10]. Voice signals sent over radios with bandwidth of approximately 3 kHz were implemented in ACARS for providing flight services and operating Air Traffic Control (ATC) system functions.

In order to increase the capacity and improve the performance, the VHF digital link or VHF data link (VDL) standards were defined by the Aeronautical Mobile Communications Panel (AMCP) in the 1990s [11]. The 19 MHz bandwidth allocated to aeronautical communications in the VHF band (118-137 MHz) is also used for VDL applications. The VHF band for VDL is divided into 760 channels with 25 kHz for each channel [12]. A more sophisticated aeronautical system is the broadband VHF (B-VHF) aeronautical communication system, which is based on multi-carrier code division multiple address (MC-CDMA) [13]. Orthogonal frequency-division multiplexing (OFDM) is employed in B-VHF with subcarrier spacing of 2 kHz. The B-VHF system has not been implemented. The majority of studies for VHF band aeronautical channels

Table 2.1. Typical Air-Ground Aeronautical Communications Systems.

Name	Band	BW	Modulation	Year	Designer	Comments
Aircraft Communications Addressing and Reporting (ACARS) [10]	VHF, 118-137 MHz	3 kHz/channel	AM	1978	ARINC Inc. (now part of Rockwell Collins Inc.)	A pioneer "modern" aeronautical communication system
VHF Digital Link (VDL) [11]	VHF, 118-137 MHz	19 MHz (25kHzX760 channels)	D8PSK	1990s	Aeronautical Mobile Communications Panel (AMCP) under EUROCONTROL [14]	Upgraded from ACARS
Broadband VHF (B-VHF) [13]	VHF, 118-137 MHz	2 kHz/subcarrier	MC-CDMA+OFDM		European 6th Framework (FP6) program	First multi-carrier modulation aeronautical link (not implemented to date)
Universal Access Transceiver (UAT) [15]	L-band, 978 MHz	3 MHz	TDMA+BCPFSK	2002		Designed for surveillance, Automatic Dependent Surveillance — Broadcast (ADS-B)
Project 34 (P34) [16]	767-773 MHz (Forward Link) 797-803 (Reverse Link)	5.4 kHz/sub-channel X 8, 16, 24 channels = 50, 100,150 kHz	OFDM	2003	Electronic Industry Association (EIA) & Telecommunications Industry Association (TIA)	Designed for public safety; candidate for future aeronautical communications (not implemented to date)
Broadband Aeronautical Multi-Carrier System (B-AMC) [17]	L-band, 980-1140 MHz	10.416 kHz/sub-channel X 48 sub-channels = 500 kHz	FDD+OFDM	2007	FAA & EUROCONTROL	Upgraded from B-VHF (not implemented to date)
L-band Digital Aeronautical Communication System of Type 1 (L-DACS1) [18] [19]	L-band, 960-1164 MHz	9.76 kHz/sub-channel X 51 channel = 498 kHz	FDD+OFDM	2009	EUROCONTROL	Based on B-AMC & P34, similar to WiMAX (not implemented to date)
L-band Digital Aeronautical Communication System of Type 2 (L-DACS2) [20]	L-band, 960-975 MHz	200 kHz/channel	TDD+GMSK	2009	EUROCONTROL	Based on GSM, UAT and VDL Two proposed systems (not implemented to date)
Microwave Landing System (MLS) [21]	C-band, 5031-5090.7 MHz	300 kHz	FM	1980s	FAA, NASA & US DOD	All-weather, precision but short range landing system
Control and Non-Payload Communications (CNPC)	L-band, 960-977 MHz & C-band, 5030-5091 MHz	Being designed			Radio Technical Commission for Aeronautics (RTCA) under US DOT	Designed for UAS integration into NAS

were before the new millennium. A summary of previous studies is provided in Table 2.2.

Reference [22] is the one of the earliest papers on the AG channel. The path loss was reported in the VHF band with aircraft altitude in the range from 10,000 to 30,000 ft. over the Pacific Ocean. The GS antennas were two dipole arrays elevated to 1450 and 1600 ft. above sea level. Beyond-the-horizon or 500+ miles propagation was proved possible for AG channel. In [23], based on empirical data, tree attenuation in the VHF band with vertically polarized antennas was found to be approximately 1.5 dB/100 ft. if the signal propagates through a forest. The signal is attenuated by 0.7 dB/100 ft. if it passes within 0.5 Fresnel ellipses. However, the 0.5 Fresnel ellipses were not defined.

Reference [24] is one of the first stochastic AG channel models. Analytical autocorrelation of two quadrature parts of the diffuse component and power spectrum of the diffuse component were proposed and validated by empirical results at UHF/VHF. The aircraft height was 4,000 ft. with velocity of 270 miles/hour within ranges of 18 miles. The LOS component was always strong and the Ricean fading model was concluded as being appropriate, but no Ricean K factor was reported. Based on AG measurements conducted near an airport in France, large scale path loss is modeled a two-ray (combined by the LOS component and ground reflection) model with free space mean power in [25].

References [26] and [27] are the first on wideband AG channel models. The measurement equipment was a sliding correlator at 135 MHz with chip rate of 5 MChips/s. The signal bandwidth was ~4 MHz. Based on two measurements taken in airports at Aspen, CO, and Duluth MN, the Ricean K factor ranged from 2.6 to 19.7 dB

with an average of 16 dB. No distributions of *K*-factor were reported. Two ray effects were observed, and the channel dispersion, quantified by the RMS-DS, was on average 4 microseconds and followed a Gaussian distribution with standard deviation of 1.2/1.5 microseconds. The path loss exponent was smaller than 2 near the airport and explained by ducting; the exponent was approximately 4 at large distances for Aspen. The large distance path loss exponent was close to 2 in Duluth and the authors concluded this as evidence of the absence of a strong ground reflection. Detailed information about the flight test was not provided, such as aircraft and GS altitudes, distance, velocity, antenna patterns and weather.

The authors of [28] classified the aeronautical channel into several classes: parking, taxiing, en-route and landing. The Doppler power spectrum, Ricean *K* factor and delay statistics in the VHF band were summarized based on previous studies [29], [30], [24], [25]. Wideband aeronautical channel models for implementation of channel emulators were proposed. No new results were provided, and the previous studies used by the authors rely on some terrestrial channels, not completely appropriate for the AG setting. The authors expanded their work in [31] with more details. The bit error ratio (BER) of OFDM quadrature phase-shift keying (QPSK), estimated via simulations, was reported based on the channel models.

2.2 L-BAND AG CHANNEL

Due to the congestion in the VHF band, many new aeronautical links were proposed in L-band, as listed in Table 2.1, including Universal Access Transceiver (UAT) [15] for surveillance, Broadband Aeronautical Multi-Carrier System (B-AMC) [17], L-band Digital Aeronautical Communication System of Type 1 (L-DACS1) [18]

and [19], L-band Digital Aeronautical Communication System of Type 2 (L-DACS2) [20] and CNPC. Another cluster of publications for the AG channel pertains to L-band. In [32], only the surface reflection was considered as multipath. An analytical two-ray model was derived and validated with narrowband experimental data taken in L-band (1463 MHz) with both vertical and horizontal polarizations. The surface roughness was modeled as a Gaussian variable which only affects the magnitude of the reflection coefficient. The measurements were made for reflection areas including calm ocean, swamp and cultivated fields. In [33], over ocean data was collected at 1.6 GHz between a satellite and aircraft. Amplitude, power spectral density, polarization and selective fading properties were reported. In [34], narrowband AG channel measurements were conducted near Chicago and San Francisco at 900 MHz. The GS height was 5~12 meters and aircraft altitude was up to 13,000 m. The link distance reached up to 320 km. The path loss was modeled via the two-ray model. Three sets of narrowband downlink (Tx on the aircraft & Rx on the ground) tests were taken at 2.3 GHz over desert and ocean in [35]. The Ricean *K* factor ranged from 7 to 24 dB. The AG channel was modeled as composite of LOS, earth surface reflection and diffuse components. Note that multipath was suppressed by using a very high gain tracking receiver antenna which yields very narrow beamwidth. The data sets show that the AG channel can be well approximated by an additive white Gaussian noise (AWGN) channel with a strong specular reflection whose amplitude is 20% to 80% that of the LOS, and with diffuse MPCs whose power is 10 to 20 dB smaller than that of the LOS. The *K* factor decreased as the earth surface reflection coefficient increases. As in other publications, much detailed information in [35] is missing, including altitude, grazing angle. One data segment in [35] had a *K* factor of -48

dB, and this was explained by strong reflections by the wing and fuselage during some specific maneuvers. The specular reflection coefficient was estimated by the maximum likelihood (ML) method.

Space diversity of the AG channel was investigated in [36] at 2 GHz with a signal bandwidth of 12.5 kHz. Four identical Rx monopoles were elevated 1.5 m above ground with three locations (motionless) on an urban street. The antennas were on corners of a square with sides of 1.5 wavelengths. The Tx monopole was mounted on the bottom of an airship. The airship flew above the city of Prague, Czech Republic, with different routes. The distance ranged 1 to 6 km, the altitude was 100 to 170 m to achieve elevation angles from 1 to 6 degrees. The spatial correlation among different antennas was below 0.3. The diversity gains with three diversity methods were reported with respect to elevation angle, location of Rxs and number of channels. The diversity gain did not significantly depend on elevation angle. The same authors of [36] expanded their work with four Rx antennas in wooded areas with measurements using similar experimental equipment [37]. The spatial correlation among antennas was below 0.2. Higher diversity gain was achieved in wooded areas than in open urban areas. In [38], the antenna diversity (spatial correlation) of AG UAV 802.11 Mesh Network was evaluated by packet loss instead of the typically used signal amplitude correlation. The frequency was not precisely specified, but was likely in the 2.4 GHz (Wi-Fi) band.

The authors of [39] reported empirical AG channel results over a smooth surfaced dry lake bed in Edwards AFB in California at L & lower S-band with a 10 MHz bandwidth. A vertical omni-directional antenna was mounted on the aircraft and a parabolic reflector tracking antenna was used on the receiving ground station. The

received power spectrum and reflection coefficient were evaluated. The AG channel was modeled as consisting of 3-rays: the LOS, specular reflection (relative amplitude 70~96% of LOS, excess delay 10-80 ns) and the third component (relative amplitude 2-8% of LOS, excess delay 155 ns, RMS-DS 74 ns). In [40], the same lead author of [39] conducted measurements at an army fort in Arizona. Four Tx antennas mounted on a helicopter (one on the roof, two on the bottom and one on the tail) with flight height of 15-20 ft. Two tracking parabolic reflector Rx antennas were elevated 60 ft. above ground. The transmitted signal was centered at 1800 MHz (upper L-band) with a 50 MHz bandwidth. The authors found that a strong LOS was always present. The RMS-DS ranged from 15 to 153 ns. The maximum excess delay was 1300 ns (power of this corresponding MPC was more than 25 dB below the strongest one). The diversity gain of aircraft antennas was on average 13 dB. In [41], wideband measurements were conducted at 2.05 GHz. A 80 Mcps direct sequence spread spectrum (DSSS) transmitter with a vertically polarized monopole was mounted on an aircraft. The receiver was located on the campus of Virginia Tech, with a four-element antenna array a few meters above the ground. The aircraft flew along constant circles with elevation angles of 7.5, 15, 22.5 and 30 degrees (altitude ranged from 1500 to 2100 feet above ground). Based on power delay profiles, the mean RMS-DS decreased from 98 to 18 ns as the elevation angle increased. Mean & maximum delay spreads were evaluated with 10, 20, 25 and 30 dB thresholds, and it was found that these delay spreads decrease as elevation angle increases. The number of MPCs was 7 or 8 for all elevation angles. The signal envelope followed a Ricean distribution but the Ricean *K* factor was not provided. Based on fading envelope CDFs, the authors concluded that small elevation angles have smaller *K* factors. Only 2.5

dB (modest) antenna diversity gains were achieved compared to a single monopole. A log-scale distance path loss model was reported at the end, with a path loss exponent of 4.1 with standard deviation of 5 dB; this is questionable since the flight track was along a constant link distance circle.

The authors of [42] simulated a coverage footprint for air-to-ground low altitude platforms in urban environments. The low altitude platforms (below 10,000 m) are motionless UAS that are designed to provide temporary wireless communication services as a base station. Two distinct 3-D simulations were conducted via ray-tracing and Matlab® at 700 MHz, 2 GHz and 5.8 GHz. Buildings were assumed to be cubic with a square horizontal cross section but different heights. According to ITU-R P.1410-2, the propagation environment is further classified into suburban, urban, dense urban, and high rise urban, based upon building density and heights. The propagation mechanisms are classified into three types: 1) LOS (free space); 2) NLOS but still receiving coverage via reflections and refraction; and 3) poor coverage that suffering deep fading resulting from consecutive reflections and diffractions. Path loss results were collected from the simulations, and path loss histograms and CDFs were provided; path loss was also estimated as a function of elevation angle.

In [43], experimental data for an AG channel were collected in a rural area at 915 MHz with a 10 MHz bandwidth signal. The aircraft was 200 m above the ground with two quarter wave helical transmitter antennas mounted under aircraft wings. A linear array of eight quarter wave helical antennas was mounted on the roof of a van for the ground station (the ground reflection is unlikely present). The aircraft flew along a circle with link distance less than 1 km. The RMS-DS was near 100 ns for most of the time but

reached a maximum of 500 ns. Spatial correlation at the GS was estimated as the cosine of the Hermitian angle, by which the presence of non-planar wave front was concluded. MIMO is useful to improve the outage probabilities and the channel capacity were also reported.

2.3 C-BAND AG CHANNEL

The limited spectrum available in L-band does not satisfy the demand of video services that may be desired for UAS. Dual-band links that employ both C-band and L-band are being designed. In this configuration, the L-band can transmit low rate messages and provide large coverage while the C-band is used to transmit video signals at relatively short distances. The microwave landing system (MLS) [21] may be the earliest C-band application in the AG channel. It was designed in the 1980s and uses a signal bandwidth as large as 300 kHz. In [44], empirical narrowband data were collected at C-band (5.8 GHz) near an airport. The aircraft (Tx) antenna was a monopole. The GS (Rx) used a directional antenna with beamwidth smaller than 10 degrees. The aircraft height was 300 ft. with distance up to 83 km. The *K* factor was reported as 0 dB for parking, 5 dB for taxiing, 10 dB for landing and 15 dB for en-route conditions. The method used for *K* factor computation and the stationarity distance over which the *K* factor was computed are not provided.

Meng and Lee published a series of AG channel papers in C-band. In [45], a blade monopole at 5.7 GHz was mounted on top of an aircraft. The aircraft flew along a circle with 5 km radius at height of 6.4 km and up to 102 km away from the GS. An elevated duct effect was not present. Wing shadowing occurred and was verified by roll and pitch angles. However, roll and pitch angles and the magnitude of shadowing were not

reported. Further study about the aircraft maneuvering shadowing effect was reported in [46]. Empirical data was collected on the South China Sea at 5.7 GHz with a straight flight track (FT) and a circular FT. Roll, pitch, yaw angles and received power over time were provided. The aircraft antenna was mounted on top of the aircraft, and flew at 3.2 km height. Two GS antennas were at heights of 7.65 m and 2.1 m. The wing shadowing was found to be 9.5 dB for the straight FT and up to 28 dB for the circular FT. The standard deviation of the received power was 6.77 & 6.49 dB for the two GS antennas. The GS spatial diversity provided no improvement to mitigate the wing shadowing.

A sounding system aiming for AG channel measurement at C-band was proposed in [47]. The system uses binary phase-shift keying (BPSK) modulation with 10 MChips/s. It's somewhat surprising that 190 ns excess delay can be detected with 100 ns delay resolution (reciprocal of 10 MChips/s), so some sort of super-resolution algorithm may have been applied to the measured data. The detailed frequency, transmitting power, noise floor, PDP update rate, minimum RMS-DS were not provided. In [48], empirical data was collected at 5.7 GHz over the South China Sea with a 20 MChips/s channel sounder. Multiple GS antenna heights (7.65 & 2.1 m) were used. The aircraft flew at three different heights of 0.37 km, 0.91 km and 1.83 km. The GS spatial diversity was provided for three aircraft heights. The higher GS antenna was more likely to have multipath than the lower. Analysis of the same set of data as reported in [48] is extended in [49]. The aircraft flew straight toward the GS with distance from 45 to 95 km. The aircraft (Tx) used a blade monopole mounted under the nose of the aircraft and the GS (Rx) used two horn antennas with beamwidths of 20 (azimuth) and 25 (elevation) degrees. The over sea AG channel was modeled as 2-ray for 86% of the time or 3-ray for

95% of the time. The probability of receiving multiple rays increases in two conditions: 1) as the height of GS increases, and 2) as the altitude of aircraft decreases. The probabilities of 1-7 rays were reported, but no excess delays of the multiple rays were provided. The RMS-DS was 20-40 ns for the 1.83 km and 0.91 km flight altitudes, and increased to 335-480 ns for the 0.37 km altitude. A surface duct was hypothesized as the lower GS antenna had a smaller path loss exponent than the higher antenna. The presence of an elevation duct was concluded from the path loss exponent $n<1$ for the 1.83 km altitude flight, whereas the value of n for the other altitudes was from 1.35 to 2.46.

The authors of [50] conducted measurements in C-band (5.12 GHz) with a 20 MHz bandwidth signal. Wing or engine shadowing was observed. Interesting to note is that the authors assumed the belly of an Airbus A320 (where the Rx blade monopole was mounted) was a very large ground plane. They used a numerical electromagnetics computation program (finite-difference time-domain, FDTD) to simulate the shadowing. Up to 15 dB shadowing loss was found and this fit the empirical path loss data.

AG channel measurements made at 8 GHz and taken over the Pacific Ocean near Oxnard were reported in [51]. The Tx was an omni-directional blade antenna mounted on the bottom of the aircraft. The Rx was a parabolic reflector antenna with diameter of 4 ft. (beamwidth unknown). The altitude of the aircraft was 2500 ft. The equipment sampled at 100 MSamples/s. Measurements of two straight FTs were conducted. Surface roughness was discussed, but ducting was not mentioned. The distance range was not reported. The authors concluded a three-ray model was appropriate, and this includes an LOS component, sea-surface reflection and another reflection. The excess delay of the third ray was 69 ns (mean, with a maximum of 283 ns) for calm sea and 54 ns (mean,

maximum 199 ns) for rough sea. The RMS-DS was 31 ns for calm sea and 20 ns for rough sea. The specular reflection magnitude was estimated as 0.68 (-1.7 dB) and 0.52 (-2.8 dB) relative to the LOS for calm and rough sea, respectively. The second reflection's magnitude was 0.06 (-12.2 dB) and 0.09 (-10.5 dB) for calm and rough sea, respectively.

Many publications do not address frequency dependence. The paper [52] is one of the most cited papers for aeronautical/satellite channels. The author provided a theoretical analysis of the earth surface scatter of the aeronautical channel between a satellite and aircraft. A 3D geometrically based single-bounce elliptical (GBSBE) model was proposed for the AG channel in [53]. This model is (roughly) frequency independent. The joint probability function for AOA and delay were derived as a function of elevation angle. The excess delay and AOA were found to increase with elevation angle. The authors only considered ground scattering (no buildings, trees and other obstacles), and the distribution of scatterers used in the simulation was not provided. The strength of scatterers was not reported either. The authors of [54] designed and conducted many tests between a UAV and ground site with commercial Wi-Fi equipment at 0.9 GHz, 2.4 GHz and 5.8 GHz. Not much useful results on the AG channel were reported. One interesting conclusion was that performance with a horizontally oriented aircraft antenna perpendicular to the flight direction was better than that with vertical antenna orientation and horizontal orientation parallel to the flight direction. Unfortunately, detailed information, including type, gain and pattern of both the GS and aircraft antennas, was missing.

The authors of [55] generated path loss and shadowing models for the AG channel based on ray-tracing. The simulation pertains to an area of central Bristol, UK

with nine GS locations. The GS antenna height was 1.5 m. The aircraft altitude ranged from 100 to 2000 m. The frequency was 200 MHz to 5 GHz. An elevation angle based path loss model was proposed. The percentage of LOS/non-LOS (NLOS) regions and shadowing pdfs were reported as well. In [56], the authors note that the AG channel signal may be blocked by the wings or other parts of the aircraft itself. The authors provided a multi-antenna approach to overcome this issue. The performance of unitary space-time codes was evaluated via analysis & simulation, but no AG channel model was reported. The authors of [57] proposed a directional antenna based protocol for a UAV mobile ad hoc network (MANET). The performance including throughout, BER and end-end delay were analyzed via simulations based on path loss model & K factors, but again no AG channel model was reported.

2.4 GAPS IN AG CHANNEL STUDIES

Most of the previous studies for the AG channel, both measurements and modeling, are for narrowband channels, and only for some specific GS local environments. Although some studies pertain to wideband channels, the mean RMS-DS values ranged from 25 to 4000 ns, which is an enormous span of more than two orders of magnitude. This indicates that substantial variety exists in these channels, and the variety has not been captured in detailed models. A TDL model was developed for the over sea environment only [58]. Other environments such as urban and suburban are expected to have more diffuse MPCs.

The stationarity distance (SD) is critical in estimation of small scale fading and spatial correlation. Only recently, with attention paid to more rapidly time-varying channels (e.g, vehicle-to-vehicle [59]), and with more accurate channel characterizations

Table 2.2. Summary of Previous AG Channel Studies.

Band	Site	*K* factor (dB)	Bandwidth (MHz)	σ_τ (ns)	Excess delay (ns)	Comments	Ref.
VHF	Over Sea	--	Narrowband			Beyond-the-horizon propagation was proved possible	[22]
	Tree Cover	--				Tree attenuation with vertical antennas is 1.5 (0.7) dB/100 ft. if the signal propagates through a forest (within 0.5 Fresnel ellipses)	[23]
	Chicago& Minneapolis	--				First stochastic AG model. Rice fading was concluded.	[24]
	Toulouse Blagnac Airport (France)	--				Path loss is modeled by 2-ray with free space mean power.	[25]
	Aspen, CO & Duluth MN	16 (2.6~19.7)	4	4000 (mean), 7200 (max)	--	First wideband model.	[26] [27]
	--	--	--	--	--	Summary of published VHF results. Classify parking, taxiing, taking off, en-route and landing scenarios.	[28] [31]
L-band & lower S-band	NASA Wallops Station, VA	--	Narrowband			1453 MHz.	[32]
	Over Sea	--				Satellite-to-Aircraft channel at 1.6 GHz.	[33]
	Flew between Chicago and San Francisco	--				Path loss was modeled as two-ray.	[34]
	Desert & Over water	9~15				Empirical reflection coefficients were reported	[35]
	Urban, Prague	--				Spatial correlation and diversity gain.	[36]
	Wooded area	--				Spatial correlation and diversity gain.	[37]
	Rural	--				802.11 MESH network. Spatial correlation.	[38]
	Dry lake bed	--	10	74 (mean)	155 (mean)	Three rays.	[39]
	Ft. Rucker, AL	--	50	15~153	1300 (max)	Helicopter-to-ground channel with 4X2 MIMO.	[40]
	Virginia Tech.	--	80	18.3~98.1	89~1570	Fading, antenna diversity were reported.	[41]
	Rural, New York	--	10	~100, <500	--	2×8 MIMO antenna diversity, spatial correlation and channel capacity.	[43]
C-band	Sendai Airport, Japan	0~15	Narrowband			*K* factor: parking 0 dB, taxiing 5 dB, landing 10 dB, en-route 15 dB.	[44]
	Over Sea	--				Wing shadowing found, but not modeled.	[45]
	Over Sea	--				Wing shadowing.	[46]
	--	--	10	--	--	Propose of sounding system in C-band.	[47]
	Over Sea	--	20	--	--	Spatial diversity & statistics of multipath	[48]
	Over Sea	--	20	20-480	--	PL model, MPCs occurrence probability vs. aircraft height.	[49]
	Sonthofen (small city), Germany	--	20	--	--	Wing & engine shadowing.	[50]
	Over Sea	--	100 MSamples/s	25	57 (mean), 283 (max)	8 GHz, three ray, modeled as calm/rough sea.	[51]

desired for wider bandwidths and longer durations, has SD even been considered. Several methods exist and estimates for SD for several terrestrial settings have been made [60]. However, the SD for AG channels has not been investigated yet, where the LOS component is predominant. In this setting the SD is expected to be larger than that in terrestrial channels.

Airframe shadowing is a special characteristic for aeronautical channels. Airframe shadowing has not been explicitly studied in detail, and models for this effect are still not available, although some example data exists [46]. Therefore, comprehensive characterization of wideband AG channel stationarity distance and airframe shadowing is of great interest.

CHAPTER 3

MEASUREMENT CAMPAIGN AND DATA PROCESSING ALGORITHMS

3.1 MEASUREMENT SITES

Although we are not able to conduct tests for all possible environments, measurements were made with the GS in several of the most typical ground environments by NASA Glenn Research Center, including,

- Over water: fresh water [61] & sea water [62] [63] [64] [58] [65] [66];
- Flat terrain: near urban [67], suburban, forest, desert;
- Hilly terrain: suburban, forest [66] [68];
- Mountainous terrain [69].

Five measurement sites were selected in the United States, as shown in Figure 3.1. Cleveland, Ohio is the location of NASA Glenn Research Center. We conducted over fresh water, flat urban and suburban measurements in Cleveland; example FTs are shown in Figure 3.2. Hilly and suburban tests were taken in Latrobe, PA, which is a town in the Appalachian Mountains; see Figure 3.3. Telluride, CO, located in the Rocky Mountains as shown in Figure 3.4, was our mountainous site. Over sea water measurements were taken over the Pacific Ocean near Oxnard, CA (see Figure 3.5). Palmdale, CA is city with flat desert terrain but a mountain ridge to the southeast. We conducted flat suburban and hilly measurements in Palmdale. The detailed GS location descriptions are listed in Table 3.1. Figures 3.7 and 3.8 show the view from the cockpit near Cleveland, and a view of the GS at Latrobe, respectively.

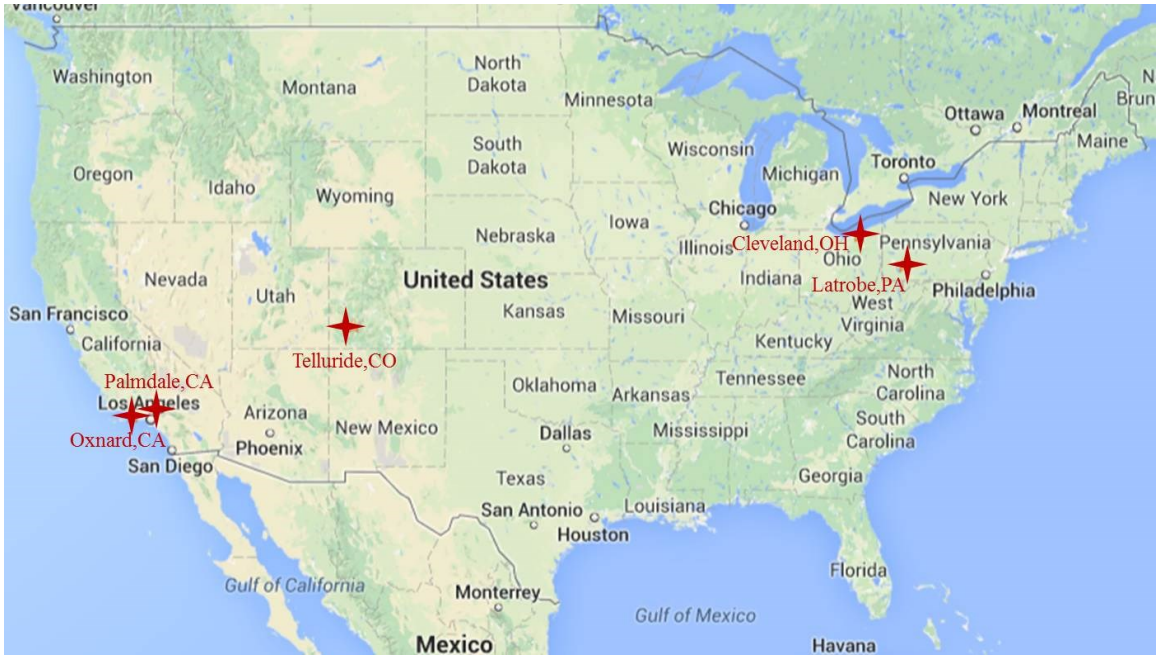

Figure 3.1. Measurement Sites in the United States.

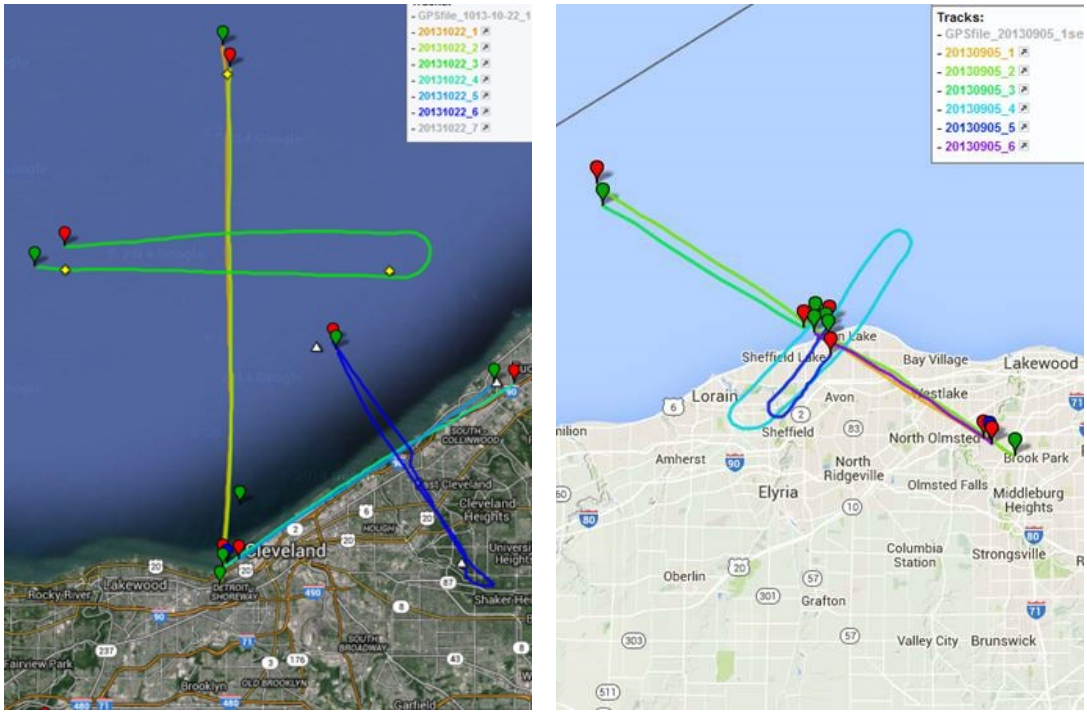

(a) (b)

Figure 3.2. Example FTs in Cleveland, OH, (a) over freshwater and urban taken on 10/22/2013; (b) suburban taken on 09/05/2013.

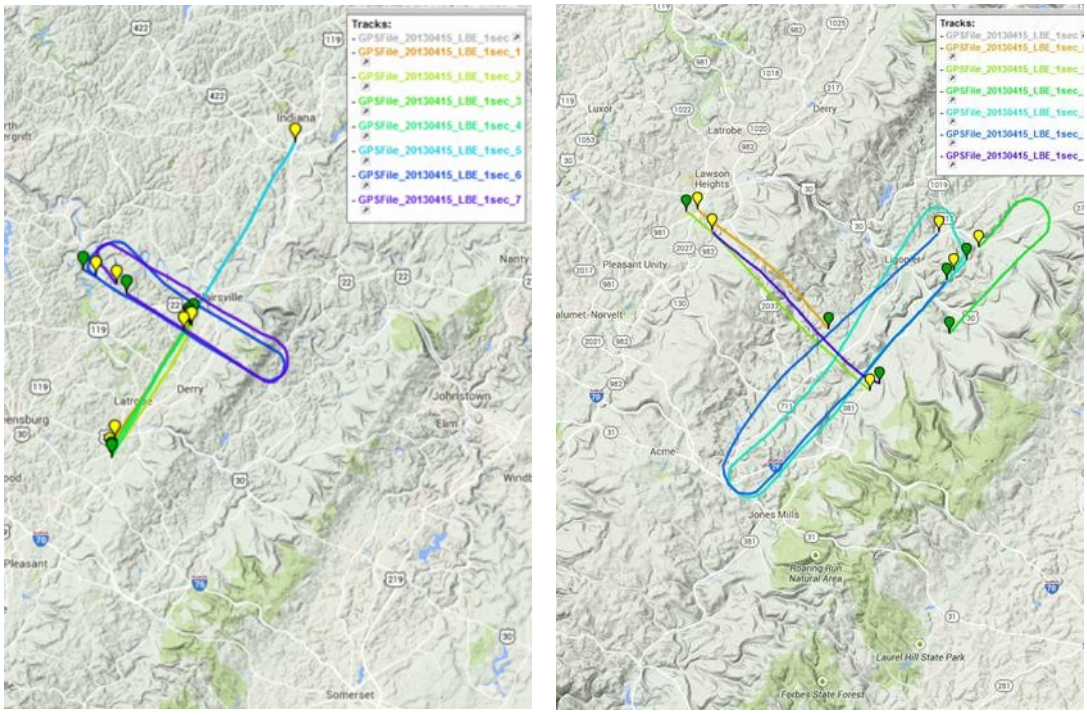

(a) (b)

Figure 3.3. Example FTs in Latrobe, PA taken on 04/15/2013, (a) suburban (over Latrobe township); (b) hilly.

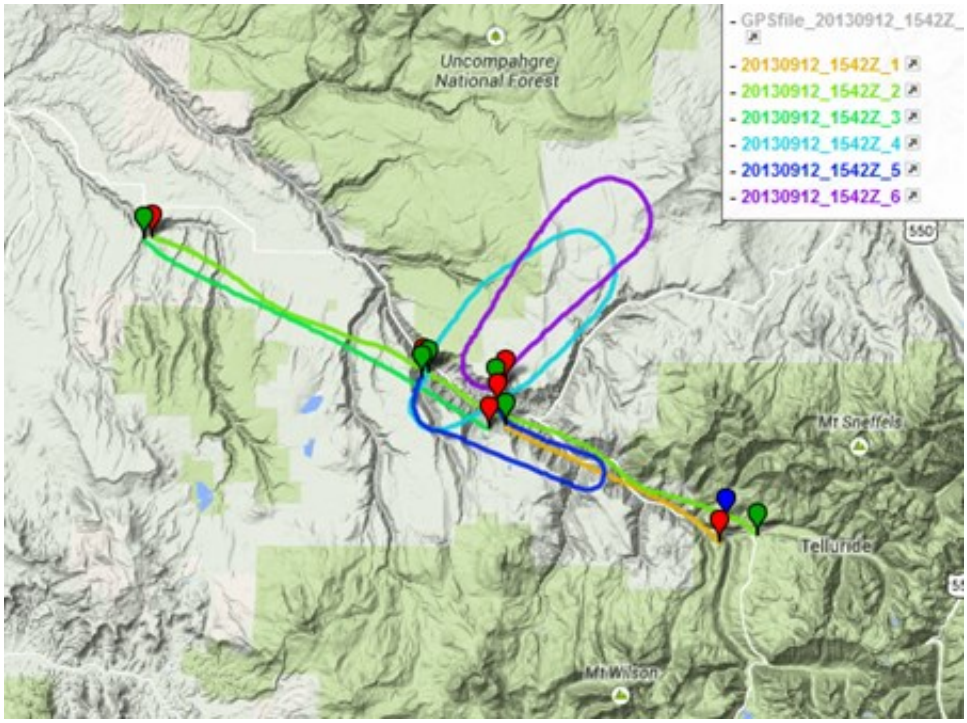

Figure 3.4. Example FTs in Telluride, CO taken on 09/12/2013, mountainous.

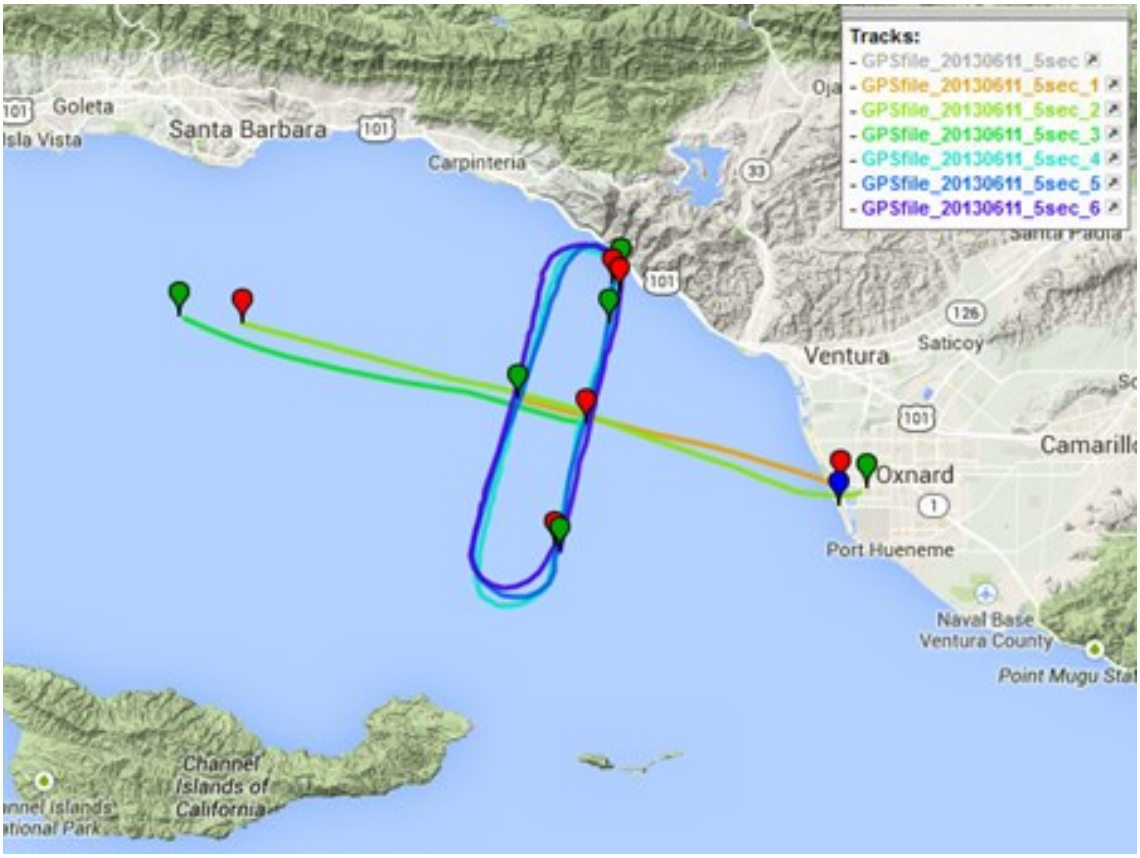

Figure 3.5. Example FTs in Oxnard, CA taken on 06/11/2013, over sea.

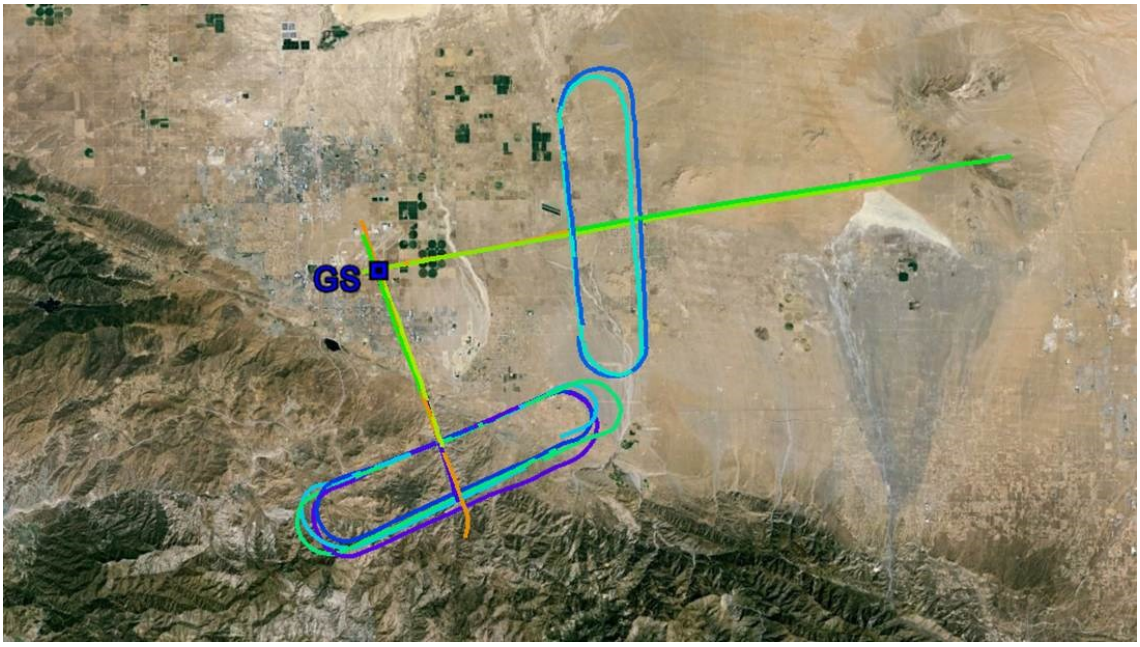

Figure 3.6. Example FTs in Palmdale, CA taken on 06/12/2013 and 06/13/2013, suburban and hilly.

Figure 3.7. View from the cockpit in Cleveland, OH.

Table 3.1. AG Channel Flight Test Environment Summary [70].

Test	Test Date	GS Location (elevation)	GS Environment	GS Location		GS Antenna Boresight (°relative to magnetic north)	Remarks
				Latitude	*Longitude*		
1	20 Mar 2013	NASA GRC (756')	Urban/suburban, some over-water, flat terrain	41º 24' 51.9''	-81º 51' 34.86''	312	AC altitude 2700' MSL
2	15 Apr 2013	Latrobe, PA (1137')	Orientation 1: mix of rural terrain & urban structures in valley, viewed from airport	40º 16' 26.03"	-79º 24' 8.49"	40	AC altitude 3200' MSL
			Orientation 2: GS antenna beam L to mountain ridge w/natural cover. Ridge extends into LOS between AC & GS			137	AC altitude 3800' MSL Ridge elevation 1896' MSL
3	11 Jun 2013	Oxnard, CA (16')	Open salt water w/few stationary structures & watercraft	34º 10' 37.28"	-119º 14' 7.386"	270	AC altitude 2650' MSL
4	12 Jun 2013	Palmdale, CA (2545')	Orientation 1: Open, flat desert & agricultural terrain. One structure in GS foreground	34º 36' 30.864"	-118º 4' 34.032"	75	AC altitude 5725' MSL
			Orientation 2: Flat, desert, urban residential with low structures in foreground. Dry, hilly terrain with natural cover.			147	AC altitude 8950' MSL, Mtn heights 3000-5500'
5	5 Sep 2013	Cleveland, OH (772')	Suburban, some over-water, flat terrain	41° 24' 52.206"	-81°51' 35.346"	312	AC altitude 2500' MSL
6	12 Sep 2013	Telluride, CO (9000')	*Very* mountainous terrain	37º 57' 14.55"	-107º 54' 15.57"	284	AC altitude 12,800' MSL
7	22 Oct 2013	Cleveland, OH (582')	Orientation 1: open freshwater	41º 29' 33.80"	-81º 44' 05.48"	360	AC altitude 2500' MSL
			Orientation 2: Cityscape view w/many tall buildings on flat terrain, adjoining open freshwater			56	

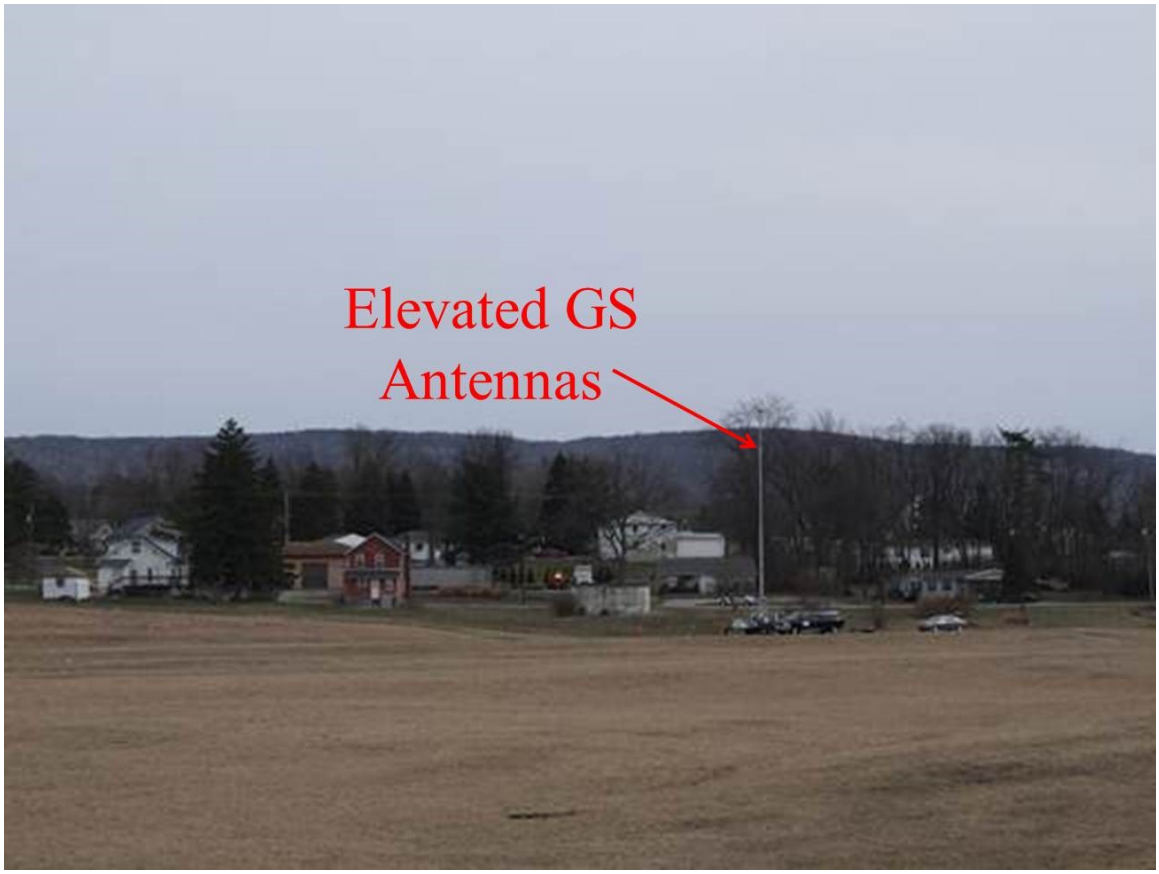

Figure 3.8. View of the GS in Latrobe, PA.

3.2 EQUIPMENT DESCRIPTION

The measurement system is composed of a channel sounder, the GS and aircraft antennas, an airplane and a transportable GS antenna tower, as well as RF cables and amplifiers. The details are described in this section.

3.2.1 CHANNEL SOUNDER

For our tests, NASA has sponsored development of a dual-band, single input multiple output (SIMO) antennas test set, termed the channel sounder. With specifications by the project principal investigator and NASA engineers, the sounder has been developed by Berkeley Varitronics Systems (BVS) [71]. The sounder is a direct sequence spread spectrum (DS-SS) stepped correlator. The transmitter unit includes an L-

band and a C-band transmitter. Two receiver units that are exactly the same were developed. Each of them contains both an L-band and a C-band receiver. This configuration allows us to make SIMO measurements simultaneously in both bands. A diagram of the sounder structure is shown in Figure 3.9. The detailed specifications are listed in Table 3.2. Photos of the transmitter and receiver are shown in Figure 3.10.

The transmit power is 10 Watts. A 7 dB gain high-power amplifier (HPA) is used at the C-band transmitter and low noise amplifiers (LNAs) are employed at all the receivers (15.5 dB gain in L-band and 30 dB gain in C-band). The cable loss is 4 dB in L-band and 7.5 dB in C-band. The HPA and LNAs are employed to extend the link range.

The output of the sounder is power delay profiles, which is the "power version" of the CIR. The maximum PDP update rate is 3000 PDPs per second. The frequency range is 960-977 MHz in L-band and 5000-5150 MHz in C-band. The center frequencies employed in the measurements were 968 MHz in L-band and 5060 MHz in C-band. The delay resolution is 200 ns (5 Mchips/s) in L-band and 20 ns (50 Mchips/s) in C-band. The PN sequence length is 1023 which yields a full delay span of 204.6 μs in L-band and 20.46 μs in C-band.

The sounder has multiple modes of operation, including (a) no filter mode, which records all 1023 chips of a PDP but yields the lowest PDP update rate; (b) power threshold mode, which only records samples whose power is no smaller than N dB (N can be set in the receiver software) below the power of the strongest sample; (c) delay window mode, which only records selected samples over a user-selected delay range; (d) peak limit mode, which only records the M (M can be set in the receiver software) largest chips. The power threshold mode b) was employed in the AG channel flight

measurements and the threshold was set to 25 dB. In mode (b) the PDP update rate ranges from 1.5 kHz to 3 kHz, and this can depend upon signal to noise ratio (SNR) as well.

The thermal noise at the Rx was evaluated in multiple conditions: (a) in the lab, with the receivers terminated by matched loads; (b) in the aircraft on the ground with all aircraft electronics turned on and receivers terminated by matched loads; and (c) in the aircraft en-route with receivers connected to LNAs and antennas, but the transmitter powered off. With a 5×10^{-4} false alarm probability (the probability that noise is identified as signal), noise level is approximately -80 dBm for the C-band receivers. The detailed analysis of thermal noise was reported in Appendix B of [65]. If we take 1 km as a reference distance, the dynamic range (the received power range between the theoretical maximum input value and the noise level) is approximately 60 dB in C-band. The dynamic range for the L-band receivers is approximately 74 dB.

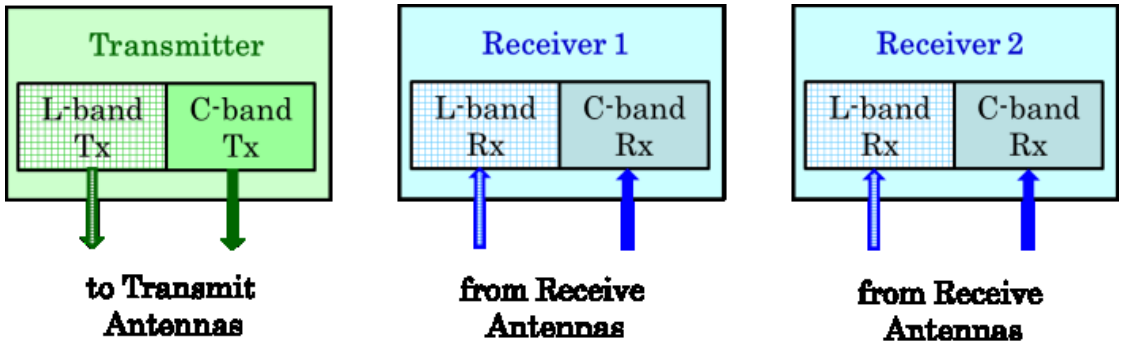

Figure 3.9. AG channel sounder structure [8].

Table 3.2. Channel sounder specifications.

Band	Signal Bandwidth (MHz)	Frequency Span (MHz)	Maximum Delay Span (μs)	Transmit Power (W)	Amplifier (dB)	LNA Gain (dB)	Cable Loss (dB)
L	5	960-977	204.6	10	--	15.5	4
C	50	5000-5150	20.46	10	7	30	7.5

Figure 3.10. Sounder Tx (left) and Rx (right, 1 of 2).

3.2.2 AIRCRAFT AND TRANSPORTABLE GS

The GRC test airplane on which the receivers are mounted is a Lockheed S-3B Viking; the locations of antennas are shown in Figure 3.11. The four aircraft antennas were on corners of a rectangle, the side lengths are 49 inches (1.24 m) between C-band Rx1 and L-band Rx1 and 52.5 inches (1.33 m) between C-band Rx2 and L-band Rx1. The intra-band separation distance (diagonal) is 1.82 m, as shown in Figure 3.12. The transmission antennas are elevated at the ground station by a tower. Figure 3.13 shows the transportable GS tower. The GS employs a 7 kW generator for powering all

components, a pneumatically-extendable (~4 m – 20 m) tower, and a cabinet for the electronic test equipment.

Figure 3.11. GRC aircraft.

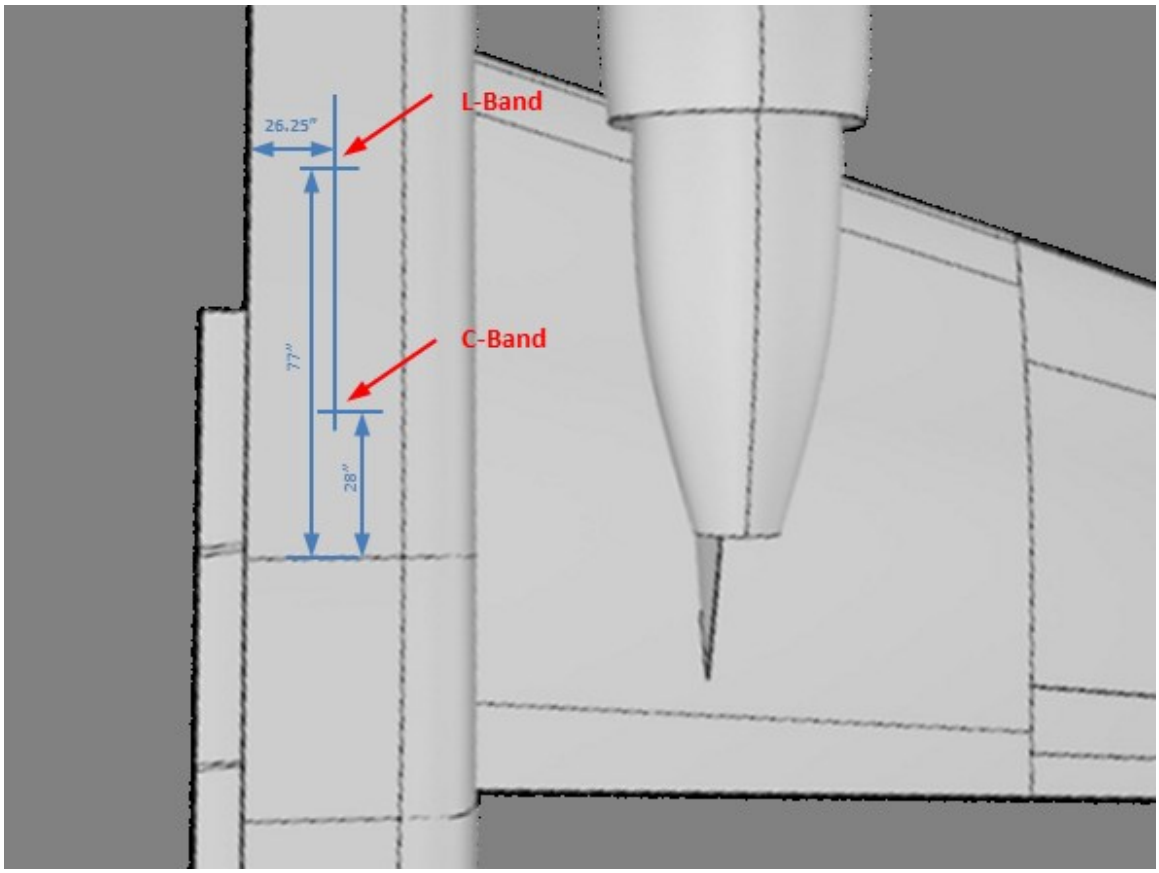

Figure 3.12. Aircraft antenna locations.

Figure 3.13. Transportable tower & GS.

3.2.3 ANTENNAS

The GS antennas are sector antennas designed by Cobham Antenna Systems [72], as shown in Figure 3.14. The C-band antenna model number is SA6-180-51V/559 and the L-band antenna model number is SA5-120-0.96-1.22V/1969. The gains are ~ 6.1 dB for C-band, and ~5.1 dB for L-band, with elevation/azimuth beamwidths of 35º/180º for

C-band and 60º/120º for L-band. The GS antenna patterns for both bands are shown Figures 3.15 and 3.16.

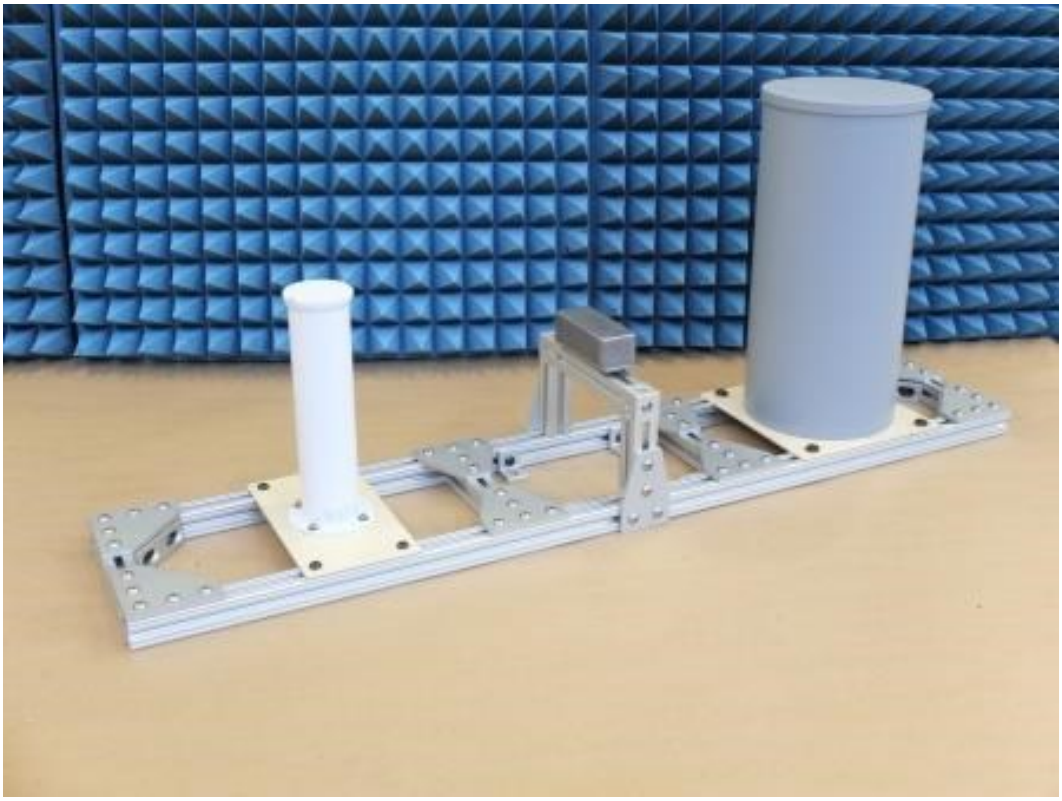

Figure 3.14. C-band (left) and L-band (right) GS antennas.

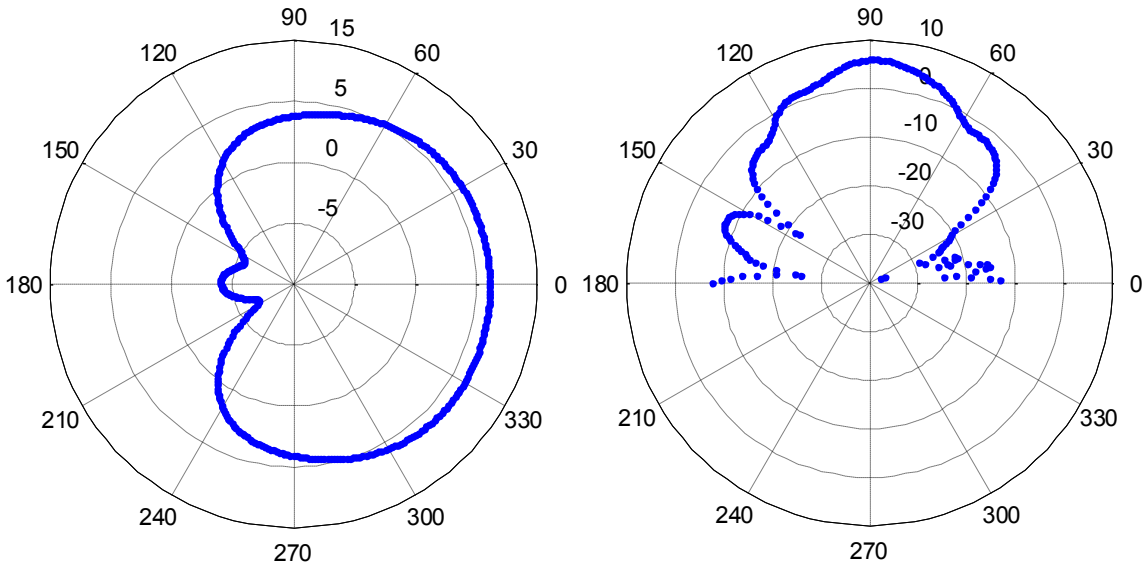

(a) (b)

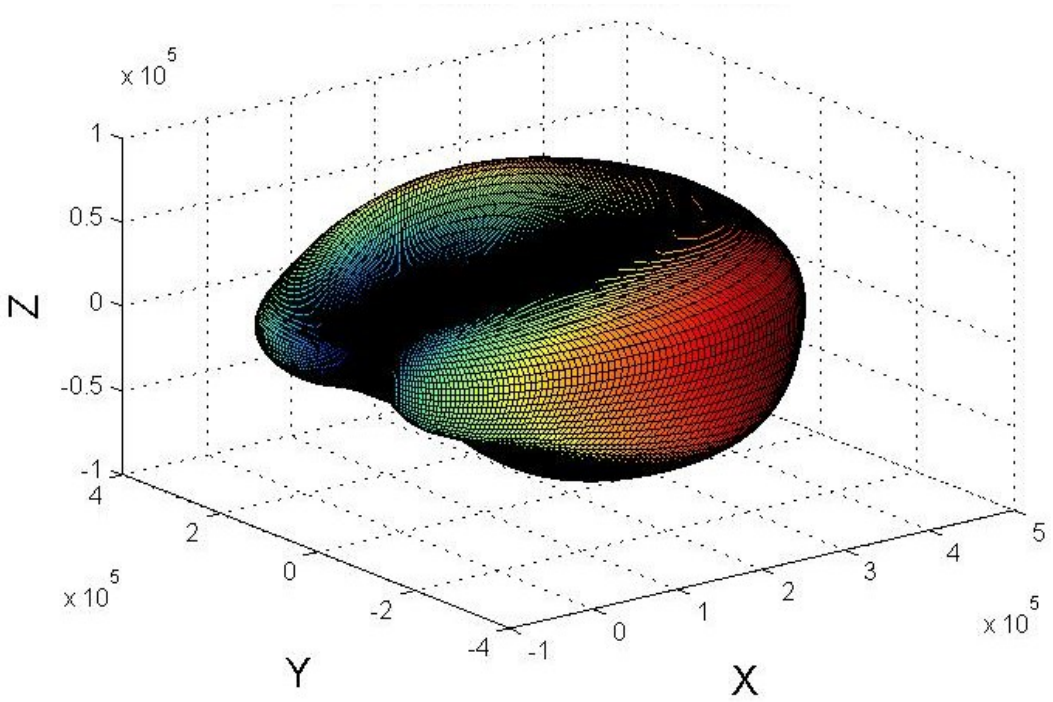

(c)

Figure 3.15. GS antenna pattern in C-band: (a) azimuth plane in dBi; (b) elevation plane in dBi; (c) three dimensional in linear scale.

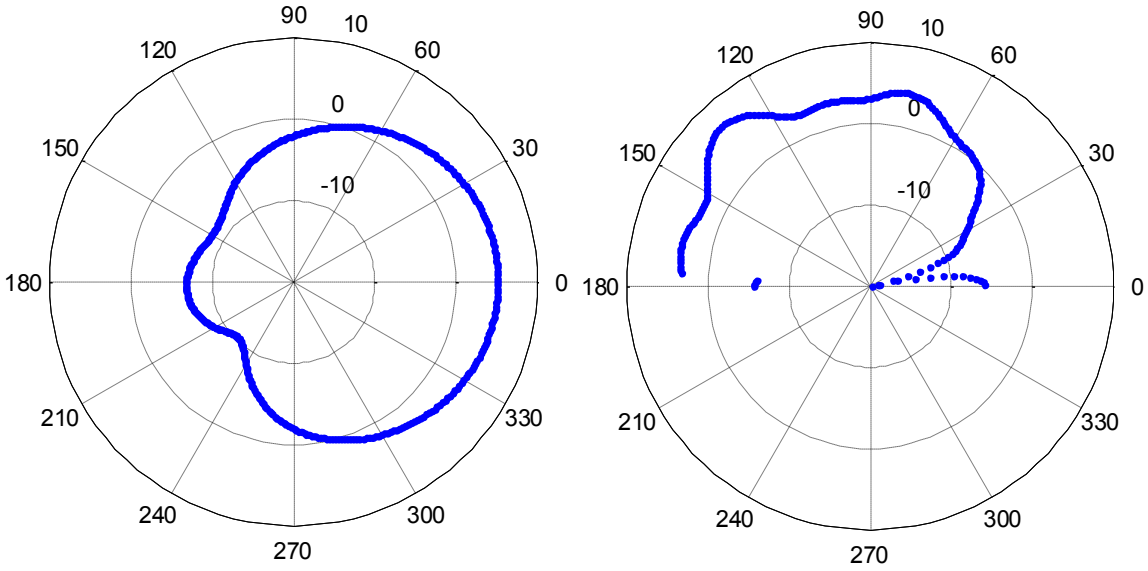

(a)

(b)

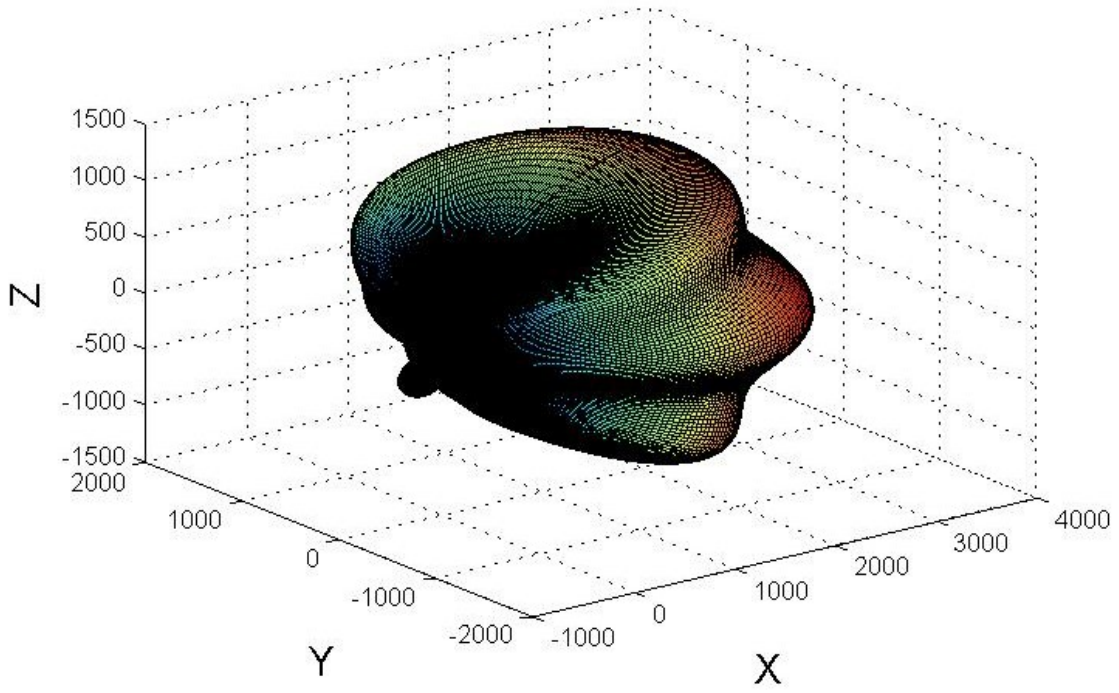

(c)

Figure 3.16. GS antenna pattern in L-band: (a) azimuth plane in dBi; (b) elevation plane in dBi; (c) three dimensional in linear scale.

The monopole "blade" antennas used on the aircraft are designed by Sensor Systems, Inc. [73]. The model numbers are S65-5366-4M for the C-band antenna and S65-5366-3L for the L-band antenna; these are shown in Figures 3.17 and 3.18, respectively. They are approximately omni-directional in azimuth, with maximum gain of 5 dB. The patterns provided by the manufacture are shown in Figure 3.19, in which the antennas are assumed mounted on the roof of the AC, but in our AG channel measurements the antennas were mounted under the belly of the AC, hence the actual patterns shown in Figure 3.15 should be flipped over. The patterns were actually measured on a one meter by one meter metal ground plate in an anechoic chamber instead of mounted on the aircraft. However, the airframe where the antennas mounted is a large metal ground plane. The patterns are strongly affected by the metallic body of the

aircraft, which introduces uncertainties into our measurements. We employ measured GS and AC antenna pattern data in our path loss analysis.

Figure 3.17. C-band AC blade antenna with LNA.

Figure 3.18. L-band AC blade antenna with LNA.

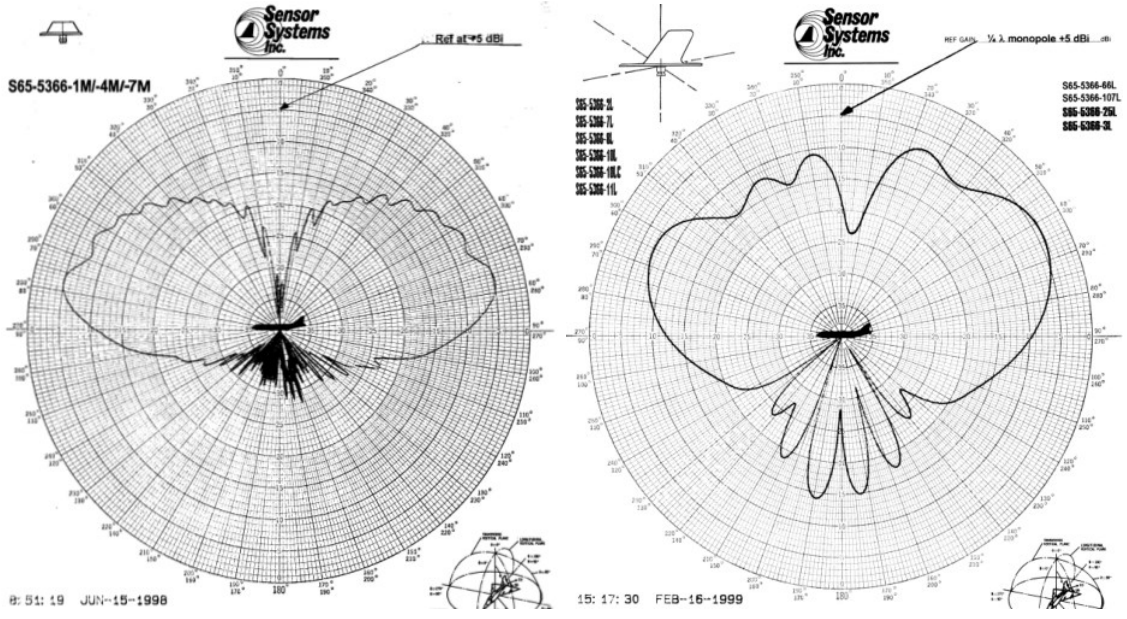

(a) (b)

Figure 3.19. AC antenna patterns in the elevation plane in (a) C-band; and (b) L-band [73].

3.2.4 EXAMPLE OF DATA FORMAT

We have four sets of input data from our flight test measurements: 1) PDPs recorded by the (four) sounder receivers; 2) GPS data recorded by the aircraft; 3) GPS information and antenna orientations of the GS; 4) other constant parameters including GS/Aircraft antenna patterns, transmitted power, cable loss, amplifier gain, bandwidth, and the conductivity, permittivity and permeability of the earth surface (ground or water).

Examples of PDPs are shown in Figure 3.20. These files include a Unix time stamp, total received power in dBm, and the highlighted grey columns are the actual PDP samples. The PDP is composed of position, which corresponds to relative delay, and the in-phase (I) and quadradure (Q) amplitude of each sample; we may record up to 2046 samples per PDP. As noted, a multipath thresold is applied so that all the samples X dB weaker than the strongest one are removed (we used X=25). The threshold affects the PDP update rate, which is ideally up to 3000 Hz. The internal GPS receiver of the sounder has not always worked properly, whereas the aircraft recorded GPS reliably, hence we used the aircraft GPS information for computing link distance vs. time. The two sets of data can be aligned by the Unix time stamp with an accuracy of 10^{-7} second.

The aircraft data provides the Unix time stamp, location information of altitude, latitude and longitude, and flight attitude information of heading, pitch angle and roll angle. We can identify the occurrance of airframe shadowing, flight direction, and link distance difference between any two antennas by the flight attitude information. The aircraft data includes other information such as velocity, acceleration and so on, as shown in Figure 3.21. Only the highlighted yellow columns are used in the data processing. The

frame (lines in Figure 3.21) update rate is is approximately 1 Hz, which is much slow than the PDP update rate.

```
Calculated Time (Seconds UTC), Frame #,Samples,Total Power (dBm),Start Position (1/2 Chips),DATA [Position (1/2 Chips) : I Data : Q Data
1370973432.1408753,18457,22,-48.1000,0,659,0.0258,0.0813,-21.3810,660,-0.0587,-0.0356,-23.2623,661,-0.2398,-0.4410,-5.9865,662,-0.3612,-0
1370973432.1415417,18459,22,-48.1000,0,526,0.0167,-0.0543,-24.9190,527,0.0189,-0.0555,-24.6307,659,-0.0733,0.0595,-20.4989,660,0.0150,-0.
1370973432.1418750,18460,22,-48.1000,0,526,-0.0037,0.0582,-24.6894,527,-0.0068,0.0552,-25.0906,659,0.0535,-0.0742,-20.7756,660,-0.0006,0.
1370973432.1422083,18461,21,-48.4600,0,526,-0.0566,0.0052,-24.9096,659,0.0756,0.0469,-21.0200,660,-0.0806,0.0177,-21.6659,661,-0.5089,-0.
1370973432.1425416,18462,21,-48.1000,0,526,-0.0162,-0.0575,-24.4766,527,-0.0128,-0.0557,-24.8572,659,-0.0353,0.0878,-20.4776,660,-0.0236,
1370973432.1432080,18464,22,-48.1000,0,526,0.0575,-0.0171,-24.4397,527,0.0546,-0.0184,-24.7866,659,-0.0902,-0.0301,-20.4367,660,0.0754,-0
1370973432.1435413,18465,21,-48.1000,0,659,0.0901,0.0053,-20.8916,660,-0.0713,0.0456,-21.4503,661,-0.5448,0.0656,-5.2127,662,-0.9473,0.0
1370973432.1438746,18466,20,-48.1000,0,659,0.0188,0.0872,-20.9905,660,-0.0598,-0.0585,-21.5512,661,-0.1942,-0.5121,-5.2295,662,-0.2670,-0
1370973432.1448743,18469,21,-48.1000,0,526,0.0379,-0.0460,-24.4991,527,0.0392,-0.0430,-24.6957,659,-0.0898,0.0198,-20.7292,660,0.0567,-0.
1370973432.1452076,18470,18,-48.1000,0,659,0.0456,0.0829,-20.4774,660,-0.0838,-0.0314,-20.9633,661,-0.3722,-0.4100,-5.1335,662,-0.5740,-0
1370973432.1455410,18471,17,-48.4600,0,659,-0.0727,0.0608,-20.4673,660,0.0311,-0.0858,-20.7993,661,0.3751,-0.4295,-4.8786,662,0.6832,-0.6
1370973432.1458743,18472,19,-48.4600,0,526,0.0560,0.0060,-24.9907,659,-0.0671,-0.0628,-20.7346,660,0.1037,0.0048,-19.6754,661,0.5148,0.26
1370973432.1462076,18473,18,-48.4600,0,526,-0.0082,0.0594,-24.4445,527,-0.0054,0.0571,-24.8247,659,0.0635,-0.0717,-20.3793,660,-0.0178,0.
1370973432.1465409,18474,20,-48.4600,0,526,-0.0593,0.0003,-24.5350,527,-0.0568,-0.0010,-24.9081,659,0.0789,0.0411,-21.0125,660,-0.1008,-0
1370973432.1468742,18475,17,-48.4600,0,526,-0.0016,-0.0559,-25.0470,659,-0.0428,0.0805,-20.8031,660,-0.0036,-0.1034,-19.7049,661,0.1788,-
1370973432.1472075,18476,19,-48.4600,0,526,0.0579,-0.0200,-24.2530,527,0.0571,-0.0208,-24.3298,659,-0.0833,-0.0402,-20.6783,660,0.1095,-0
1370973432.1478739,18478,18,-48.1000,0,526,0.0247,0.0550,-24.3947,659,0.0195,-0.0909,-20.6356,660,0.0362,0.1027,-19.2585,661,-0.0118,0.60
1370973432.1482072,18479,17,-48.1000,0,526,-0.0399,-0.0452,-24.4028,527,-0.0414,-0.0408,-24.7176,659,0.0109,0.0948,-20.4077,660,-0.0750,-
1370973432.1485405,18480,16,-48.1000,0,526,0.0379,-0.0446,-24.6505,527,0.0363,-0.0437,-24.9158,659,-0.0951,0.0133,-20.3528,660,0.0790,-0.
```

Figure 3.20. Example sounder data (PDPs).

	UTC times	Attitude Ti	True Head	Platform H	Pitch (Degr	Roll (Degre	OnTime (N	E/W Veloc	N/S Velocit	Vertical Ve	Blended Al	Latitude (D	Longitude	E/W Accel
2	1.37E+09													
3	1.37E+09	3129536	95.71289	95.71289	2.856445	-0.49988	473	0	0	0	2517.5	34.61287	-118.075	-0.15625
4	1.37E+09	4180224	95.7074	95.7074	2.856445	-0.49988	474	0	0	0	2511.5	34.61287	-118.075	0.3125
5	1.37E+09	915520	95.7074	95.7074	2.845459	-0.49988	475	0	0	0	2511.5	34.61286	-118.075	0.15625
6	1.37E+09	1892032	95.71289	95.71289	2.839966	-0.49988	476	0	0	0	2511	34.61288	-118.075	0.09375
7	1.37E+09	2919296	95.7074	95.7074	2.856445	-0.49439	477	0	0	0	2515	34.61291	-118.075	-0.10938
8	1.37E+09	705280	95.7074	95.7074	2.850952	-0.49439	479	0	0	0	2521	34.61297	-118.075	0.0625
9	1.37E+09	756096	95.7074	95.7074	2.850952	-0.49988	479	0	0	0	2521	34.61297	-118.075	0.140625
10	1.37E+09	1759936	95.7074	95.7074	2.850952	-0.49439	480	0	0	0	2521.5	34.61299	-118.075	-0.20313
11	1.37E+09	2736384	95.7019	95.7019	2.850952	-0.49439	481	0	0	0	2519.5	34.613	-118.075	-0.20313
12	1.37E+09	3736320	95.7019	95.7019	2.850952	-0.49439	482	0	0	0	2517.5	34.61298	-118.075	-0.4375
13	1.37E+09	647424	95.7019	95.7019	2.845459	-0.49439	483	0	0	0	2513.5	34.61295	-118.075	0.25
14	1.37E+09	1498880	95.7019	95.7019	2.850952	-0.49439	484	0	0	0	2515	34.61293	-118.075	-0.20313
15	1.37E+09	2627712	95.7019	95.7019	2.850952	-0.49439	485	0	0	0	2516.5	34.61293	-118.075	-0.10938
16	1.37E+09	335616	95.7074	95.7074	2.850952	-0.49439	487	0	0	0	2525.5	34.61295	-118.075	0.1875
17	1.37E+09	1237888	95.7019	95.7019	2.845459	-0.49439	488	0	0	0	2528	34.61296	-118.075	-0.35938
18	1.37E+09	2366720	95.69641	95.69641	2.850952	-0.49439	489	0	0	0	2527.5	34.61297	-118.075	-0.26563
19	1.37E+09	3370560	95.7019	95.7019	2.850952	-0.48889	490	0	0	0	2526.5	34.61296	-118.075	0.015625
20	1.37E+09	1004224	95.7019	95.7019	2.850952	-0.49439	492	0	0	0	2523.5	34.61294	-118.075	0

Figure 3.21. Example airbus data (GPS & Flight Attitude).

3.3 DATA PROCESSING ALGORITHM

The overall data processing algorithm is shown in Figure 3.22. Yellow blocks denote inputs and green blocks are outputs. Parameters ε, μ and σ denote relative dielectric constant, conductivity in S/m and relative permeability of the earth surface, respectively. D_{LOS} is the link distance between aircraft and the GS. The angles $\angle_{Ele}$, $\angle_{Azi}$, $\angle_{Heading}$, $\angle_{Pitch}$, $\angle_{Roll}$, and $\angle_{Yaw}$ are elevation angle, azimuth angle, heading, pitch and yaw angles of the aircraft in degrees, respectively. Parameters G_t, G_r and G_{LNA} are transmitter

antenna gain, receiver and LNA gains in dBi, respectively. Term P_t is the transmit power and L_C is the cable loss. The term *Anlt PL* denotes the path loss in dB estimated by the analytical two-ray method, and *Meas PL* denotes the measured path loss in dB.

Since the sampling rate is twice the chip rate, two adjacent samples are combined vectorially. This process is called "pairing". The number of chips per PDP is up to 1023 (number of samples per PDP is up to 2046). Then we shift (circularly rotate) the strongest chip to the 5^{th} chip index (the MPCs are always later than the LOS component, but due to the effect of some analog filters applied in the sounder, a few chips prior to the LOS chip have appreciable energy as well, hence based upon the overall sounder filter response we choose five as the index of strongest chip). Several noise removal algorithms are applied. The "Noise thresholding" and "MPC persistence check" are the two steps to remove the noise. The processed PDPs can be aligned with link distance D_{LOS} with the Unix time stamp.

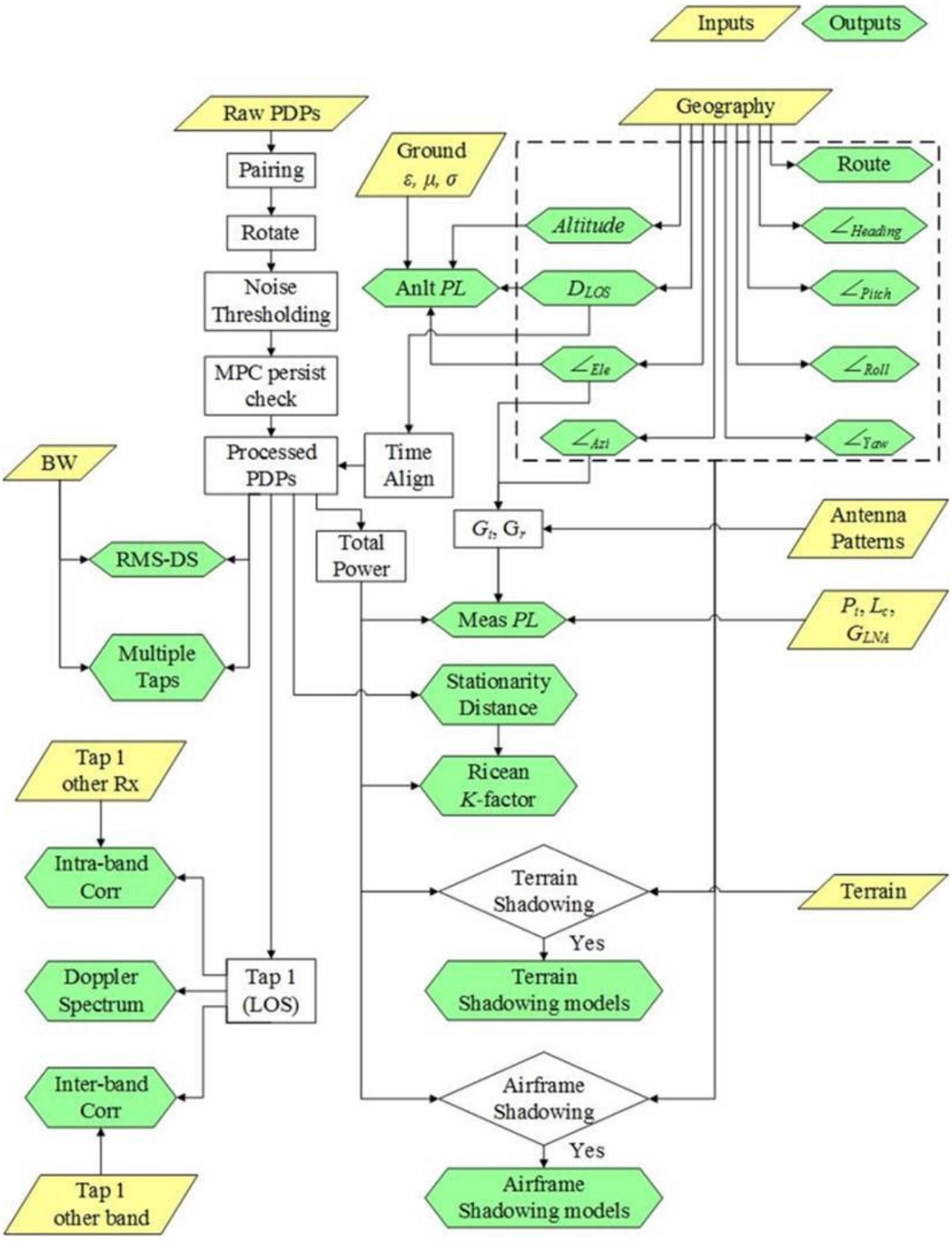

Figure 3.22. Data processing algorithm.

Altitude, heading, pitch angle and roll angle are recorded by the aircraft data directly. The flight route, elevation angle, azimuth angle and link distance D_{LOS} can be calculated by the GPS information of both aircraft and GS.

The measured path loss PL can be computed by the total received power P_r, transmitted power P_t, antenna gains G_t, G_r, LNA gain G_{LNA} and cable loss L_c, yielding

$$PL = P_t + G_t + G_r + G_{LNA} - L_c - P_r. \tag{3.1}$$

The RMS-DS is the most widely used measure of time dispersion. It's mathematically expressed by [74]

$$\sigma_\tau = \sqrt{\frac{\sum_{k=0}^{L-1} \alpha_k^2 \tau_k^2}{\sum_{k=0}^{L-1} \alpha_k^2} - \mu_\tau^2}, \tag{3.2}$$

where α_k is the amplitude of the k^{th} MPC out of L total MPCs in the PDP, τ_k is the k^{th} MPC delay (in increment of 20 ns for C-band and 200 ns for L-band), and μ_τ is the mean excess delay, given by

$$\mu_\tau = \frac{\sum_{k=0}^{L-1} \alpha_k^2 \tau_k}{\sum_{k=0}^{L-1} \alpha_k^2}. \tag{3.3}$$

The occurrence of airframe shadowing or building/obstacle shadowing is evident in some of the PL values; these occurrences are verified using geometric information and terrain information. Generating shadowing models is one of our future tasks. A tapped delay line model and the correlation between taps can be derived from the processed PDPs as well.

"Tap 1" in Fig. 17 pertains to the amplitude of strongest chip (LOS MPC). The cross correlation coefficient between the LOS MPC of two receivers is computed by equation (3.4)

$$\rho_{A_{Rx1},A_{Rx2}} = \frac{E[(A_{Rx1} - \mu_{A_{Rx1}})(A_{Rx2} - \mu_{A_{Rx2}})]}{\sigma_{A_{Rx1}} \sigma_{A_{Rx2}}} \tag{3.4}$$

where the E denotes expectation, $A_{Rx1} = (A_{Rx1,1}, A_{Rx1,1}, \dots, A_{Rx1,i}, \dots, A_{Rx1,n})$ is the amplitude of the LOS component (a single chip per PDP) of receiver 1, and $A_{Rx2} = (A_{Rx2,1}, A_{Rx2,1}, \dots, A_{Rx2,i}, \dots, A_{Rx2,n})$ is the amplitude of the LoS component of receiver 2. The "i's" denote PDP Index, and the "n's" denote the length of the vectors over which correlation is computed. Receivers 1 and 2 are two receivers in the same band for intra-band correlation, but we also generalize to compute correlations across the two bands (inter-band correlation).

The Doppler spectrum of the LOS components can be found via a the Fourier transform of "Tap 1" A_{Rx1} or A_{Rx2}. These spectra will provide a measure of fading rate.

3.3.1 GPS DATA PROCESSING

The GPS data processing algorithm is illustrated in Figure 3.23. The GPS information is firstly converted to the earth-centered earth-fixed (ECEF) coordinates [75] by which the link distance D_{LOS} and free space path loss PL_{FS} can be easily computed, and then converted to the east, north up (ENU) coordinates [75] by which the elevation angle $\angle_{Ele}$ and azimuth angle $\angle_{Azi}$ can be estimated. The earth reflection based deterministic models--flat earth two ray and curved earth two ray--are computed using all the geometric information. Angles $\angle_{Ele,2}$ and $\angle_{Ele,3}$ denote the second and third elevation angle calculation methods based on flat and curved earth surfaces, respectively. Angle $\angle_{\varphi}$ is the grazing angle, and Γ denotes reflection coefficient. The phase delay $\Delta Phase$ is used to compute total path loss of the two ray models $PL_{tot,2ray}$. The time delay $\Delta Time$ is employed to calculate the RMS delay spread. All the useful analytical results are saved in an "*AnltRslt*" matrix as inputs of the main data processing algorithm shown in Figure 3.22.

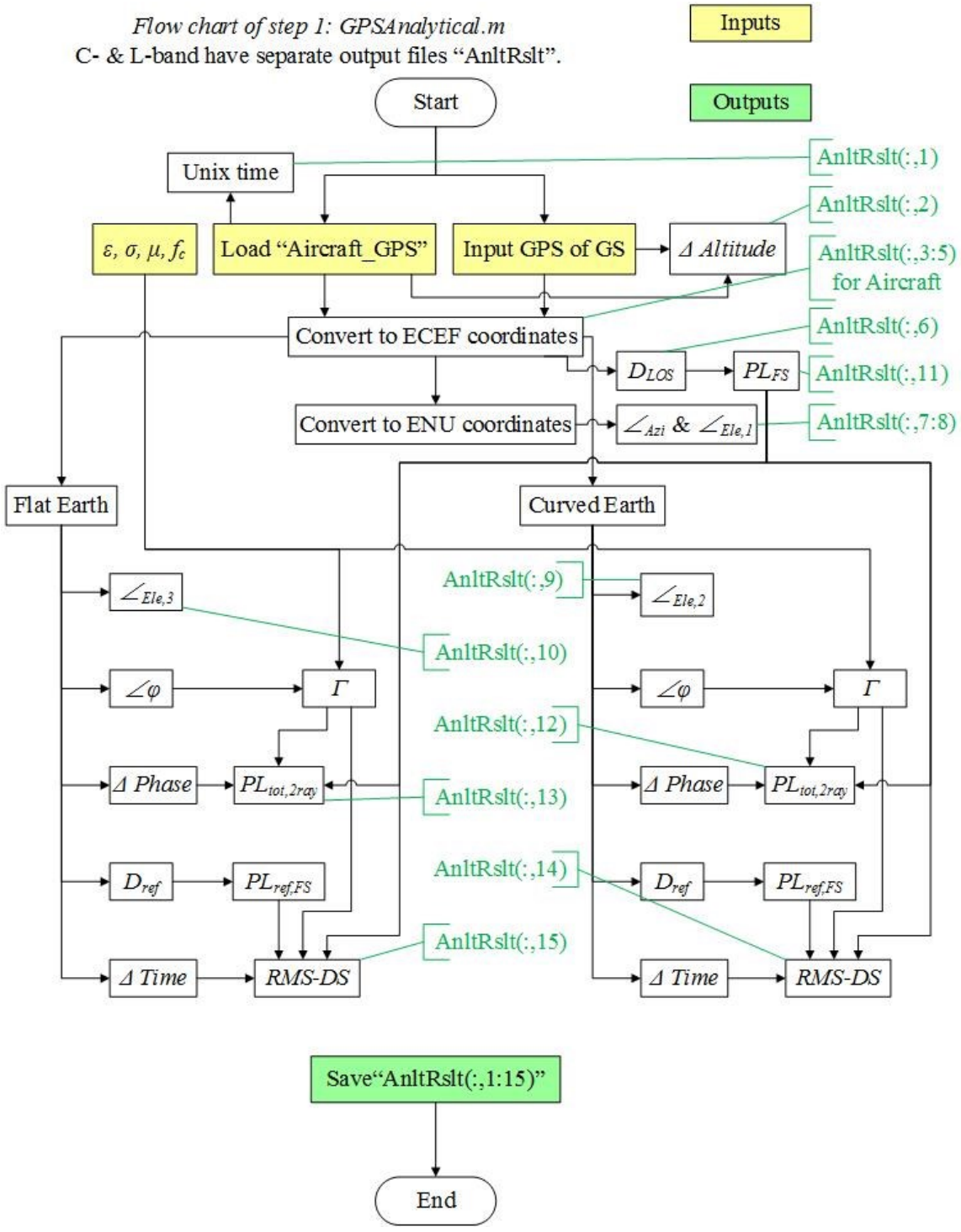

Figure 3.23. GPS data processing algorithm.

3.3.2 RAW PDP PROCESSING

The raw PDPs collected by NASA Glenn Research Center are in-phase (I) and quadrature (Q) components of samples. Each of the 1023 chips can be generated by combining two adjacent samples vectorially. Again, we call this step "pairing". The pairing algorithm is illustrated in Figure 3.24. A multipath threshold *MPThr* of typically 25 dB or 30 dB can be applied on chips, however, since a 25 dB power threshold was employed on samples when the sounder recorded the raw PDPs as described in section 3.2.1, we do not apply the multipath threshold. Then the PDPs are circularly rotated so that the strongest chip (likely the LOS component) is at the fifth position out of 1023.

The data of a whole FT may contain over one million PDPs; such file sizes cannot be processed by Matlab®, hence NASA Glenn Research Center divided the data into multiple files and each file included 10,000 PDPs. Letter *i* in Figure 3.24 denotes the file index. The processed PDPs are saved in matrices "BeforeNoiseThrd_PDP" and some important measured results such as the UNIX time stamp, total received power and power of the LOS chip are saved in matrices are saved in "MeasRslt". Each of these matrices contains 10,000 PDPs as well.

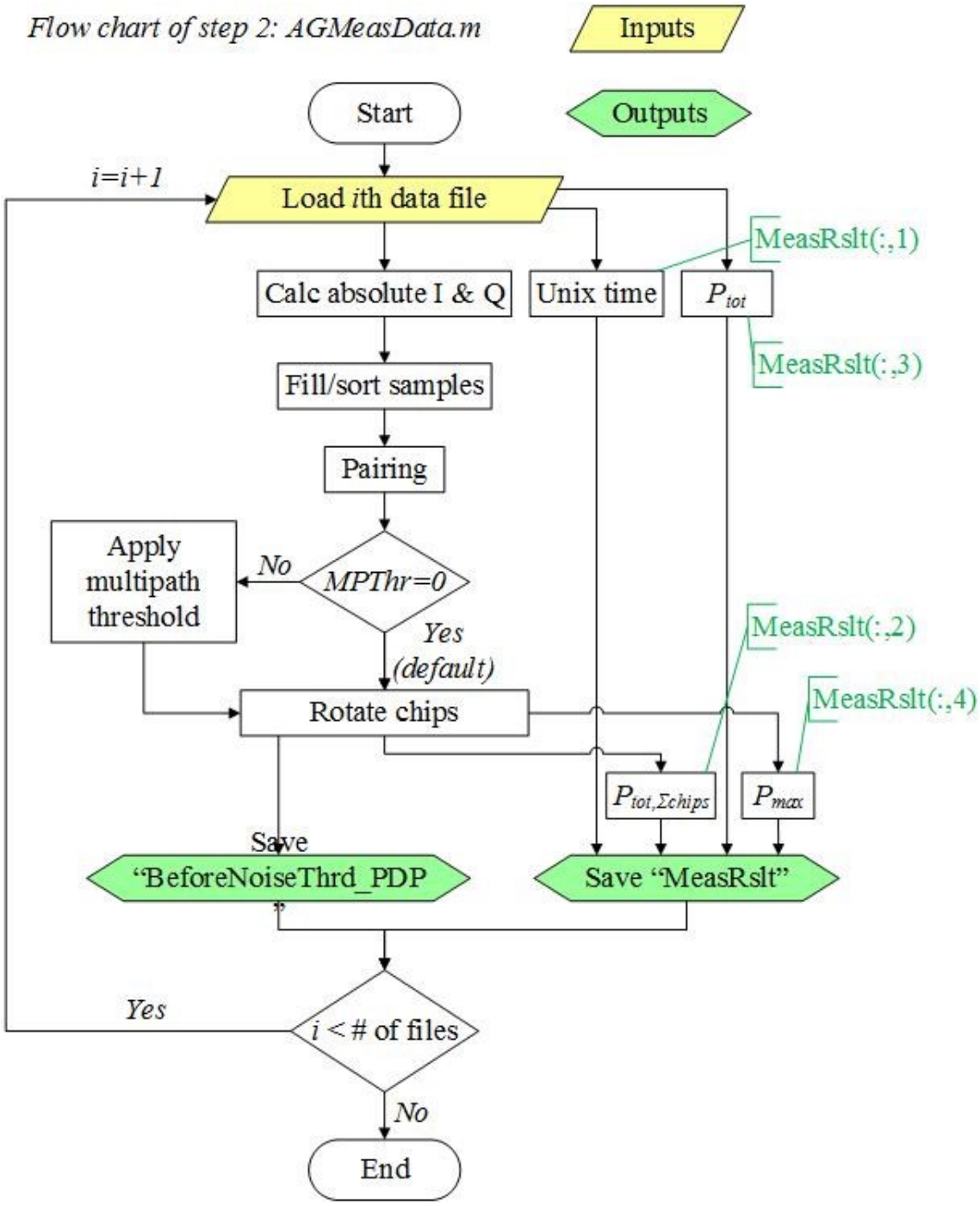

Figure 3.24. Pairing algorithm.

3.3.3 NOISE THRESHOLDING ALGORITHMS

Three noise thresholding algorithms are employed for the AG channel PDPs which are also discussed in Appendix C of [65]

- power threshold based on noise level;
- delay gate;
- persistence check.

The first two algorithms are illustrated in Figure 3.25. The analytical noise threshold is a constant for all scenarios, and this was estimated by a flight test with transmitter powered off, taken in Cleveland, OH in 10/22/2013. The empirical noise threshold is an instantaneous value evaluated by the power of chips at the latter part of a PDP where true MPCs are unlikely to be present (based upon analysis of the flight geometry), and using a false alarm probability of 0.0005 [65]. However, since the power threshold mode (see section 3.2.1) was set at the sounder so that most often, very few (often zero) noise chips were recorded, the empirical noise threshold is not applicable for all data. We hence employ the analytical threshold in the algorithm. If a noise chip with power below the noise threshold is found, the chip will be removed if it's in C-band, and the whole PDP will be removed if it's in L-band (the L-band sounder occasionally had "bad" PDPs that contained only noise chips due to an infrequent malfunction of the L-band channel sounder).

The second noise removal algorithm, the delay gate, is applied next. As noted, MPCs with chip index larger than 950 in C-band and 95 in L-band (excess delay of approximately 19 μs) are unlikely present for most flight geometries. These large-delay MPCs are removed since some noise chips stronger than the noise threshold may exist.

These noise chips remain after the analytical threshold if the false alarm probability is not small enough, but if we chose a smaller false alarm probability, some true MPCs may be removed by the noise threshold. The choice of false alarm probability is an engineering judgement.

Even if the delay gate is not applied, chips with index larger than 950 need to be removed since a "false" MPC was present after the 950^{th} chip. This false MPC was discovered in laboratory tests, and is simply an anomalous (yet deterministic) result of sounder hardware/software imperfections. The detailed analysis regarding this false MPC was reported in [76]. The processed PDPs are saved in matrices "AfterNoiseThrd_PDP" and the RMS-DS is merged into the measured results matrices "MeasRslt".

The third noise removal algorithm, the MPC persistence check, is illustrated in Figure 3.26. If a MPC is present in a single PDP and never shows up again in nearby PDPs, it is almost surely noise. A true MPC must last for some period of time. We consider a MPC as a true MPC if it is present at least twice in 11 consecutive PDPs, otherwise it is removed. The processed PDPs are saved in matrices "AfterPersistCheck_PDP" and the RMS-DS is re-computed and merged into the measured results matrices "MeasRslt".

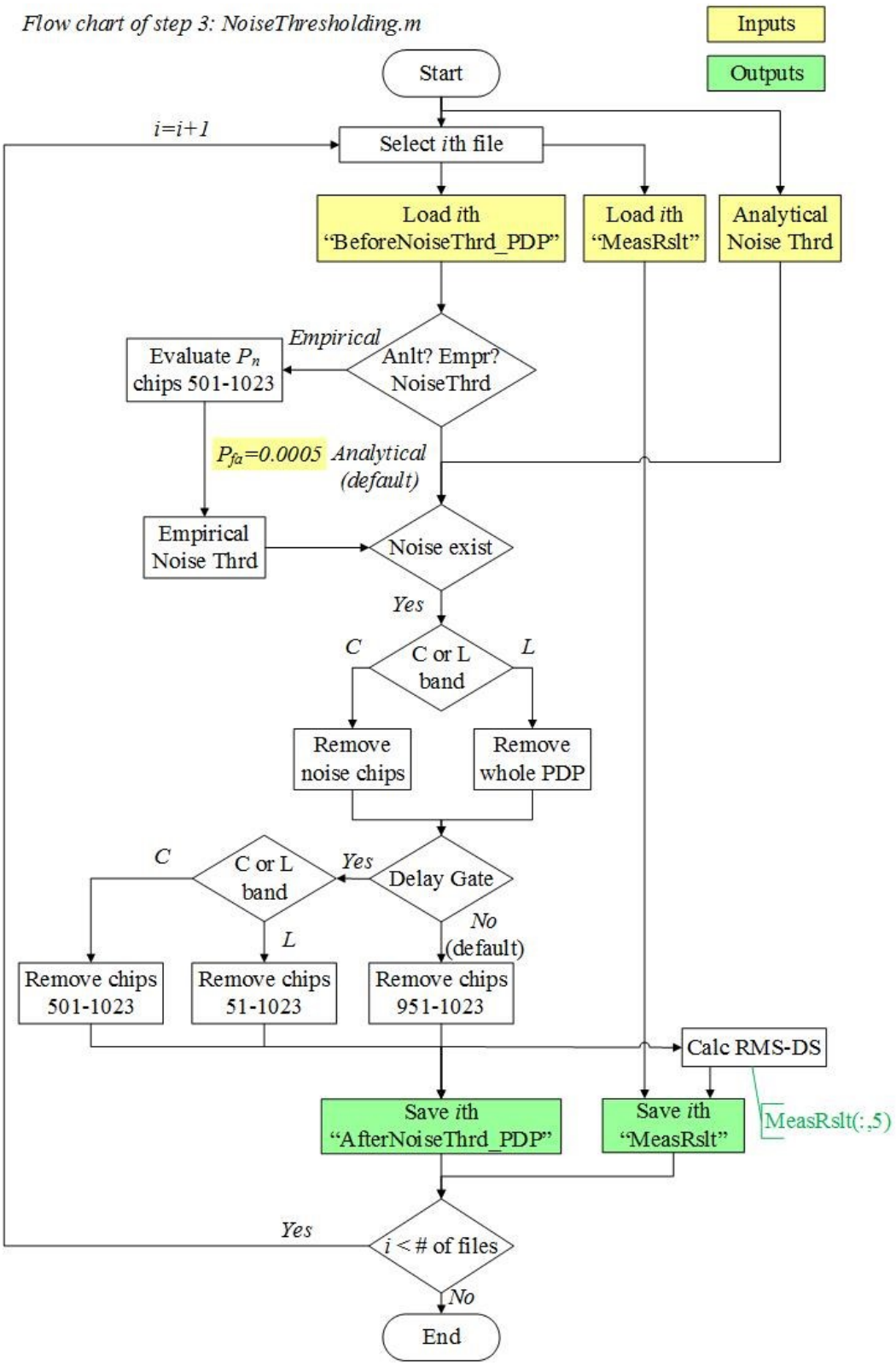

Figure 3.25. Noise thresholding algorithms.

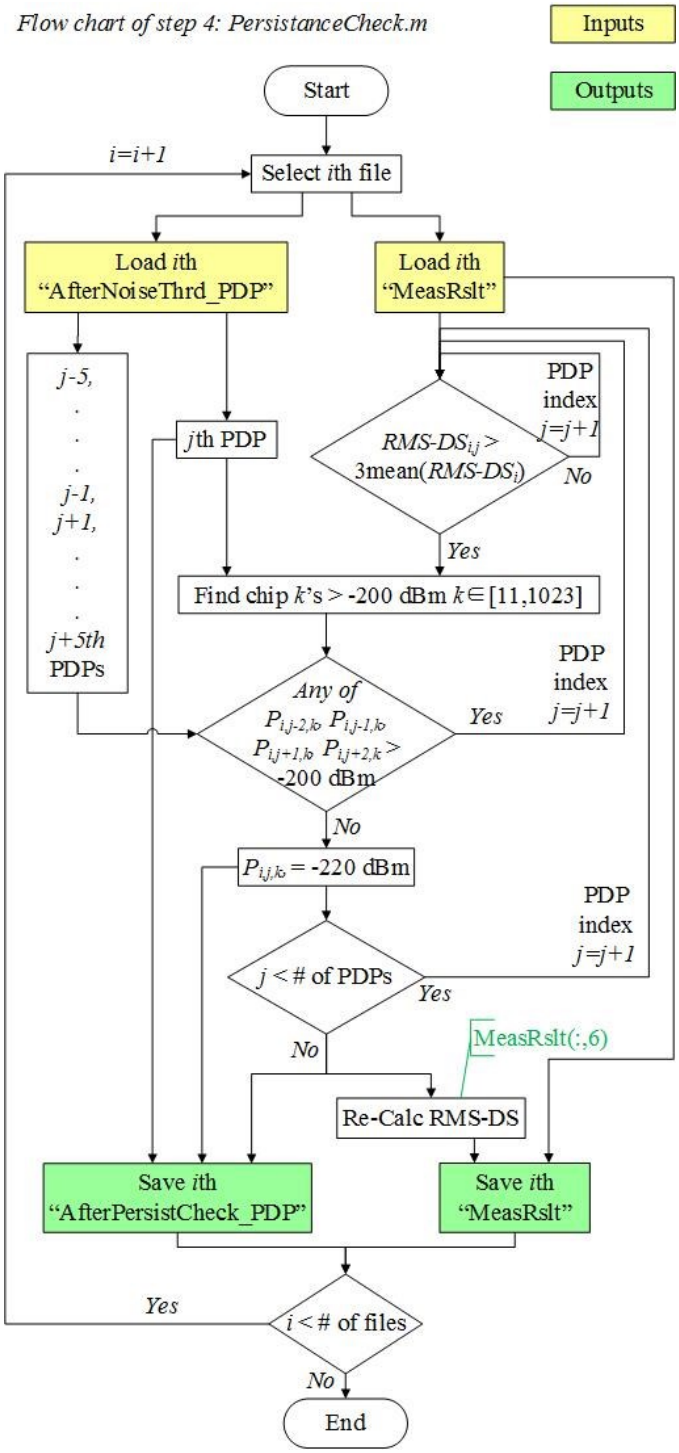

Figure 3.26. MPCs persistence check algorithm.

3.4 BACK-TO-BACK EVALUATION

The sounder Tx and Rx were connected in a "back-to-back" (B2B) mode (Tx and Rx were connected directly by RF cables, attenuators and splitters, without any wireless channel) in the NASA GRC laboratory to confirm the sounder's fundamental ability to resolve MPCs, and to gauge the actual measurable resolution in the delay domain. Since the sounder Tx must apply filtering for spectral containment, this affects the delay resolution. Most of the filtering is done digitally, and Figure 3.27 shows the filtering operations in both bands. Figure 3.28 shows a resulting L-band back-to-back impulse response, which is the response of the sounder itself, with an ideal channel (an RF cable). The response is the convolution of the Tx filters, Rx filters, and the (triangular) DS-SS sequence autocorrelation (the sequences are maximal-length shift register sequences typically called *m*-sequences [74]). The response (blue spikes) in Figure 3.28 is very close to that computed by analysis (red curve), using the known filter parameters of Figure 3.27 [70] and [77], thus confirming expected performance in this back-to-back case.

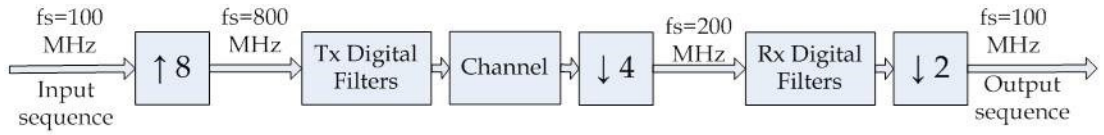

(a) C-band filtering

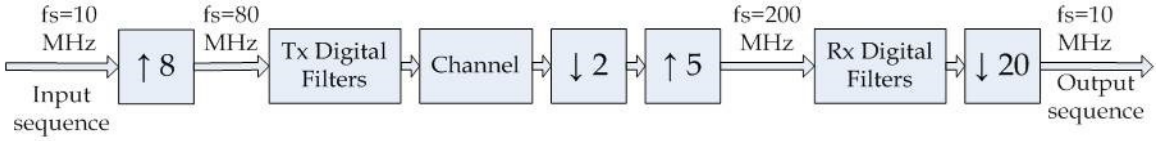

(b) L band filtering

Figure 3.27. Signal processing associated with filtering for the (a) C-band and (b) L-band sounders.

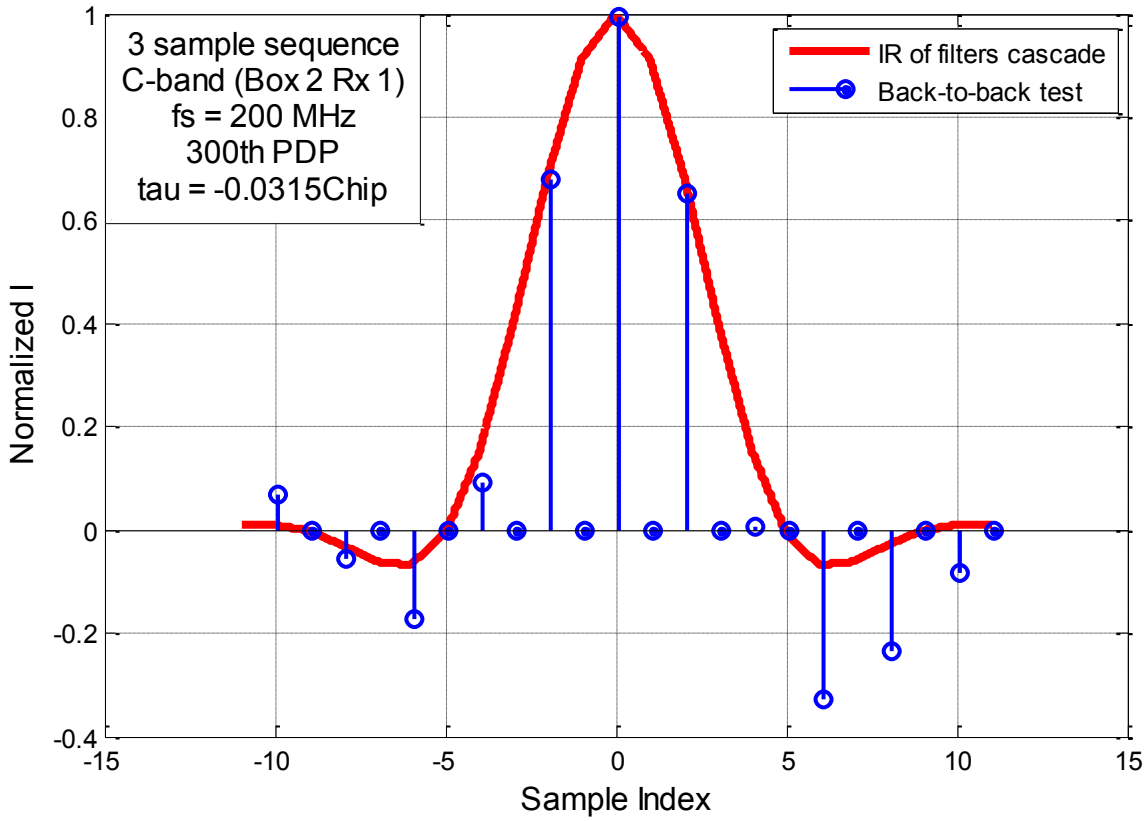

Figure 3.28. Back to back L-band impulse response.

Table 3.3 lists the RMS-DS of the single path back-to-back measurements in C-band. The RMS-DS is approximately 10 ns, and it's close to the analytical result of 8.3 ns. The RMS-DS in L-band is approximately 100 ns [76].

We also conducted *two-path* back-to-back tests. The setup is shown in Figure 3.29. Channel one is a short cable and channel two is a long cable along with a 15 dB attenuator. The relative delay between the two channels is 186 ns. As shown in Figure 3.30, the two paths are unresolvable in L-band (delay resolution 200 ns). Table 3.4 lists the RMS-DS of the two path back-to-back test in C-band. The RMS-DS in C-band is approximately 49 ns, which is close to the analytical result.

Table 3.3. C-band back-to-back single-path RMS-DS statistics (ns), for data of 11 Feb 2013, Rx 1 [78].

RMS-DS Statistics	Multipath Threshold (dB)			
	25	*30*	*35*	*40*
Analytical	8.3			
Mean	9.7	10.0	10.2	10.4
Median	9.7	9.9	10.2	10.4
Max	9.8	10.3	10.5	10.7
Min	9.5	9.7	10.0	10.1
Standard deviation	0.12	0.22	0.16	0.18

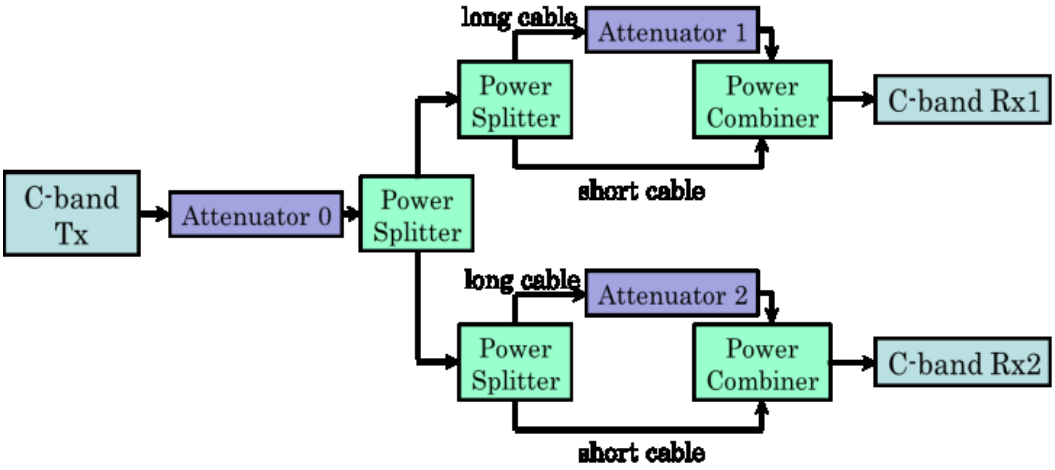

Figure 3.29. Back to back laboratory 2-path test [8].

Table 3.4. C-band back-to-back 2-path RMS-DS statistics (ns), for both C-band receivers, data of 11 March 2013 (25 dB multipath threshold) [8].

RMS-DS Statistic		Rx 1	Rx 2
Analytical		49.0	49.0
Measured	*Mean*	48.7	49.0
	Median	48.7	49.0
	Max	52.0	51.5
	Min	42.8	46.3
	Standard deviation	1.3	0.7

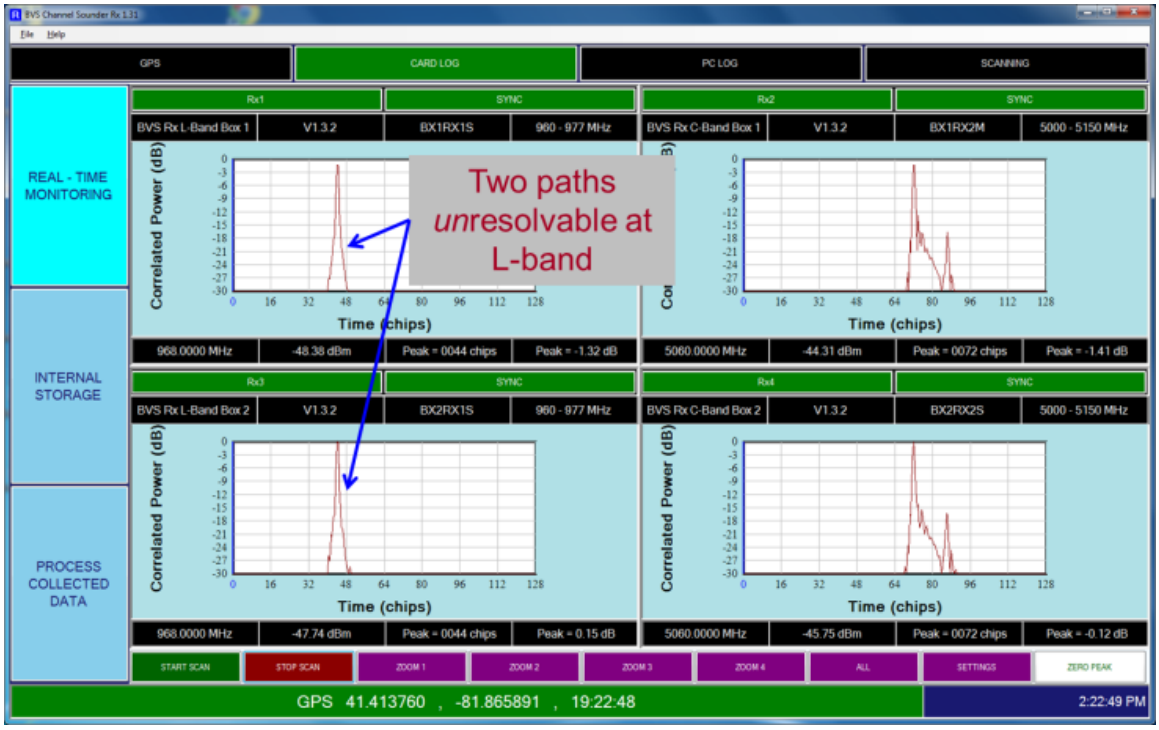

Figure 3.30. “Screen shot” of sounder IR in back-to-back testing; left: L-band, right: C-band [8].

3.5 STATIONARITY DISTANCE

The AG channel is statistically non-stationary beyond some time interval because of the relatively fast aircraft velocity and to a lesser degree because of moving scatterers. It is vital to determine the region of space over which the channel is wide sense stationary, or in other words the region over which channel statistics can be assumed constant. The stationarity distance is applied in the AG channel project for: (a) removing large scale path loss in order to evaluate small scale fading; (b) generating statistics of small scale fading over the SD; and (c) generating statistics of inter-receiver correlations over the SD.

Aiming for cellular application in 1985, William Lee analytically investigated the necessary length over which the local average power is computed [79]. The author

assumed NLOS condition and Rayleigh fading. The distance over which large-scale fading (shadowing) effects could be assumed roughly constant was determined to be 20 to 40 wavelengths. The number of samples in a local average window (20 to 40 wavelengths) should be no smaller than 36. However, the AG channel almost always has LOS component and yields Ricean fading. Its SD has to be reconsidered. The local average window length over Ricean, Nakagami or Weibull distributed channels is hard to evaluate analytically since the power density function (PDF) of these distributions are much more complicated than that of Ricean. The SD for AG channel can also be studied via empirical data based methods:

- Temporal PDP correlation coefficient (TPCC) [80] is a wideband method which could be based on single-input single-output (SISO) antennas or SIMO antennas if the PDPs at two separate antennas are very similar;
- Correlation matrix distance (CMD) is a narrowband method based on multiple-input multiple-output (MIMO) or SIMO systems which measures the spatial autocorrelation matrix change of the channel. CMD was used for V2V channels [59], [60], [81].
- Spectral divergence measures the distance between non-normalized positive spectral densities [82], [83], [84], [85].
- Shadow fading correlation [86] is the autocorrelation of shadowing. The decorrelation distance measures how fast the local environment changes to establish a stationarity distance. This traditional channel statistic is not recommended for the AG channel since in LOS channels, there is no shadowing by obstacles in the environment.

Based on the characteristics of both the AG channel and our channel sounder, we employed TPCC and CMD methods [64] and [58].

The TPCC begins with PDP given by

$$PDP(\tau, t_i) = \sum_{k=1}^{L_i} \left(\alpha_{k,i}\right)^2 \delta\left(\tau - \tau_{k,i}\right), \tag{3.5}$$

where τ denotes delay, i denotes PDP index (corresponding to time or distance), L_i is the number of chips in the i^{th} PDP, and $\alpha_{k,i}$ denotes the received signal amplitude of the k^{th} chip in the i^{th} PDP. The authors of [80] then average N instantaneous PDPs to smooth the small scale fading effects and remove equipment related variation

$$PDP_{avg,N}(\tau, t_i) = \frac{1}{N} \sum_{i}^{i+N-1} P(\tau, t_i). \tag{3.6}$$

The averaging distance of 200λ (N can be determined by converting the 200λ value based upon the PDP update rate and aircraft velocity) was selected since the periodic variation of C-band received power caused by a slow relative sampling clock drift between Tx and Rx [70].

The TPCC is computed as follows:

$$c(\Delta t, t_i) = \frac{\int PDP_{avg,N}(\tau, t_i) PDP_{avg,N}(\tau, t_i + \Delta t) d\tau}{max\left\{\int \left[PDP_{avg,N}(\tau, t_i)\right]^2 d\tau, \int \left[PDP_{avg,N}(\tau, t_i + \Delta t)\right]^2 d\tau\right\}}. \tag{3.7}$$

The coefficient quantifies the similarity of the average PDP between time t_i and time $t_i+\Delta t$. Coefficient $c(\Delta t, t_i)$ ranges between 0 and 1. Close to "1" means the channel changes very slowly or is quasi-stationary, and a smaller $c(\Delta t, t_i)$ means the channel is varying fast or is non-stationary. We select the SD value of distance Δx (corresponding to Δt and flight velocity v, $\Delta x = v\ \Delta t$) such that $c(\Delta t, t_i) > 0.9$. The very high probability threshold 0.9 is conservative, i.e., if $c(\Delta t, t_i) > 0.9$, then we have very high confidence that the channel is stationary within this distance. Example values of $c(\Delta x, d_i)$ for C-band Rx1

of FT1 taken over the Pacific Ocean near Oxnard, CA are shown in Figure 3.31. The large variation of SD is due to the sampling clock drift. The statistics of SD Δx are listed in Table 3.5. The median value[4] of SD for the over sea FT1 is approximately 15 m or 250λ in C-band, which is much larger than 20λ to 40λ proposed by [79] for the terrestrial NLOS condition, and this is reasonable since an LOS component is always present in our AG channel (excepting perhaps in cases where airframe shadowing occurs—this is discussed in Chapter 5.3). The median SD values for other scenarios (urban, suburban, over freshwater, hilly and mountainous) ranged from 10 to 35 m. We found that the Ricean *K*-factor or inter-receiver correlation is *not* sensitive to small variation of SD. They only significantly vary when the SD changes by an order of magnitude or more. The 10 to 35 m SD yields almost the same *K*-factor and inter-receiver correlation results. The value 15 m SD is employed in estimations of Ricean *K*-factor and inter-receiver correlations.

The L-band MPCs are unlikely resolvable in nearly all settings due to the small L-band bandwidth of 5 MHz. The L-band SD is expected to be larger than the C-band SD since L-band has a physically longer wavelength, and channel changes occur at (some) rate proportional to wavelength. We hence conservatively use the 15 m as our L-band stationarity distance as well.

[4] Note that other authors who have estimated SD also come up with a range of values (e.g., for the V2V case [59], [60] and [81]). SD is not constant, but is actually a random variable itself. SD must be characterized statistically.

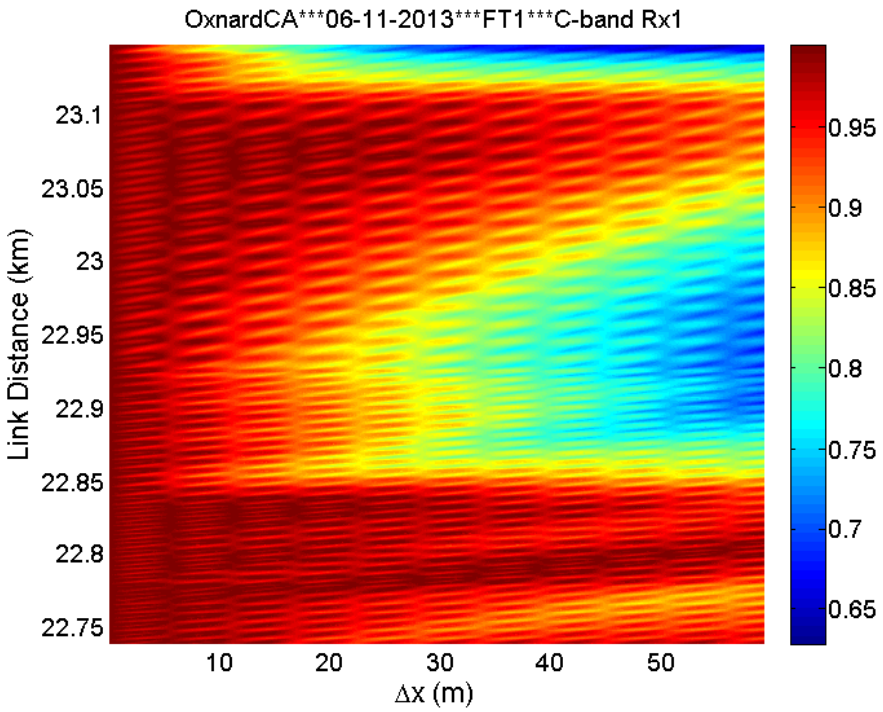

Figure 3.31. Contour of C-band TPCC vs. link distance *d* vs. *Δx* for segment of C-band Rx1 taken in FT1 in Oxnard, CA [58].

Table 3.5. C-band stationarity distance statistics, over-sea FT1 [58].

		TPCC		**collinearity**
		Rx1	**Rx2**	
Mean	(m)	23.5	19.0	12.2
	(λ's)	396.6	321.2	205.3
Median	(m)	15.2	14.4	6.4
	(λ's)	256.1	242.0	108.4
10th percentile	(m)	5.5	5.2	3.0
	(λ's)	92.9	87.3	49.8
Min	(m)	0.97	0.91	1.1
	('λs)	16.4	15.4	19.0

The second method to evaluate SD is the correlation matric distance [59]. CMD is between 0 and 1, with a smaller CMD meaning highly correlated and a larger CMD meaning uncorrelated. In order to be consistent with TPCC and the usual interpretation of

correlation, we calculate the collinearity=1-CMD [87], which also ranges from 0 (uncorrelated) to 1 (highly correlated). The CIR $h_{mn}(\tau,t_i)$ is the response between the n^{th} Tx antenna and the m^{th} Rx antenna m. Sample $h_{mn}(t_i)$ is the narrowband complex channel response (complex gain) at time t_i, which is a vectorially combined $h_{mn}(\tau,t_i)$ over the delay domain

$$h_{mn}(t_i) = \sum_{k=1}^{L_i} \alpha_{k,i} e^{j\phi_{k,i}}. \tag{3.8}$$

Our channel sounder has 1×2 SIMO antennas. The vectorized Rx CIRs are

$$\boldsymbol{h}(t_i) = \begin{bmatrix} h_{11}(t_i) \\ h_{21}(t_i) \end{bmatrix}. \tag{3.9}$$

Hence we can find the correlation matrix (at the Rx)

$$R(t_i) = \frac{1}{N} \sum_{k=i}^{i+N-1} \boldsymbol{h}(t_k) \boldsymbol{h}^H(t_k) \tag{3.10}$$

where N denotes the number of narrowband channel responses used, which is set to be the same as that employed for the TPCC in (3.6), the superscript H is Hermitian transpose. Our metric is

$$collinearity(\Delta t, t_i) = 1 - d_c(\Delta t, t_i) = \frac{tr\{R(t_i)R(t_i+\Delta t)\}}{\|R(t_i)\|_F \|R(t_i+\Delta t)\|_F} = \frac{tr\{R(t_i)R(t_i+\Delta t)\}}{\sqrt{tr[R^H(t_i)R(t_i)]tr[R^H(t_i+\Delta t)R(t_i+\Delta t)]}}, \tag{3.11}$$

where tr denotes matrix trace, and $\|\cdot\|_F$ denotes the Frobenius norm.

As with TPCC, SD is selected as the distance Δx (corresponding to Δt and flight velocity v, $\Delta x = v\,\Delta t$) such that $collinearity(\Delta t,t_i) > 0.9$. Again, the threshold 0.9 is conservative. The authors of [59] used 0.8 as their collinearity threshold. The threshold is sensitive to averaging window length N. Due to the sampling clock drift effect of our channel sounder, we employ a longer N (number of PDPs collected in 200λ in C-band

and 30λ in L-band) than that used in [59] of 25 consecutive PDPs, hence our threshold 0.9 is relatively larger than the threshold of 0.8 employed in [59].

Figure 3.32 shows a contour of *collinearity($\Delta t, t_i$)* for the same FT1 as shown in Figure 3.31 for the TPCC. The statistics of *collinearity($\Delta t, t_i$)* are also provided in Table 3.5. The median value 6.4 m is of the same order as the 15 m TPCC results. We have tried both values for our estimations of Ricean K-factor and inter-receiver correlation, and results with both values of SD are essentially the same. Therefore, the SD results from the collinearity and TPCC methods generally agree with each other. We chose 15 m as the stationarity distance for the AG channel data processing for both C-band and L-band.

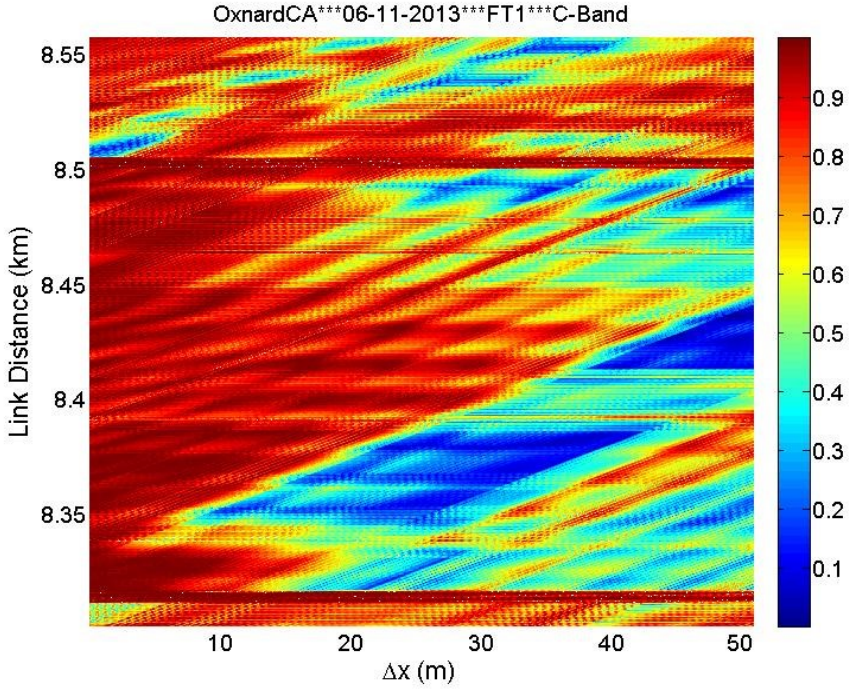

Figure 3.32. Contour of collinearity vs. link distance *d* vs. *Δx* for segment of C-band Rx1 taken in FT1 in Oxnard, CA [58].

CHAPTER 4

EARTH REFLECTION BASED DETERMINISTIC MODELS AND IMPROVEMENTS

A "two ray" model with the LOS component as one ray and the earth reflection as the other ray is a typical path loss model for several scenarios. As the GS antenna is elevated and the aircraft flies in the sky, a two-ray model is expected to fit the AG channel in many cases. We developed two earth reflection deterministic models based on flat earth and curved earth conditions, [88] and [89]. The curved earth two-ray model should be implemented for larger distances since it's more accurate, whereas the flat earth two-ray is preferred for short distances for its simplicity. We also applied multiple modifications or improvements for the earth reflection deterministic models, including spherical earth divergence, atmospheric refraction and earth surface roughness. Corrections for surface roughness are applicable for both flat and curved earth cases, whereas the refractivity and divergence factors are only applied in the curved earth approximation. The detailed formulas, effects and discussion regarding these quantities are summarized in this chapter. Section 4.5 provides multiple boundaries for the CE2R model.

4.1 FLAT EARTH TWO RAY

The flat earth geometry is illustrated in Figure 4.1 [9][5]. Variables h_G and h_A are the antenna heights of GS and aircraft, respectively, and d is the distance on the earth

[5] The development here only provides additional detail and comparison with the CE2R model, and does not describe anything new.

between the points directly beneath the aircraft and the GS. (Tacitly assumed is that the antenna dimensions are small relative to the heights.) The length of LOS path $R_{1,k}$ is expressed as

$$R_{1,k} = \sqrt{d_k^2 + (h_{A,k} - h_G)^2}, \tag{4.1}$$

with c the speed of light and subscript k indicates a time or distance index. The delay of the LOS component is

$$\tau_{0,k} = R_{1,k}/c. \tag{4.2}$$

Via the Friis free-space transmission equation [90], we can find the LOS amplitude coefficient:

$$\alpha_{0,k} = \frac{c}{4\pi f_c}\frac{1}{R_{1,k}}. \tag{4.3}$$

The length of the reflected path $R_{2,k}$ is

$$R_{2,k} = l_{1,k} + l_{2,k} = \sqrt{d_k^2 + (h_{A,k} + h_G)^2} = \sqrt{R_{1,k}^2 + 4h_{A,k}h_G}. \tag{4.4}$$

Then, the delay of the earth surface reflection is

$$\tau_{g,k} = R_{2,k}/c = \sqrt{R_{1,k}^2 + 4h_{A,k}h_G}/c. \tag{4.5}$$

The reflected component's amplitude coefficient is

$$\alpha_{g,k} = \frac{c}{4\pi f_c}\frac{1}{R_{2,k}}, \tag{4.6}$$

and ψ is the grazing angle

$$\psi_k = \tan^{-1}\left(\frac{h_{A,k}+h_G}{d_k}\right) = \tan^{-1}\left(\frac{h_{A,k}+h_G}{\sqrt{R_{1,k}^2-(h_{A,k}-h_G)^2}}\right). \tag{4.7}$$

The elevation angle can be found as

$$\theta_{e,k} = \sin^{-1}\left(\frac{h_{A,k}-h_G}{R_{1,k}}\right), \tag{4.8}$$

and the phase delay between the LOS and the earth surface reflection is

$$\Delta\phi_k = \frac{2\pi\Delta R_k}{\lambda} = \frac{2\pi f_c(R_{2,k}-R_{1,k})}{c} = 2\pi f_c(\sqrt{R_{1,k}^2 + 4h_{A,k}h_G} - R_{1,k})/c \tag{4.9}$$

From [91], we obtain the reflection coefficient for both vertical and horizontal polarizations (note that most aircraft will employ vertically polarized antennas)

$$\Gamma_{v,k,1} = \frac{[\varepsilon_r - j\sigma/(2\pi f_c\varepsilon_0)]\sin(\psi_k) - \sqrt{\varepsilon_r - j\sigma/(2\pi f_c\varepsilon_0) - \cos^2(\psi_k)}}{[\varepsilon_r - j\sigma/(2\pi f_c\varepsilon_0)]\sin(\psi_k) + \sqrt{\varepsilon_r - j\sigma/(2\pi f_c\varepsilon_0) - \cos^2(\psi_k)}} \tag{4.10}$$

$$\Gamma_{h,k,1} = \frac{\sin(\psi_k) - \sqrt{\varepsilon_r - j\sigma/(2\pi f_c\varepsilon_0) - \cos^2(\psi_k)}}{\sin(\psi_k) + \sqrt{\varepsilon_r - j\sigma/(2\pi f_c\varepsilon_0) - \cos^2(\psi_k)}}. \tag{4.11}$$

where ε_r is the dielectric constant or relative permittivity, ε_0 denotes the vacuum permittivity, which is approximately 8.85×10^{-12} F/m, σ denotes the conductivity in S/m, and we assume that the reflection objects do not contain any magnetic materials ($\mu=\mu_0$). Using these results, the CIR is expressed as

$$h_{2-ray}(\tau,k) = \alpha_{0,k}\delta(\tau-\tau_{0,k}) + \alpha_{g,k}e^{-j\Delta\phi_k}\Gamma_k\delta(\tau-\tau_{g,k}) \tag{4.12}$$

For convenience, we can also normalize the LOS component amplitude to one, yielding

$$h_{2-ray}^N(\tau,k) = \delta(\tau-\tau_{0,k}) + (\alpha_{g,k}/\alpha_{0,k})e^{-j\Delta\phi_k}\Gamma_k\delta(\tau-\tau_{g,k}). \tag{4.13}$$

Some typical values of the electrical constants of the earth (permittivity ε_r, conductivity σ and permeability μ_r) are listed in Table 4.1 [9].

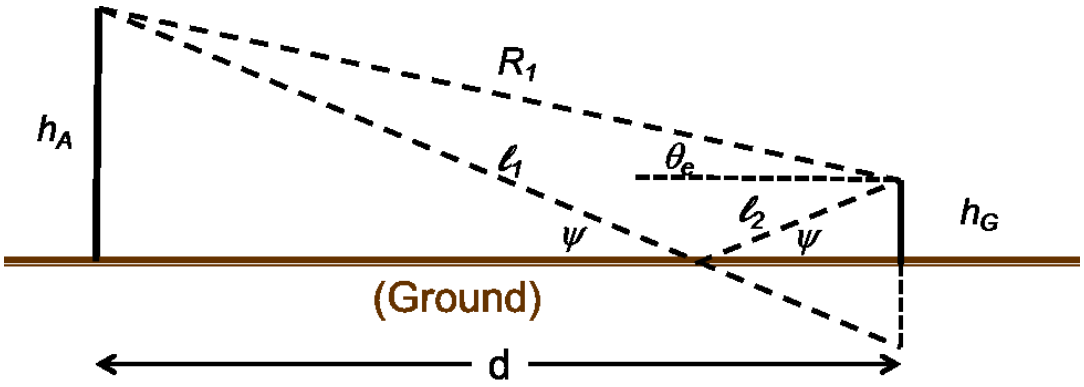

Figure 4.1. Geometry for flat-earth approximation.

Table 4.1. Typical values of ground electrical constants [9].

	Conductivity σ (S/m)	Dielectric constant ε_r	Relative permeability μ_r
Poor Ground (Dry)	0.001	4 - 7	1
Average Ground	0.005	15	1
Good Ground (Wet)	0.02	25 - 30	1
Sea water	5	81	1
Fresh water	0.01	81	1

4.2 CURVED EARTH TWO RAY

The CE2R model is illustrated in Figure 4.2 [92]. Since aircraft can fly several hundred meters or even several kilometers above the ground, and the link distance can be up to 40 km in our measurements, the curved earth approximation is expected to fit the empirical data more accurately than the flat earth approximation. The computation of the curved earth case is more complex than that in the flat earth case.

In Figure 4.2 point A denotes the aircraft, point B is the GS and point C denotes the earth center. The effective earth radius *ka* is used instead of the true earth radius to account for atmospheric refraction, where the atmospheric refractivity constant *k* is a function of altitude meteorological conditions; details regarding *k* are described in section 4.3.2. The earth radius *a* is based on the equatorial radius a_e, polar radius a_p and latitude φ as

$$a = \sqrt{\frac{(a_e^2 cos\varphi)^2 + (a_p^2 sin\varphi)^2}{(a_e cos\varphi)^2 + (a_p sin\varphi)^2}}, \tag{4.14}$$

where the equatorial radius (semi-major axis) a_e is 6378.137 km and polar radius (semi-minor axis) a_p is 6356.752 km [93]. The latitude φ of measurements sites in our AG channel measurement campaign ranged from 34.2º (Oxnard, CA) to 41.5º (Cleveland, OH), therefore the earth radius was between 6371.427 and 6368.795 km.

We proceed with analysis following [88], referring to Figure 4.2. First, angle $q_k=\theta_{1,k}+\theta_{2,k}$ can be computed via the law of cosines with known the GS antenna height h_G, the aircraft antenna height $h_{A,k}$ and the link distance $R_{1,k}$

$$R_{1,k}^2 = (ka + h_{A,k})^2 + (ka + h_G)^2 - 2\big(ka + h_{A,k}\big)(ka + h_G)\cos(q_k). \quad (4.15)$$

Then we compute Tx-Rx distance on the earth surface d_k

$$d_k = kaq_k, \quad (4.16)$$

and then three necessary quantities [94]:

$$m_k = \frac{d_k^2}{4ka(h_{A,k}+h_G)} \quad (4.17)$$

$$c_k = \frac{h_{A,k}-h_G}{h_{A,k}+h_G} \quad (4.18)$$

$$b_k = 2\sqrt{\frac{m_k+1}{3m_k}}\cos\{\frac{\pi}{3} + \frac{1}{3}\arccos[\frac{3c_k}{2}\sqrt{\frac{3m_k}{(m_k+1)^2}}]\}. \quad (4.19)$$

Next we find the earth surface distances and angle $\theta_{l,k}$

$$d_{1,k} = d_k(1 + b_k)/2 \quad (4.20)$$

$$d_{2,k} = d_k - d_{1,k} \quad (4.21)$$

$$\theta_{1,k} = d_{1,k}/(ka) \quad (4.22)$$

and grazing angle

$$\Psi_k = \frac{h_{A,k}+h_G}{d_k}[1 - m_k(1 + b_k^2)]. \quad (4.23)$$

Then we calculate the path length difference between the LOS and earth surface reflected components

$$\Delta R_k = 2d_{1,k}d_{2,k}\Psi_k^2/d_k, \quad (4.24)$$

hence the path length of the earth surface reflection is

$$R_{2,k} = R_{1,k} + \Delta R_k, \quad (4.25)$$

with which we can find the phase delay between the LOS component and earth surface reflection $\Delta\phi_k$ by (4.9), and the reflection coefficients Γ_k by (4.10) and (4.11).

What remains is the elevation angle; for this we first compute the angle v_k in Figure 4.2

$$v_k = \frac{\pi}{2} - q_k, \tag{4.26}$$

and via the law of sines

$$p_k = \frac{(ka+h_G)sin(q_k)}{sin(v_k)}, \tag{4.27}$$

then via the law of cosines the angle ϕ_k can be found

$$(ka + h_G)^2 = R_{1,k}^2 + (ka + h_{A,k})^2 - 2R_{1,k}(ka + h_{A,k})\cos(\phi_k), \tag{4.28}$$

and the angle β_k can be computed via the law of sines,

$$\beta_k = sin^{-1}[\frac{R_{1,k}\sin(\phi_k)}{p_k}], \tag{4.29}$$

then the elevation angle $\theta_{e,k}$ for CE2R is

$$\theta_{e,k} = \pi - \phi_k - \beta_k. \tag{4.30}$$

Finally the 2-ray CIR follows by employing these in (4.12) or (4.13). Comparison of the CE2R, FE2R and example empirical (measured) L-band path loss is shown in Figure 4.3, in which the empirical data is a data segment of flight track 2 taken at Oxnard, CA with link distance from 5 to 45 km. The CE2R model fits the measurements better than the FE2R does. The CE2R and FE2R models have almost the same two lobe magnitude values, but their phases are significantly different.

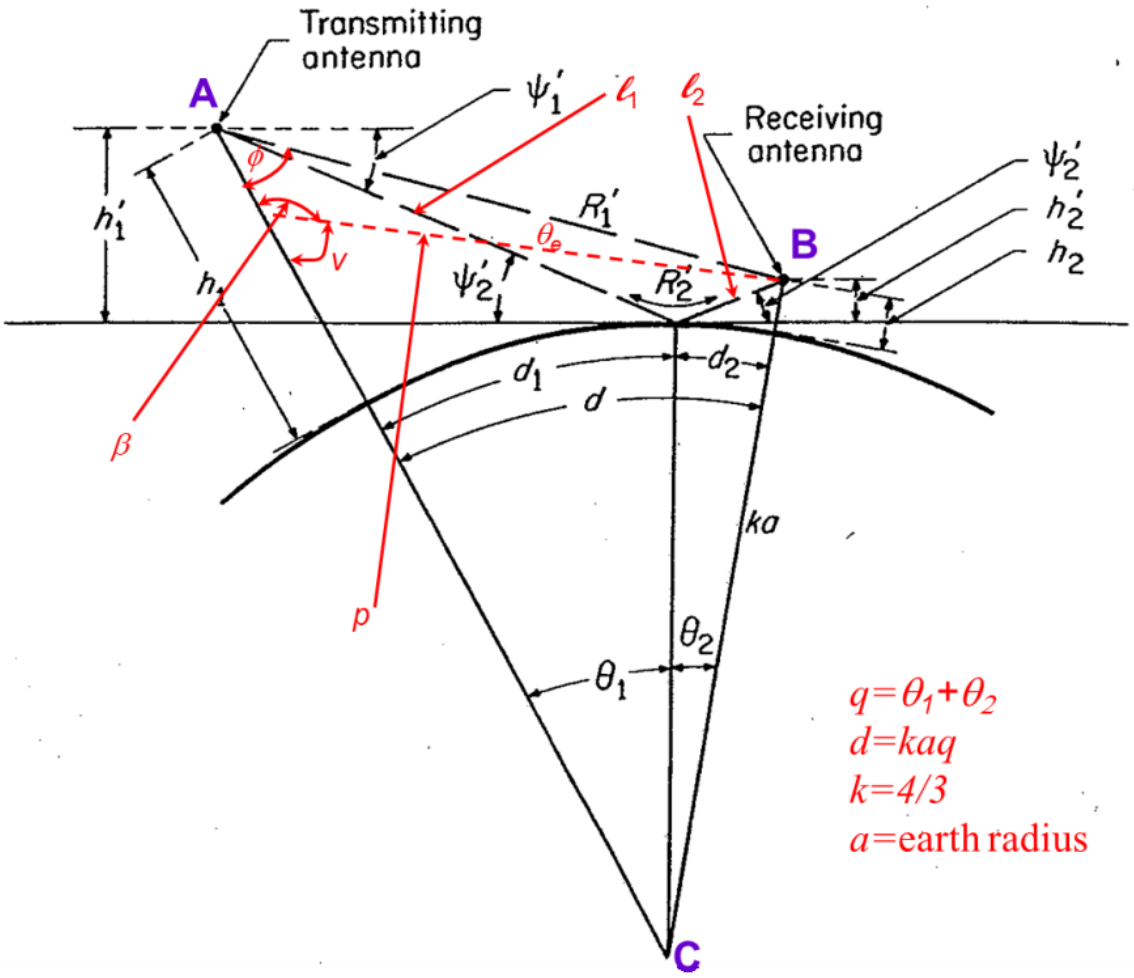

Figure 4.2. Geometry for curved-earth approximations (modified from [92]).

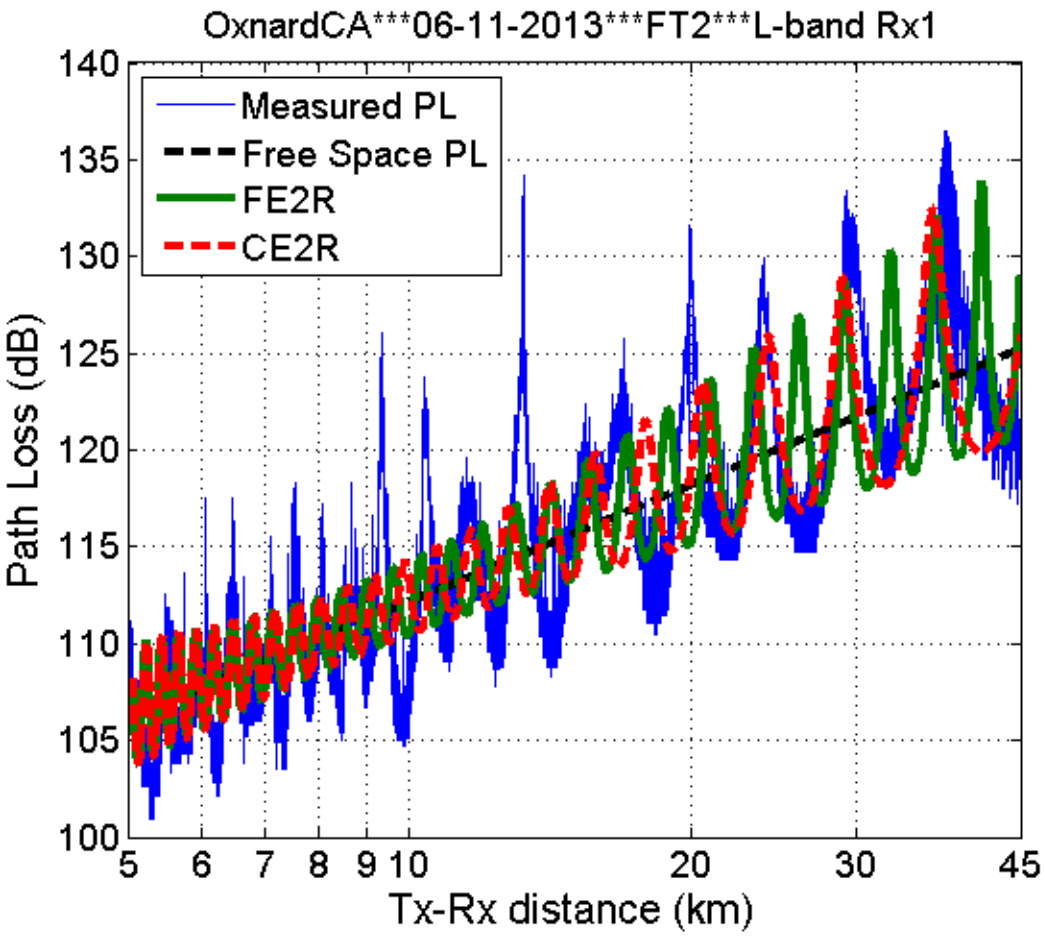

Figure 4.3. CE2R and FE2R model fits for empirical path loss vs. distance.

4.3 IMPROVEMENTS FOR THE EARTH REFLECTION DETERMINISTIC MODELS

4.3.1 SPHERICAL EARTH DIVERGENCE

The signals reflected by a spherical surface will spatially diverge. The energy lost due to the divergence increases as the distance increases, and as h_A, h_G and the radius of the sphere decrease. The reflection divergence factor D_k is always between zero and one, and this factor will multiply the surface reflection amplitude in (4.12) or (4.13). Via the law of cosines, as shown in Figure 4.2, the lengths between the reflection point and the aircraft $l_{1,k}$, and the GS, $l_{2,k}$, are

$$l_{1,k}^2 = (ka + h_{A,k})^2 + (ka)^2 - 2(ka)(ka + h_{A,k})\cos(\theta_{1,k}), \quad (4.31)$$

$$l_{2,k} = R_{2,k} - l_{1,k}. \quad (4.32)$$

The reflection divergence factor is then given by [88]

$$D_k = [1 + \frac{2}{kasin(\Psi_k)} \frac{l_{1,k} l_{2,k}}{l_{1,k} + l_{2,k}}]^{-1/2}. \quad (4.33)$$

The adjusted reflection coefficient $\Gamma_{k,2}$ is $\Gamma_{k,1}$ by (4.10) or (4.11) in CE2R model

$$\Gamma_{k,2} = D_k \Gamma_{k,1}. \quad (4.34)$$

The reflection divergence factor for one of our actual flight tracks is shown in Figure 4.4. In this over ocean FT taken near Oxnard, CA, the GS altitude was 20 m, the aircraft altitude ranged from 796 to 804 m, and the Tx-Rx distance was between 1 and 45 km. The divergence factor decreased with link distance, and was between 0.99 and 1, hence for most of our applications we can approximate D_k as one.

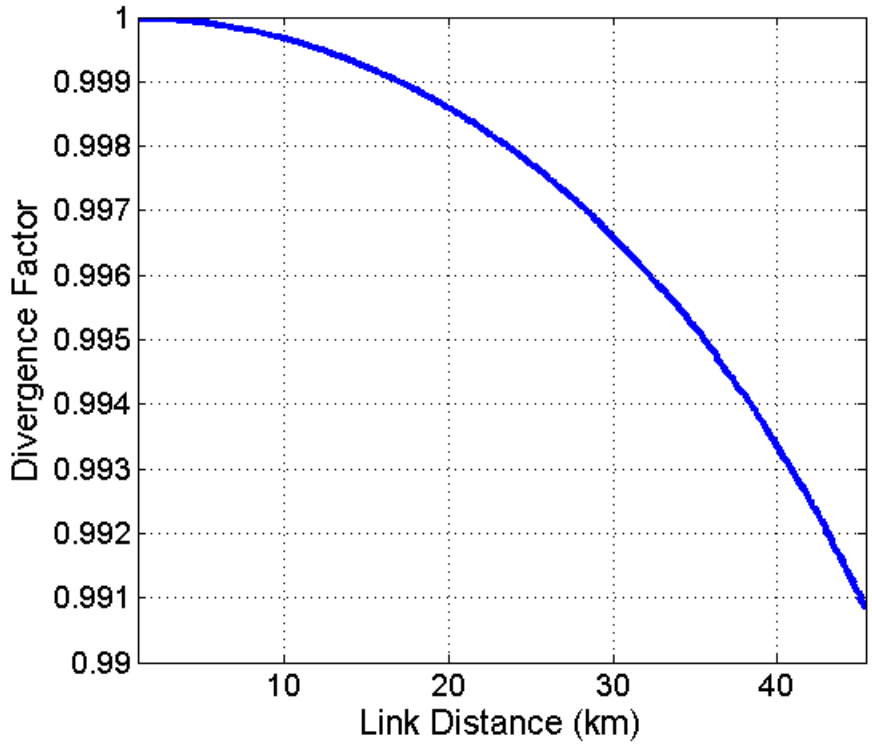

Figure 4.4. Divergence factor versus link distance, over Sea FT2.

4.3.2 ATMOSPHERIC REFRACTION

The propagating electromagnetic wave deviates from a straight line path as it passes through the atmosphere, and this physical phenomenon is termed atmospheric refraction. It is due to the electromagnetic wave velocity through air increasing with deceased air density as a function of altitude. As shown in Figure 4.5, the electromagnetic wave actually propagates longer than would a straight line path between Tx and Rx so that a refractivity coefficient needs to be applied to estimate the true path distance.

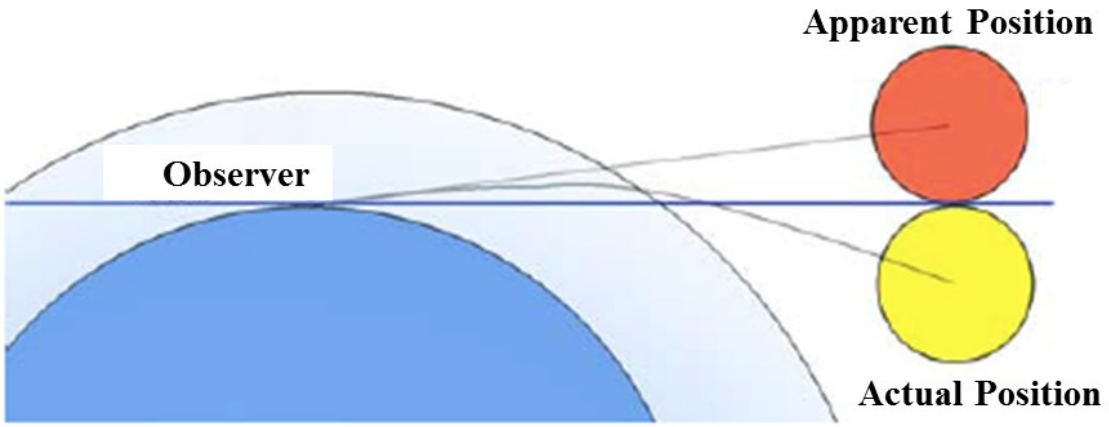

Figure 4.5. Illustration of atmosphere refraction.

The atmospheric refractivity can be expressed as

$$N = (n-1) \times 10^6 = \frac{77.6}{T}\left(p + 4810\,\frac{e}{T}\right), \tag{4.35}$$

where n is the refractive index, p is the total pressure in millibars, e is the partial pressure of water vapor in millibars, and T is the absolute temperature in degrees Kelvin. Pressure typically decreases exponentially with altitude, and the same is true for the refractive index. This has led to the definition of the atmospheric refractivity N in terms of "N-units", and the Recommendation ITU-R P.834-5 [95] and the Consultative Committee on International Radio (CCIR) employ the following approximation:

$$N(h) = 315 \times e^{-0.136h} \tag{4.36}$$

where height h is expressed in kilometers. Refractive coefficient k is defined as

$$k = \frac{1}{1+a\times 10^{-6}\frac{dN}{dh}} \tag{4.37}$$

where a denotes the earth radius in km. An alternative (linear) approximation to (4.36) is dN/dh=-39 N-units/km under standard atmospheric conditions.

The relation between altitude h and refractive coefficient k is shown in Figure 4.6. The refractivity coefficient approximation of 4/3, as the red line in Figure 4.6, is widely used for near earth surface communication systems. It is based on the mean value over the first kilometer of atmosphere in a temperate climate. However, for the AG channel, the aircraft altitude can be much larger than 1 km. In our data processing, the refractivity coefficient is a variable dependent on the mean altitude value between the GS and aircraft $(h_A+h_G)/2$.

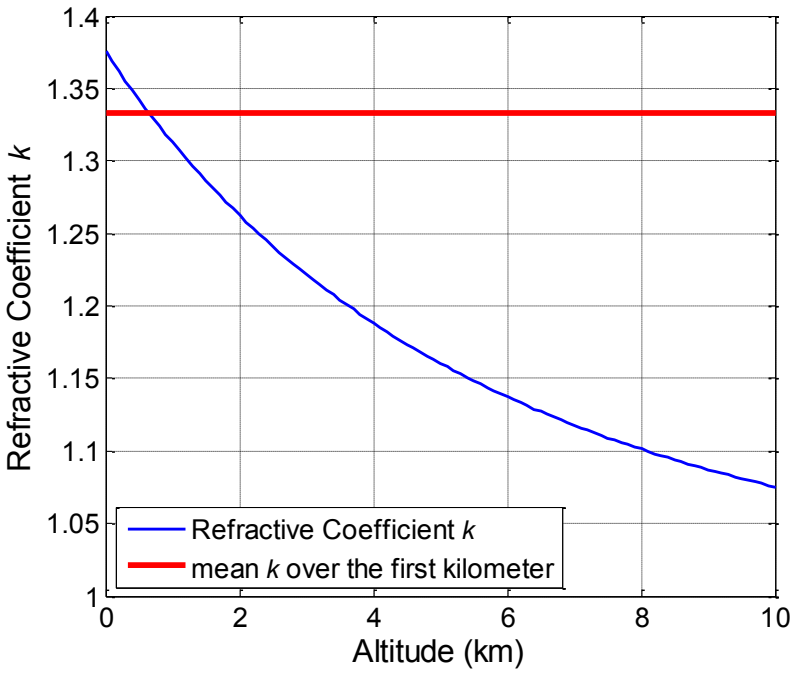

Figure 4.6. Refractivity coefficient k vs. altitude h.

As illustrated in Figure 4.7 and Table 4.2, positive values of *dN/dh* yield refractive coefficient *k* values from 0 to 1, and the effective radius in CE2R is smaller than the true earth radius *a*, causing the radio wave to propagate away from the horizon (bent upward). A zero *dN/dh* value indicates a constant refractivity versus altitude or an effective radius equal to *a*. Negative values of *dN/dh* yield *k* larger than one, hence the radio wave propagates towards the horizon (bent downward). If *dN/dh* is equal to -157 N-units/km, *k* becomes infinite, hence the effective radius becomes infinite and no bending occurs at all. When *dN/dh* is smaller than -157 N-units/km, the refractive coefficient *k* becomes a negative value. This non-standard condition is termed ducting", which will be described in subsection 4.4.3.

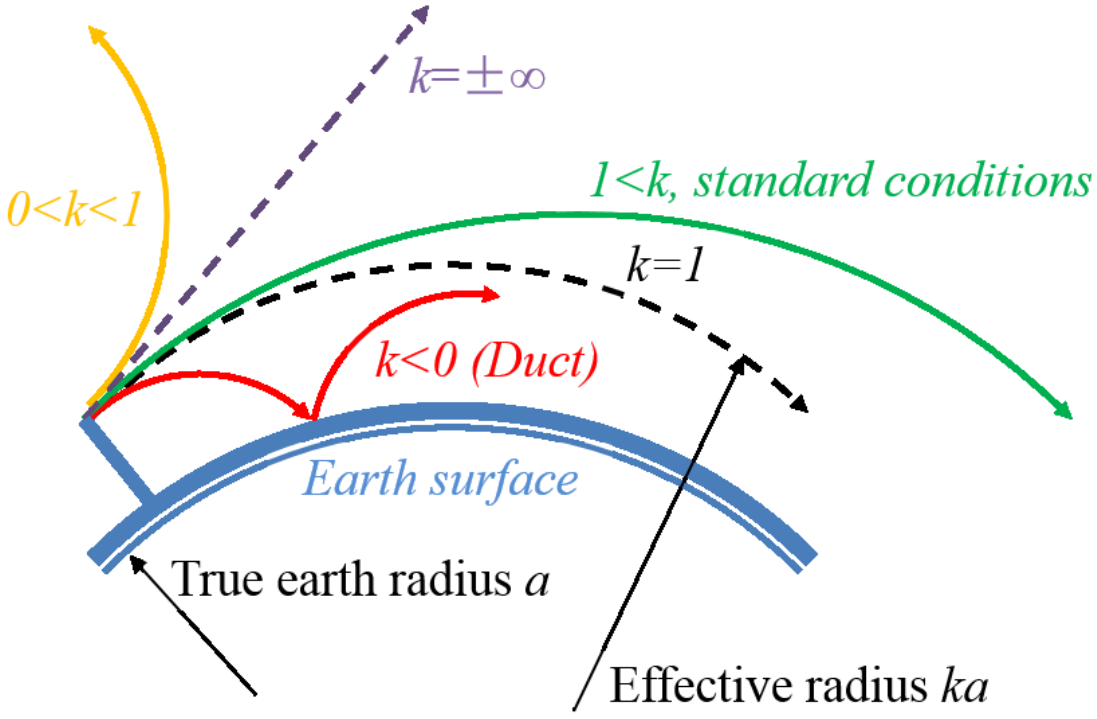

Figure 4.7. Diagram of refraction mechanisms.

Table 4.2. Refraction condition summary.

dN/dh	*k*	Effective radius	Bending
0 < dN/dh	*0 < k < 1*	*< a*	upward
dN/dh = 0	*k = 1*	*= a*	same curvature as earth surface
-157 < dN/dh < 0	*1 < k*	*> a*	downward
dN/dh = -157	*k = ±∞*	*= ±∞*	straight
dN/dh < -157	*k < 0*	*< 0*	downward, trapping

4.3.3 SURFACE ROUGHNESS

When the earth is smooth, the reflection will be specular, and when rough enough, the signals will be scattered instead of reflected. In other words, the reflected signals are dispersed into multiple directions. In this case, the energy that propagates to the receiver can be significantly less than that estimated via α_g and Γ. Roughness is dependent on wavelength λ. The roughness of the ground can be estimated by geographic information, and for water surfaces roughness can be estimated by wind speed [91].

The surface reflection coefficient magnitude is affected by the surface roughness, in which surface elevation is most often modeled as a Gaussian random variable with standard deviation σ_h. Then, just as for divergence, the smooth surface reflection coefficient magnitude $|\Gamma_0|$ is modified by multiplication of the roughness factor. For water, this roughness factor is computed using the Miller-Brown surface roughness model [96]:

$$\Gamma_{k,3} = \Gamma_{k,2} e^{-2(2\pi g)^2} I_0[2(2\pi g)^2], \tag{4.38}$$

where I_0 is the first-kind zero-order modified Bessel function, and g is given by

$$g = \sigma_h \sin(\Psi_k) / \lambda, \tag{4.39}$$

where Ψ_k denotes the grazing angle. For a water surface reflection, σ_h is related to wind speed according to the Philips' saturation curve spectrum [97]

$$\sigma_h = 0.0051u^2, \tag{4.40}$$

where u is wind speed in meters per second.

We extend results of Figure 4.3 to Figure 4.8 to show the effects of rough sea surface with multiple wind speed values. Comparisons of sea surface reflection coefficient magnitude in both L- and C-band are shown in Figures 4.9 and 4.10; the comparisons include CE2R and FE2R, with/without divergence factor applied, and with different wind speeds. As discussed, the magnitude of the reflection coefficient and two ray lobes are noticeably affected by the wind speed.

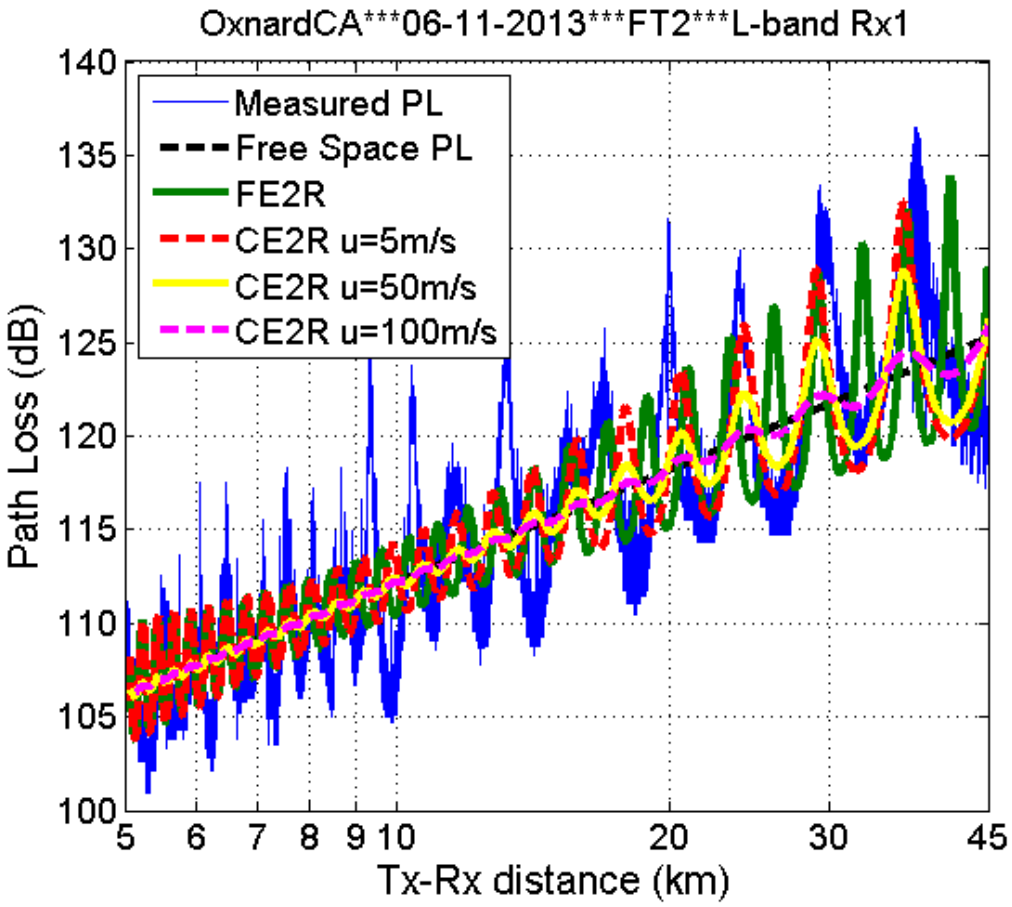

Figure 4.8. Path loss vs. distance showing the effects of rough sea surface.

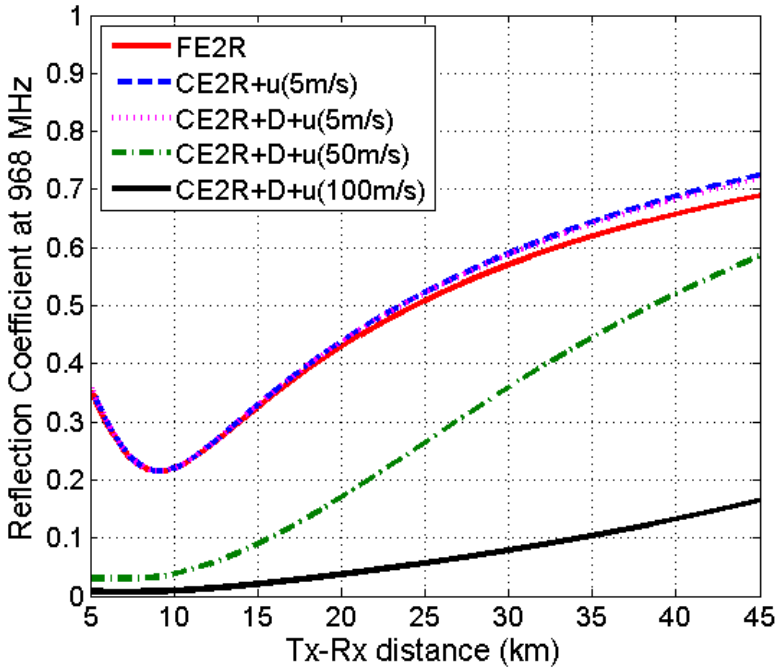

Figure 4.9. Magnitude of reflection coefficient vs. distance in L-band for various conditions.

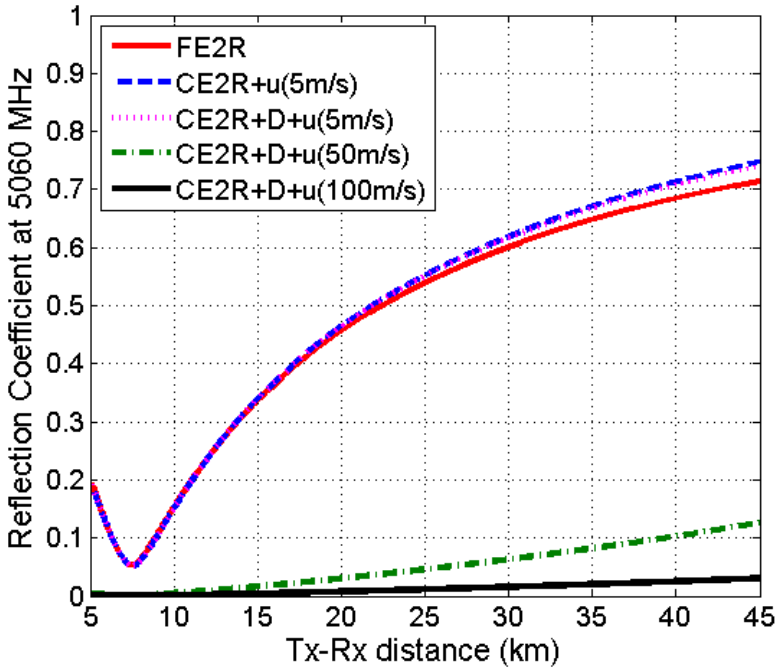

Figure 4.10. Magnitude of reflection coefficient vs. distance in C-band for various conditions.

4.4 FURTHER CONSIDERATIONS FOR AG PROPAGATION

The radio wave propagating in the AG channel is affected or occasionally influenced by some additional effects, including rain attenuation, atmospheric gaseous attenuation, ducting and foliage attenuation. Since our AG channel measurements were conducted in clear weather and with high elevated GS antennas, no hydrometeor effects or foliage attenuation were present. Ducting was not observed in our experimental data as well. In this section these effects will be briefly described.

4.4.1 ATMOSPHERIC GAS EFFECTS

The radio wave energy can be absorbed by water-vapor, oxygen and nitrogen. This atmospheric attenuation is a function of frequency, air pressure, temperature and water-vapor density. Experimental results and models are provided by Recommendation ITU-R P.676-10 [98]. The gaseous attenuation near sea level is approximately 0.03 dB/km at 1 GHz and 0.04 dB/km at 5 GHz, with air pressure 1013 hPa, temperature 15 ºC and water-vapor density of 7.5 g/m. The gaseous attenuation caused by water-vapor is much smaller than that caused by dry air (oxygen and nitrogen) at frequencies smaller than 10 GHz. Therefore the gaseous attenuation for all measured AG scenarios is unlikely larger than 0.03 dB/km at 1 GHz and 0.04 dB/km at 5 GHz as the pressure and water-vapor density for other settings are both smaller than those at sea level, moreover, the gaseous attenuation decreases as the altitude increases [99] hence the AG channel at other GS altitudes has smaller gaseous attenuation than at sea level. The AG channel propagation path is no larger than 45 km in our measurement campaign, so the gaseous attenuation is smaller than 1.8 dB. The gas attenuation is not applied in our CR2R

deterministic model, but it should be considered if the propagation length is large (e.g., 100 km link distance yields a gas attenuation of 4 dB in C-band and 3 dB in L-band).

4.4.2 HYDROMETEOR ATTENUATION

In the previous subsection the water in gaseous state was considered. Water in liquid and solid states, in the form of fog, clouds, ice, snow, rain, and so on, may also affect the path loss. Water in nongaseous state in the atmosphere is generally termed "hydrometeors". Solid water (ice and snow) absorb much less electromagnetic energy at microwave frequencies than does liquid water. The sizes of liquid water particles in clouds and fog are very small (radius usually smaller than 100 μm), so the attenuation at frequencies smaller than 10 GHz is negligible. The attenuation due to clouds and fog for frequencies higher than 10 GHz is reported in Recommendation ITU-R P. 840-6 [100].

Rain is the most significant factor in radio wave propagation among all kinds of hydrometeors. Rain attenuation increases with frequency as well as with the rainfall rate. Based upon the prediction methods and parameters provided by Recommendation ITU-R P.838-3 [101], the authors of [99] generate rain attenuation versus frequency and selected rain rates. The rain attenuation at 5 GHz is approximately 0.01 dB/km for a rainfall rate of 10 mm/hour (light rain) and is 0.4 dB/km for a rainfall rate of 100 mm/hour (strong thunderstorm). The rain attenuation at 1 GHz is much smaller than 0.01 dB/km, and is hence negligible for all but the longest links.

4.4.3 DUCTING

Ducting is an atmospheric effect that only occurs in anomalous conditions in which the atmospheric refractivity decreases unusually rapidly as the altitude increases. Ducts can be viewed as leaky waveguides, and as such, the signal power enhancements

caused by ducts can be utilized by near surface communication systems. Ducts can also have strong impact on radar systems [102]. As mentioned in subsection 4.3.2 and equation (4.37), the refractive coefficient k becomes negative when dN/dh<-157 N-units/km, yielding a downward bending of the radio wave, and this is termed a duct. Ducts only occur in some specific altitude ranges. As the red curve shows in Figure 4.7, the radio wave in the duct is bent toward the earth surface. If the surface is smooth enough, the bent radio wave is reflected, and it propagates and curves back to the earth surface again. The "trapping" phenomenon of bending and specular reflections acts as waveguide.

Ducts can be classified into three categories: 1) evaporation duct; 2) surface based duct; and 3) elevated duct [99], [103]. Evaporation ducts occur over water with height ranging from 0 to 40 m above the surface, with an average duct height of 13 m worldwide [104], [105], [106]. The evaporation duct formation is due to the extremely rapid moisture decrease near the water surface. Evaporation ducts are nearly permanent and only affect frequencies above approximately 2 GHz.

The surface-based duct extends down to the earth surface with worldwide average thickness of 85 m. It only occurs from 1% to 46 % (worldwide average 8%) of the time and is independent of frequency. The elevated duct occurs in an altitude range that is above the earth surface. The worldwide bottom height of elevated ducts ranges from 600 to 1500 m with duct thickness of a few hundred meters. Elevated ducts are caused by the rapid advection between a dry, warm air layer above a moist, cool air layer. The elevated duct plays an essential role for radar systems and is usually considered independent of frequency. The yearly average occurrence, strength and thickness of surface-based and

elevated ducts and the bottom height of the elevated duct for different locations in the world are provided in Recommendation ITU-R P.453-10 [107].

The authors of [108] and [109] hypothesized the presence of ducts based on empirical AG channel testing conducted over the South China Sea at 5.7 GHz. The aircraft altitude was 0.37, 0.91 and 1.83 km and the GS antenna heights were 2.1 and 7.65 m. The average signal power enhancement caused by a combination of evaporation duct and elevated duct was 0.11 dB/km. The variation of the enhancement was modeled as a Gaussian with standard deviation of 0.01 dB/km.

Ducting can be modeled by ray-tracing method, but doing so requires knowledge of the local refractivity index variation as a function of altitude, which is unavailable for our AG measurements. Again, based upon the empirical path loss collected in our AG measurements campaign, no ducting was observed.

4.5 BOUNDARIES FOR CURVED EARTH MODEL

4.5.1 BOUNDARY OF VALID GRAZING ANGLE

The CE2R cannot be used if the link range is so long that diffraction phenomena become preponderant [88]. This maximum link range limitation is expressed by the minimum grazing angle,

$$\Psi_{k,min} = (2100/f_C)^{1/3}, \tag{4.41}$$

where the minimum grazing angle $\Psi_{k,min}$ is in milliradians and f_C is the center frequency in MHz [94]. The value of $\Psi_{k,min}$ is approximately 0.074 degrees for 968 MHz and 0.043 degrees for 5060 MHz.

The grazing angle cannot exceed a maximum value of $\Psi_{k,max} = \pi/2$ radians. Approximations are introduced by three intermediate quantities m_k, c_k and b_k in equations

(4.17)-(4.19). The grazing angle estimated by these quantities can be larger than π/2 at short distances, which is of course incorrect, and this can cause some incorrect results. Hence the maximum grazing angle has to be limited to π/2.

From eq. (4.23) and (4.19) the grazing angle is given by

$$\psi_k = \frac{h_{A,k}+h_G}{d_k}\frac{4ka(h_{A,k}+h_G)-d_k{}^2(1+b_k{}^2)}{4ka(h_{A,k}+h_G)} = \frac{4ka(h_{A,k}+h_G)-d_k{}^2(1+b_k{}^2)}{4kad_k}. \quad (4.42)$$

Since b_k is always between 0 and 1, $1 + b_k{}^2 < 2$. For short distances where d_k is only up to a few hundred meters, $d_k{}^2(1 + b_k{}^2) \ll 4ka(h_{A,k} + h_G)$, or $d_k{}^2 \ll 2ka(h_{A,k} + h_G)$. (Note that even for very small values of $h_{A,k}$ and h_G, e.g., $h_{A,k}$+h_G~20 m, and k~1, since a~6380 km, the inequality generally holds very well, e.g., the left side is less than 1/100th the right side for these parameters with d_k<1.1 km). Using the limit of $\Psi_{k,min}$, the grazing angle limitation for CE2R is

$$\left(\frac{2100}{f_{MHz}}\right)^{\frac{1}{3}}(mrad) < \psi_k < \frac{\pi}{2}, \quad (4.43)$$

where the upper limit is simply based upon geometry (a grazing angle larger than π/2 implies that the propagation geometry changes and/or propagation direction also changes, in which geometric parameters should be re-defined). Then we have for "short" distances

$$\psi_k \cong \frac{4ka(h_{A,k}+h_G)}{4kad_k} = \frac{h_{A,k}+h_G}{d_k} < \frac{\pi}{2}. \quad (4.44)$$

Thus for our "short" link distance condition, the great circle path distance d_k limit for use of the CE2R model is

$$\frac{2}{\pi}(h_{A,k} + h_G) < d_k < \frac{h_{A,k}+h_G}{\left(\frac{2100}{f_{MHz}}\right)^{\frac{1}{3}}(mrad)}. \quad (4.45)$$

The maximum and minimum horizontal distance d_k for multiple values of GS and aircraft height are shown in Figures 4.11, 4.12 and 4.13, respectively. In our AG channel

measurement campaign, the GS height was 20 m, the aircraft height was always larger 510 m and the link range was less than 50 km. We never reached the minimum grazing angle (maximum d_k). The minimum d_k values shown in Figure 4.13 are always outside the half power main beam of the GS antennas where the PDPs are removed in the data processing. Therefore, all the PDPs we used in our channel modeling satisfy eq. (4.45).

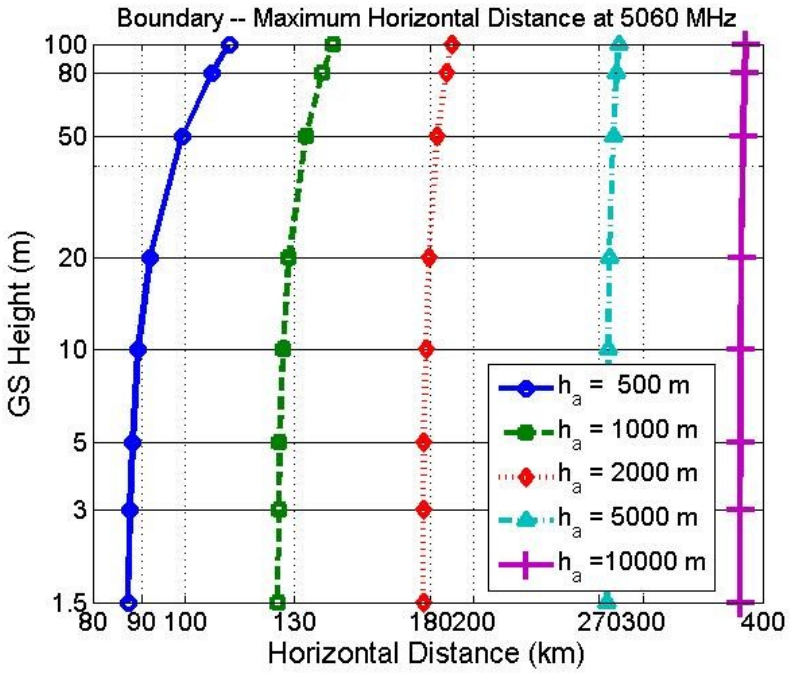

Figure 4.11. GS height and aircraft height vs. maximum horizontal distance for CE2R at 5060 MHz, based on the minimum grazing angle, h_a denotes aircraft height.

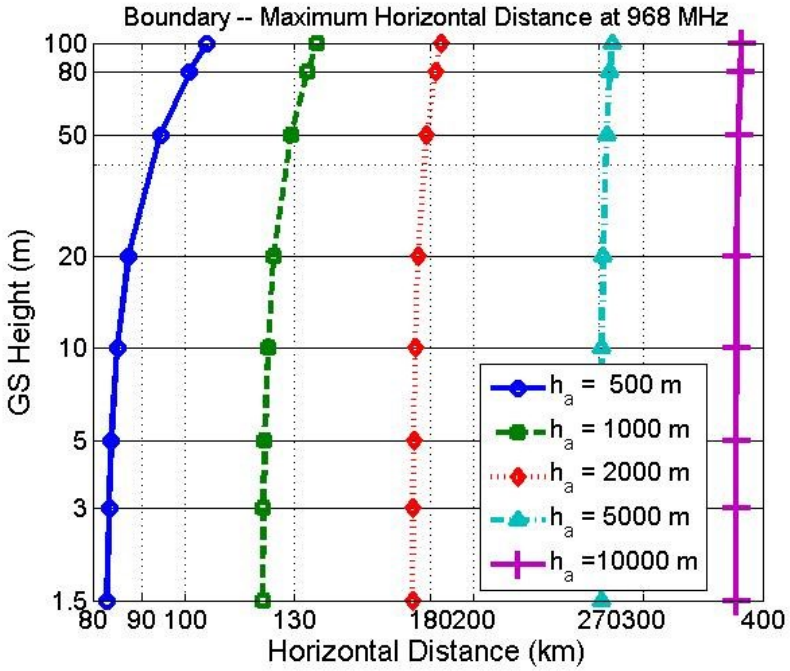

Figure 4.12. GS height and aircraft height vs. maximum horizontal distance for CE2R at 968 MHz, based on the minimum grazing angle, h_a denotes aircraft height.

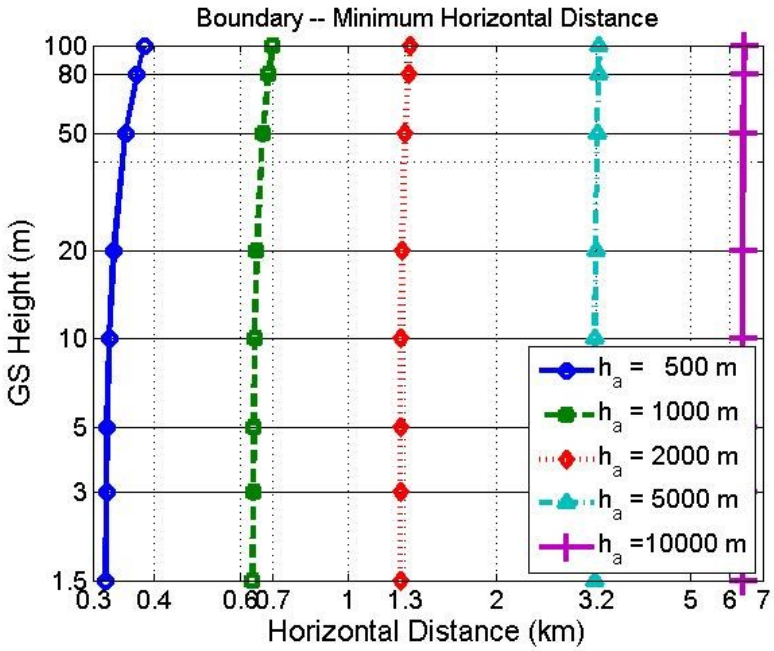

Figure 4.13. GS height and aircraft height minimum horizontal distance for CE2R, based on the maximum grazing angle, h_a denotes aircraft height.

4.5.2 BOUNDARY OF RESOLVABLE CE2R

The delay resolution of the 50 MHz bandwidth C-band channel sounder is 20 ns. The LOS and earth surface reflection are resolvable at small distances. Since the path length difference between the two rays (LOS and surface reflection) decreases as the link distance increases, beyond a specific value of distance, the two rays lie in the same 20 ns delay bin and are hence *unresolvable* by the sounder. The resolvable boundary, as a function of the AC height, the GS antenna height and link distance, is shown in Figure 4.14. The GS antenna height was 20 m (red line) in the measurement campaign and the AC height of the over sea data collected in Oxnard, CA was approximately 800 m. The 50 MHz C-band two rays were unresolvable when the link distance was larger than 5.38 km.

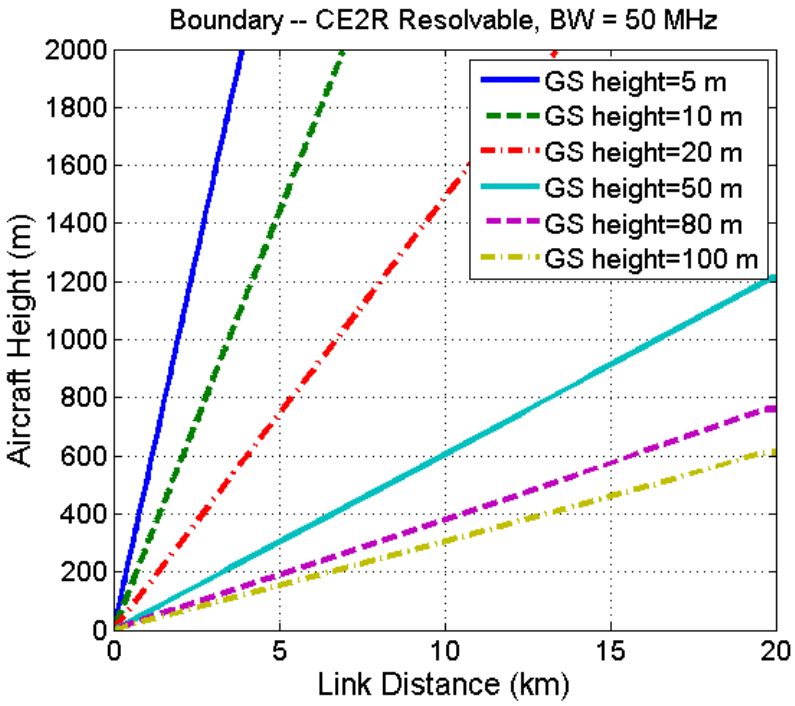

Figure 4.14. CE2R resolvable boundary for 50 MHz bandwidth.

The L-band sounder bandwidth is 5 MHz, yielding delay resolution of 200 ns. The two rays are always unresolvable with the GS antenna lower than 30 m. The bandwidth can be in effect converted to smaller values by combining adjacent chips within a PDP, e.g., 1 MHz in C-band or 200 kHz in L-band. With the 20 m GS antenna height, any of the 1 MHz or 200 kHz bandwidths do *not* allow the LOS and earth surface reflection to be resolvable.

4.5.3 BOUNDARY OF BEYOND LOS

As the aircraft may fly far away from the GS, the LOS can be blocked by the earth, and this condition is termed beyond line of sight (b-LOS). The boundaries of the b-LOS region for multiple GS antenna heights are shown in Figure 4.15. The LOS was never blocked by the smooth earth surface in our AG channel project (as the Tx-Rx distance was no larger than 45 km).

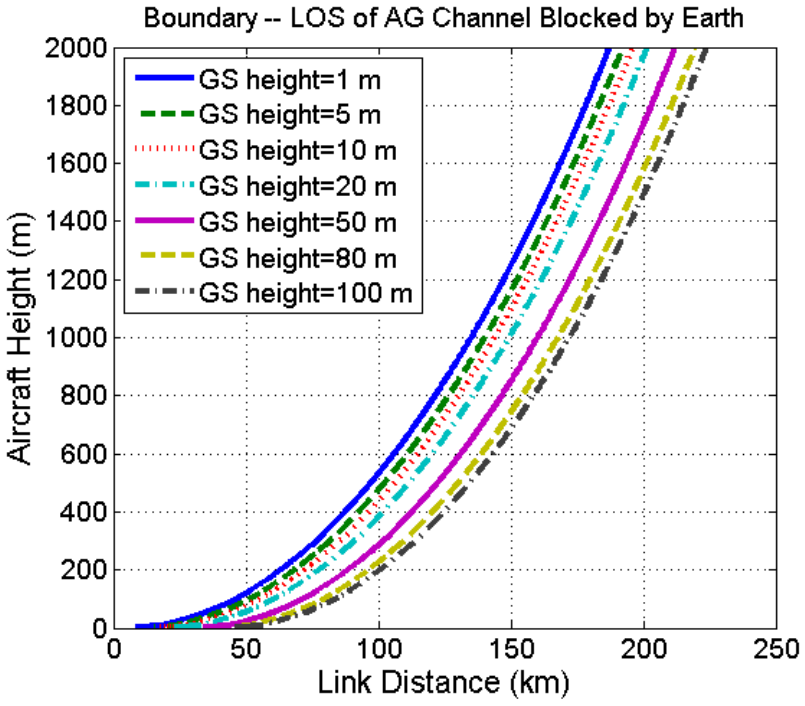

Figure 4.15. Boundary of beyond LOS.

4.5.4 BOUNDARY OF NEGATIVE ELEVATION ANGLE

Another interesting condition for the curved earth air-ground radio propagation path is that the elevation angle may be equal to or even smaller than zero. Since the AC antennas are likely mounted on the bottom of the fuselage, the LOS may be blocked by the aircraft itself when the elevation angle is negative. The boundary of negative elevation angle is shown in Figure 4.16. The elevation angle becomes negative when the link distance and aircraft height values are on the lower right of the curves. The elevation angle was always positive in our AG channel measurement campaign.

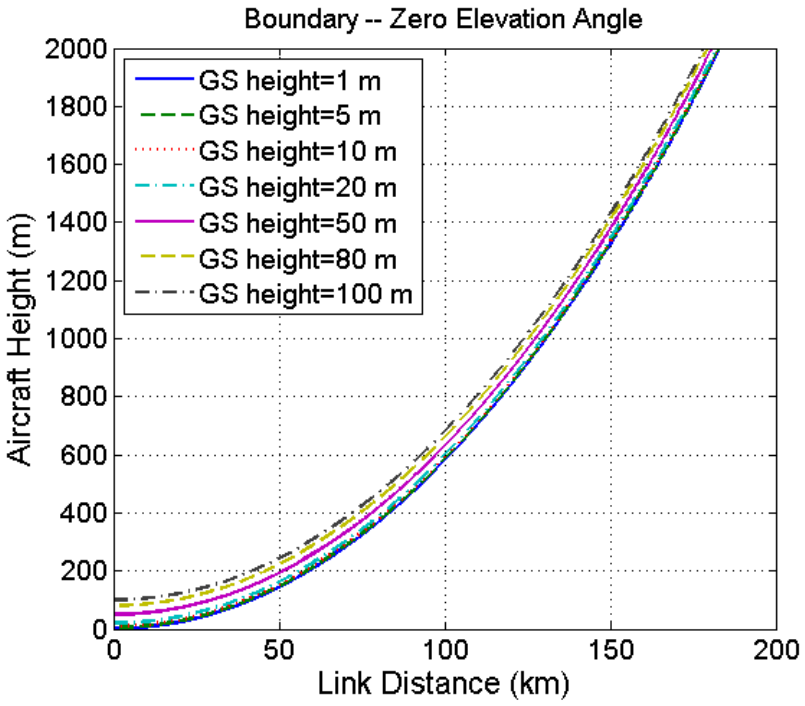

Figure 4.16. Boundary of zero elevation angle in curved earth model.

CHAPTER 5

NARROWBAND AG CHANNEL MODELS

Narrowband models estimate the attenuation (sometimes also phase) caused by the radio propagation channels. The term narrowband is in contrast to wideband, which quantifies delay dispersion or multipath in the channels. Specifically, a narrowband channel is one in which the transfer function can be considered to have constant gain and linear phase over bandwidth; in this sense narrowband is synonymous with distortionless. In the limit, this corresponds to the transfer function at a single frequency6.

Narrowband AG channel models can be viewed as being composed of large scale path loss, small scale fading and airframe shadowing, as illustrated in Figure 5.1. Note that order of processing in Figure 5.1 is immaterial; this results from the assumed independence of the physical effects causing each of the three phenomena. The large scale path loss is described by a log-distance path loss model [90] and/or the CE2R model. Small scale fading is characterized by Ricean *K* factors since the LOS component is almost always present in the AG channel. The LOS component can be obstructed by the aircraft itself during some specific maneuvers. The airframe shadowing depth and duration are quantitatively investigated. Methods to reproduce the airframe shadowing attenuation are proposed.

[6] For channels modeled statistically, using the classical formulation of Bello [110], for wide-sense stationary uncorrelated scattering (WSSUS) conditions, a narrowband channel is one in which the transfer function is considered only for frequency spans much less than the channel coherence bandwidth. This yields the constant-gain, linear-phase condition.

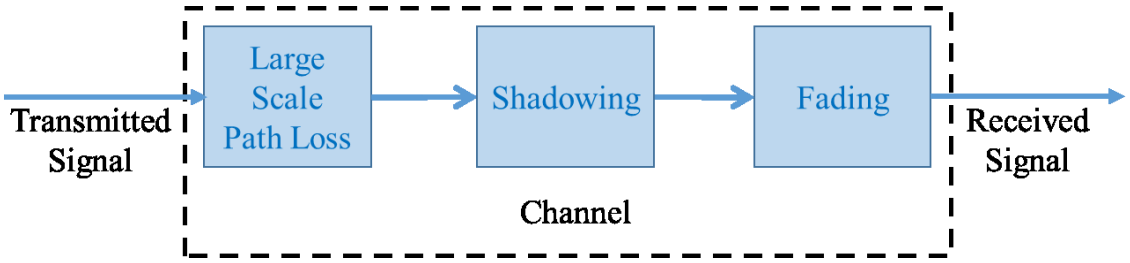

Figure 5.1. Narrowband AG Channel Models.

5.1 LARGE SCALE PATH LOSS MODEL

As described in Section 4.4, extra atmospheric attenuation can be caused by hydrometeors and atmospheric gases. Ducts can enhance the received signal strength. However, no precipitation occurred during our measurements and no ducting effects were observed from our data. Since these effects can be incorporated using standard techniques [101], we do not address them further. The empirical path loss *PL(R)* in dB, as a function of link range *R,* is computed from the received power $P_r(R)$ and parameters of the measurement setup,

$$PL(R) = P_t + G_t + G_r + G_{HPA} + G_{LNA} - L_C - P_r(R), \quad (5.1)$$

where P_t denotes transmitted power in dBm; G_t, G_r, G_{HPA}, G_{LNA} denote gains in dBi of the transmitter antenna, receiver antenna, high-power amplifier, and low noise amplifier, respectively; and L_C is the cable loss. Parameters P_t, G_{HPA}, G_{LNA} and L_C are provided in Table 3.2; the G_t and G_r values are shown in Figures 3.15, 3.16 and 3.19, which are dynamically based on instantaneous elevation angle and azimuth angle.

Example results for the over sea setting are shown in Figures 5.2 and 5.3, along with free space path loss, and CE2R and FE2R model results. Two-ray lobes can be clearly observed from the measured path loss, particularly for the L-band results.

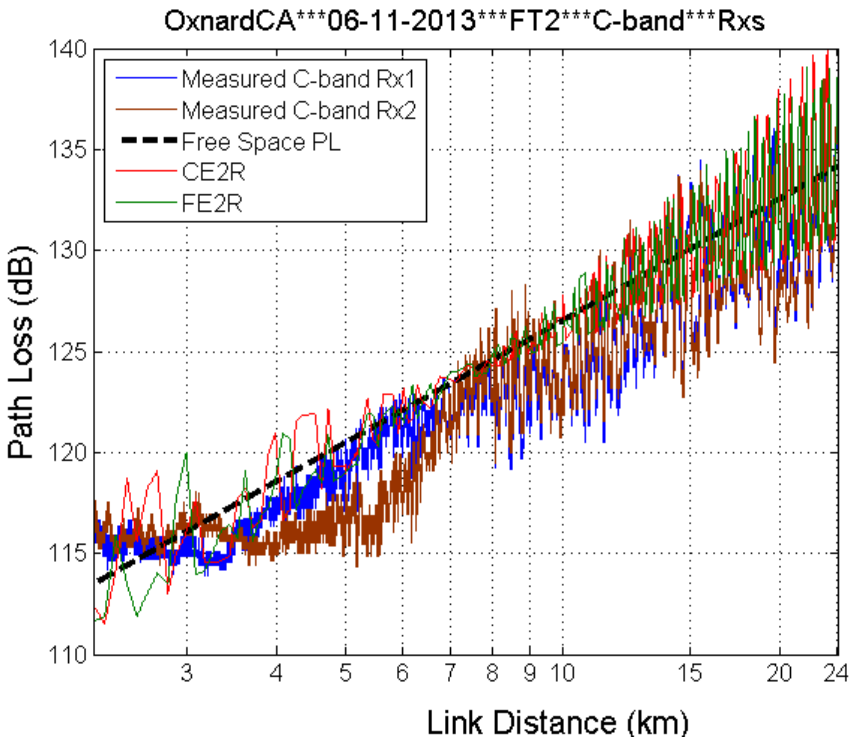

Figure 5.2. C-band path loss vs. link distance for over sea environment [58].

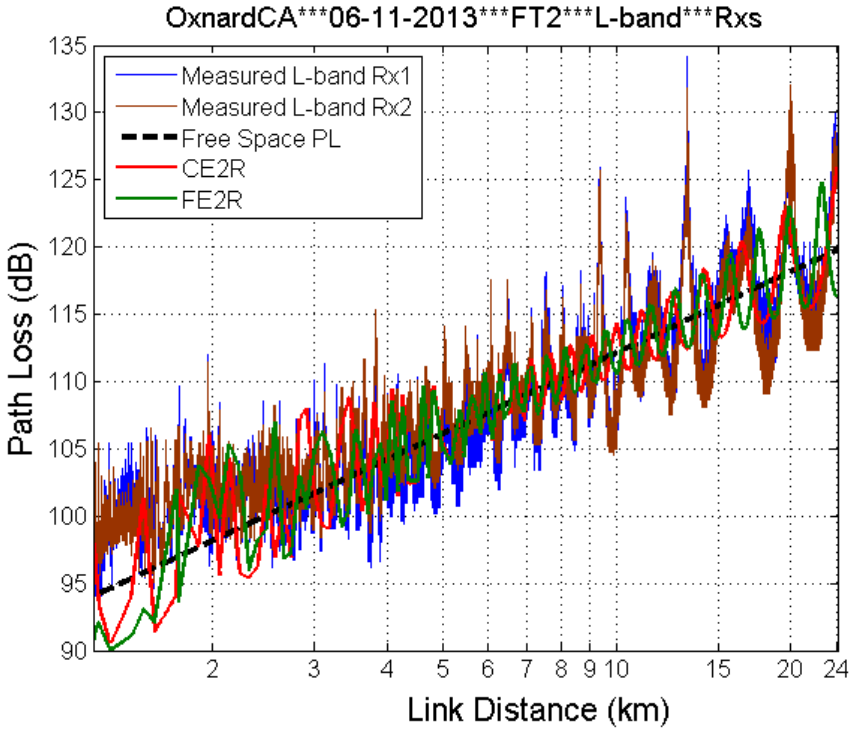

Figure 5.3. L-band path loss vs. link distance for over sea environment [58].

The log-distance path loss model form is one of the most widely used models to quantify large scale attenuation caused by the radio propagation channel [90]. The classic log-distance path loss model is as follows,

$$PL(R) = A_0 + 10n\log_{10}(R/R_{min}) + X \quad (5.2)$$

where A_0 denotes the path loss in dB at the minimum link distance R_{min}, n is the (dimensionless) path loss exponent, X denotes a zero-mean Gaussian random variable with standard deviation σ_X dB. In order to improve accuracy, we proposed a correction for our log-distance model, which adds another term to (5.2) to yield,

$$PL(R) = A_0 + 10n\log_{10}(R/R_{min}) + \zeta F + X, \qquad R_{min} \le R \le R_{max} \quad (5.3)$$

where variable ζ=-1 denotes that the aircraft is flying toward the GS, ζ=+1 denotes flying away from the GS, and F is the (positive) adjustment factor in dB for different flight directions. The path loss difference between attenuations recorded for flights in different directions is likely due to the aircraft pitch angle, which affects the aircraft antenna gain; moderate airframe shadowing may also contribute. Multiple corrections for the two-ray models are also applied, specifically,

$$PL(R) = CE2R(R) + B + \zeta F - 20\log_{10}[a(R)], \qquad \psi_{min} < \psi < \frac{\pi}{2} \quad (5.4)$$

where *CE2R(R)* denotes the path loss estimated by the CE2R model described in Section 4.2; B denotes the overall bias between the CE2R model and the measured path loss; *a(R)* is a memoryless (unfiltered) Ricean fading random variable, whose parameters are estimated in Section 5.2; the minimum grazing angle ψ_{min}(mrad) is $(2100/f_{MHz})^{1/3}$ as described in Section 4.5.1. Note that the B's and F's do differ for different GS environments as well as for different elevation angles.

The measured path loss, and log-distance and CE2R path loss model results for the over sea environment are shown in Figures 5.4 and 5.5, which include measured path loss for two flight tracks (one flew straight toward the GS and the other flew away from the GS) with two Rxs in each FT. The free space path loss model results are also plotted in Figures 5.4 and 5.5. The path loss model parameters are listed in Table 5.1. The standard deviations are 2.6 dB and 4.2 dB, for C-band and L-band, respectively, which indicates that the log-distance model fits the measured data very well. Typical standard deviations for terrestrial cellular log-distance path loss models range from 3-12 dB [90], so our AG channel path loss model accuracy is quite good. The larger standard deviation in L-band than C-band is because L-band yields larger 2-ray attenuation peaks—this is because the water surface is more reflective at L-band, and the surface reflection cancellation of the LOS component is stronger. The path loss models for the over freshwater environment are shown in Figures 5.6 and 5.7. The path loss difference at short distance between different flight directions is due to aircraft antenna effects.

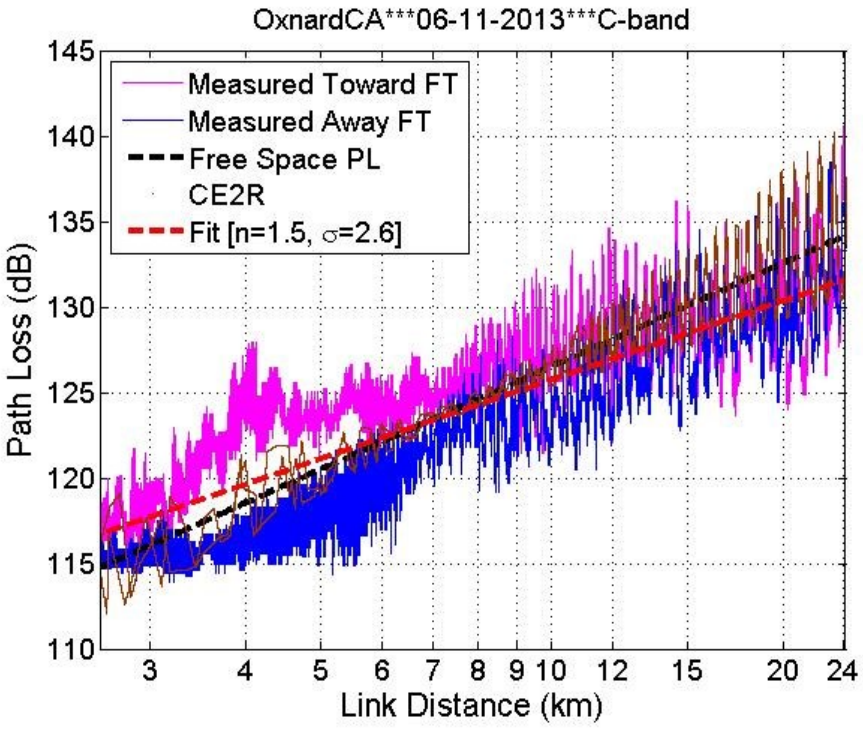

Figure 5.4. C-band path loss models for over sea environment taken in Oxnard, CA on 6/11/2013.

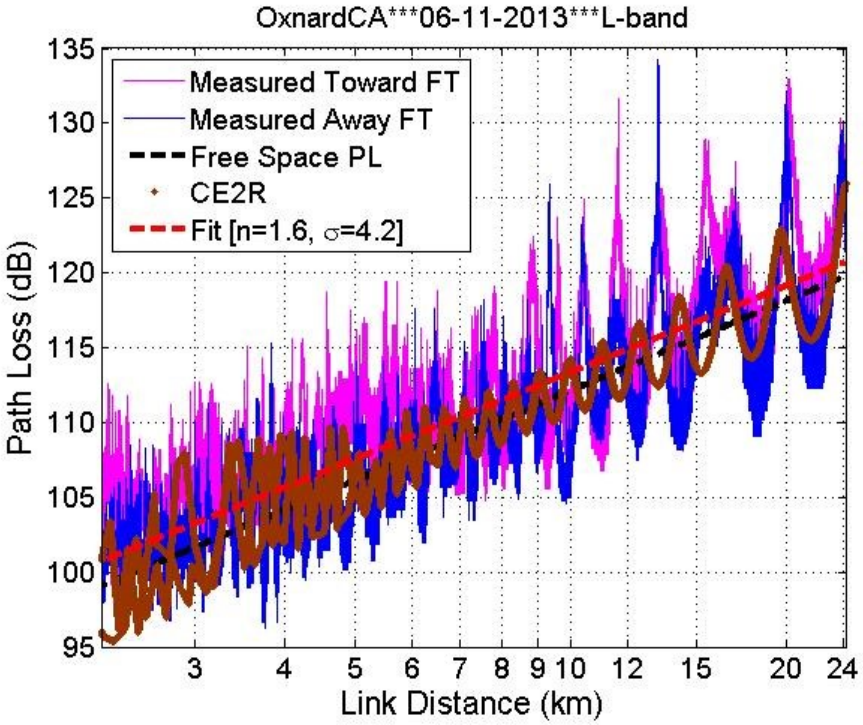

Figure 5.5. L-band path loss models for over sea environment taken in Oxnard, CA on 6/11/2013.

Table 5.1. Parameters of log-distance and CE2R path loss models.

Setting		Sea, Oxnard 6/11/2013		Fresh, Cleveland 10/22/2013		Aggregate suburban, Palmdale, Latrobe and Cleveland		Hilly, Palmdale 6/12/2013	
Band		**C-band**	**L-band**	**C-band**	**L-band**	**C-band**	**L-band**	**C-band**	**L-band**
Log-distance	A_0 **(dB)**	116.7	100.7	116.3	104.4	116.7	98.2	123.9	106.5
	n	1.5	1.9	1.9	1.9	1.5	1.7	1.0	1.3
	σ_X **(dB)**	2.6	4.2	3.1	3.8	2.9	3.1	2.2	3.9
	X_{max}**(dB)**	9.0	18.5	9.1	13.3	10.4	16.5	6.8	17.8
	F **(dB)**	0.8	1.0	1.8	1.4	0.0	1.1	0.9	0.7
CE2R	B **(dB)**	-1.1	1.1	-0.3	1.6	-0.5	1.8	-1.0	1.8
Distance range	R_{min} **(km)**	2.6	2.2	3.0	3.0	2.6	1.3	5.4	2.8
	R_{max} **(km)**	24.1	24.1	28.1	28.1	16.9	16.9	21.0	21.0

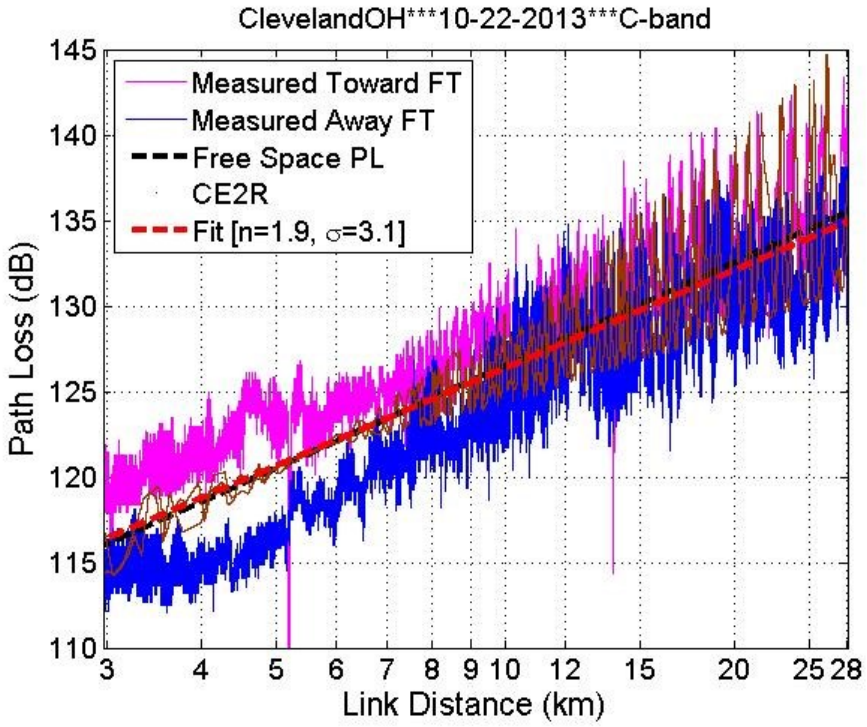

Figure 5.6. C-band path loss models for over freshwater environment taken in Cleveland, OH on 10/22/2013.

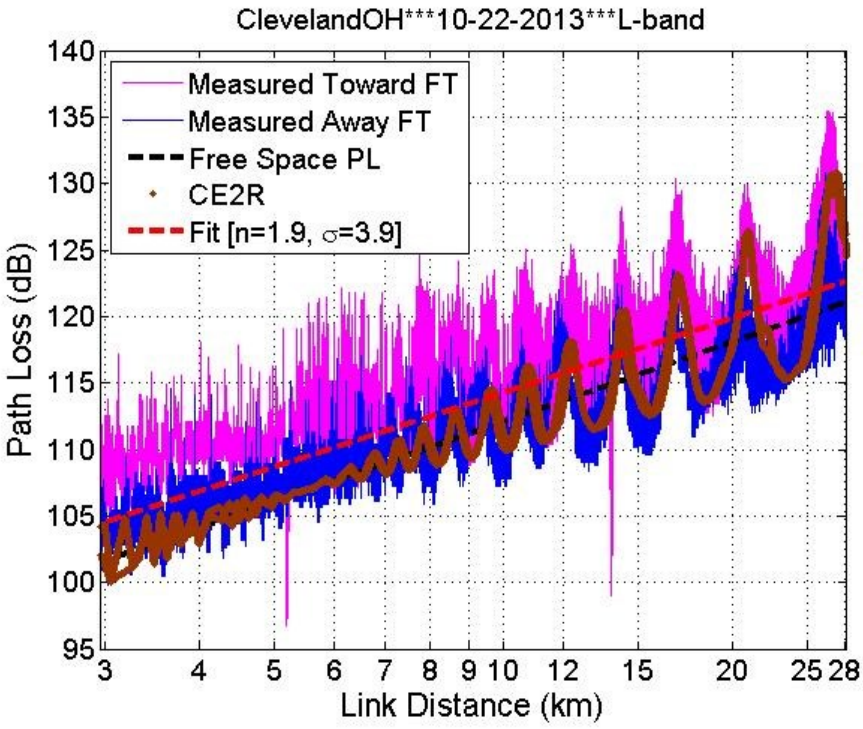

Figure 5.7. L-band path loss models for over freshwater environment taken in Cleveland, OH on 10/22/2013.

The CE2R model also fits some suburban and hilly terrain settings. Whether or not the CE2R (or FE2R) model can be applied does not depend on the terrain condition (flat and smooth or not) of the entire FT, but depends on the local terrain condition surrounding the "reflection point" at the distance we term the "Q radius" from the GS. As illustrated in Figure 5.8[7], we assume the earth surface reflection point is Q m away from the GS. Based on a "similar triangles" relation, Q is given by

$$\frac{Q}{d-Q} = \frac{h_G}{h_A}, \tag{5.5}$$

hence

$$Q = \frac{dh_G}{h_A+h_G}, \tag{5.6}$$

[7] Although Figure 5.8 shows a flat earth surface case, the relation in eq. (5.5) is still true for the curved earth case since the grazing angles ψ on the left and right sides of the reflection point are the same. Figure 5.8 is illustrated as flat earth for simplicity.

where d denotes the horizontal distance in meters between the GS and the aircraft, and h_G and h_A denote heights of the GS and the aircraft, respectively. Although the aircraft flies over hills or buildings, the local terrain surrounding the reflection point Q m from the GS can still be flat[8], such that CE2R (or FE2R) is applicable.

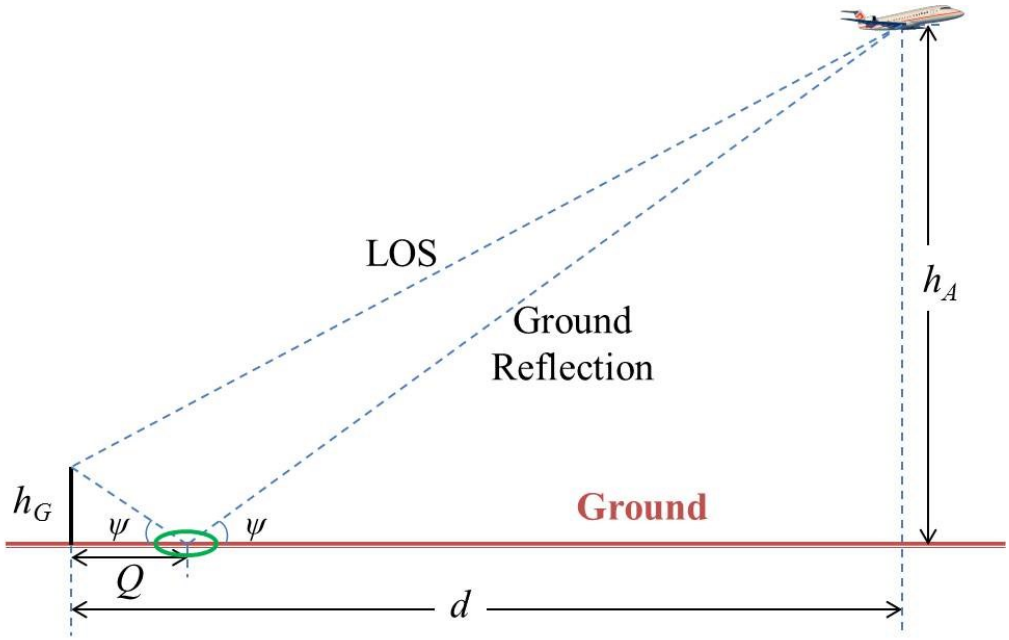

Figure 5.8. Diagram of earth surface reflection point.

Since the GS was located at an airport or on flat ground for the hilly and suburban data sets taken in Palmdale and Latrobe, and the ground near the GS is very flat without large obstacles (neither natural nor man-made), the ground reflection is strong and the CE2R model is appropriate. Some example results are shown in Figures 5.9 to 5.12. The path loss models parameters for hilly and suburban environments are listed in Table 5.1. We have three sets of data for suburban environments. The aggregate results are reported in Table 5.1.

[8] Since the received signal is affected by energy inside multiple Fresnel zones, the signals reflected over an area of the surface (the "reflection area" indicated by the small green region in Figure 5.8) can reach the receivers. Therefore, the actual reflection area (green region) within which the ground is flat and relatively smooth must be considered for a strong specular surface reflection, and CE2R or FE2R validity. For most geometries, the dimension of the reflection area (green region) is small relative to distance Q.

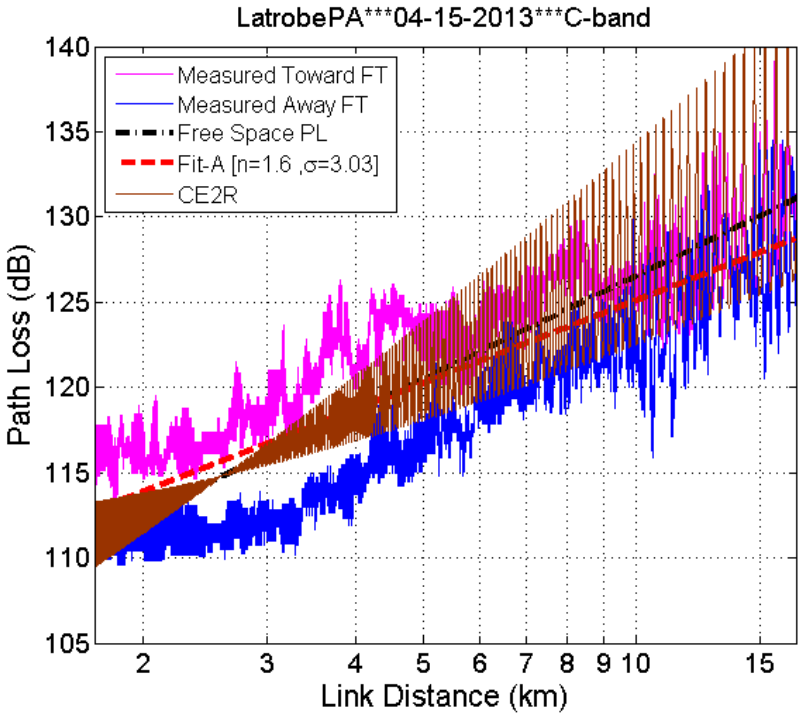

Figure 5.9. C-band path loss models for suburban environment taken in Latrobe, PA on 4/15/2013.

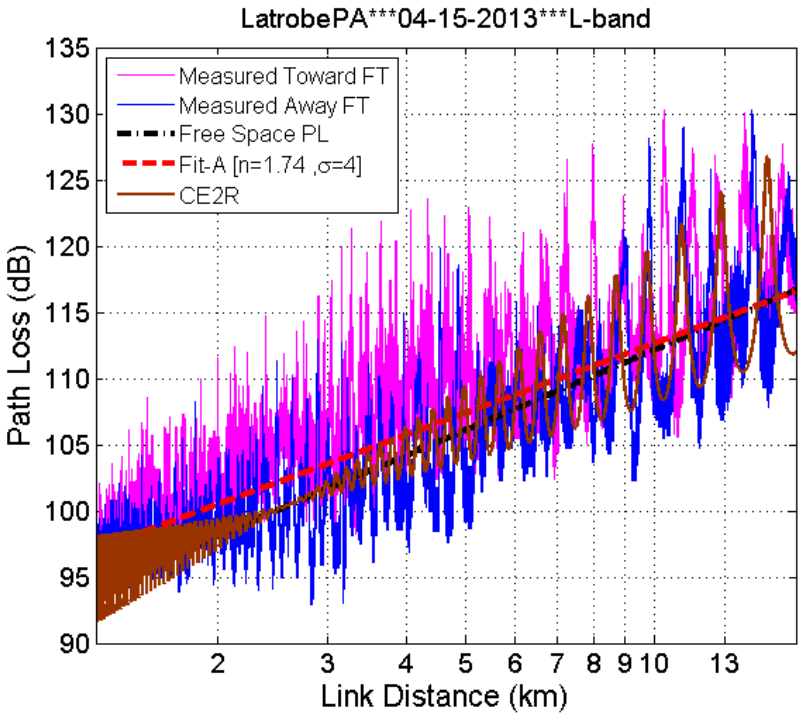

Figure 5.10. L-band path loss models for suburban environment taken in Latrobe, PA on 4/15/2013.

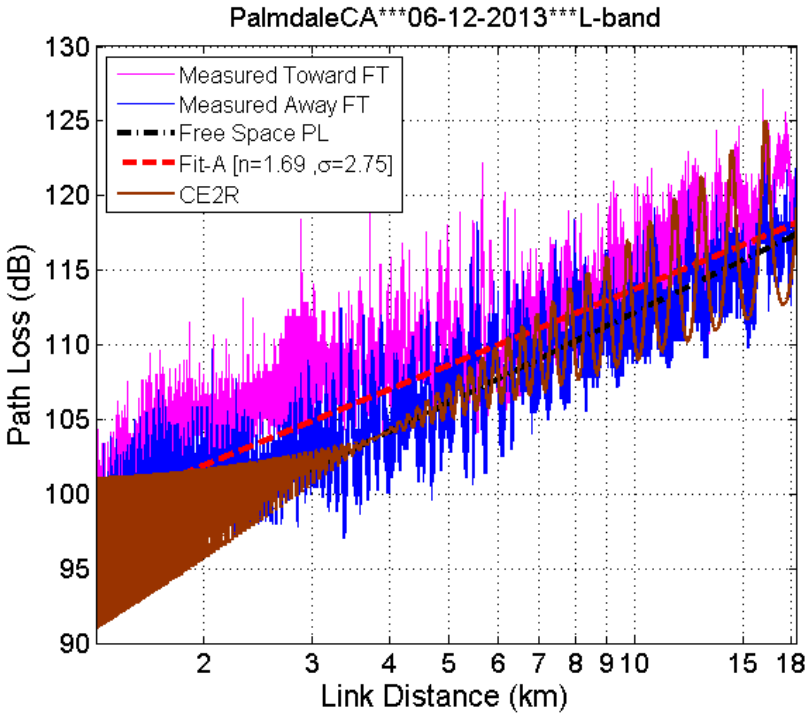

Figure 5.11. L-band path loss models for suburban environment taken in Palmdale, CA on 6/12/2013.

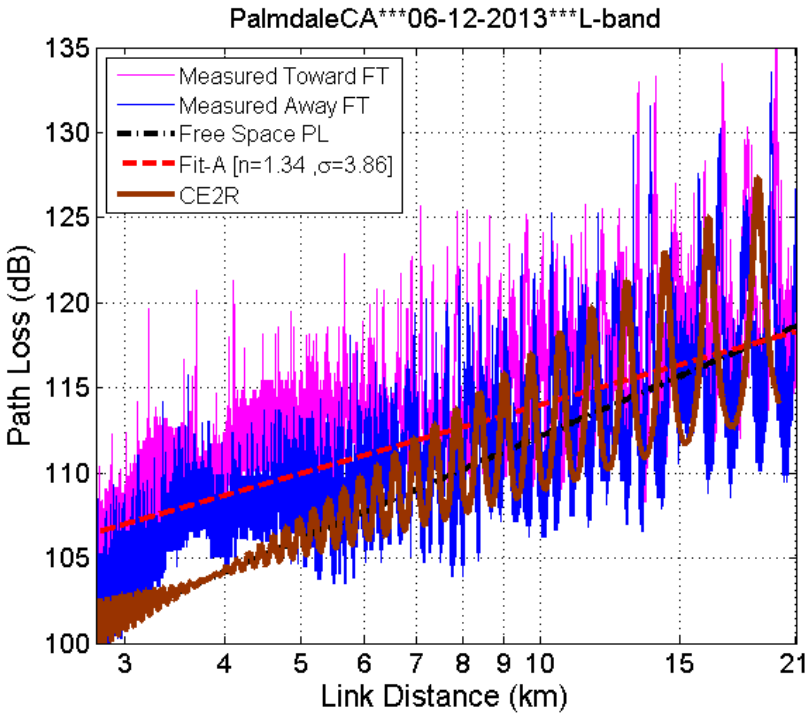

Figure 5.12. L-band path loss models for hilly environment taken in Palmdale, CA on 6/12/2013.

For the other two major environment types, mountainous and near-urban, the CE2R model will not fit well. In the near-urban case, a harbor with many boats and many large buildings were near the GS right beneath the flight track in the near-urban environment of Cleveland, OH. Large mountain ridges were near the GS for the mountainous data taken in Telluride, CO. These large obstacles tend to scatter the ground reflection, so that no prominent two-ray lobes were observed in these environments. The path loss is modeled by the log-distance model only. The parameters are provided in Table 5.2. Example measured path loss and log-distance model results are shown in Figures 5.13 to 5.16. Again, the standard deviations are smaller than 3.5 dB, indicating that the log-distance models agree with the measured data very well.

Table 5.2. Parameters of log-distance path loss models.

Setting		**Near-urban, Cleveland 10/22/2013**		**Mountainous, Telluride 9/12/2013**	
Band		**C-band**	**L-band**	**C-band**	**L-band**
Log-distance	A_0 **(dB)**	110.4	99.4	119.7	102.7
	n	2.0	1.7	1.7	1.6
	σ_X **(dB)**	3.2	2.6	2.8	3.5
	X_{max}**(dB)**	14.1	17.8	7.6	13.0
	F **(dB)**	2.3	1.8	4.5	4.8
Distance range	R_{min} **(km)**	1.7	1.6	3.4	1.8
	R_{max} **(km)**	19.0	19.0	19.4	19.4

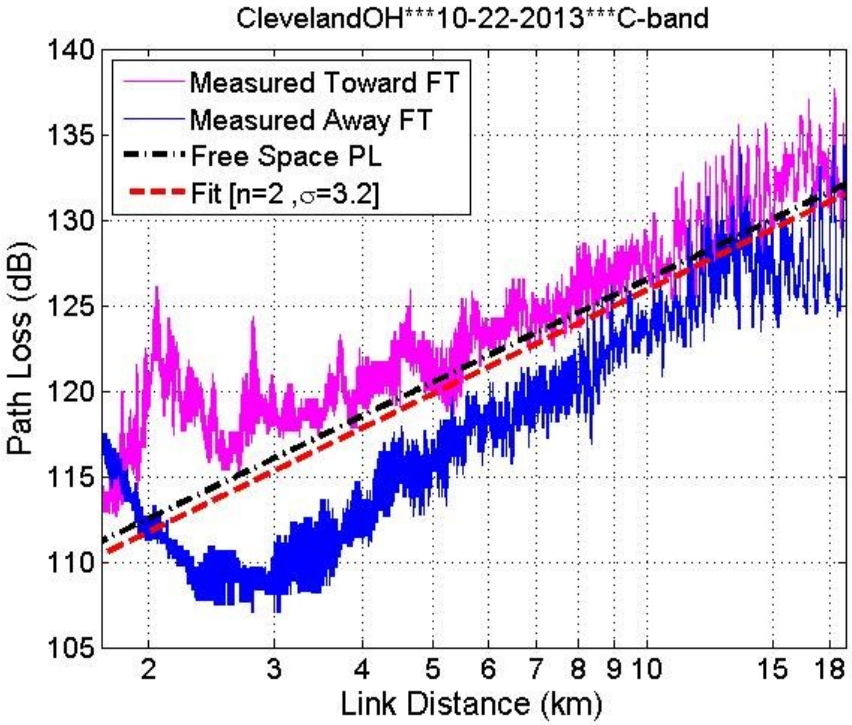

Figure 5.13. C-band path loss models for near-urban environment taken in Cleveland, OH on 10/22/2013.

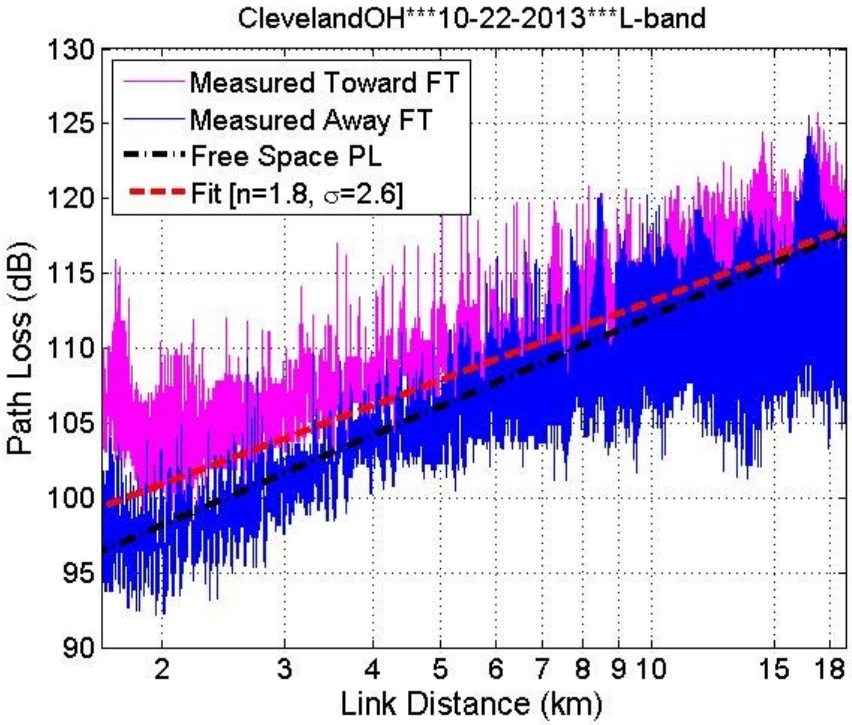

Figure 5.14. L-band path loss models for near-urban environment taken in Cleveland, OH on 10/22/2013.

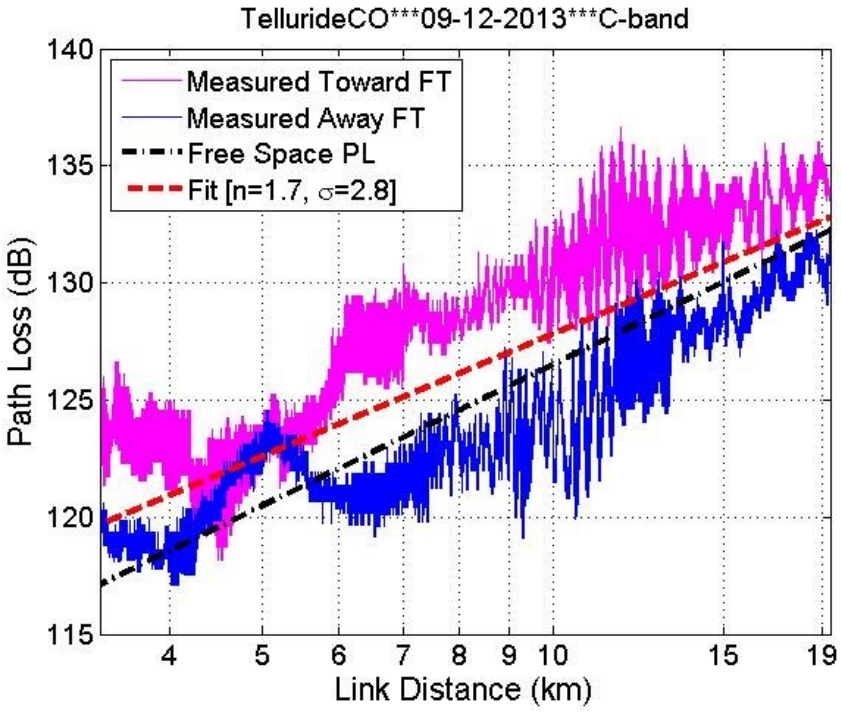

Figure 5.15. C-band path loss models for mountainous environment taken in Telluride, CO on 9/12/2013.

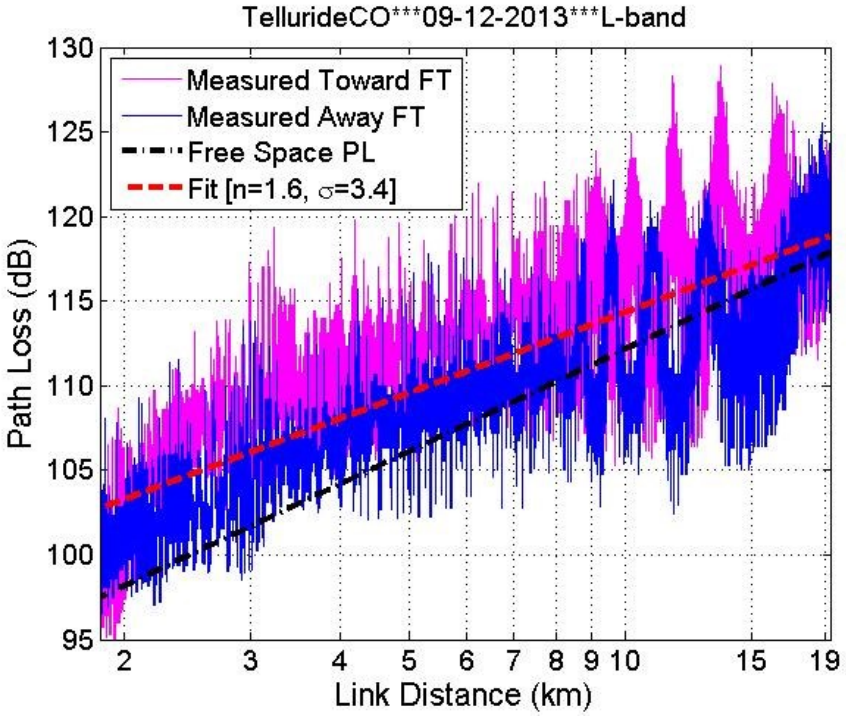

Figure 5.16. L-band path loss models for mountainous environment taken in Telluride, CO on 9/12/2013.

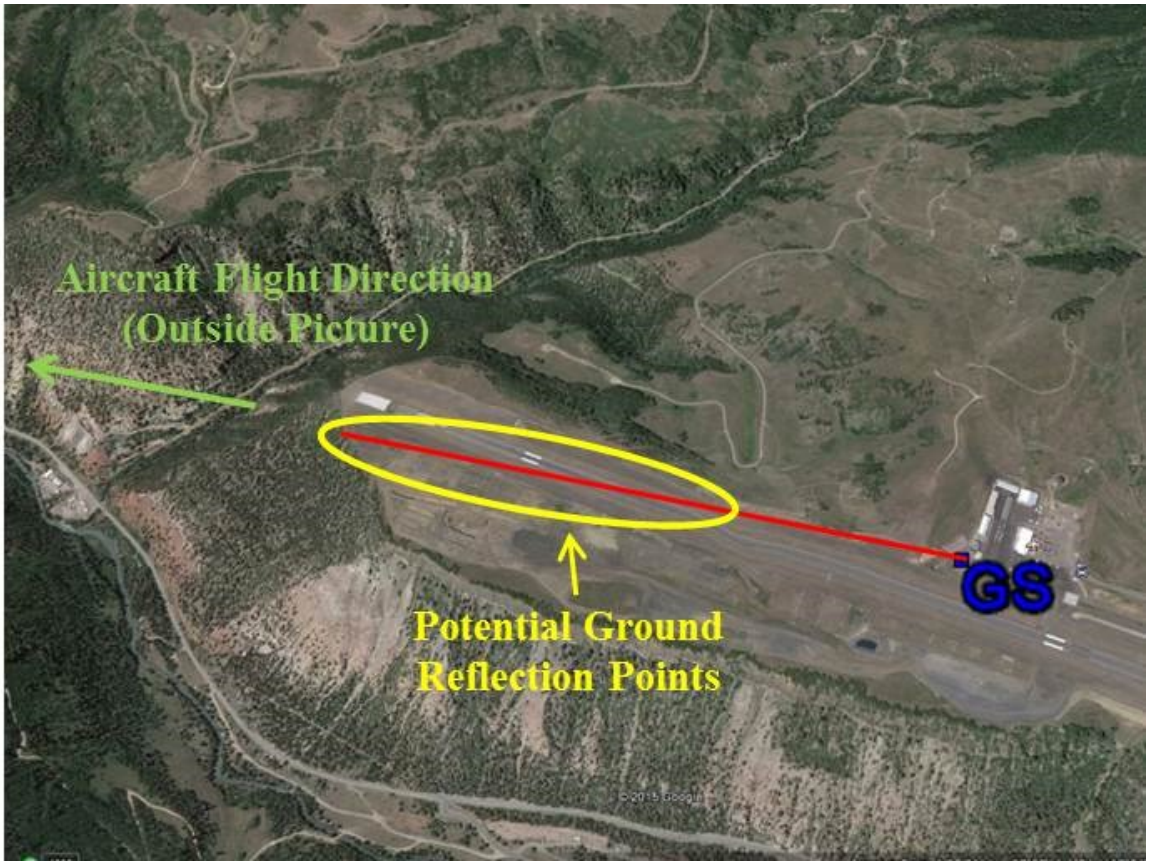

Figure 5.17. Potential ground reflection points in Telluride regional airport.

As shown in Figure 5.16, the L-band path loss results taken in Telluride, CO appear to contain 2-ray lobes beyond approximately 8 km. The potential ground reflection points in the Telluride regional airport where the GS was located are illustrated in Figure 5.17. A segment of flat runway provides the flat and smooth area for the earth surface reflection. The 2-ray lobes were only present in a segment of the flight track. They vanished beyond approximately 25 km because the reflection points moved to the left outside the yellow circle in Figure 5.17 (no longer on the flat runway, but in the rough valley), where the earth surface reflection is scattered, and the geometry of 2-ray model is totally changed. The geometry of the flight route where the 2-ray lobes appear correspond to the reflection area defined approximately by the yellow region indicated in

Figure 5.17. Therefore, although CE2R is not expected to fit the path loss in mountainous terrain, it can still work for some small segments.

5.2 SMALL SCALE FADING

The small scale fading is the received signal amplitude fast variation due to multipath, which is usually treated statistically. The small scale fading can be studied by use multiple statistics, such as the received envelope distribution, level crossing rate (LCR) and average fade duration (AFD) [6]. The received envelope distribution is the most typical method used for characterization. Along with temporal characteristics, this completely specifies the small-scale fading. The received signal amplitude follows a Ricean distribution in the LOS condition, and it follows a Rayleigh distribution in the NLOS condition. The Ricean degenerates to the Rayleigh when the Ricean K factor is very small. The fading can also be modeled by Nakagami and Weibull distributions. Each of these distributions has a parameter (for all distributions, we assume unity average energy, as is common practice). The Nakagami m factor larger than 1 can be viewed as a Ricean condition. The Weibull β factor larger than 2 is similar. A Weibull β value smaller than 2 or a Nakagami m<1 indicates that the fading is worse than Rayleigh. Since the LOS component is almost always present in the AG channel, the Ricean distribution is employed in our investigation.

The probability density function of a Ricean random variable is given by [6]

$$p(x) = \frac{x}{\sigma^2}\exp(-\frac{x^2+s^2}{2\sigma^2})I_0(\frac{xs}{\sigma^2}), \tag{5.7}$$

where $I_0(\cdot)$ is the zeroth order modified Bessel function of the first kind, x denotes the amplitude of the received signal, s^2 is the power of the LOS component and $2\sigma^2$ denotes the power of the diffuse components. The definition of K factor in decibels is

$$K = 10log_{10}(\frac{s^2}{2\sigma^2}). \quad (5.8)$$

Large K values imply the LOS component is much stronger than the diffuse components (from scatterers). A K smaller than 0 dB indicates the energy in the LOS component is comparable to or smaller than that from the scatterers.

5.2.1 RICEAN *K*-FACTOR ESTIMATION ALGORITHM

In order to estimate the small scale fading, the effects of the large scale path loss and/or shadowing should be removed in advance of processing. In our case, the received signal is normalized to the local average power in dB

$$P_{r,mov}(R) = \sum_{i-W/2}^{i+W/2} \frac{P_r(R_i)}{W}, \quad (5.9)$$

where W is a moving average window length, which is the number of PDPs within our SD of 15 m. With PDP update rate of approximately 3 kHz and flight velocity of 60-90 m/s, W is approximately 50-75 PDPs. Then the fading amplitude in linear scale is given by

$$F(R) = 10^{\frac{[P_r(R) - P_{r,mov}(R)]}{20}}. \quad (5.10)$$

Then we make the fading amplitude unit-energy, as is standard practice, which yields

$$F_N(R) = \sqrt{F^2(R)/\overline{F^2(R)}}, \quad (5.11)$$

where $\overline{F^2(R)}$ is the mean of $F^2(R)$ over length W. $F_N(R)$ is a real positive vector with length W that has unit-energy[9].

[9] The $a(R)$ in eq. (5.4) is also a real positive vector with unit energy. Vectors $a(R)$ and $F_N(R)$ are similar but have two differences: 1) $F_N(R)$ is generated by measured data, but $a(R)$ is generated by a theoretical method for computer analysis or simulations; 2) the length of these two vectors may not be equal. The length of $a(R)$ is the number of PDPs for the entire flight track if a single K factor value is employed, and it can be as small as W if a distance dependent K factor vector is used.

The Ricean K factor was estimated for the measured $F_N(R)$ data via two methods: 1) the maximum likelihood (ML) fit of the measured data $F_N(R)$ to a Ricean pdf via a Matlab® built-in function (the fit probability distribution object to data, "fitdist" in "Statistics Toolbox"); and 2) a moment based (MB) method. Based on the fourth order moment based method [111], the K factor in decibels is computed by

$$K_{MB} = 10log_{10}(\frac{-2\mu_2^2+\mu_4-\mu_2\sqrt{2\mu_2^2-\mu_4}}{\mu_2^2-\mu_4}), \tag{5.12}$$

where μ_2 is the second order moment of $F_N(R)$, and μ_4 is the fourth order moment of $F_N(R)$,

$$\mu_2 = \frac{1}{W}\sum_{i-W/2}^{i+W/2}[F_N(R_i)]^2, \tag{5.13}$$

$$\mu_4 = \frac{1}{W}\sum_{i-W/2}^{i+W/2}[F_N(R_i)]^4. \tag{5.14}$$

5.2.2 EXAMPLE *K*-FACTOR RESULTS

An example set of AG channel K factors for the over sea environment FT1 are shown in Figures 5.18 to 5.21. These results are for both bands and all receivers. The results based on the ML and MB methods essentially agree with each other. A linear fit for K factor in decibels versus link distance R in km is given by [112]

$$K(R) = K_0 + n_K(R - R_{min}) + Y, \tag{5.15}$$

where K_0 is a constant at the minimum link distance R_{min}, n_K denotes the slope, and Y denotes a zero mean Gaussian random variable with standard deviation σ_Y. The slope n_K is sometimes positive and sometimes negative in different FTs and environments. The magnitude of n_K is on the order of one tenth or less. Thus $K(R) \cong K_0 + Y$ provides a very good approximation [58]. For the simplest approximation one can employ a constant K factor $K(R) \cong K_0$. The L-band K factor results are a strong function of the 2-ray channel,

and to a lesser degree, a function of the intermittent multipath. Example *K* factors versus link distance for small distance segments--1 km range and 100 m range--for both bands, are shown in Figures 5.22 to 5.25. The statistics and linear fit parameters are provided in Table 5.3.

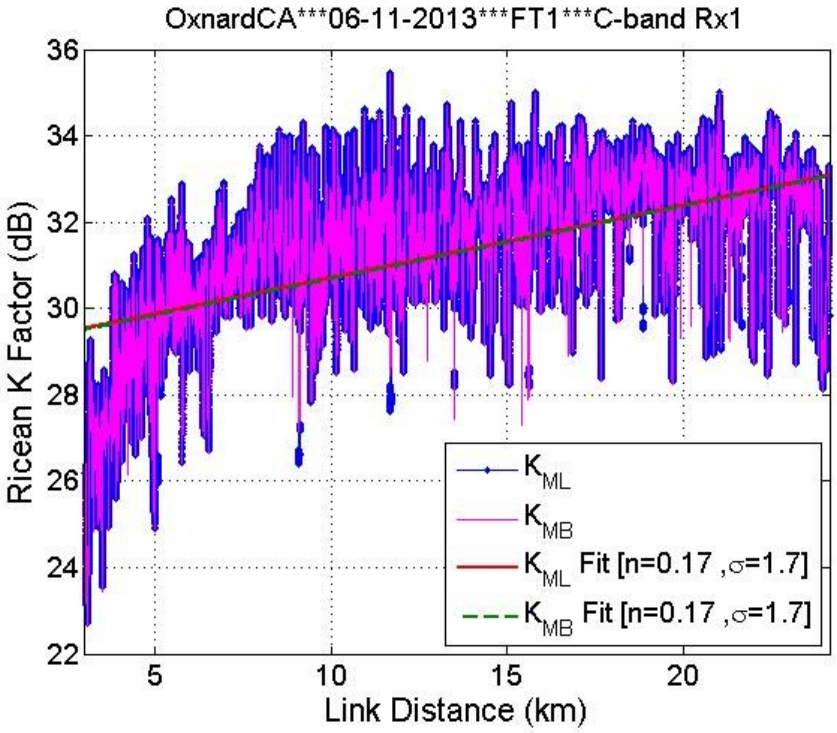

Figure 5.18. Ricean *K* factor vs. link distance for over sea environment FT1, C-band Rx1 [64].

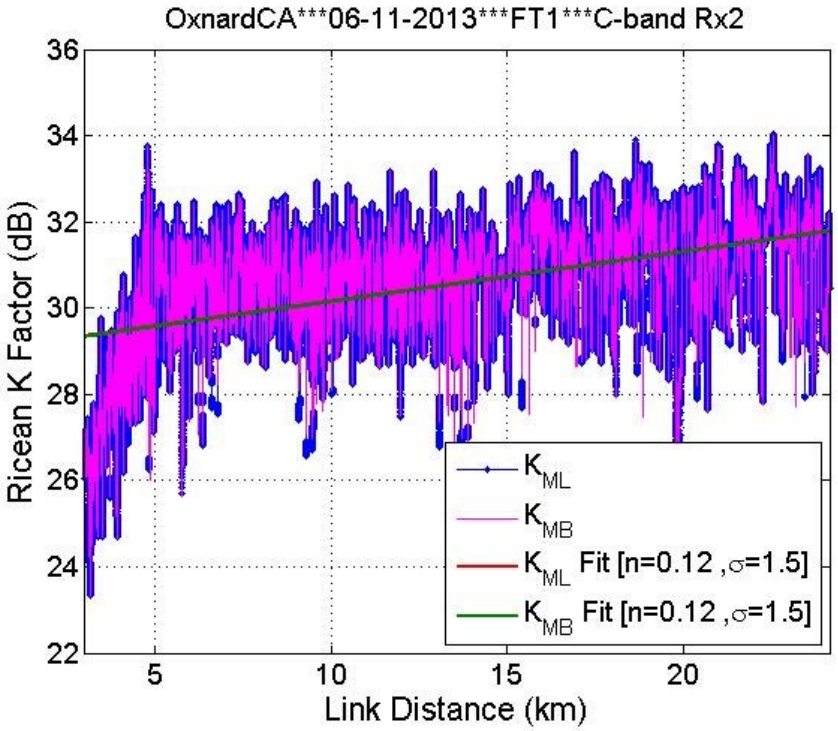

Figure 5.19. Ricean *K* factor vs. link distance for over sea environment FT1, C-band Rx2.

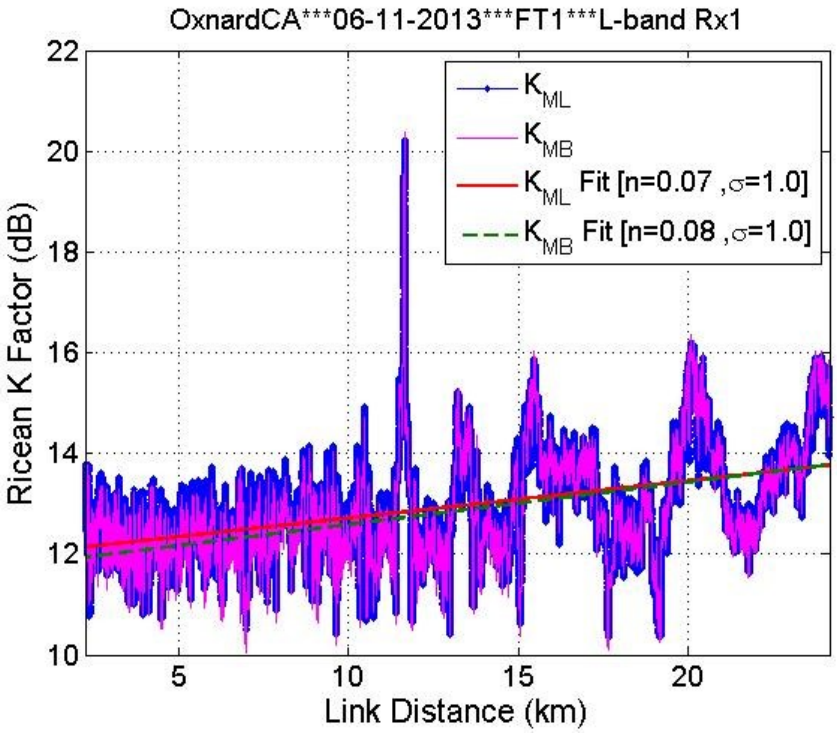

Figure 5.20. Ricean *K* factor vs. link distance for over sea environment FT1, L-band Rx1 [64].

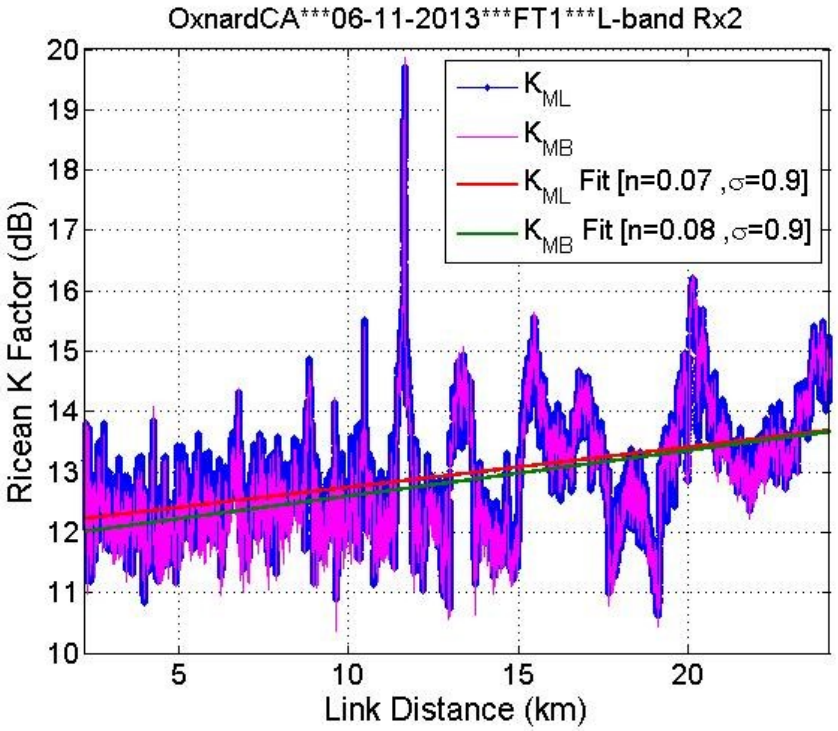

Figure 5.21. Ricean *K* factor vs. link distance for over sea environment FT1, L-band Rx2.

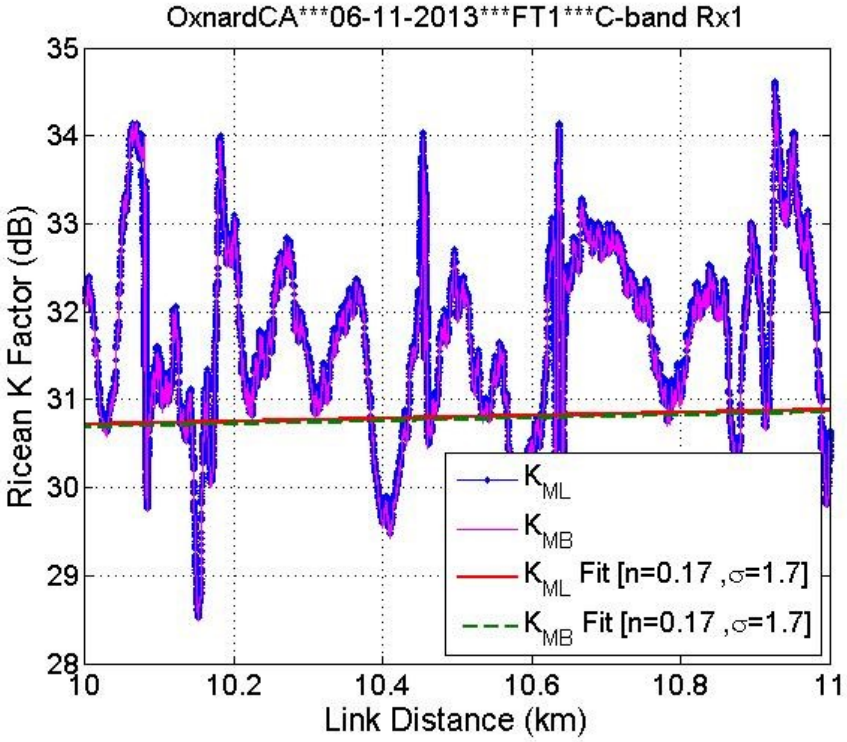

Figure 5.22. Ricean *K* factor vs. link distance for over sea environment FT1, C-band Rx1; segment of Figure 5.18 from 10 to 11 km.

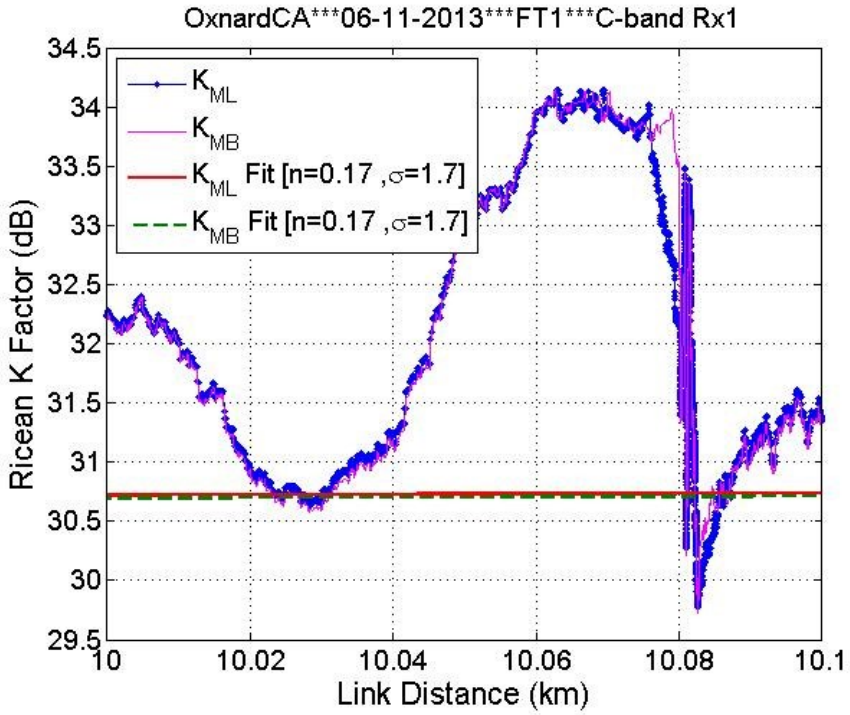

Figure 5.23. Ricean *K* factor vs. link distance for over sea environment FT1, C-band Rx1; segment of Figure 5.18 from 10 to 10.1 km.

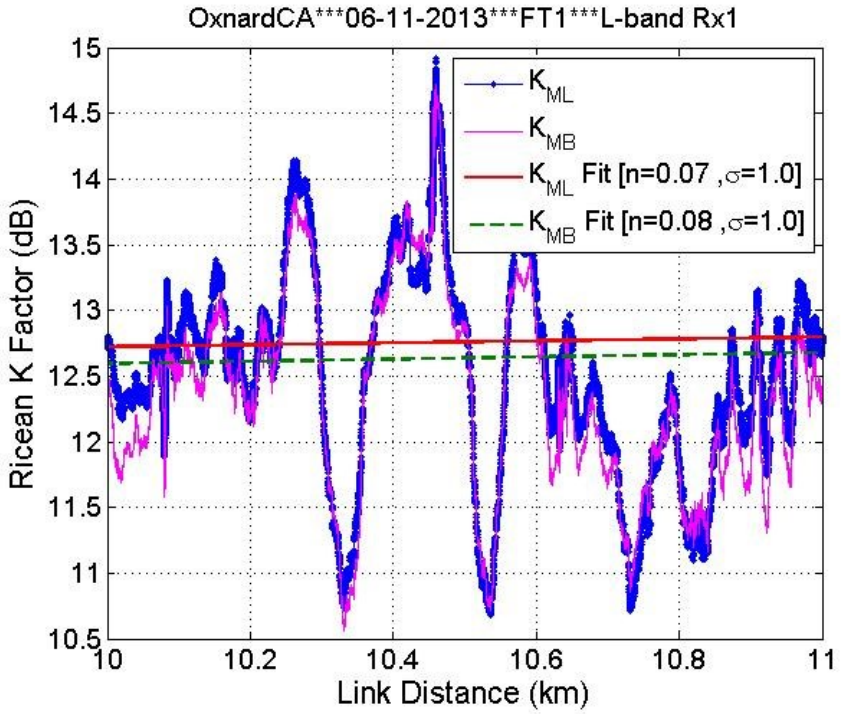

Figure 5.24. Ricean *K* factor vs. link distance for over sea environment FT1, L-band Rx1; segment of Figure 5.20 from 10 to 11 km.

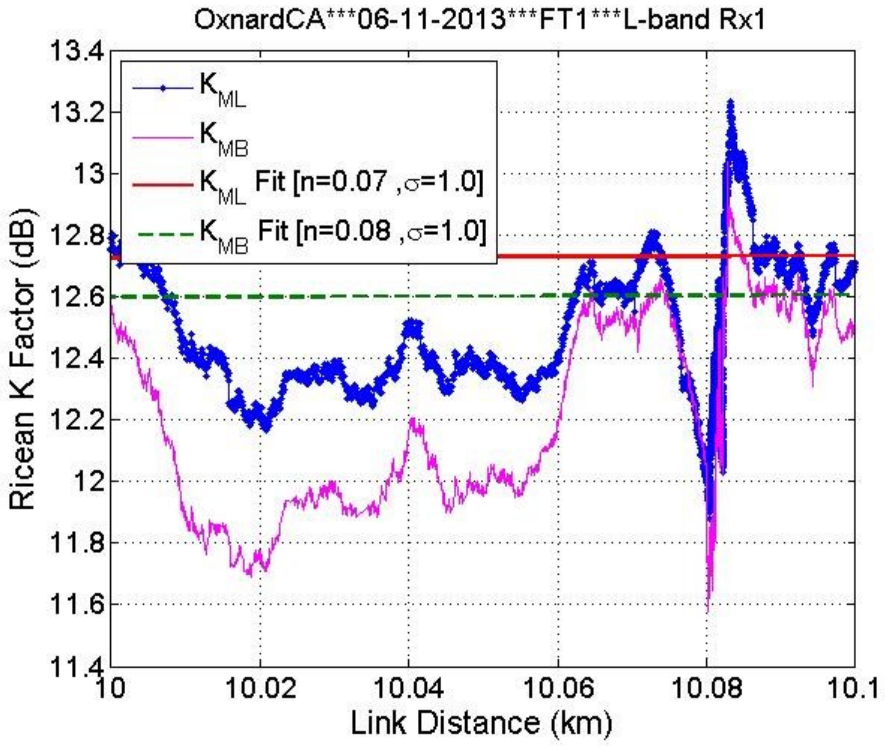

Figure 5.25. Ricean *K* factor vs. link distance for over sea environment FT1, L-band Rx1; segment of Figure 5.20 from 10 to 10.1 km.

Table 5.3. Statistics of Ricean *K* factor for over sea environment FT1.

Oxnard, CA 11 June 2013 Over Sea, FT1 flew straight toward the GS									
Ricean *K* factor		**C-band**				**L-band**			
		Rx1		**Rx2**		**Rx1**		**Rx2**	
Methods		K_{ML}	K_{MB}	K_{ML}	K_{MB}	K_{ML}	K_{MB}	K_{ML}	K_{MB}
Linear fit of *K* factor	K_0**(dB)**	29.1	29.0	29.0	29.0	12.0	11.8	12.1	11.9
	n_K	0.17	0.17	0.12	0.12	0.07	0.08	0.07	0.08
	σ_Y **(dB)**	1.7	1.7	1.5	1.5	1.0	1.0	0.9	0.9
	R_{max}**(km)**	3.0	3.0	3.0	3.0	2.2	2.2	2.2	2.2
	R_{Min}**(km)**	24.1	24.1	24.1	24.1	24.1	24.1	24.1	24.1
Statistics of *K* factor (dB)	**Max**	35.5	35.4	34.0	34.0	20.2	20.4	19.7	19.9
	Min	22.7	22.7	23.3	23.3	10.3	10.0	10.6	10.4
	Median	31.3	31.3	30.6	30.6	12.9	12.8	12.9	12.8
	μ	31.7	31.6	30.9	30.9	12.7	12.6	12.8	12.6
	σ	2.0	2.0	1.7	1.6	1.1	1.1	1.0	1.0

The *K* factors of all the straight FTs for the over sea environment were combined together, and the aggregate statistics and *K* factor fit results are provided in Table 5.4.

The aggregate *K* factors for over freshwater, near-urban, suburban, hilly and mountainous environments are listed in Tables 5.5 to 5.9, respectively. The *K* factors do not change much over different environments. This is due to the predominance of the LOS component in our AG channels in all GS local environments; the diffuse components are sparse and relatively weak. The Ricean *K* factor is on average 28.7 dB in C-band and 13.1 dB in L-band for all the GS local environments.

Table 5.4. Statistics of aggregate Ricean *K* factor for over sea environment [58].

Oxnard, CA 11 June 2013 Over Sea, all straight FTs					
Ricean *K* factor		**C-band**		**L-band**	
Methods		K_{ML}	K_{MB}	K_{ML}	K_{MB}
Linear fit of *K* factor	$\boldsymbol{K_0}$**(dB)**	29.9	28.5	11.7	11.5
	$\boldsymbol{n_K}$	0.08	0.12	0.08	0.08
	$\boldsymbol{\sigma_Y}$ **(dB)**	1.7	1.8	1.1	1.1
	$\boldsymbol{R_{max}}$**(km)**	2.6	2.6	2.2	2.2
	$\boldsymbol{R_{Min}}$**(km)**	24.1	24.1	24.1	24.1
Statistics of *K* factor (dB)	**Max**	35.6	35.6	20.7	22.1
	Min	11.1	11.8	9.4	7.8
	Median	31.0	30.3	12.7	12.7
	$\boldsymbol{\mu}$	31.3	30.5	12.5	12.5
	$\boldsymbol{\sigma}$	1.8	1.9	1.2	1.3

Table 5.5. Statistics of aggregate Ricean *K* factor for over freshwater environment.

Cleveland, OH 22 October 2013 Over Lake Erie, all straight FTs (FT2&3)					
Ricean *K* factor		**C-band**		**L-band**	
Methods		K_{ML}	K_{MB}	K_{ML}	K_{MB}
Linear fit of *K* factor	$\boldsymbol{K_0}$**(dB)**	25.5	25.5	12.8	12.7
	$\boldsymbol{n}$	0.10	0.10	0.01	0.03
	$\boldsymbol{\sigma_X}$ **(dB)**	1.7	1.7	1.5	1.3
	$\boldsymbol{R_{max}}$**(km)**	2.5	2.5	2.0	2.0
	$\boldsymbol{R_{Min}}$**(km)**	28.1	28.1	28.1	28.1
Statistics of *K* factor (dB)	**Max**	33.0	33.0	16.5	16.6
	Min	12.4	12.8	8.7	7.3
	Median	27.0	27.0	12.9	13.1
	$\boldsymbol{\mu}$	27.3	27.3	12.8	13.1
	$\boldsymbol{\sigma}$	1.8	1.8	1.5	1.3

Table 5.6. Statistics of aggregate Ricean *K* factor for near-urban environment.

Cleveland, OH 22 October 2013 near-urban, all straight FTs (FT5&6)					
Ricean *K* factor		**C-band**		**L-band**	
Methods		K_{ML}	K_{MB}	K_{ML}	K_{MB}
Linear fit of *K* factor	$\boldsymbol{K_0}$**(dB)**	26.0	26.0	13.0	13.0
	$\boldsymbol{n_K}$	0.12	0.12	-0.10	-0.11
	$\boldsymbol{\sigma_Y}$ **(dB)**	1.6	1.6	2.3	2.2
	$\boldsymbol{R_{max}}$**(km)**	1.9	1.9	1.7	1.7
	$\boldsymbol{R_{Min}}$**(km)**	19.0	19.0	19.0	19.0
Statistics of *K* factor (dB)	**Max**	33.7	33.7	14.7	14.9
	Min	12.3	12.7	-86.2	-23.5
	Median	27.4	27.4	12.0	11.9
	$\boldsymbol{\mu}$	27.5	27.5	12.4	12.5
	$\boldsymbol{\sigma}$	1.8	1.7	2.3	2.3

Table 5.7. Statistics of aggregate Ricean *K* factor for suburban environment.

Latrobe, PA 15 April 2013 Suburban, all straight FTs (FT1, 2, 3, 4 & 5)					
Ricean *K* factor		**C-band**		**L-band**	
Methods		K_{ML}	K_{MB}	K_{ML}	K_{MB}
Linear fit of *K* factor	$\boldsymbol{K_0}$**(dB)**	27.6	27.6	12.5	12.2
	$\boldsymbol{n_K}$	0.09	0.09	0.10	0.11
	$\boldsymbol{\sigma_Y}$ **(dB)**	2.3	2.3	1.1	1.2
	$\boldsymbol{R_{max}}$**(km)**	1.7	1.7	0.9	0.9
	$\boldsymbol{R_{Min}}$**(km)**	41.4	41.4	41.4	41.4
Statistics of *K* factor (dB)	**Max**	40.2	40.2	20.5	20.4
	Min	7.9	6.9	6.5	5.2
	Median	28.7	28.7	13.8	13.6
	$\boldsymbol{\mu}$	28.6	28.6	13.7	13.4
	$\boldsymbol{\sigma}$	2.4	2.4	1.5	1.6

Table 5.8. Statistics of aggregate Ricean *K* factor for hilly environment.

Palmdale, CA 12 June 2013 Hilly, all straight FTs (FT6, 7, 8 & 9)					
Ricean *K* factor		**C-band**		**L-band**	
Methods		K_{ML}	K_{MB}	K_{ML}	K_{MB}
Linear fit of *K* factor	$\boldsymbol{K_0}$**(dB)**	29.6	29.6	11.8	11.5
	$\boldsymbol{n_K}$	0.00	0.00	0.07	0.07
	$\boldsymbol{\sigma_Y}$ **(dB)**	2.1	2.1	1.3	1.4
	$\boldsymbol{R_{max}}$**(km)**	5.2	5.2	2.7	2.7
	$\boldsymbol{R_{Min}}$**(km)**	23.8	23.8	23.8	23.8
Statistics of *K* factor (dB)	**Max**	35.7	35.8	23.2	23.2
	Min	12.3	12.8	9.3	-6.3
	Median	29.6	29.6	12.6	12.3
	$\boldsymbol{\mu}$	29.8	29.8	12.3	12.1
	$\boldsymbol{\sigma}$	2.1	2.1	1.3	1.4

Table 5.9. Statistics of aggregate Ricean *K* factor for mountainous environment.

Telluride, CO 12 Sept. 2013 Mountainous, all straight FTs (FT2, 3, 4, 8 & 9)					
Ricean *K* factor		**C-band**		**L-band**	
Methods		K_{ML}	K_{MB}	K_{ML}	K_{MB}
Linear fit of *K* factor	$\boldsymbol{K_0}$**(dB)**	29.8	29.8	12.4	12.0
	$\boldsymbol{n_K}$	-0.02	-0.02	0.06	0.06
	$\boldsymbol{\sigma_Y}$ **(dB)**	2.3	2.2	1.0	1.6
	$\boldsymbol{R_{max}}$**(km)**	3.4	3.4	1.9	1.9
	$\boldsymbol{R_{Min}}$**(km)**	47.5	47.5	47.5	47.5
Statistics of *K* factor (dB)	**Max**	40.5	40.5	16.6	16.7
	Min	12.8	13.2	5.1	-3.0
	Median	29.4	29.4	13.8	13.4
	$\boldsymbol{\mu}$	29.4	29.4	13.8	13.5
	$\boldsymbol{\sigma}$	2.3	2.3	1.3	1.8

5.2.3 *K*-FACTOR IN AIRFRAME SHADOWING

The LOS component was obstructed in airframe shadowing events, where the aircraft roll angle is large enough that the wings or engines block the LOS between aircraft antennas and GS antennas. The small scale fading decreases during this shadowing. Example L-band *K* factor results in an airframe shadowing event that occurred over Lake Erie are shown in Figure 5.26 [113]. The *K* factor is approximately 15 dB outside the shadowing area, and dropped to below -20 dB in the shadowing area.

Since the C-band received power was below the receiver's noise floor for part of the C-band shadowing event, the C-band *K* factor is not reliable during this airframe shadowing event.

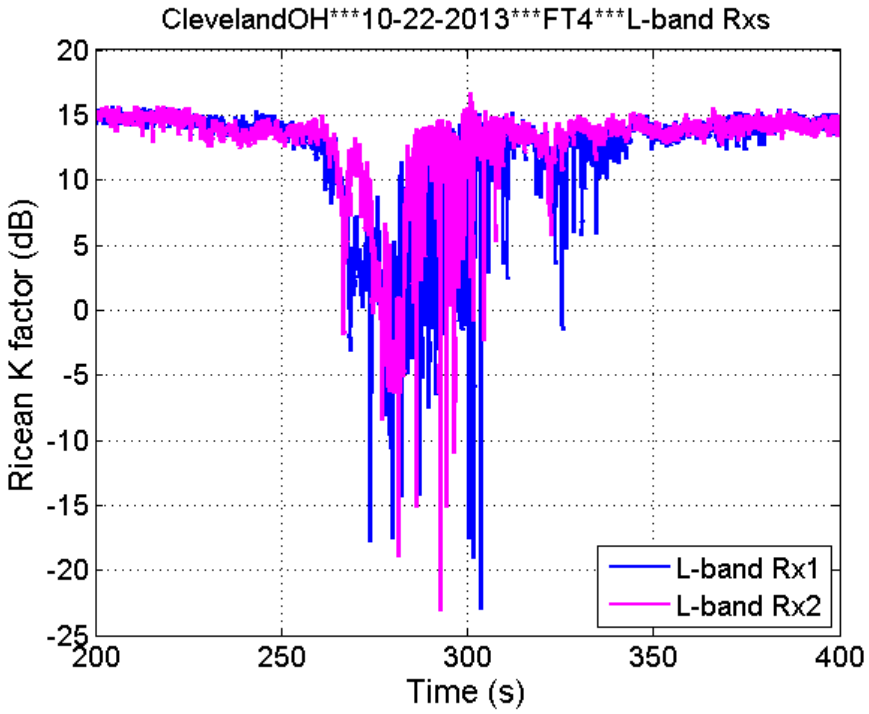

Figure 5.26. Ricean *K* factor in airframe shadowing area, over Lake Erie FT4 L-band Rxs [113].

5.3 AIRFRAME SHADOWING

5.3.1 EXAMPLE AIRFRAME SHADOWING RESULTS

An example airframe shadowing (AFS) event collected over Lake Erie was provided in [113]. Another example AFS event is presented in this section, for data that was collected over the Mojave Desert near Palmdale, CA. The flight route and the area where AFS event occurred in Google Earth® are shown in Figure 5.27, and the flight route in ECEF coordinates is plotted in Figure 5.28. Two AFS events occurred when the aircraft was making "U-turns". The definition of aircraft roll angle is illustrated in Figure

5.29. The positive roll angle denotes that the left wing is higher than the right wing. The roll angle of the measurement airplane is plotted in Figure 5.30.

We analyze the circled area where the example AFS event occurred. The maximum roll angle was 26.9º in this AFS event. The elevation angle was approximately 5.2º. The link distance between the aircraft and the GS in the circled area was between 20.5 and 22.2 km. The aircraft velocity was approximately 100 m/s. The heights of aircraft and GS antennas were 1925 and 20 m above the ground, respectively. The PDP update rate was approximately 2660 PDPs per second for each of our four receivers.

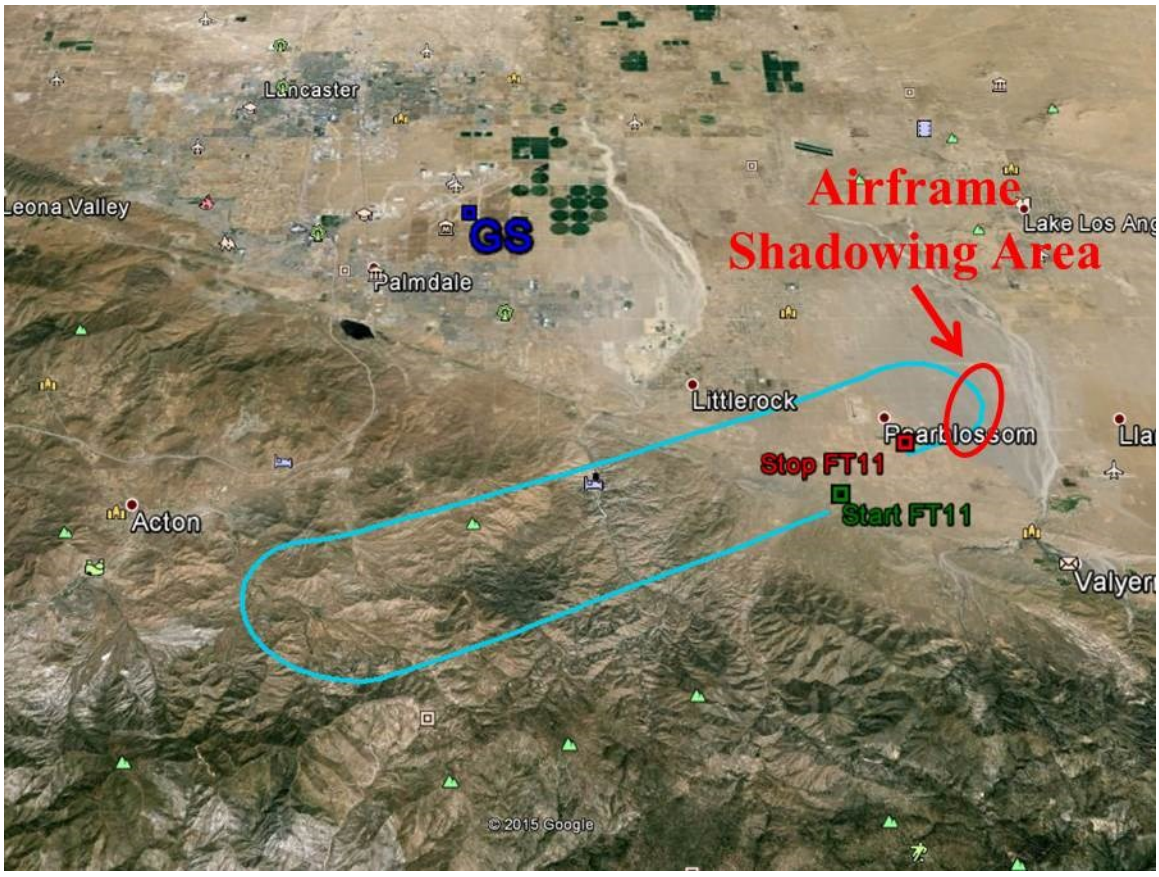

Figure 5.27. Flight route of FT11 in Palmdale, CA on 12 June 2013 in Google Earth®.

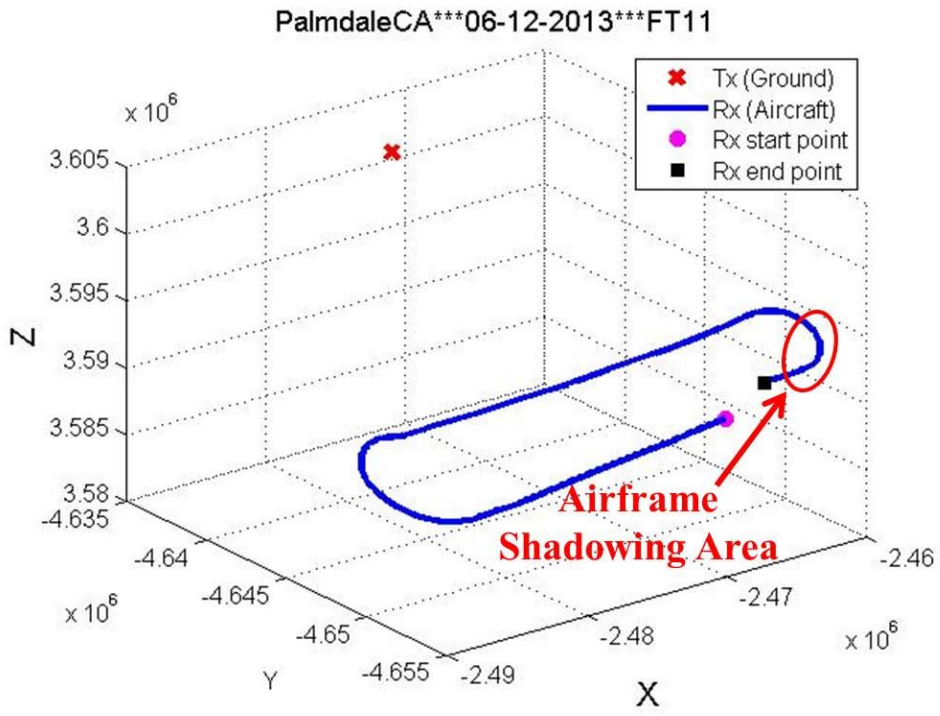

Figure 5.28. Flight route of FT11 in Palmdale, CA on 12 June 2013 in ECEF coordinates.

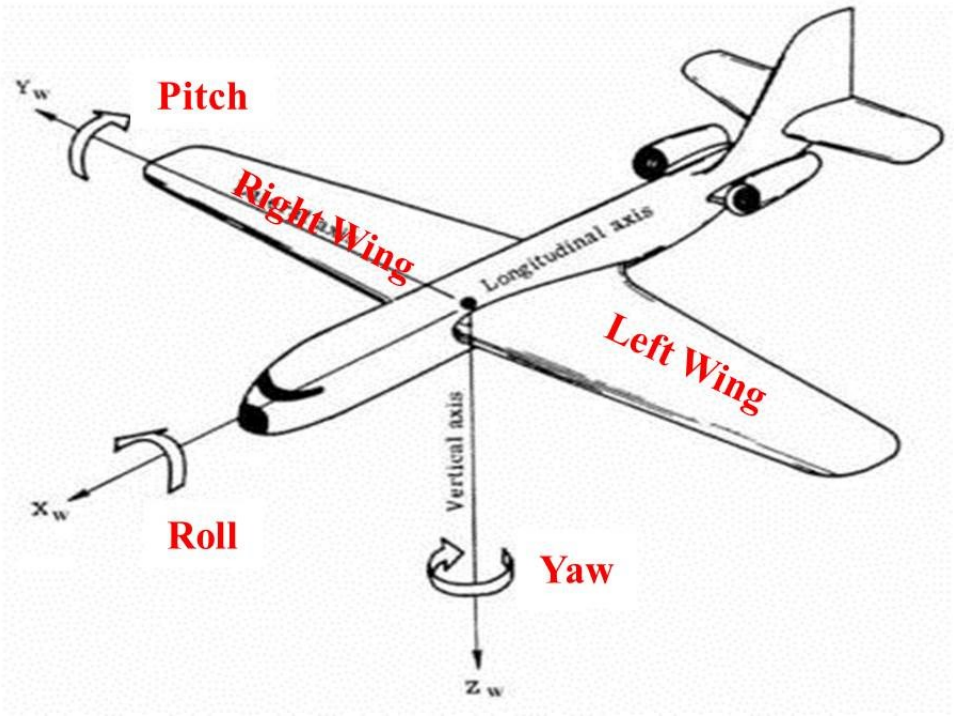

Figure 5.29. Definition of aircraft roll angle [113].

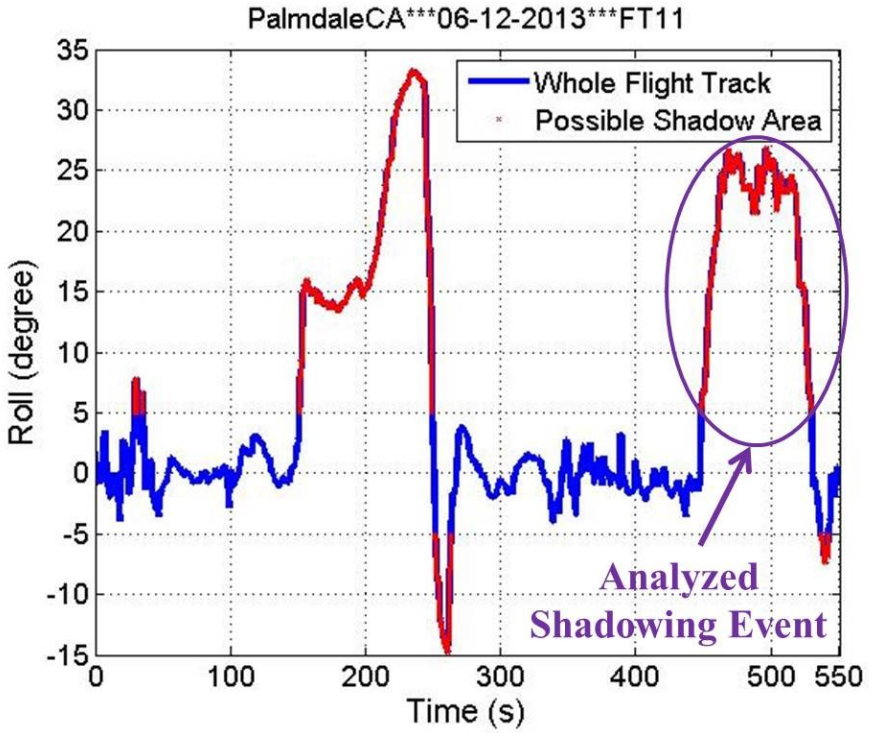

Figure 5.30. Roll angle of FT11 in Palmdale, CA on 12 June 2013.

Airframe shadowing occurrs when the LOS component is blocked by part of the aircraft (in our case, wings or engines). It requires not only a large roll angle, but also the flight direction (heading) must differs from the azimuth angle, i.e., the difference between the heading angle and azimuth angle $\angle_{HA}$ should be large enough. The angle $\angle_{HA}$ versus measured time is shown in Figure 5.31.

Three criteria are employed to determine start and stop positions of an airframe shadowing event:

a) Roll angle larger than 5º, as indicated in the red segments in Figure 5.30;

b) Angle $\angle_{HA}$ larger than 30º, as shown by the red region in Figure 5.31;

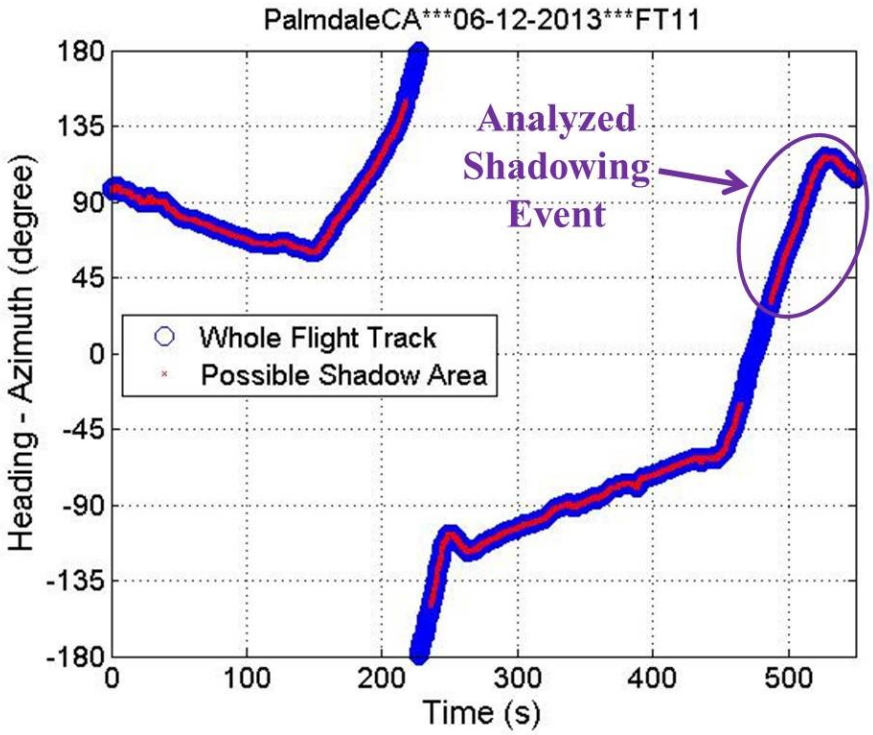

Figure 5.31. Difference between aircraft heading and azimuth angles, FT11 in Palmdale, CA on 12 June 2013.

c) Measured received power P_r at least 5 dB[10] smaller than the received power estimated by the log-distance path loss model.

The measured received power P_r in the AFS area for two C-band Rxs are shown in Figure 5.32. The cumulative distribution functions (CDFs) of P_r in AFS area are plotted in Figure 5.33. The shadowing duration for the two C-band receivers are 52.4 and 48.9 s. The maximum shadowing losses are 33.9 and 33 dB. Note that the noise level of our C-band receivers with 0.0005 false alarm probability (see Section 3.3.3) is approximately -80 dBm. Some P_r values below the noise level might be overestimated. Therefore, the maximum shadowing loss could be larger than 33.9 and 33 dB.

[10] The measured received power has small fluctuations up to a few decibels. The 5 dB value was chosen as a compromise: it is small enough to ensure inclusion of a large number of PDPs in AFS events to enable accurate statistical estimates, and large enough to avoid "false starts" or "false stops" of AFS events from the signal fluctuation. Similarly, the 5º roll angle and 30º $\angle_{HA}$ thresholds are also engineering judgements.

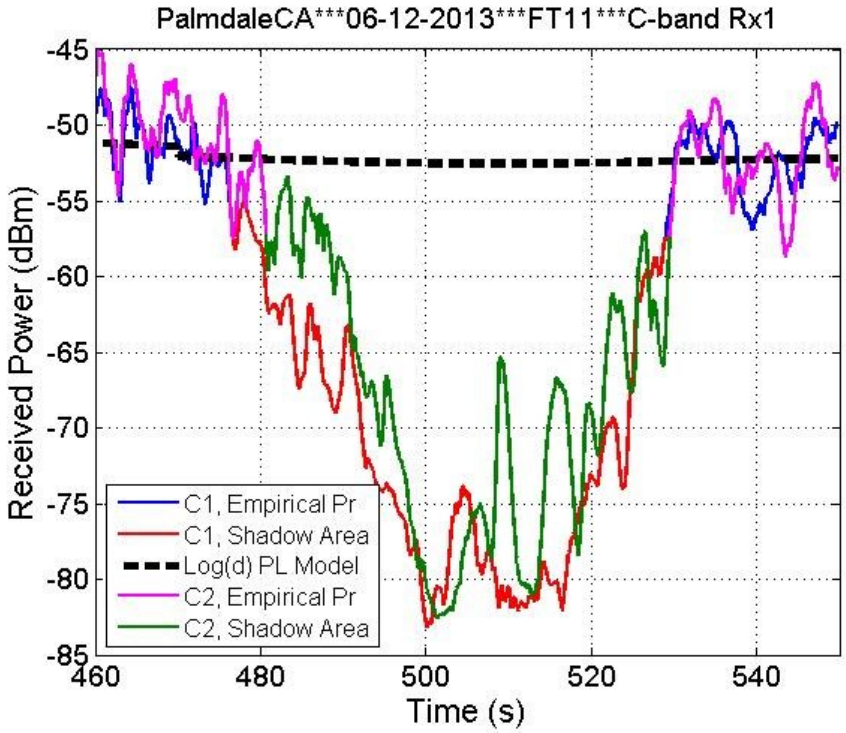

Figure 5.32. C-band airframe shadowing depth and duration, Palmdale, CA 12 June 2013 FT11, C1 & C2 denote C-band Rx1 and Rx2 respectively.

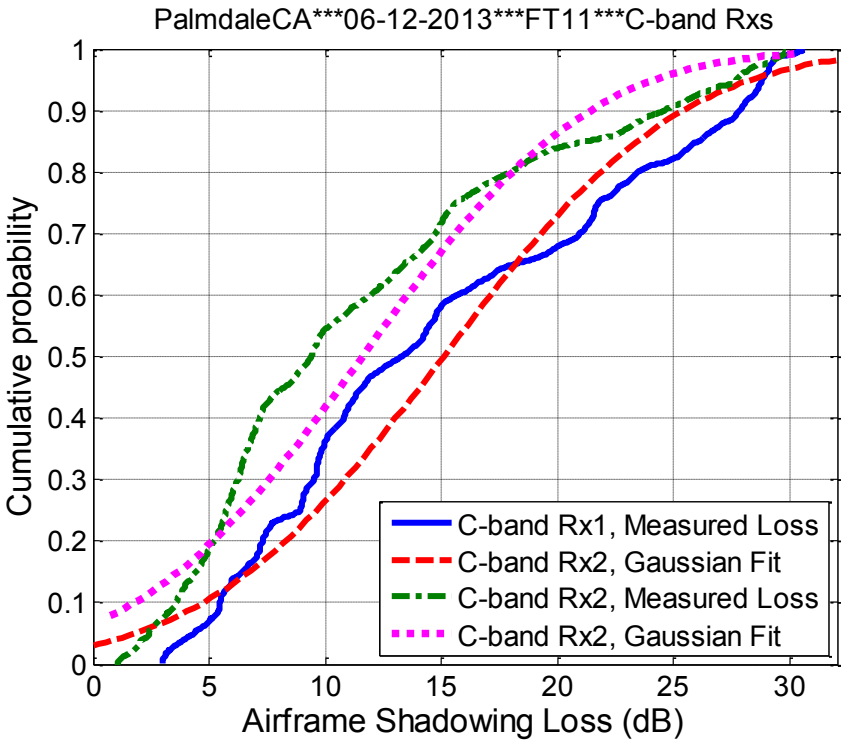

Figure 5.33. CDF of C-band shadowing depth, Palmdale, CA 12 June 2013 FT11.

The measured P_r vs. time results for the L-band receivers during the AFS event are plotted in Figure 5.34, and their CDFs are shown in Figure 5.35. The maximum shadowing losses are 43.4 and 25.7 dB, and the shadowing durations are 36.3 and 33.2 s for the two receivers. The CDFs of P_r in the AFS area were fit by Gaussian distributions. The Gaussian parameters and statistics of this example AFS event for all four receivers are listed in Table 5.10.

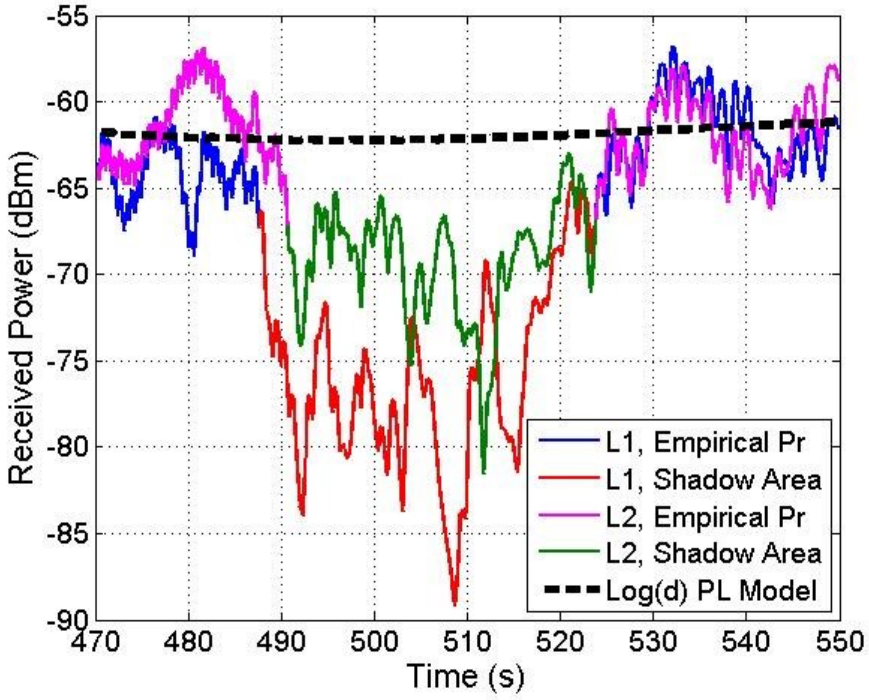

Figure 5.34. L-band airframe shadowing depth and duration, Palmdale, CA 12 June 2013 FT11, L1 & L2 denote L-band Rx1 and Rx2 respectively.

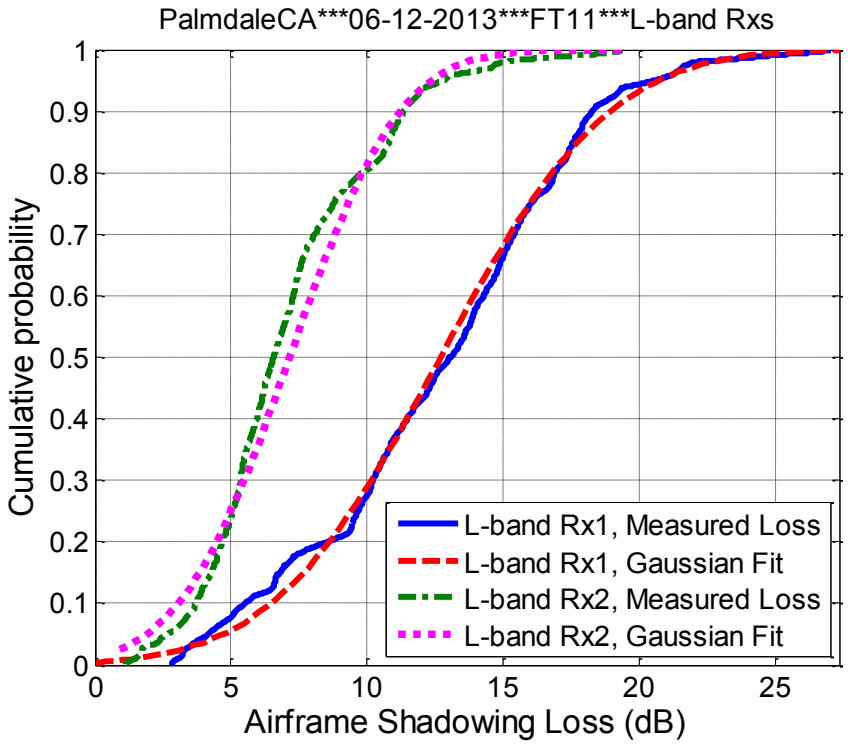

Figure 5.35. CDF of L-band shadowing depth, Palmdale, CA 12 June 2013 FT11.

Table 5.10. Statistics of airframe shadowing depth and duration, Palmdale, CA 12 June 2013 FT11.

		C-band		L-band	
		Rx1	**Rx2**	**Rx1**	**Rx2**
Shadow Duration (s)		52.4	48.9	36.3	33.2
Shadow Loss (dB)	*Max*	33.9	33.0	43.3	25.7
	Min	1.8	0.0	0.0	0.0
	Mean	15.1	11.6	12.7	7.1
	Median	13.2	9.1	12.9	6.6
	Standard Deviation	8.2	7.9	5.1	3.4
Link Distance (km)	*Max*	22.2	22.2	22.2	22.2
	Min	20.1	20.5	21.1	21.3
Max Roll Angle (degree)		26.9			
Elevation Angle (degree)		5.2			

The C-band sequence of PDPs in the AFS event is shown in Figure 5.36. The big null in the middle near 500 s is caused by the wing shadowing.

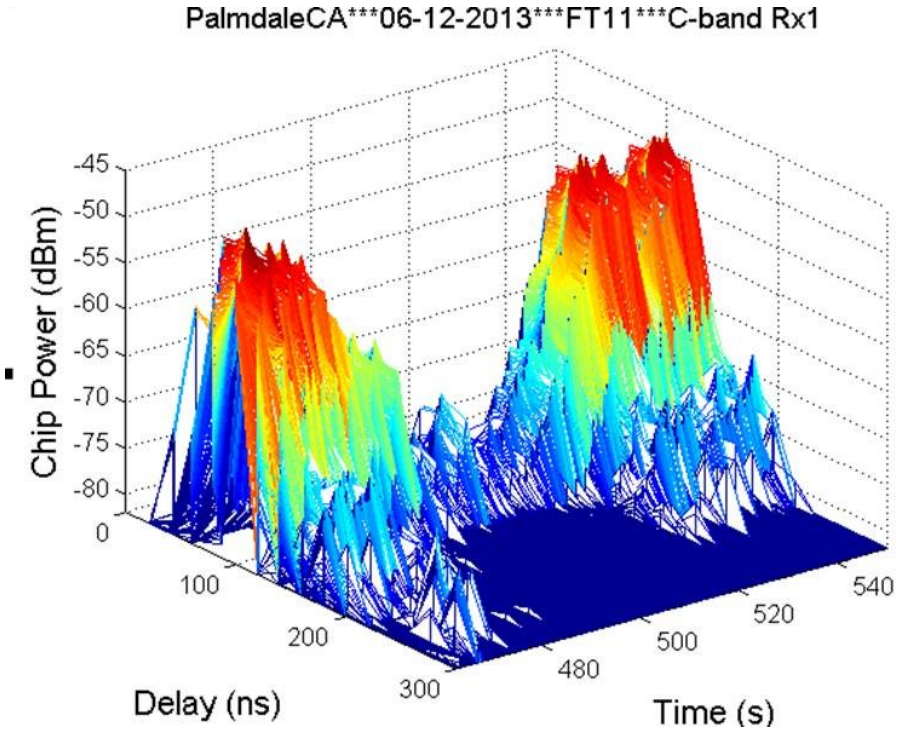

Figure 5.36. Sequence of C-band PDPs in airframe shadowing area, Palmdale, CA 12 June 2013 FT11.

The magnitude of received power difference between two intra-band receivers is termed instantaneous diversity gain. This "instantaneous" measure in a sense represents the maximum attainable selection diversity against shadowing, applicable for our specific aircraft and antenna locations. The diversity gains versus time for both bands are shown in Figure 5.37. The channel responses of the two Rxs are essentially the same outside the AFS area, as the diversity gain is typically smaller than 5 dB. However, the diversity gain is up to 20 dB in L-band and 16 dB in C-band in the AFS area. Multiple aircraft antennas could significantly mitigate the airframe shadowing, even in this case where all antennas are on the same side of the aircraft. The diversity gain is expected to increase if two aircraft antennas are mounted further away, e.g., at the end of two wings or one under the cockpit and the other under the tail or on the top. In [46], the authors experimentally

analyzed the diversity gain provided by multiple GS antennas (a few meters separation distance), and found this almost useless to mitigate the airframe shadowing.

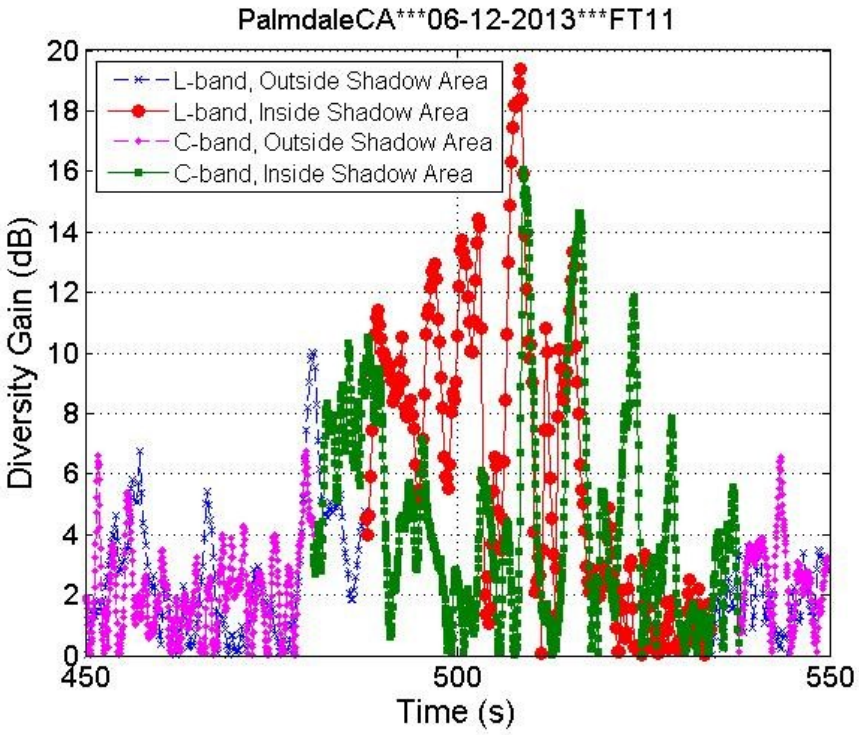

Figure 5.37. Aircraft antenna diversity gain in airframe shadowing area, Palmdale, CA 12 June 2013 FT11.

5.3.2 AIRFRAME SHADOWING MODELS

NASA Glenn Research Center has collected 58 AFS events in our measurement campaign. Since we have two receivers in each band, 111 C-band and 98 L-band shadowing events[11] are available for generating statistics of shadowing duration and depth. In this section we provide the statistics of AFS depth and duration.

The histogram of shadowing durations for C-band and L-band are plotted in Figures 5.38 and 5.39, respectively. The histograms are fitted by truncated Gaussian

[11] Numbers of C-band (111) and L-band (98) shadowing events are smaller than twice 58 because 1) some receivers were not functioning during some FTs; and 2) when AFS occurred on one receiver, it may not have occurred on all other receivers. All the 209 AFS events have been checked by the three criteria described in Section 5.3.1.

distributions. In these figures, μ denotes mean and *std* denotes standard deviation. The term "truncated" means that all non-positive values generated by the Gaussian fit should be ignored—we do not fit modified pdfs to the histograms simply because the probability of negative durations is small enough so that ignoring these should be inconsequential. The average shadowing duration is 35 s in C-band and 25.5 s in L-band. The duration depends on aircraft flight velocity and maneuver. The flight velocity was between 60 to 100 m/s, which is relatively slow for typical commercial airplanes; our velocity was intentionally slow in order to record as many PDPs as possible in our measurements. Hence the shadowing duration in practical flight actions is expected to be shorter than what we report in Figures 5.38 and 5.39. The C-band shadowing duration is on average 10 seconds longer than the L-band duration. This is because the C-band signal at shorter wavelength than L-band incurs an electrically larger obstruction, i.e., the size of the aircraft wings is relatively larger in C-band.

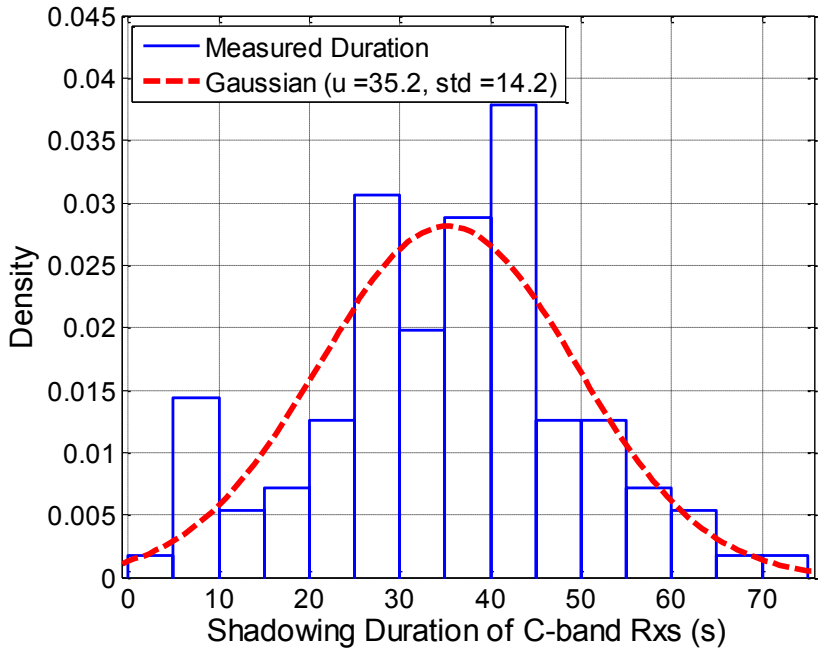

Figure 5.38. Histogram of C-band airframe shadowing duration.

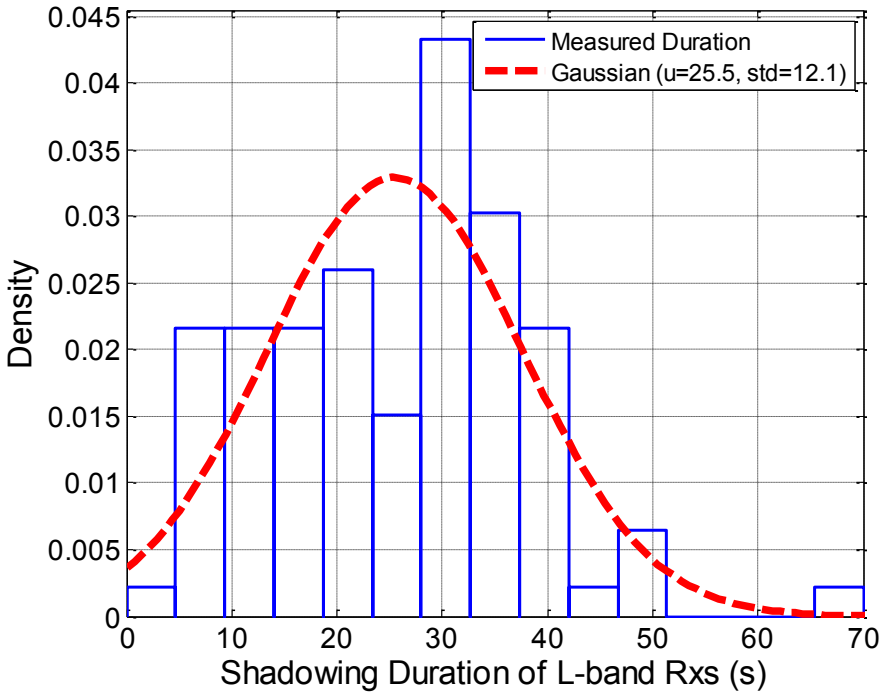

Figure 5.39. Histogram of L-band airframe shadowing duration.

The shadowing loss is modeled based upon the median values for each AFS event. The maximum and mean shadowing loss are strongly affected by fading, and C-band maximum and mean shadowing loss are further influenced by the Rx's noise level. We also checked the 90th and 70th percentiles shadowing loss values, which are also affected by the C-band Rx's noise level. Therefore, the median values provide a fairly reliable estimation of shadowing loss. The histograms of median shadowing loss for C-band and L-band are shown in Figures 5.40 and 5.41, respectively. Their CDFs are plotted in Figure 5.42. The histograms are fit by truncated Gaussian distributions, for simplicity. The median shadowing loss is on average 15.5 dB in C-band and 10.8 dB in L-band. The C-band shadowing loss is approximately 5 dB larger than the L-band loss. Again, this is due to the relatively larger size of the aircraft wing in C-band than in L-band.

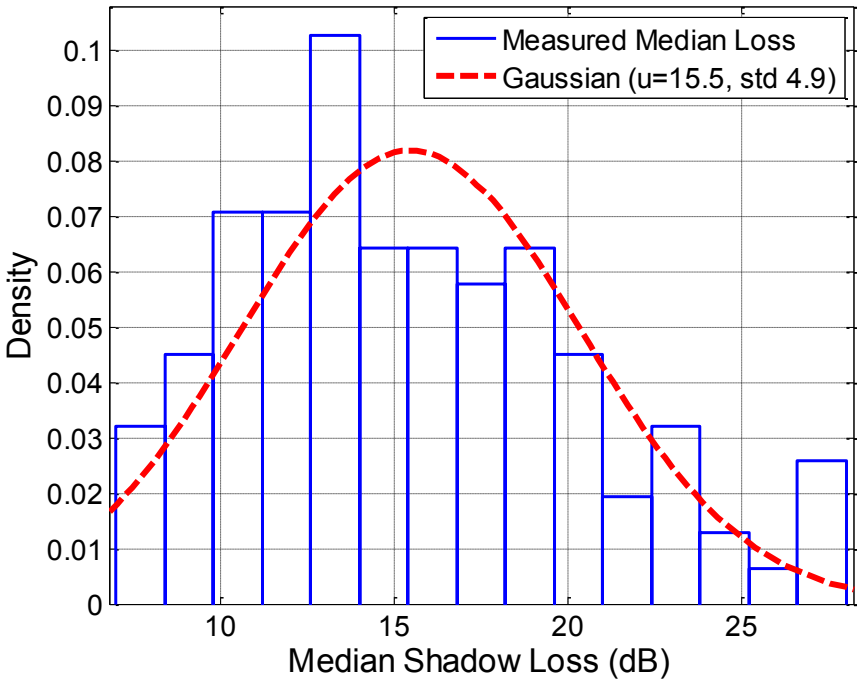

Figure 5.40. Histogram of median shadowing loss in C-band.

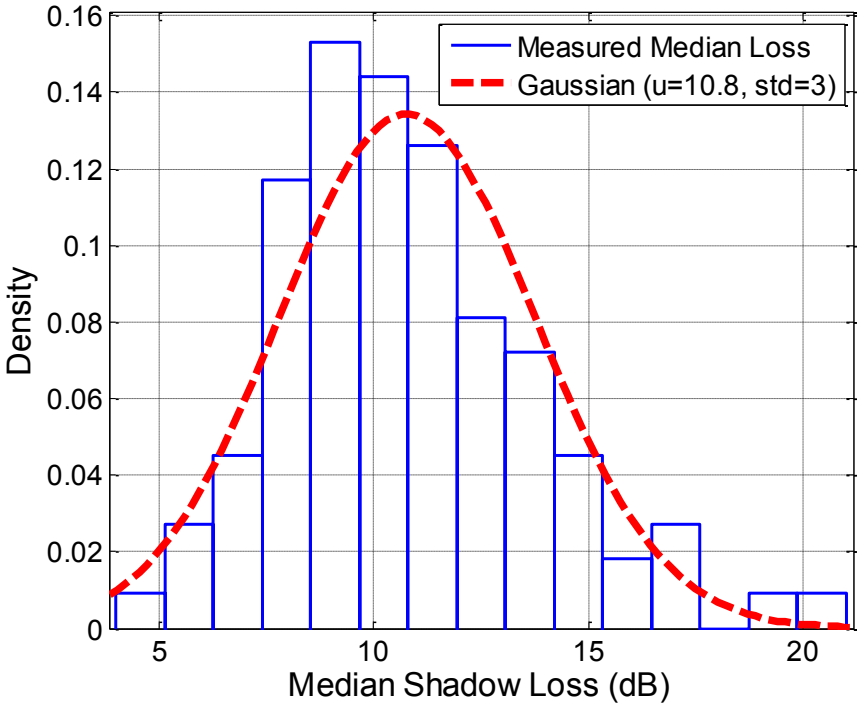

Figure 5.41. Histogram of median shadowing loss in L-band.

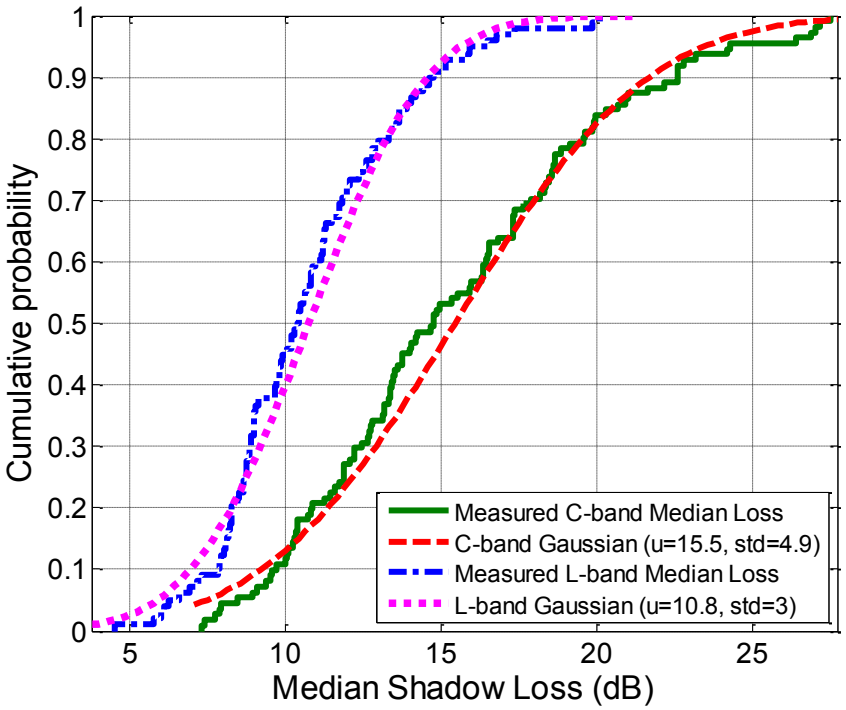

Figure 5.42. CDF of median shadowing loss.

The maximum shadowing loss in L-band is plotted in Figure 5.43. Gaussian, Generalized Extreme Value (GEV) and Weibull fits found by the Matlab® function distribution fitting tool "dfittool" via the maximum likelihood criteria are also shown in Figure 5.43, where "beta" denotes the Weibull β factor. The GEV fit the measured data the best. The C-band maximum shadowing loss is sometimes underestimated by the noise floor, so we do not provide C-band maximum shadowing loss statistics.

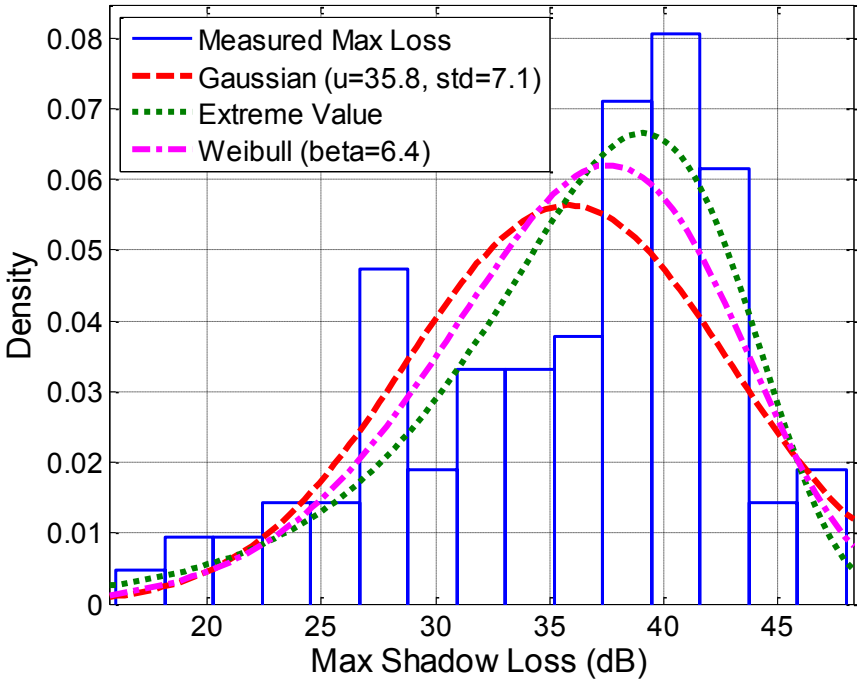

Figure 5.43. Histogram of maximum shadowing loss in L-band.

The median shadowing loss versus roll angle is shown in Figure 5.44. (Note that these results are specific to the S-3B aircraft, but should translate to other aircraft of similar size.) A linear fit was found to describe the relationship between the median shadowing loss *S* and Roll angle *Roll* in degrees as

$$S(Roll) = A_{S.Roll} + n_{S,Roll}(Roll - Roll_{min}) + X_{S,Roll}, \quad (5.16)$$

where $A_{S,Roll}$ denotes the reference shadowing loss at the minimum roll angle $Roll_{min}$, $n_{S,Roll}$ denotes the slope, and $X_{S,Roll}$ denotes a zero-mean random variable with standard deviation of $\sigma_{X,S,Roll}$. The linear fit parameters are provided in Tables 5.11, and these fits can be interpreted as pertaining to aircraft similar in size to the S-3B, with antennas on the bottom. The shadowing loss increases as the maximum magnitude of roll angle increases, as expected. The C-band shadowing loss increases faster than L-band loss with

roll angle. The joint PDF of maximum roll angle vs. median shadowing loss for both bands are shown in Figures 5.45 and 5.46.

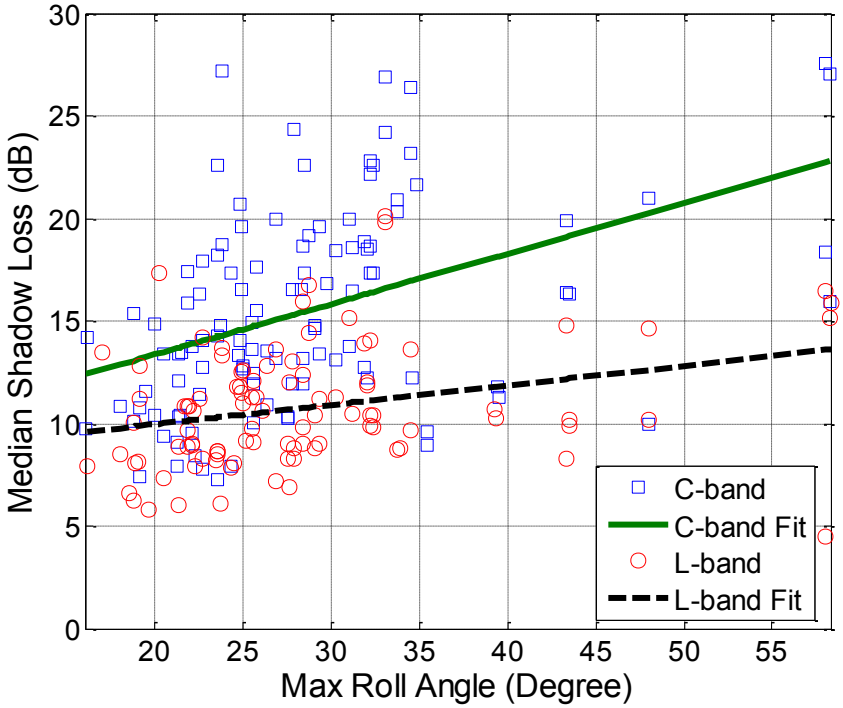

Figure 5.44. Median shadowing loss vs. maximum roll angles.

Table 5.11. Parameters of linear fits for median shadowing loss vs. roll angle.

Median shadowing loss vs. roll angle		
	L-band	*C-band*
$n_{S,Roll}$	0.09	0.25
$A_{S,Roll}$	9.6	12.4
$\sigma_{X,S,Roll}$	2.8	4.4
Min Roll Angle $Roll_{min}$	16.1	16.1
Max Roll Angle	58.3	58.3

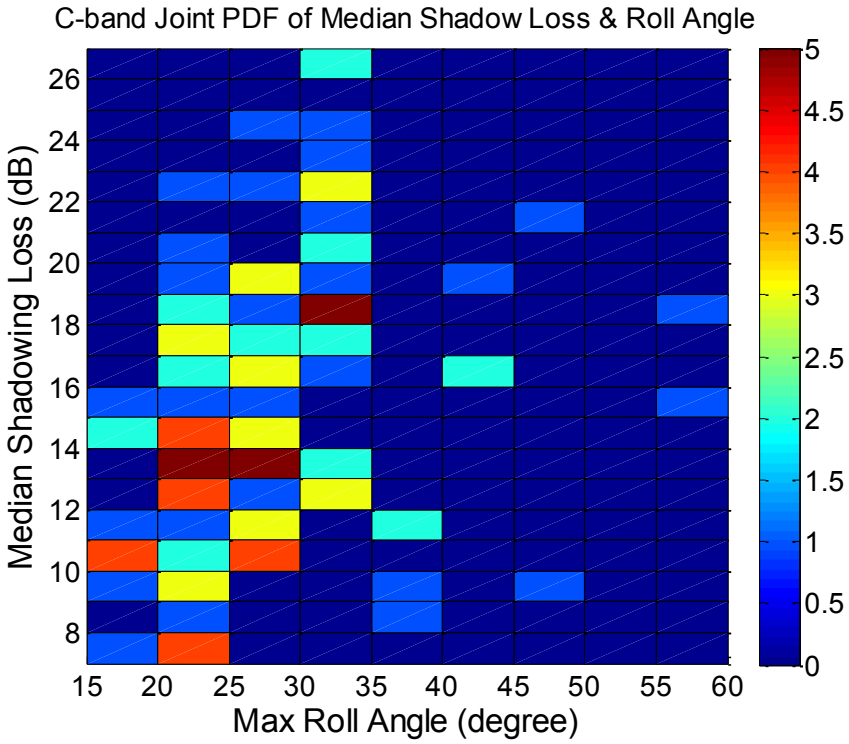

Figure 5.45. C-band joint PDF of median shadowing loss vs. maximum roll angle.

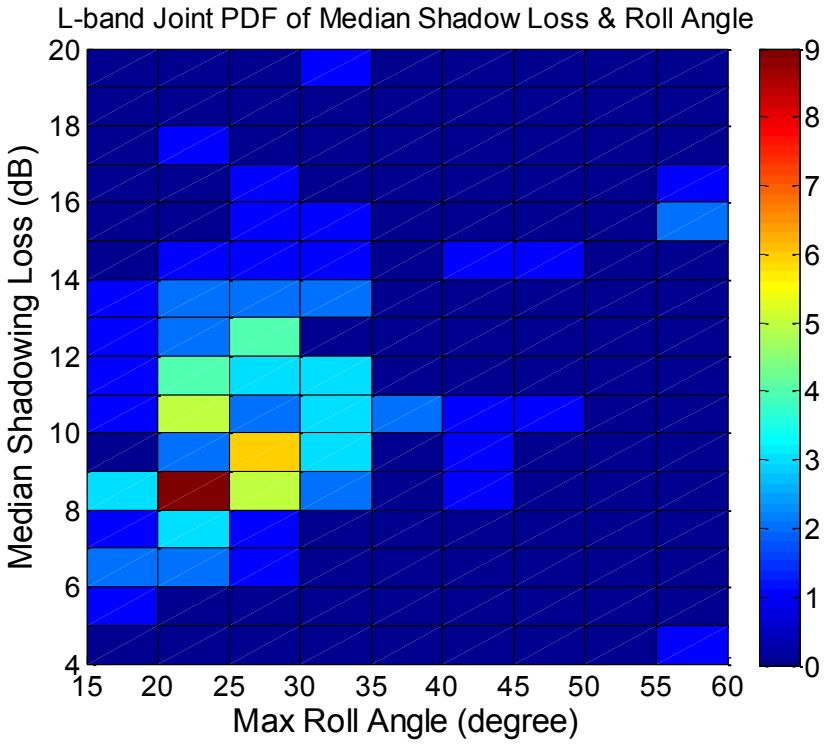

Figure 5.46. L-band joint PDF of median shadowing loss vs. maximum roll angle.

The median shadowing loss versus duration is shown in Figure 5.47. The L-band maximum shadowing loss versus duration is shown in Figure 5.48. A linear fit was found to describe the relationship between the shadowing loss S and shadowing duration D in seconds,

$$S(D) = A_{S,D} + n_{S,D}(D - D_{min}) + X_{S,D}, \tag{5.17}$$

where $A_{S,D}$ denotes the reference shadowing loss at the minimum shadowing duration D_{min}, $n_{S,D}$ denotes the slope and $X_{S,D}$ denotes a zero-mean random variable with standard deviation of $\sigma_{X,S,D}$. The linear fit parameters are provided in Table 5.12. The median shadowing loss is *not* strongly correlated with shadowing duration, which may be somewhat unexpected. The L-band maximum shadowing loss though does increase with duration, yet the standard deviation of the fit to maximum L-band loss is quite large, hence the linear relationship is not very accurate. The joint PDFs of shadowing loss and shadowing duration for both bands are shown in Figures 5.49 to 5.51.

Table 5.12. Parameters of linear fits for shadowing loss vs. duration.

Shadowing loss vs. duration			
	Max Loss	*Median Loss*	
	L-band		*C-band*
$\boldsymbol{n_{S,D}}$	0.24	0.03	-0.03
$\boldsymbol{A_{S,D}}$	31	10.1	16.3
$\boldsymbol{\sigma_{X,S,D}}$	6.3	3.0	4.8
Min Duration $\boldsymbol{D_{min}}$	4.6	4.6	4.9
Max Duration	69.1	69.1	71.9

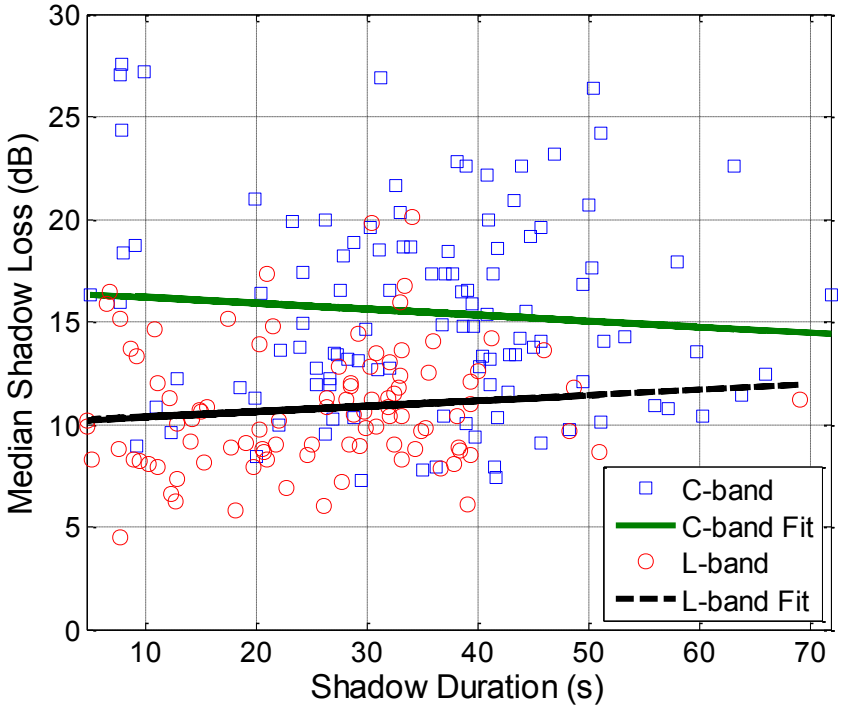

Figure 5.47. Median shadowing loss vs. duration.

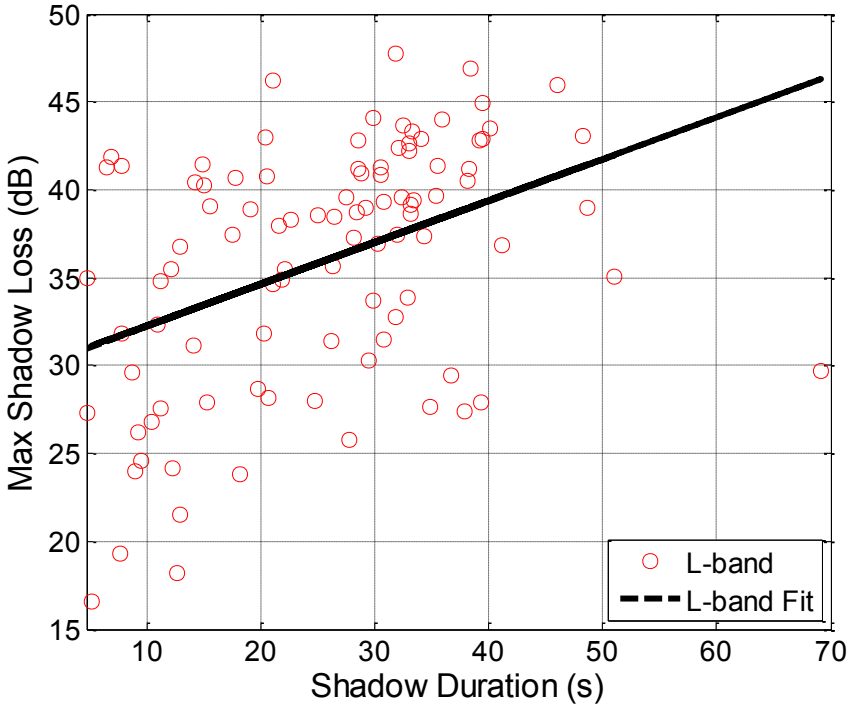

Figure 5.48. L-band maximum shadowing loss vs. duration.

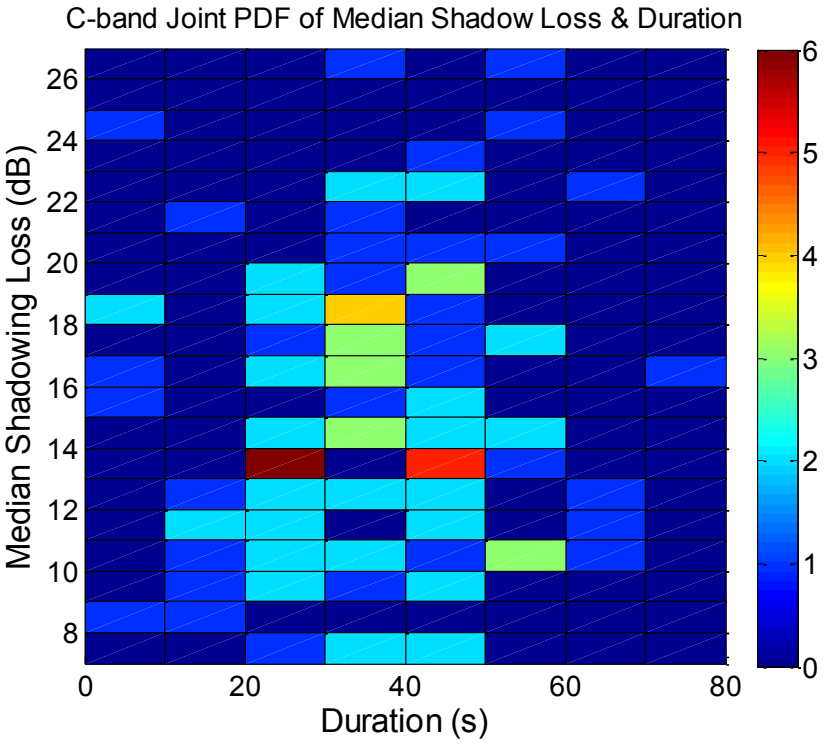

Figure 4.49. C-band joint PDF of median shadowing loss vs. duration.

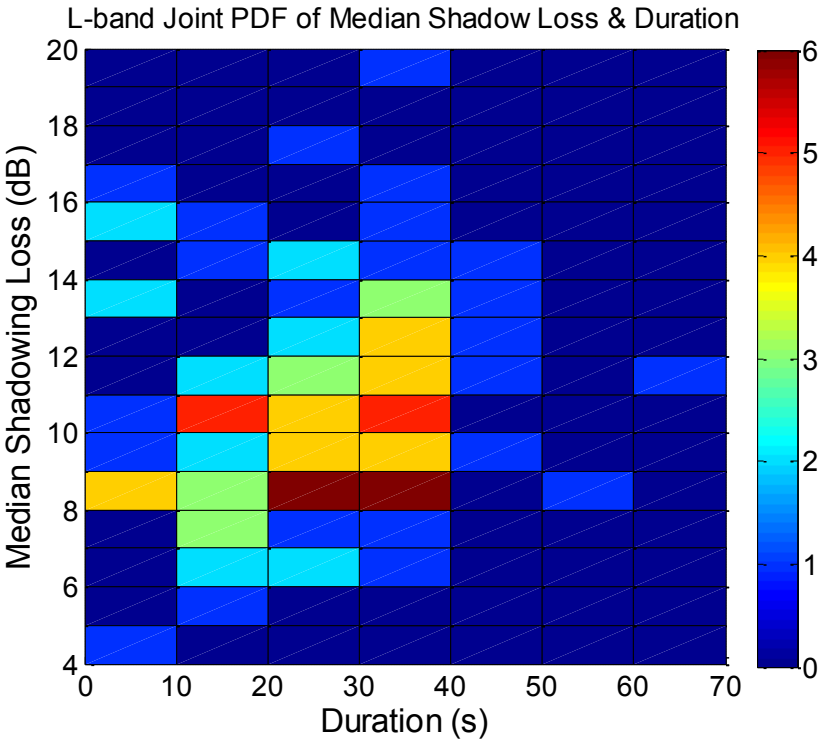

Figure 4.50. L-band joint PDF of median shadowing loss vs. duration.

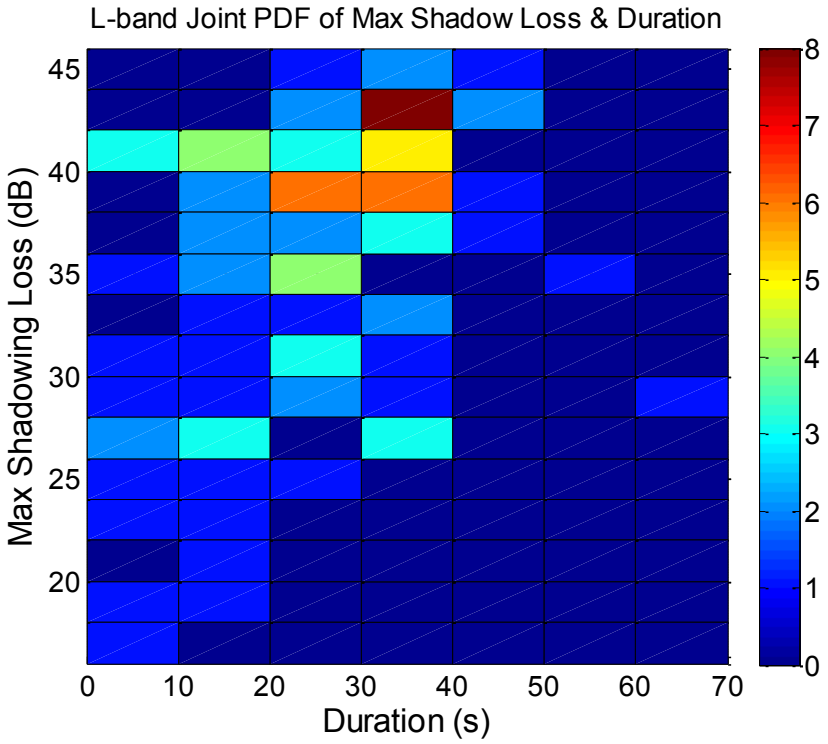

Figure 4.51. L-band joint PDF of maximum shadowing loss vs. duration.

5.3.3 SIMULATING AIRFRAME SHADOWING

We model shadowing loss as a function of time because aircraft maneuvers that cause shadowing do not depend upon link range R. The narrowband total path loss $L_T(t)$ accounts for both large scale path loss and wing shadowing loss, which can be modeled as follows,

$$L_T(t) = PL(t) + L_S(t), \tag{5.18}$$

where $L_S(t)$ denotes shadowing loss over time, $L_T(t)$ and path loss $PL(t)$ over time can be converted to functions of link range $L_T(R)$ and $PL(R)$ by,

$$R = v_H t \cos(\angle_{HA}) \cos\theta + v_V t \sin\theta, \tag{5.19}$$

where $\angle_{HA}$ is the angle between aircraft heading and azimuth angles and θ denotes elevation angle, v_H and v_V denote the aircraft velocity in the horizontal and vertical planes, respectively. Note that all velocities and angles in (5.19) are themselves time

dependent, but the time variation of these parameters is generally slow. Since the elevation angle was only a few degrees in our measurements and the vertical velocity was negligible, (5.19) can be reduced to a two dimensional approximation in the horizontal plane as

$$R \cong vtcos(\angle_{HA}), \tag{5.20}$$

where *v* denotes the combined or horizontal velocity. The relationship between link range *R* and time *t* should be considered three dimensionally when parameters (elevation angle and vertical velocity) in the vertical plane are significant. The path loss *PL(t)* in eq. (5.18) can be obtained from *PL(R)* via (5.3) or (5.4) outside the AFS region. The path loss *PL(R)* is *only* the first two terms in eq. (5.3) inside the AFS region. The third terms in (5.3) and (5.4) are the direction adjustments ζF, which are not applied in the AFS region, since the magnitude of direction angle $|\angle_{HA}|$ is between 30º and 150º, hence the flight direction is neither straight toward nor straight away from the GS. The fourth terms in (5.3) and (5.4) account for small scale (faster) variation, which should not be employed during shadowing since the fading characteristics in the AFS are different--fading in the AFS is considered separately.

The airframe shadowing loss $L_S(t)$ is given by,

$$L_S(t) = Sf(t) - 20log_{10}[a(t)], \tag{5.21}$$

where *S* denotes the magnitude of wing shadowing loss, which is a random variable, but is constant for each AFS event; *a(t)* denotes a Ricean fading random variable with *K*=0 dB (other options are also applicable); and *f(t)* denotes a shape function (maximum of 1) versus percentage of the shadowing event duration, which is a cubic spline interpolation as shown in Figure 5.52. This function is a least squares third-order polynomial fit which

passes through three control points $(t_i, f(t_i)) \in \{(0,0), (0.5,1), (1,0)\}$. The cubic spline interpolation is given by $f(t)$ to yield [114],

$$f(t) = a_i(t - t_i)^3 + b_i(t - t_i)^2 + c_i(t - t_i) + d_i. \quad (5.22)$$

where a_i, b_i, c_i and d_i are coefficients defined by control points $(t_i, f(t_i))$.

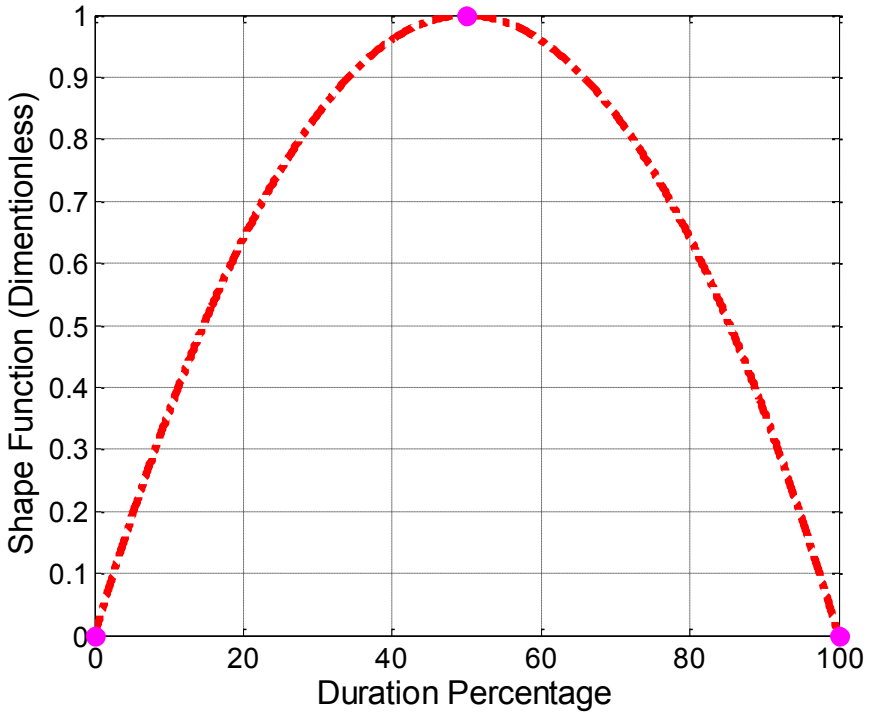

Figure 5.52. Shadowing shape function vs. shadowing duration percentage.

As noted, we describe the combined path loss and shadowing simulation as a function of time. If detailed geometric information for the flight to be simulated is available, then a modified version of our algorithm must be used, in which shadowing depth S and duration D both depend upon roll and heading angles as described in Section 5.3.1. We describe only the time-based algorithm here. Our time-based algorithm is also "vector-based," in that we generate complete vectors of the required variables in their entirety within several algorithm steps. For most modern simulation platforms, this will not pose a problem in terms of storage, but if such a problem occurs, the algorithm can be

modified to work in a loop wherein the required variables are generated sequentially. We also allow for multiple *(J)* shadowing events per simulation, and assume no overlapping shadowing events. The algorithm can also be modified to "merge" overlapping shadowing events if desired.

The path loss plus shadowing simulation is implemented as follows:

1. Define a time vector $t=[t_0, t_1, t_2,\ldots, t_{i-1}, t_i, t_{i+1},\ldots, t_N]$. Actual values of t are arbitrary, but generally the m^{th} time increment $\Delta t_m=t_m-t_{m-1}$ between any two time values (any $m\in\{1, 2, \ldots N\}$) is a constant Δt for all m—this is our assumption here. If desired, values of t can be converted to link range R or symbol units as previously described. For a given flight path, this conversion yields a corresponding range vector $R=[R_0, R_1, R_2,\ldots, R_{i-1}, R_i, R_{i+1},\ldots, R_N]$.

2. Compute *PL(t)* according to the desired model (log-distance or CE2R). This yields the vector $PL=[PL_0, PL_1, PL_2,\ldots, PL_{i-1}, PL_i, PL_{i+1},\ldots, PL_N]$.

3. Select the number of shadowing events J. Then select the J airframe shadowing start times $t_{x,j}\subset[t_0, t_N), j\in\{1, 2, \ldots, j, \ldots, k, \ldots, J\}$. These can be drawn according to any desired distribution over the flight duration (if any of these random start times are identical, e.g., $t_{x,j}=t_{y,k}$ for any $x\neq y$, re-draw these repeated random start times $t_{x,j}$ so that all start times are distinct).

4. Select the J shadowing depth random variables D_j from the appropriate Gaussian distribution of Figures 5.38 or 5.39. If any shadowing events overlap ($t_{x,j}\leq t_{y,k}\leq t_{x+Dj,j}$, for $y>x$), re-draw either the start time or duration random variables to remove overlaps.

5. From a distribution specified by Figures 5.40 and 5.41, generate the median airframe shadowing magnitudes S_j in dB. (An alternative is to generate a roll angle dependent shadowing loss $S_j(Roll)$ according to (5.16). This would require specification of a roll vector vs. time.

6. For each of the J shadowing events, from shape function $f(t)$ specified by Figure 5.52 and (5.22), and the shadowing loss magnitudes S_j generated by step 5, set the instantaneous shadowing loss sample values within the shadowing events as $S_j f(\frac{t_i - t_{x,j}}{D_j})$. Note that the instantaneous shadowing loss is 5 dB at the start and stop points $t_i = t_{x,j}$ and $t_i = t_{x,j} + D_j$ since our measured shadowing loss starts and stops at 5 dB, see Section 5.3.1[12].

7. Apply small scale fading $a(t)$ to all the instantaneous shadowing loss samples $S_j f(\frac{t_i - t_{x,j}}{D_j})$ created by step 6. During the shadowing events, shadowing loss in decibels is then,

$$L_S(t_i) = S_j f(\frac{t_i - t_{x,j}}{D_j}) - 20log_{10}[a(t_i)]. \quad (5.23)$$

8. The narrowband total path loss $L_T(t_i) = PL(t_i) + L_S(t_i)$, where path loss $PL(t_i)$ is the first two terms in (5.3) and shadowing loss $L_S(t_i)$ yields (5.23).

An example result from this procedure of generating $L_S(t)$ for a single shadowing event (J=1) is shown in Figure 5.53, where S=15.5 dB is employed for C-band.

[12] The total path loss $L_S(t)$ may have discontinuities at the start and stop points of the AFS event, which is due to the 5 dB threshold employed here; this may also occur if the CE2R path loss model is used outside the AFS region. These discontinuities won't significantly affect link budget or outage estimation. The discontinuities can be mitigated by applying a local moving average if desired.

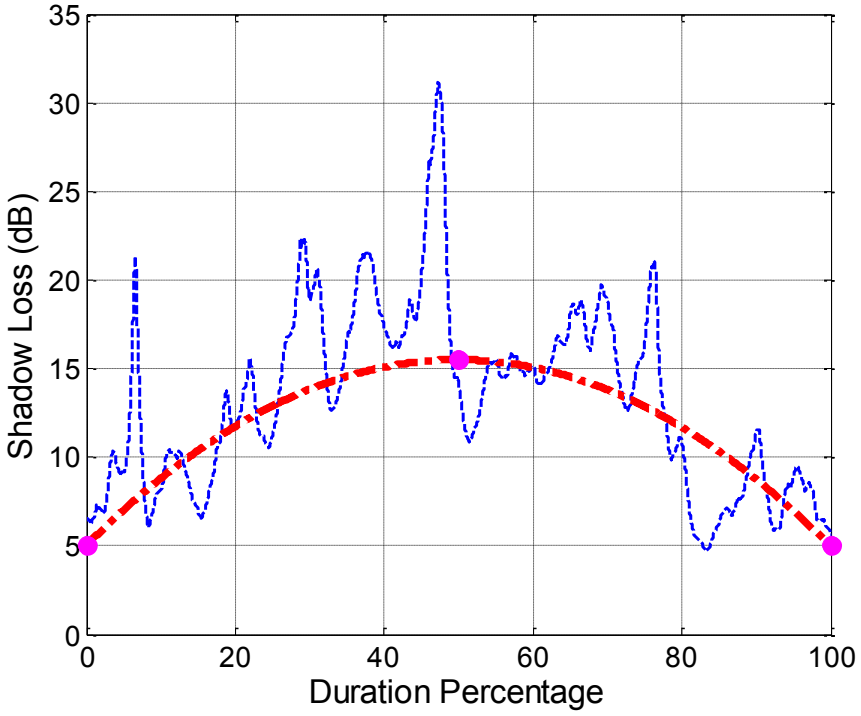

Figure 5.53. C-band instantaneous shadowing loss with fading vs. shadowing duration percentage.

All the above procedures were applied to the AFS event collected in Palmdale, CA FT11 C-band Rx1 and L-band Rx1. The measured received power and AFS models are shown in Figures 5.54 and 5.55, respectively. Note that both measured and modeled received power values are moving averaged over 1000 PDPs. This particular Palmdale shadowing event is somewhat asymmetric, so our cubic (or any symmetric) function won't fit perfectly. This is flight maneuver and aircraft shape specific. Some of our measured shadowing events are more symmetric, and some show the "opposite" asymmetry. However, the asymmetry does not affect statistics and distributions of the shadowing loss. The CDFs of measured and modeled airframe shadowing loss are plotted in Figures 5.56 and 5.57.

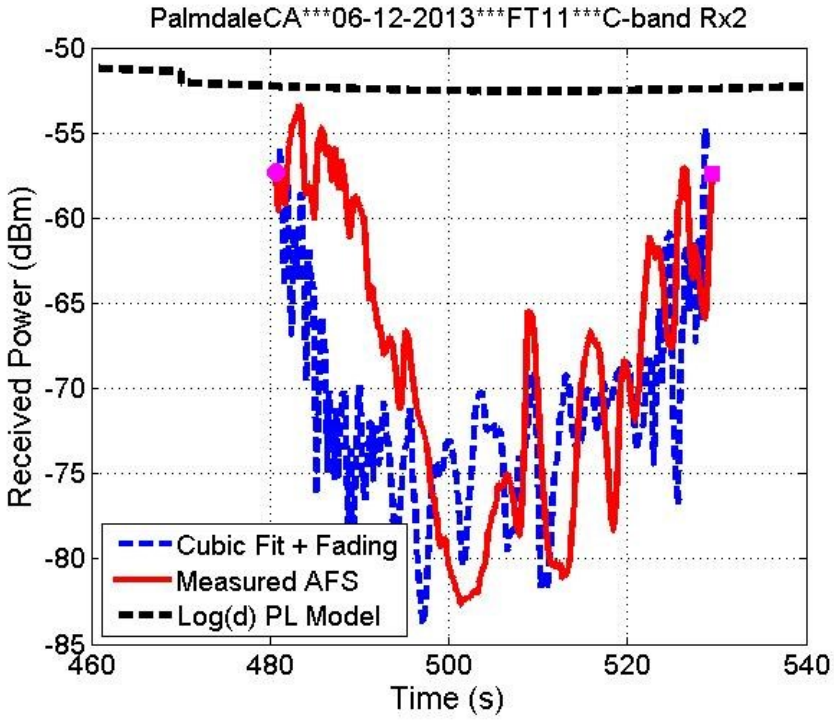

Figure 5.54. Measured & modeled airframe shadowing, Palmdale, CA FT11, C-band Rx2.

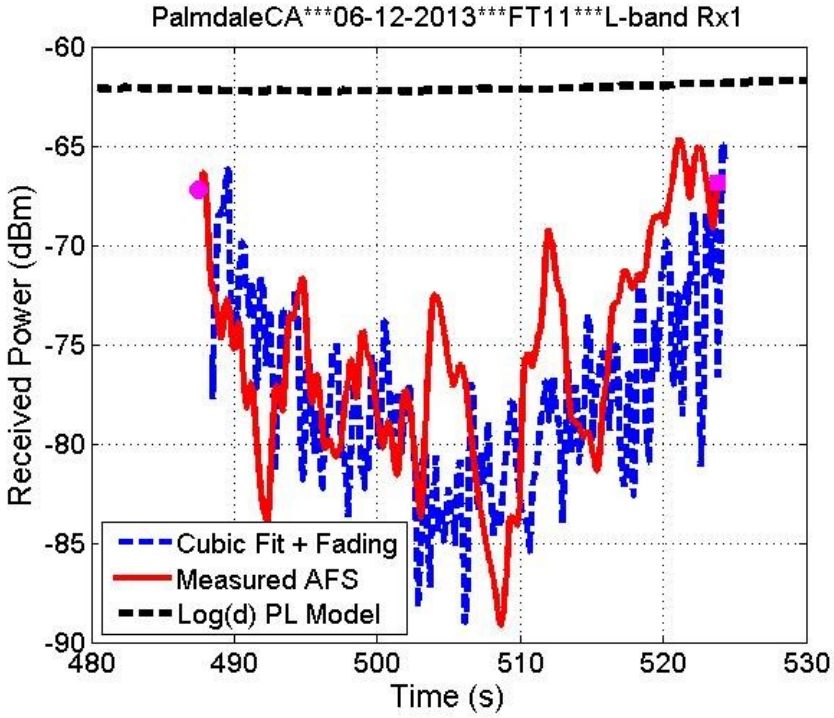

Figure 5.55. Measured & modeled airframe shadowing, Palmdale, CA FT11, L-band Rx1.

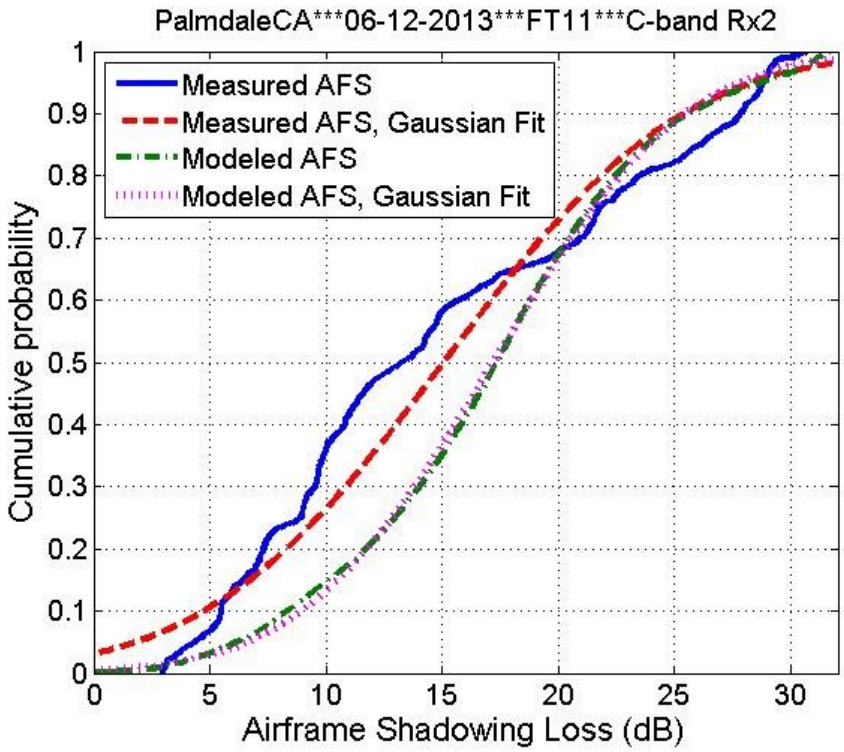

Figure 5.56. CDFs of measured and modeled shadowing loss, Palmdale, CA C-band Rx2.

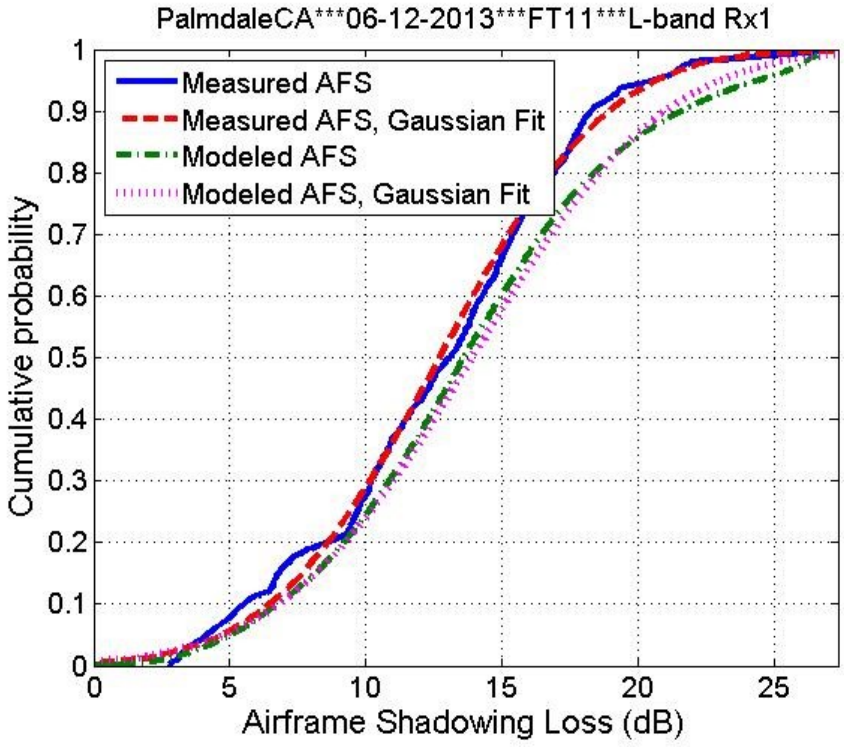

Figure 5.57. CDFs of measured and modeled shadowing loss, Palmdale, CA L-band Rx1.

5.4 SUMMARY

In this chapter, narrowband AG channel models that include large scale path loss, small scale fading and optional airframe shadowing were presented. All these characteristics of AG channels can be combined together with the algorithms and models provided in this chapter. These narrowband models estimate the total attenuation caused by the channel, which is useful to evaluate link budgets and estimate outages (see Figure 1.1), as well as performance of any air-to-ground radio communication system in terms of metrics such as BER, channel capacity, throughput and so on.

Future work for the narrowband AG channel includes

1. Modeling terrain shadowing. Unfortunately, no valid data to quantify terrain shadowing was collected in our measurement campaign. Comparisons with established diffraction models should be done.

2. Modeling building and/or tree shadowing for small UAS. Small UAS can fly at very low altitudes of tens of meters or a few hundred meters above the ground, hence the LOS can be obstructed by large buildings or trees, and this could significantly degrade a radio link. Small UAS less than 55 pounds in weight and flying below 500 ft are not required to use the CNPC link in the United States [115]. Comparison with other obstruction/diffraction results should be done. The building/tree shadowing is also of interest for other applications in other frequency bands, e.g., Wi-Fi and LTE.

CHAPTER 6

WIDEBAND AG CHANNEL MODELS

Wideband models estimate delay dispersion and multipath in radio propagation channels. The term wideband is in contrast to narrowband, where the latter primarily quantifies attenuation in the channels. If the bandwidth of the channel in which the gain is constant and the phase is linear is smaller than the bandwidth of the transmitted signal, frequency selective fading caused by the channels occurs [90]. In this condition, the received signals include multiple copies of the attenuated and delayed transmitted waveform. This kind of distortion induces inter-symbol interference in single-carrier signals, or unequal subcarrier fading on multicarrier signals.

Multiple delay dispersion measures of a wideband channel can be derived from PDPs, including mean excess delay as (3.3), RMS delay spread as (3.2), excess delay spread (X dB), delay window and delay interval. Excess delay is the relative delay between a MPC and the first arrived path (which is the LOS component if it is present). The excess delay, also termed maximum excess delay, is the maximum delay in a PDP at which the power of a MPC is less than X dB below that of the strongest MPC [90]. The delay window W_q is defined as the duration of the middle portion of a PDP that contains q% of the total energy [116]. The delay interval I_p is the delay difference between two points that first rising cross the p dB below the power of the strongest MPC and the point that falling below the p dB threshold [9].

RMS-DS is the most widely used measure, which can be employed to estimate BER [117] and [118] and coherence bandwidth [119] under some assumptions. We report RMS-DS and maximum excess delay for the AG channels. The wideband AG channels are also quantitatively modeled by tapped delay line structures. Only the C-band wideband results are reported since physical MPCs at various delays in C-band are likely to also occur at L-band, at the same delays, albeit with different amplitudes and phases. Moreover, the 200 ns L-band delay resolution is not small enough to identify all MPCs. The L-band TDL models will be created in the near future.

6.1 DELAY DISPERSION

In this section example RMS-DS versus link range, example individual PDPs, and sequences of PDPs and their statistics in the AG channels for multiple GS local environments will be presented. The C-band RMS-DS versus link range for the suburban environment at Latrobe, PA is shown in Figure 6.1 [68], where RMS-DS values are computed for each individual PDP and then moving averaged over window lengths of 100 and 1000 RMS-DS values. The RMS-DS was approximately 10 ns, which is the minimum achievable value for our C-band sounder (see Section 3.4), but with numerous "bumps" up to 85 ns. The sequence of PDPs for the entire FT1 is shown in Figure 6.2, which contains 444,074 PDPs. The LOS component is set to a delay of 100 ns in our post processing. The maximum excess delay is approximately 4 μs. The number of scatterers (MPCs) decreases as the link range increases. The scatterers are only present for a short duration. Two examples of RMS-DS bumps near 5800 m and 9100 m are analyzed in more detail.

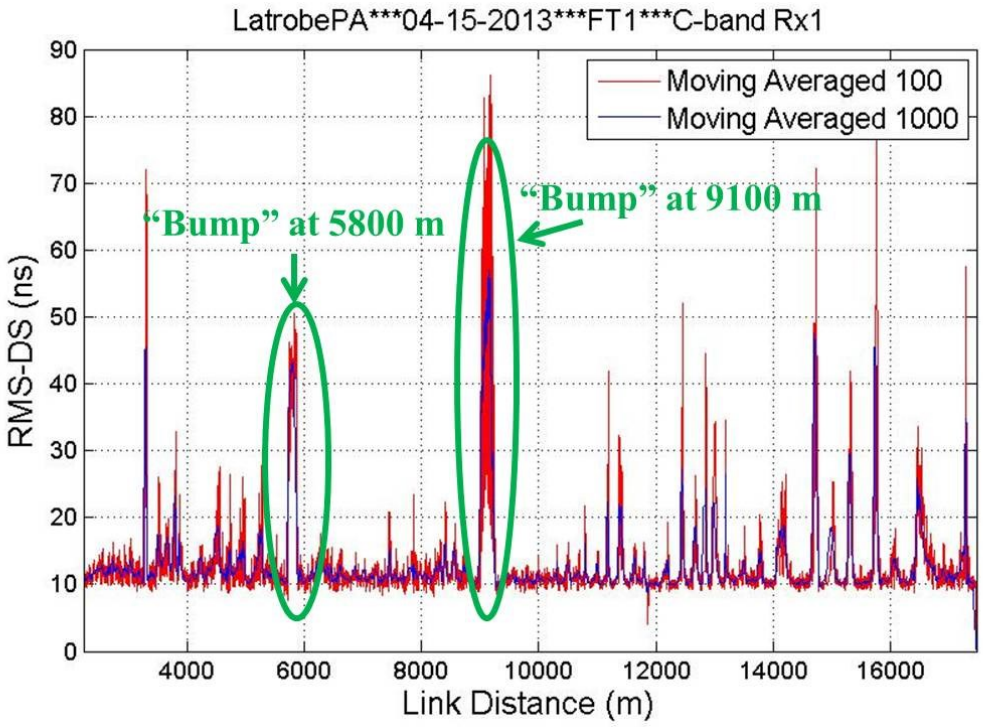

Figure 6.1. RMS-DS for entire FT1 at Latrobe, PA C-band Rx1 [68].

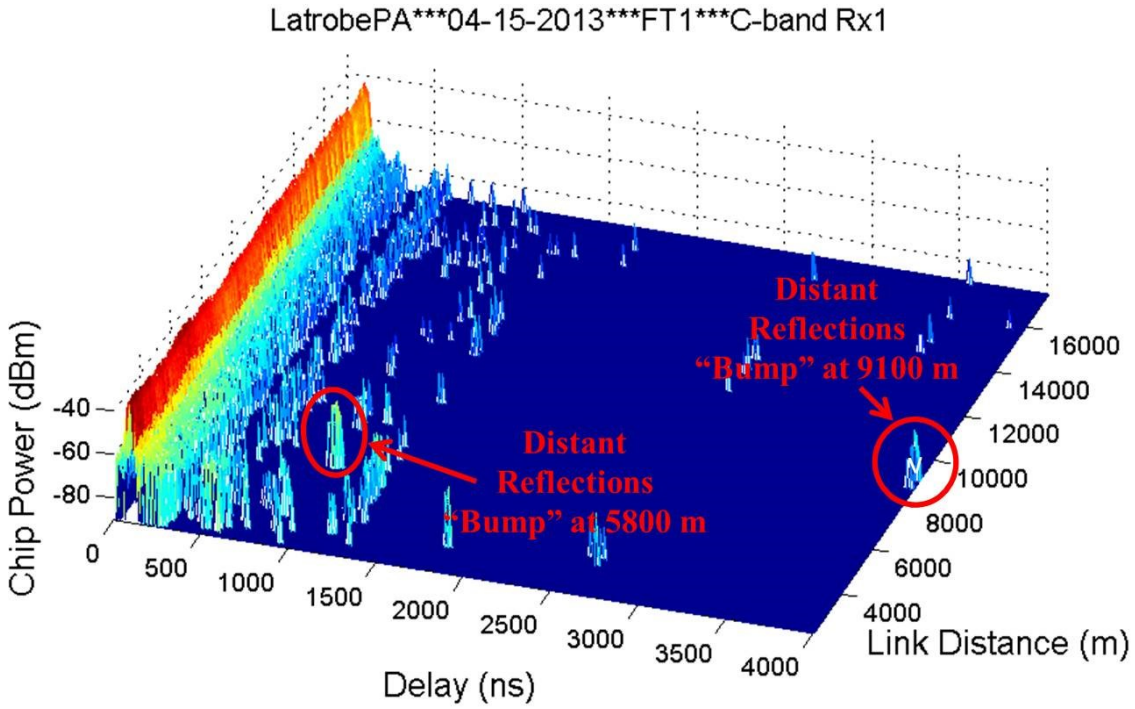

Figure 6.2. Sequence of PDPs for FT1 at Latrobe, PA C-band Rx1 [68].

The instantaneous RMS-DS along with its moving average (window length of 1000) versus link range for a bump near 5800 m is plotted in Figure 6.3. The RMS-DS gradually increases from 10 ns to 50 ns from 5730 m and decreases slowly to 10 ns at 5880 m, with the maximum value in this bump of approximately 70 ns. The corresponding sequence of PDPs is illustrated in Figure 6.4. Some scattered energy is present at delays less than 300 ns and a cluster of MPCs is present near 1 μs, as the red circle in Figure 6.4 indicates. An example individual PDP at 5771.6 m is shown in Figure 6.5. There are numerous scatterers at delays less than 200 ns. The distant reflection is approximately 25 dB weaker than the LOS component. The relative delay of the distant reflection slightly changes over link distance (time) as the aircraft moves. The bump duration is nearly 200 m, and this is related to the size of the scattering object. This cluster of MPCs is likely reflections from large buildings in the Latrobe township.

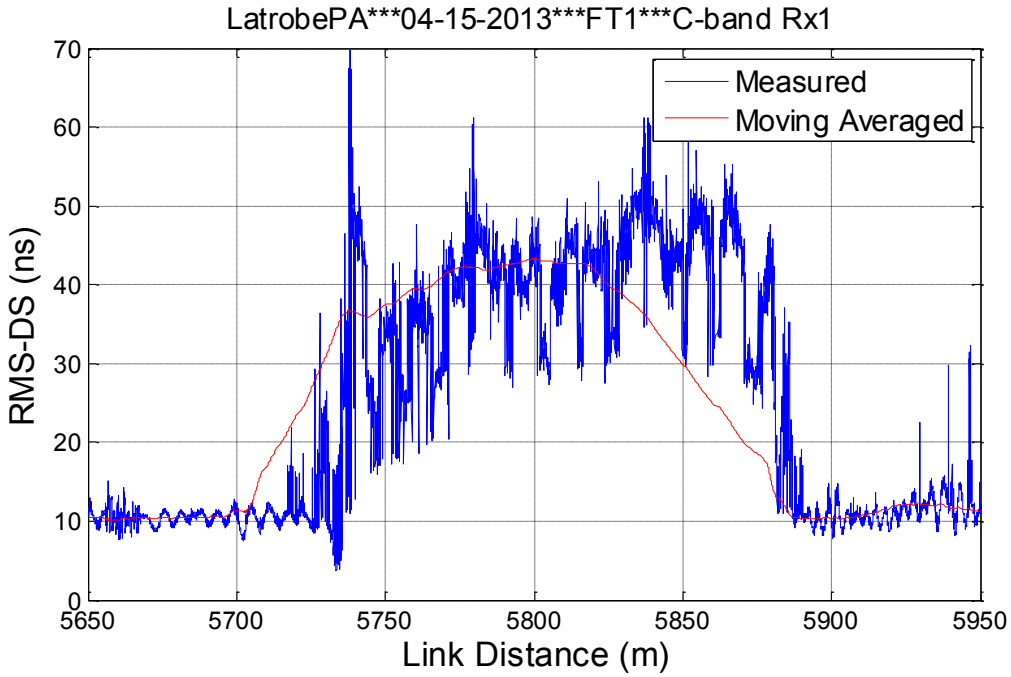

Figure 6.3. RMS-DS vs. link distance for bump near 5800 m in FT1 at Latrobe, PA C-band Rx1 [68].

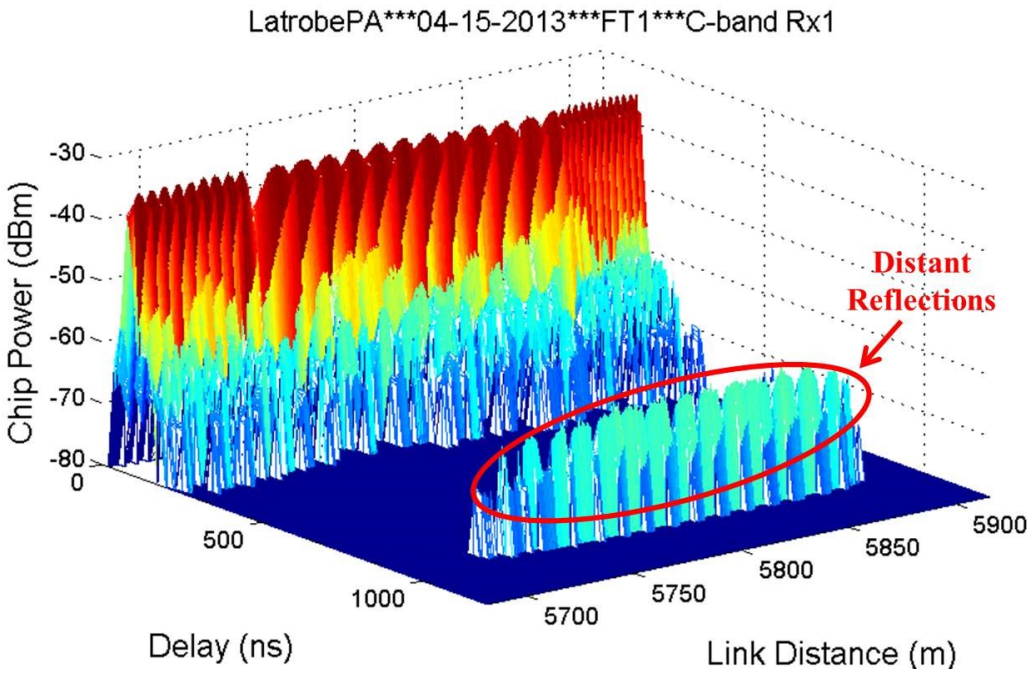

Figure 6.4. Sequence of PDPs for RMS-DS bump near 5800 in FT1 at Latrobe, PA C-band Rx1 [68].

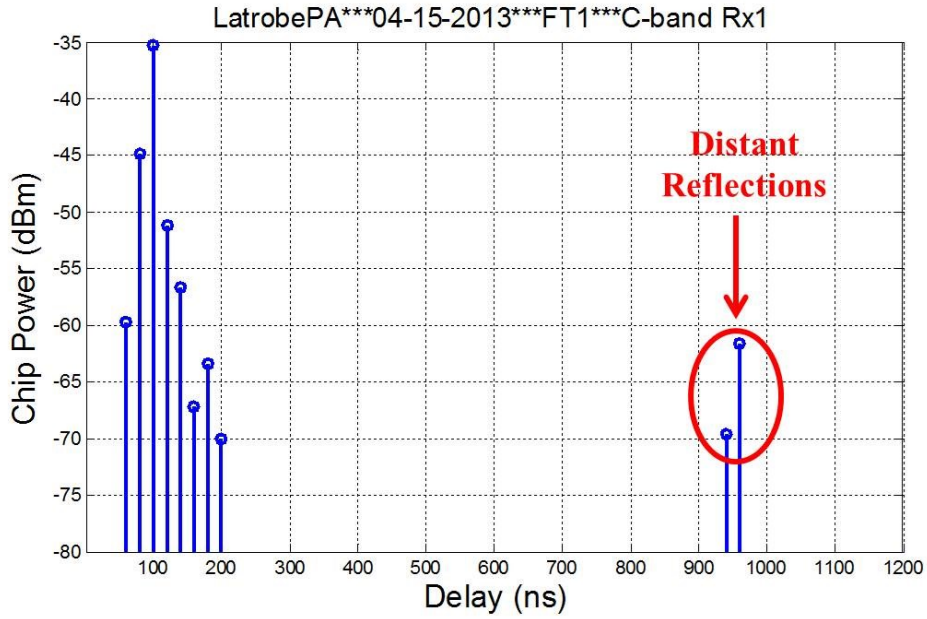

Figure 6.5. Example individual PDP from Figures 6.3 and 6.4 at link distance of 5771.6 m in FT1 at Latrobe, PA C-band Rx1 [68].

Another RMS-DS bump near link distance 9100 m is shown in Figures 6.6 and 6.7 with an example individual PDP at 9098.8 m as plotted in Figure 6.8. This bump

duration is nearly 300 m. A cluster of weak MPCs with delay near 4 μs is present; these are more than 30 dB below the power of the LOS component, and likely emanate from a mountain ridge on the east of the flight route [68].

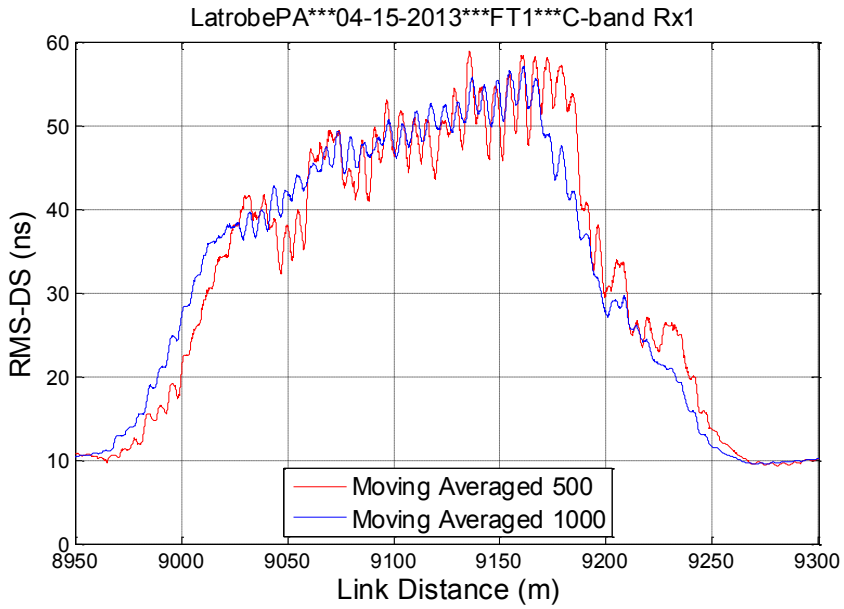

Figure 6.6. RMS-DS vs. link distance for bump near 9100 m in FT1 at Latrobe, PA C-band Rx1 [68].

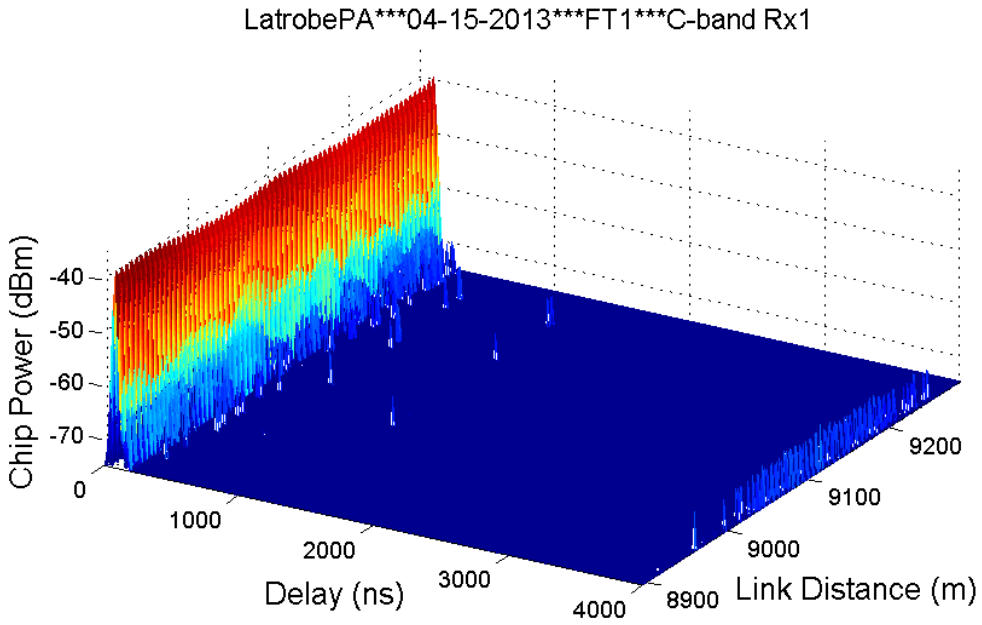

Figure 6.7. Sequence of PDPs for RMS-DS bump near 9100 in FT1 at Latrobe, PA C-band Rx1 [68].

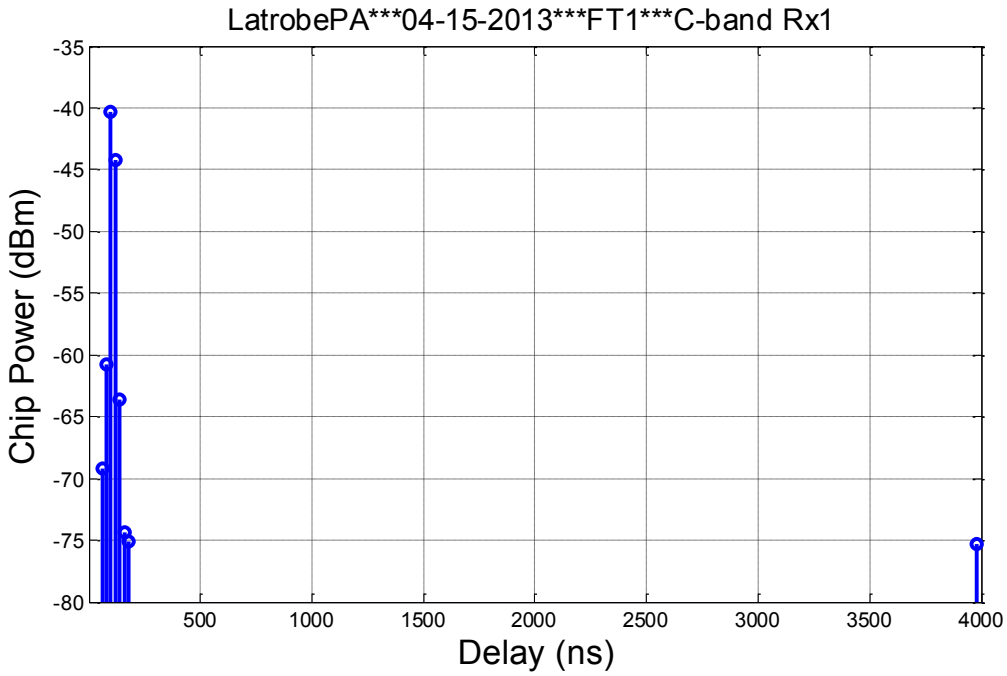

Figure 6.8. Example individual PDP from Figures 6.6 and 6.7 at link distance of 9098.8 m in FT1 at Latrobe, PA C-band Rx1 [68].

An example RMS-DS for over freshwater environment on Lake Erie was analyzed in [61]. The GS location and flight route in ECEF coordinates of an oval shaped FT4 are illustrated in Figure 6.9. The RMS-DS versus time for the entire FT4 is plotted in Figure 6.10. Some large RMS-DS values are present in the middle of the FT when the aircraft was making a "U-turn". This region is indicated by the blue dotted line in Figure 6.9. The sequence of PDPs for this segment is plotted in Figure 6.11. Some MPCs are present with delay between 0.5 and 1 μs. Based on the geometry, the potential reflectors are multiple large buildings, three harbors with boats, water barriers, oil tanks and light houses as indicated in Figure 6.12.

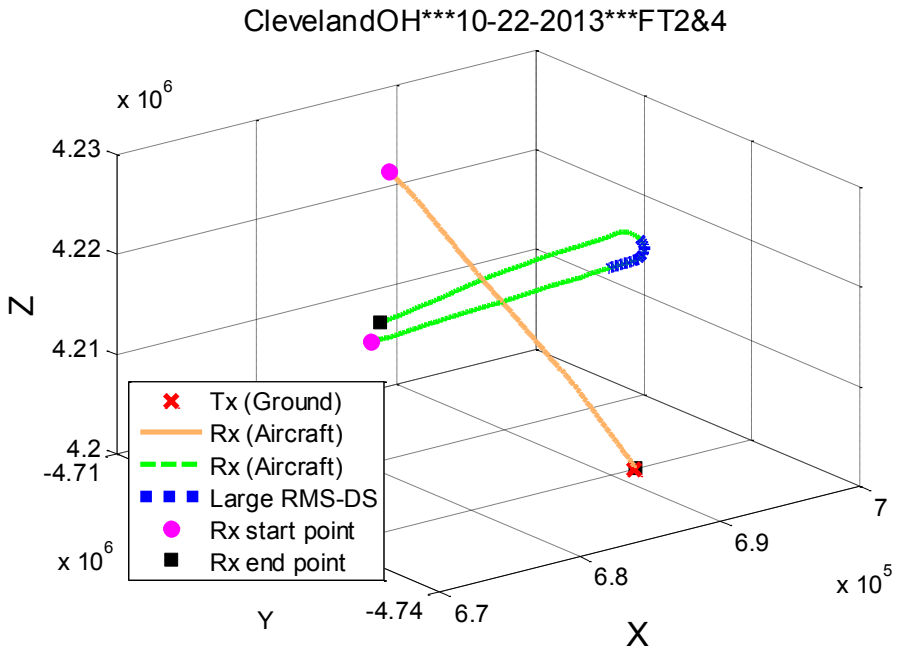

Figure 6.9. GS and flight route in ECEF coordinates for over freshwater environment in Cleveland, OH [61].

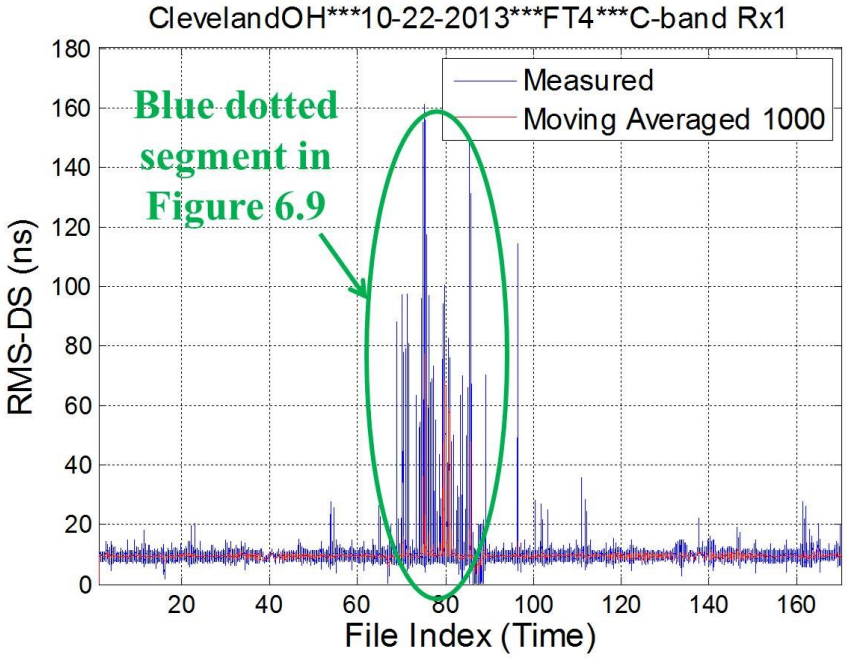

Figure 6.10. RMS-DS vs. time in FT4 for over freshwater environment in Cleveland, OH C-band Rx1 [61].

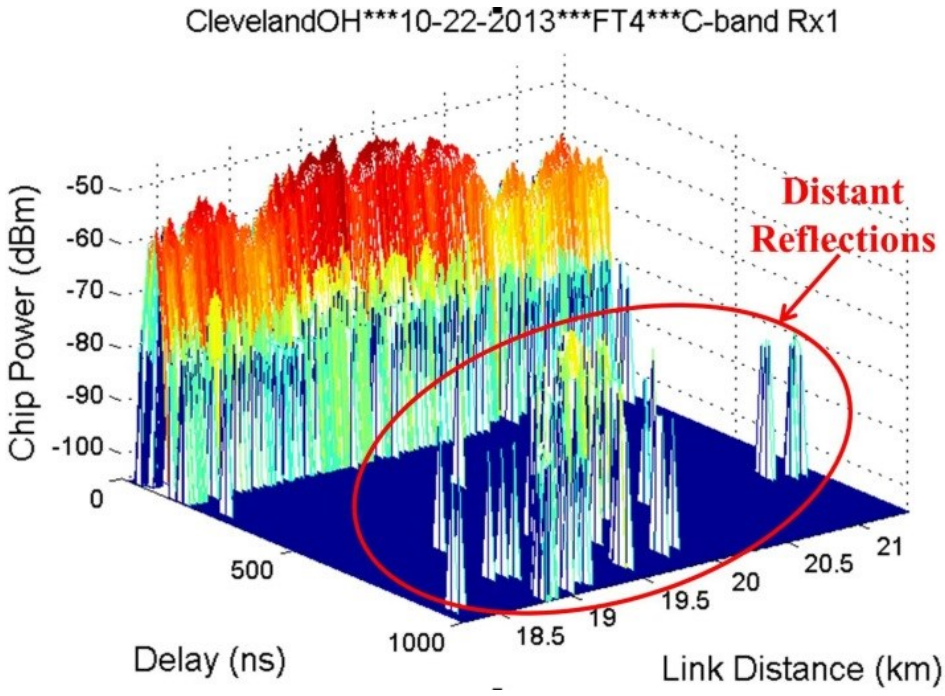

Figure 6.11. Sequence of PDPs in FT4 for over freshwater environment in Cleveland, OH C-band Rx1 [61].

Figure 6.12. Potential reflectors for MPCs in Figure 6.11 in Google Maps® [61].

Figure 6.13 shows the GS location and flight route in Google Earth® of FT3 (green straight line) in the mountainous environment of Telluride, CO [69], where the blue balloon is the GS location. The RMS-DS versus link range for the entire FT3 is plotted in Figure 6.14. The RMS-DS has several bumps near 10 km that reach or exceed 100 ns. An enlarged version of these bumps is plotted in Figure 6.15 and the corresponding sequence of PDPs is shown in Figure 6.16. The diffuse components can be divided into two clusters. Cluster #1 is the set of rich scatterers with delays less than 0.5 μs and cluster #2 is the set of MPCs with delays near 1 μs. Potential reflectors for these two clusters of MPCs are hills #1 and #2 indicated in Figure 6.13.

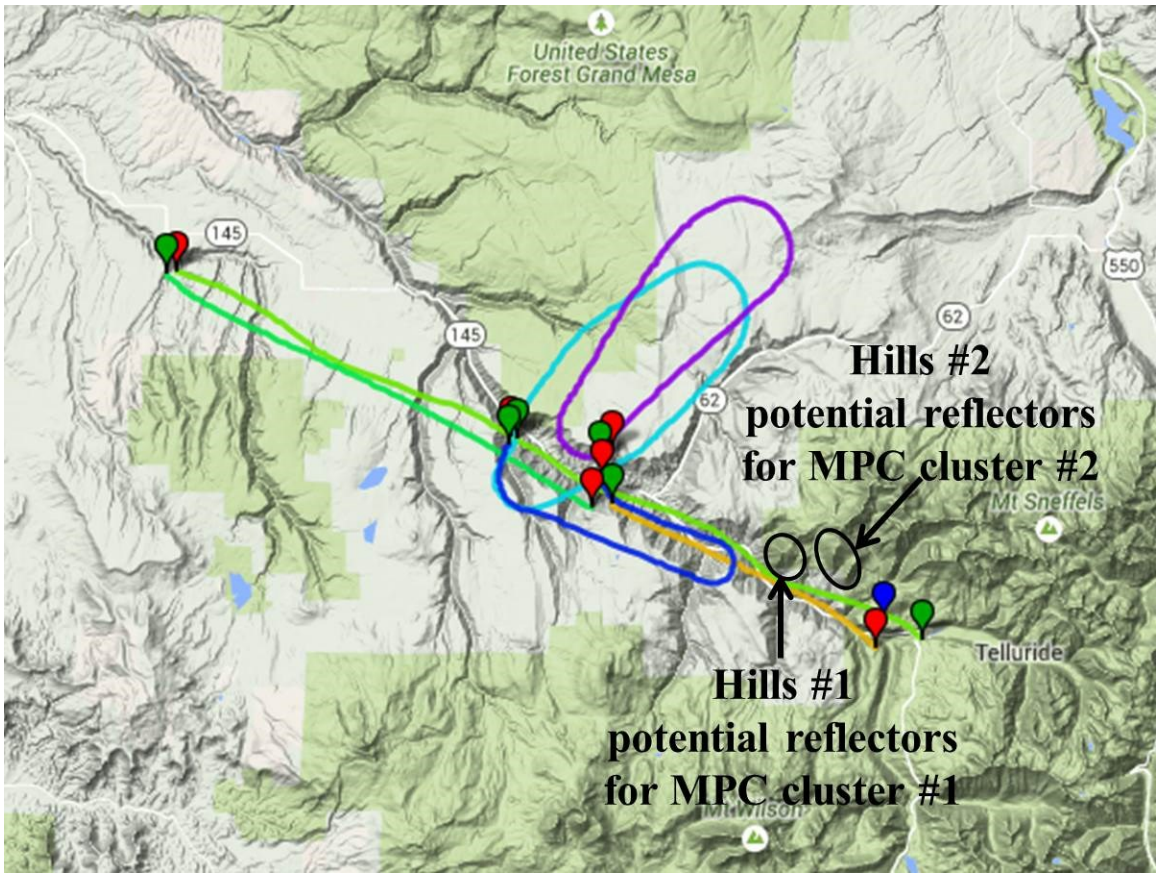

Figure 6.13. GS and flight route in Google Earth® for mountainous environment in Telluride, CO [69].

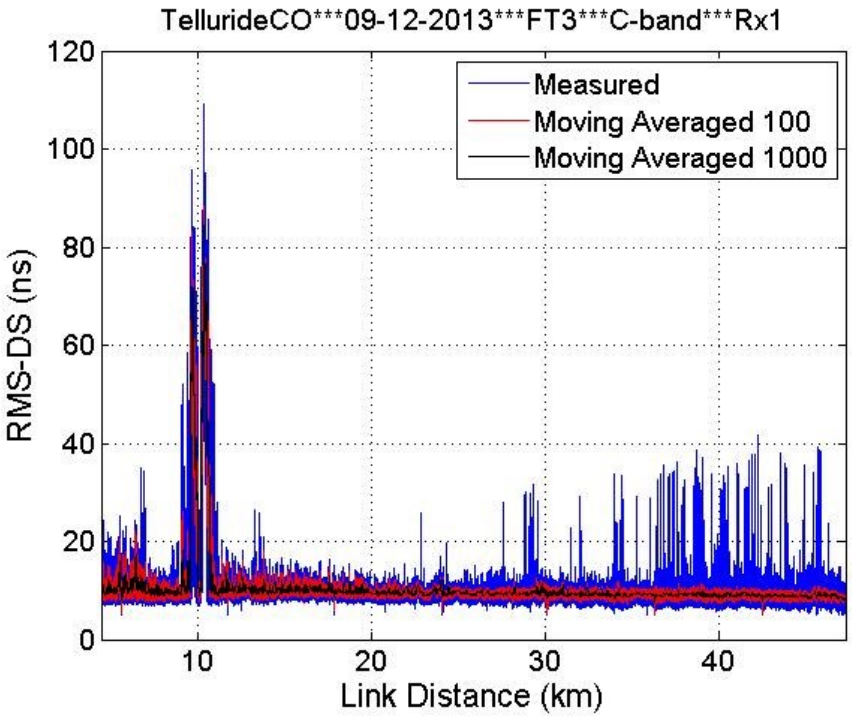

Figure 6.14. RMS-DS vs. link distance for entire FT3 at Telluride, CO C-band Rx1 [69].

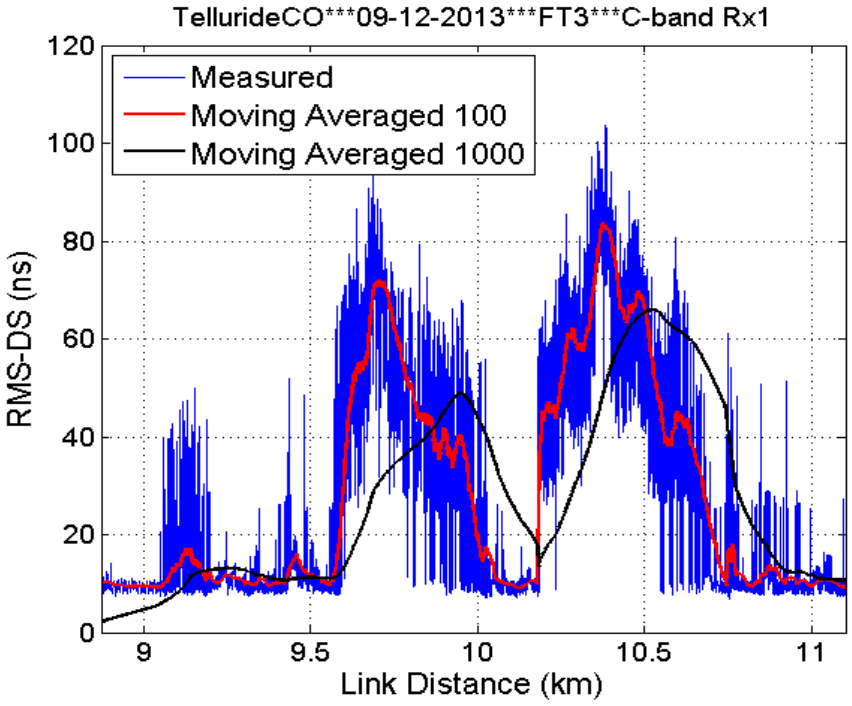

Figure 6.15. RMS-DS vs. link distance for the bumps near 10 km in FT3 at Telluride, CO C-band Rx1 [69].

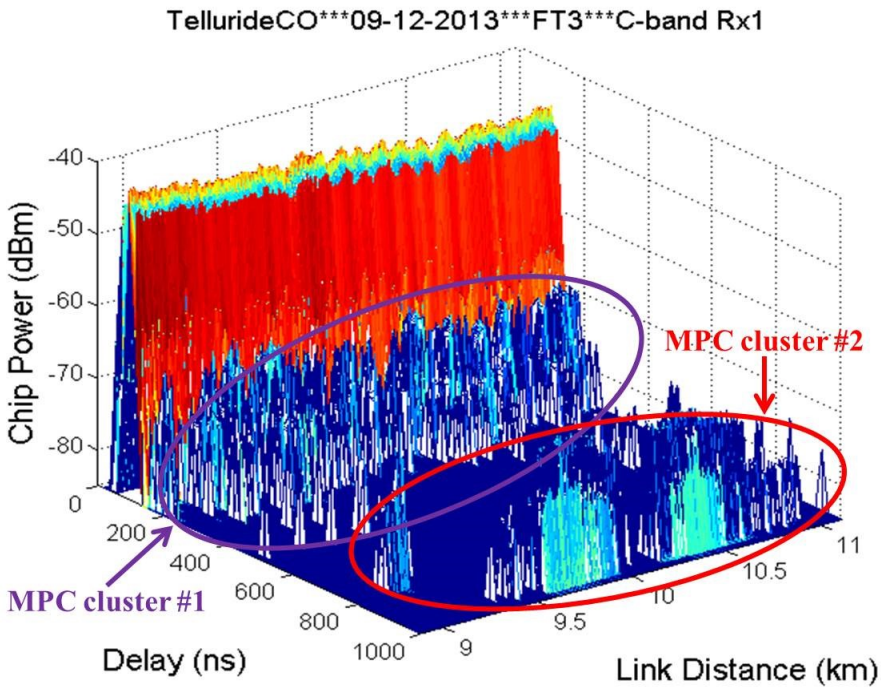

Figure 6.16. Sequence of PDPs for the RMS-DS bump in FT3 at Telluride, CO C-band Rx1 [69].

RMS-DS results for multiple straight FTs and for two C-band Rxs were combined together, for the over-water settings. The aggregate RMS-DS versus link range for over sea and freshwater environments are shown in Figures 6.17 and 6.18. The over water cases are relatively clean. The over sea RMS-DS bump near 5 km is likely due to reflections from some large oil tanks near the coast line on the northeast of the GS. The over freshwater bumps are likely reflections from buildings, water barriers and harbors on the ground (see Figure 6.12). Statistics of RMS-DS are provided in Table 6.1. Note that in Figures 6.17 and 6.18, some zero RMS-DS values appear at large distances, where the received power values are relatively low. Due to the filtering effect inside out receivers (see Section 3.4), the MPCs (due to the filtering effect) near the strongest one were below the noise threshold. They are removed in our post processing hence the RMS-DS values are small.

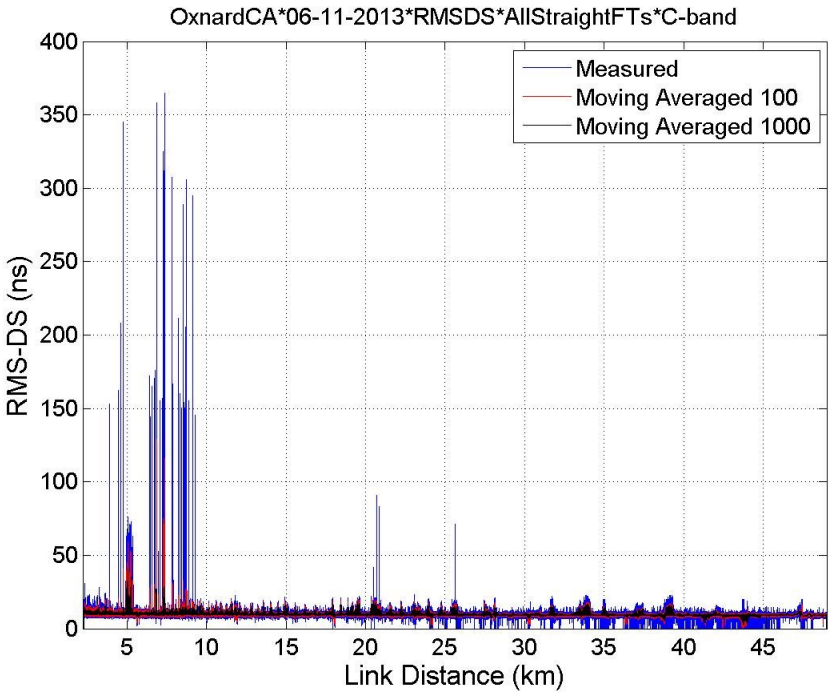

Figure 6.17. Aggregate C-band RMS-DS vs. link distance for over sea environment taken in Oxnard, CA on June 11th 2013.

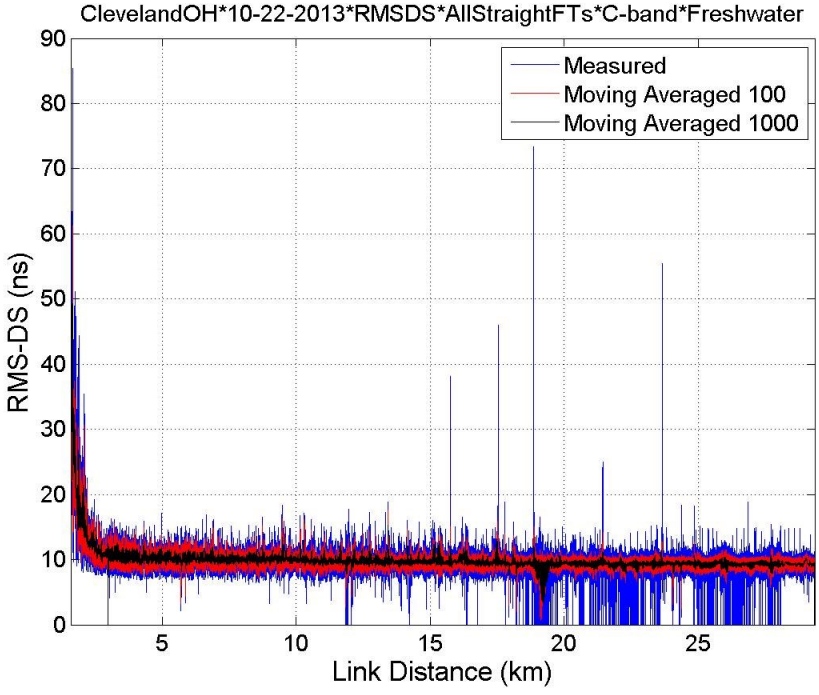

Figure 6.18. Aggregate C-band RMS-DS vs. link distance for over freshwater environment taken in Cleveland, OH on September 22nd 2013.

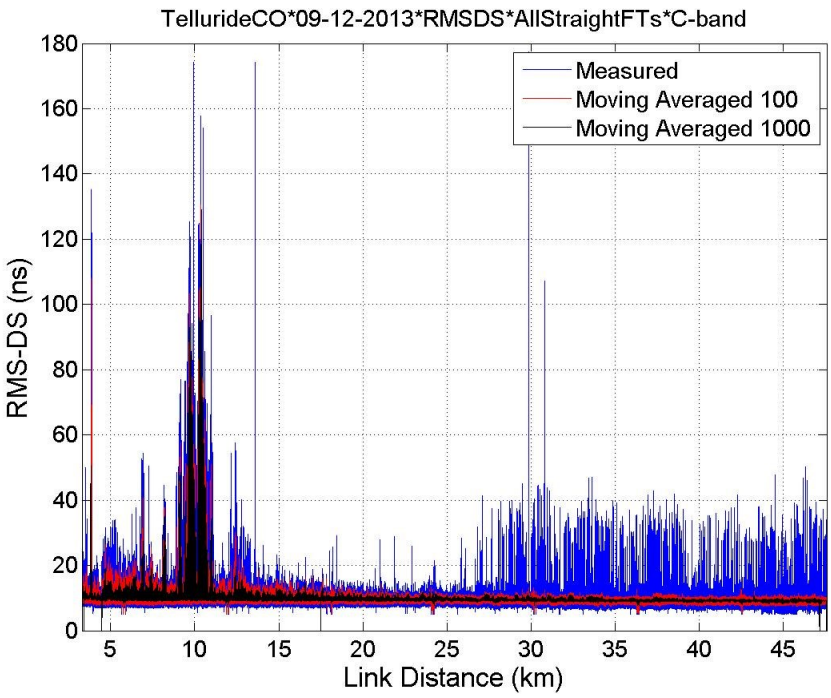

Figure 6.19. Aggregate C-band RMS-DS vs. link distance for mountainous environment taken in Telluride, CO on September 12th 2013.

The aggregate RMS-DS for mountainous and hilly environments taken in Telluride, Latrobe and Palmdale are shown in Figures 6.19 to 6.21, respectively. The mountainous RMS-DS results have some large bumps at link distances less than 15 km. They are likely reflections from mountainous ridges with bare rocks, as analyzed in Figures 6.13 to 6.16.

For two hilly environments shown in Figures 6.20 and 6.21, the GS locations were near townships, and hence reflections were present for nearly the entire range of distances. The hills in Latrobe are unlikely to provide strong reflections since they are covered by vegetation, but the hills can provide stronger reflections for the Palmdale data since the hillsides are uncovered in this area near the Mojave Desert.

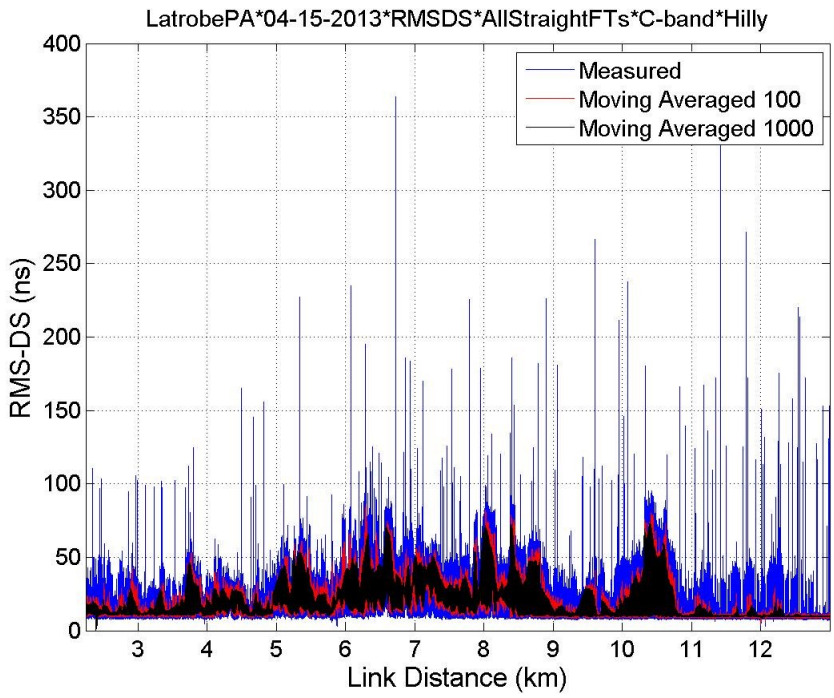

Figure 6.20. Aggregate C-band RMS-DS vs. link distance for hilly environment taken in Latrobe, PA on April 15th 2013.

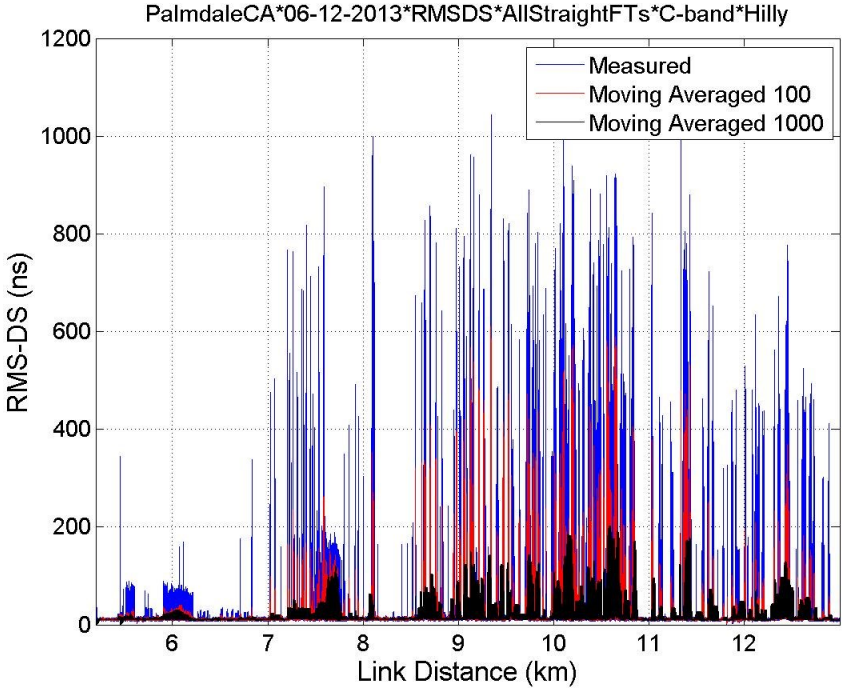

Figure 6.21. Aggregate C-band RMS-DS vs. link distance for hilly environment taken in Palmdale, CA on June 12th 2013.

Table 6.1. Statistics of RMS-DS of selected FTs for over sea, freshwater, mountainous and hilly environments.

	Setting	*Over Sea*	*Over Freshwater*	*Mountainous*	*Hilly*	
Aggregate RMS-DS for multiple environments	**Location**	Oxnard, CA	Cleveland, OH	Telluride, CO	Latrobe, PA	Palmdale, CA
	Date	6/11/2013	10/22/2013	9/12/2013	4/15/2013	6/12/2013
	FT Index	1,2,3,8,9,10	2 & 3	2,3,4,8,9	8 & 9	6,7,8,9
	h_{AC}-h_{GS}(m)	766-779	559-562	1160-1588	788-790	1903-1906
	# of PDPs	12,297,449	4,036,787	10,049,502	1,182,234	1,783,603
	d_{min}(km)	2.23	1.58	3.34	2.24	5.19
	d_{max}(km)	48.99	29.35	47.59	13.00	13.00
Instantaneous RMS-DS (ns)	**Mean**	9.8	9.9	10.1	17.8	19.3
	Median	9.8	9.9	9.8	11.3	11.7
	Max	364.7	85.4	177.4	371.3	1044.3
	Standard deviation	2.0	1.9	4.4	12.5	51.1
Moving Averaged over 100 PDPs	**Mean**	9.8	9.9	10.1	17.8	19.3
	Median	9.7	9.8	9.7	12.1	11.7
	Max	129.3	61.2	130.5	86.2	609.1
	Standard deviation	1.5	1.7	4.2	11.7	40.1
Moving Averaged over 1000 PDPs	**Mean**	9.8	9.9	10.1	17.7	19.3
	Median	9.6	9.7	9.5	12.4	11.8
	Max	40.9	49.3	118.6	73.2	202.5
	Standard deviation	1.2	1.5	4.1	11.2	22.3

The aggregate C-band RMS-DS versus link range for desert (Palmdale, CA June 12th 2013), suburban (Latrobe, PA April 15th 2013 and Cleveland, OH September 5th 2013) and near-urban (Cleveland, OH October 22nd 2013) environments are shown in Figures 6.22 to 6.25, respectively. Their statistics are listed in Table 6.2. Since numerous buildings were near the GS for this set of Palmdale data, and these could be potential reflectors, the RMS-DS for the desert environment has large values that are maintained for long durations. This is also true for the suburban environment in Latrobe since the aircraft flew over the township.

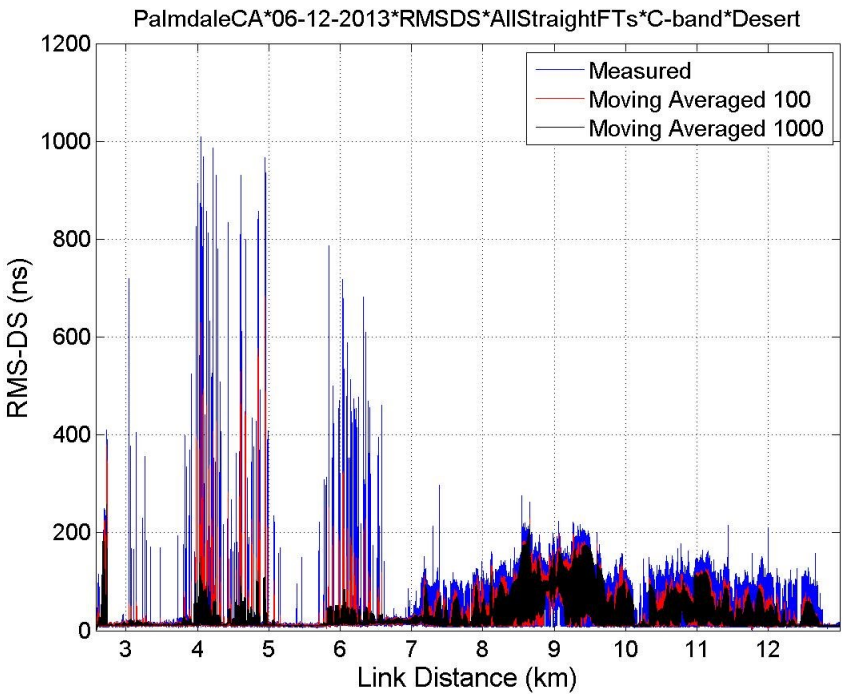

Figure 6.22. Aggregate C-band RMS-DS vs. link distance for desert environment taken in Palmdale, CA on June 12th 2013.

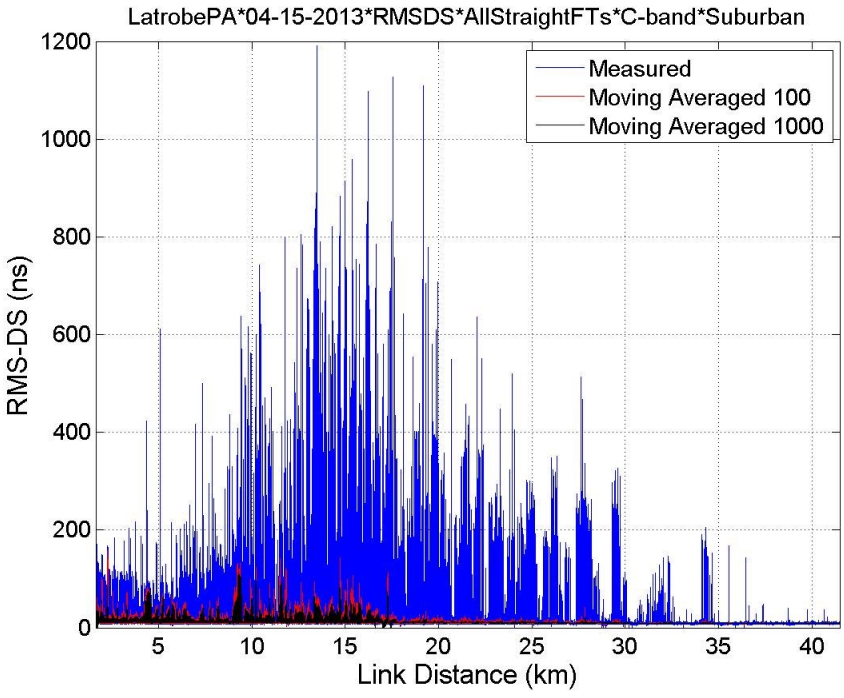

Figure 6.23. Aggregate C-band RMS-DS vs. link distance for suburban environment taken in Latrobe, PA on April 15th 2013.

The RMS-DS for the suburban environment in Cleveland does not have too many bumps since trees and other vegetation are predominant in the area beneath the flight route near the GS, and this serves to attenuate reflections. However, some bumps are still present due to some large exposed buildings.

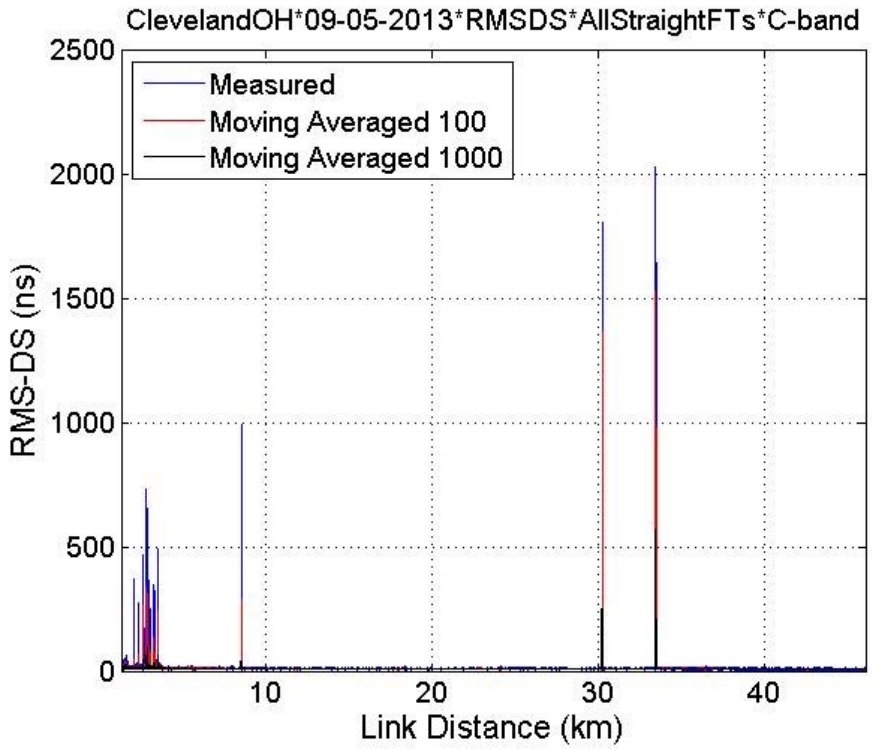

Figure 6.24. Aggregate C-band RMS-DS vs. link distance for suburban environment taken in Cleveland, OH on September 5th 2013.

As expected, the RMS-DS for the near urban environment has numerous bumps since the building density and height are both large in this area. The bumps are present for all distances. CDF of RMS-DS for the near urban environment is shown in Figure 6.26.

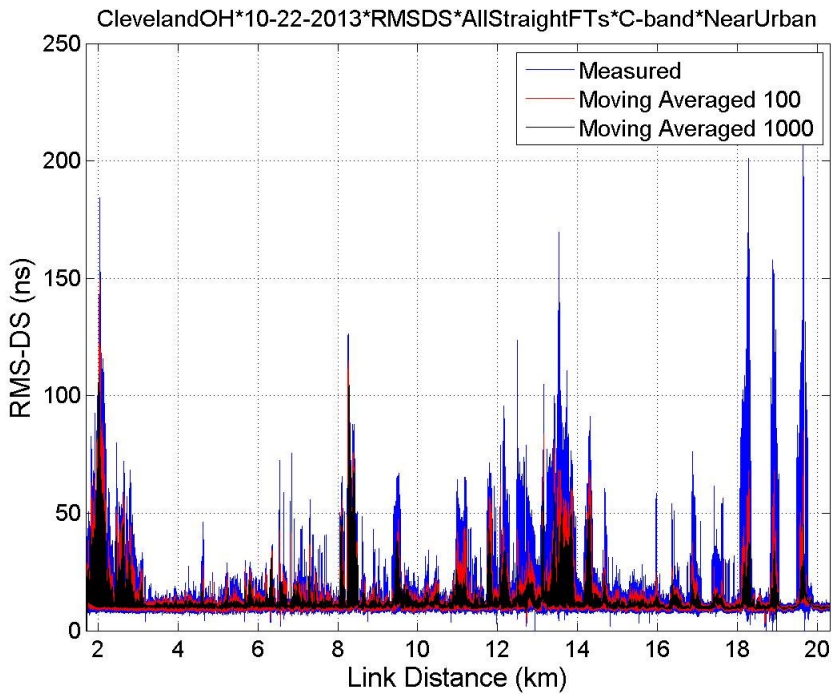

Figure 6.25. Aggregate C-band RMS-DS vs. link distance for near-urban environment taken in Cleveland, OH on October 22nd 2013.

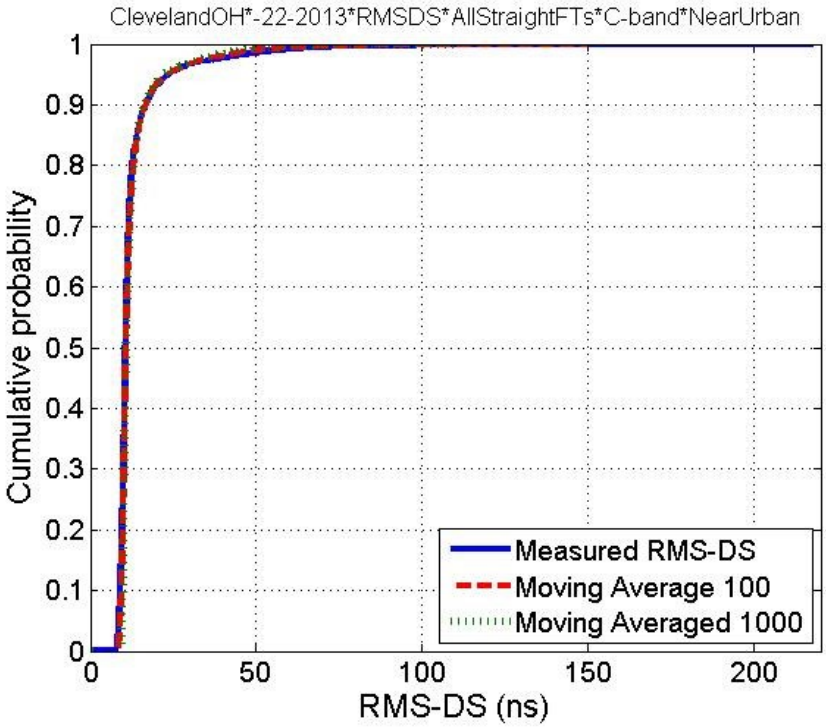

Figure 6.26. CDF of aggregate C-band RMS-DS for near-urban environment taken in Cleveland, OH on October 22nd 2013.

Table 6.2. Statistics of RMS-DS of selected FTs for desert, suburban and near-urban environments.

	Setting	*Desert*	*Suburban*	*Suburban*	*Near-Urban*
Aggregate RMS-DS for multiple environments	**Location**	Palmdale, CA	Latrobe, PA	Cleveland, OH	Cleveland, OH
	Date	6/12/2013	4/15/2013	9/5/2013	10/22/2013
	FT Index	1,2,3	1,2,3,4,5	1,2,3,6	5,6
	h_{AC}-h_{GS}(m)	892-917	598-601	491-518	535-539
	# of PDPs	1,232,379	3,476,494	8,135,292	2,756,131
	d_{min}(km)	2.58	1.64	1.38	1.69
	d_{max}(km)	13.00	41.49	46.02	20.31
Instantaneous RMS-DS (ns)	**Mean**	29.5	13.9	9.9	12.8
	Median	11.8	11.0	9.6	10.6
	Max	1009.1	1190.8	2029.5	217.5
	Standard deviation	44.0	13.6	17.4	8.5
Moving Averaged over 100 PDPs	**Mean**	29.5	13.9	9.9	12.8
	Median	12.7	11.4	9.5	10.7
	Max	684.1	157.8	1528.8	149.3
	Standard deviation	38.5	8.3	15.2	7.5
Moving Averaged over 1000 PDPs	**Mean**	29.5	13.8	9.9	12.8
	Median	13.9	11.6	9.4	10.8
	Max	258.1	113.1	568.5	109.6
	Standard deviation	32.6	7.2	8.9	6.9

6.2 TAPPED DELAY LINE MODELS

Since the MPCs are sparse for the AG channel and scatterers are only present for a short duration, we employ a tapped delay line model which is composed of

1. the LOS component,

2. the earth surface reflection (for over water and some flat terrains for which the ground is flat within Q m from the GS based on the criterion in (5.6)—the earth surface reflection is not present for mountainous and near urban environments), and

3. intermittent MPCs.

For the over water AG channel, the intermittent MPCs are the 3rd ray only due to the sparsity of diffuse components. The intermittent MPCs for other environments may extend to 4th or 5th or even larger numbers of rays. These will be addressed in journal

papers in the near future. In this section, our TDL models will focus on the intermittent 3rd ray for the over water environments. The three ray TDL model is illustrated in Figure 6.27 and the CIR follows [58],

$$h(\tau,t) = h_{CE2R,F}(\tau,t) + z_3(t)\alpha_3(t)e^{-j\phi_3(t)}\delta(\tau-\tau_3(t)), \quad (6.1)$$

where the first term $h_{CE2R,F}(\tau,t)$ denotes the CE2R model for frequency F; $z_3(t)\in\{0,1\}$ denotes a presence/absence (birth/death or on/off) parameter for the intermittent 3rd ray; $\alpha_3(t)$ and $\phi_3(t)$ are the amplitude and phase of the 3rd ray, respectively; $\tau_3(t)$ denotes excess delay of the intermittent 3rd ray.

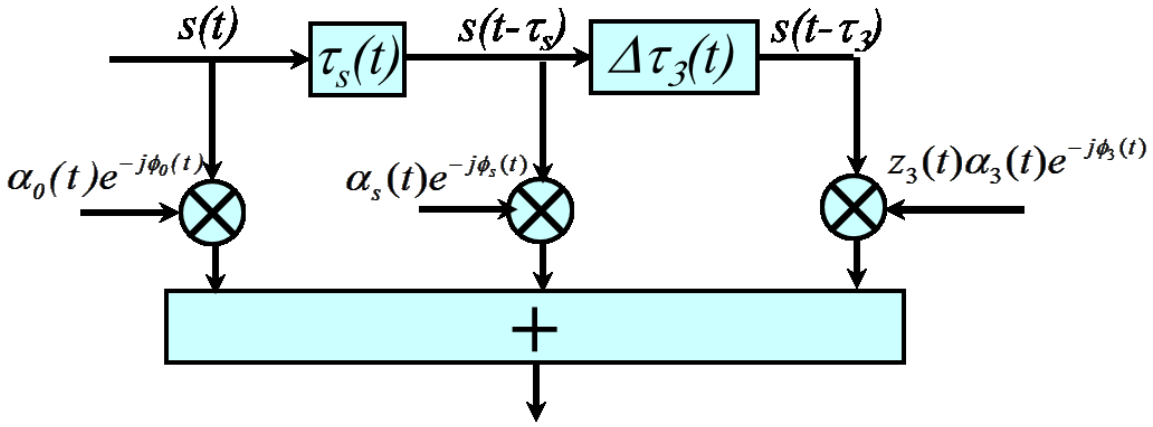

Figure 6.27. Tapped delay line model [58].

For the intermittent 3rd ray, statistical models are provided for the probability of occurrence, duration D_3, excess delay, and relative power with respect to power of the LOS component. All these parameters are expressed as functions of link range. The link range can be converted to time by flight velocity and direction as desired. Exponential fits based on least squares criteria are employed to model these parameters, which yields

$$p(R) = ae^{bR}, \quad (6.2)$$

where *p(R)* denotes any one of the three parameters: the 3rd ray occurrence probability (dimensionless between 0 and 1), the duration in meters, or the excess delay in nanoseconds, as a function of link range *R* in km; *a* and *b* are parameters that control the exponential fits.

The intermittent 3rd ray occurrence probability as a function of link range, along with the exponential fits for the over sea and freshwater environments are shown in Figures 6.28 and 6.29. The duration vs. link range is shown in Figures 6.30 and 6.31. The exponential fits parameters are listed in Table 6.3, where the root mean square deviations (RMSE) of the fits are also provided.

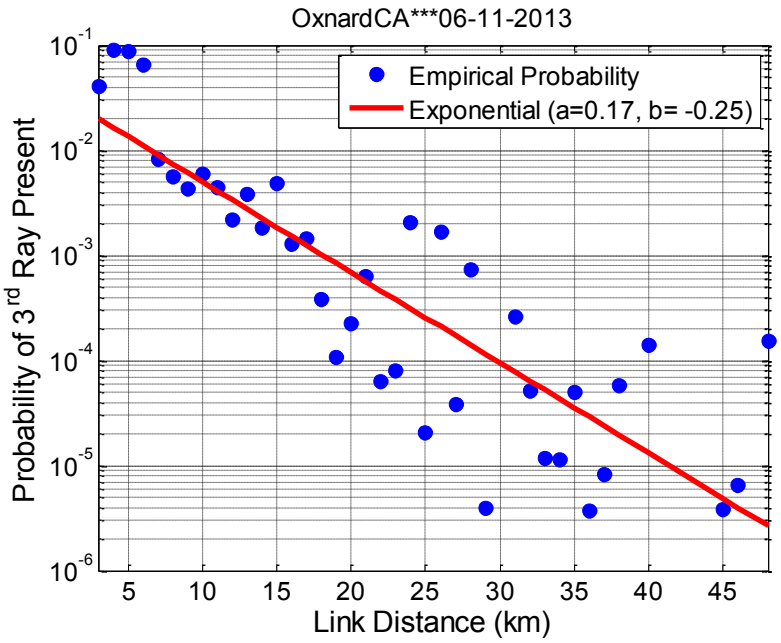

Figure 6.28. Intermittent 3rd ray fractional on probability vs. link range for over sea environment [58].

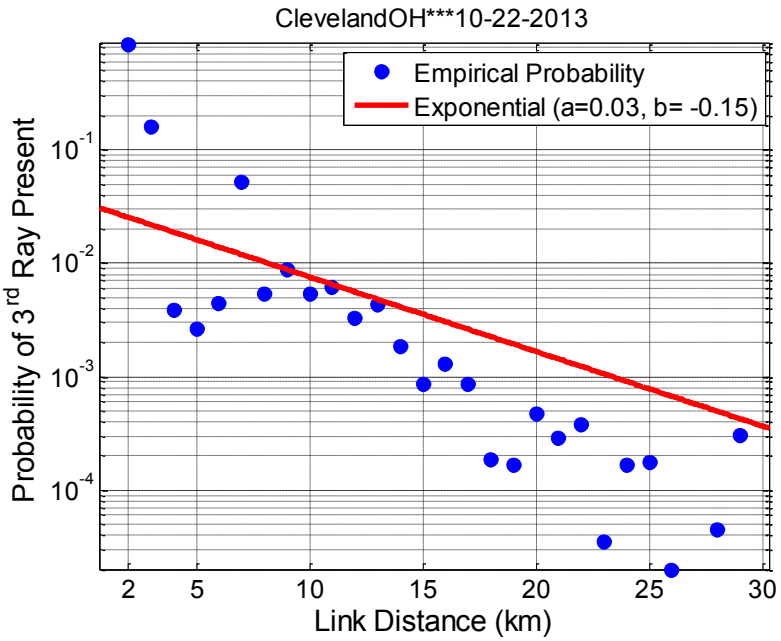

Figure 6.29. Intermittent 3rd ray fractional on probability vs. link range for over freshwater environment [58].

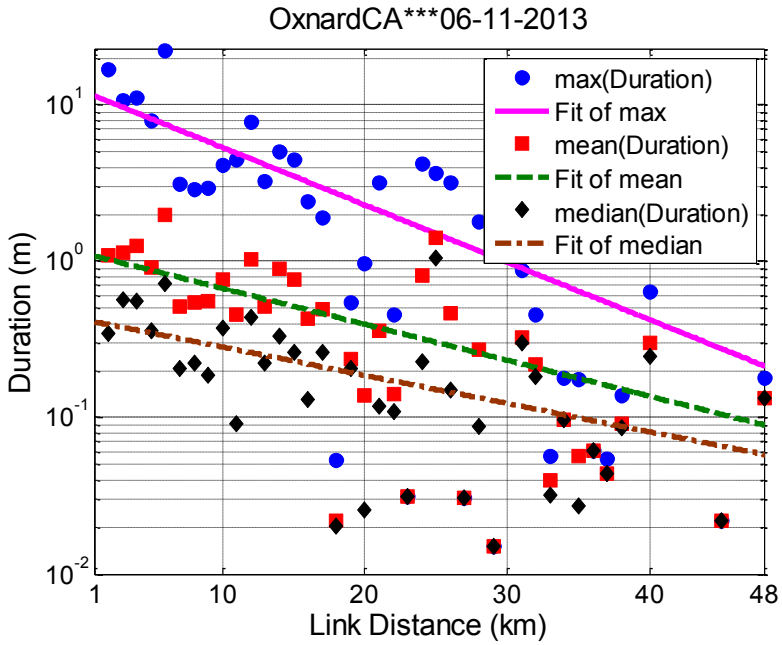

Figure 6.30. Intermittent 3rd ray duration vs. link range for over sea environment [58].

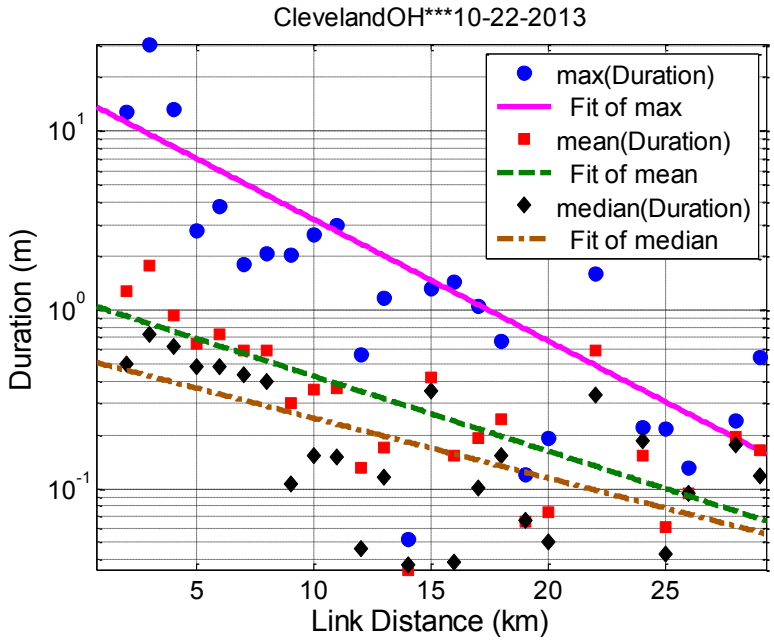

Figure 6.31. Intermittent 3rd ray duration vs. link range for over freshwater environment [58].

The relative power of the intermittent 3rd ray is well modeled by a Gaussian distribution with mean μ_3 dB smaller than the power of the LOS component and standard deviation σ_3 dB. The over freshwater environment yields μ_3=23.3, σ_3=3.9, and the over sea environment yields μ_3=22.6, σ_3=5.2. The phase of the intermittent 3rd ray ϕ_3 is uniformly distributed between 0 and 2π.

The excess delay of the intermittent 3rd ray versus link range is shown in Figures 6.32 and 6.33. The excess delays for the over sea environment are classified into two sets: (1) 6 μs ≤ τ_3 ≤7 μs (not shown in Figure 6.32) with probability of 0.0077; and (2) 0.1 μs ≤ τ_3 ≤1.1 μs with probability of 0.9923. The excess delay for the over freshwater environment ranges between 0.1 and 0.9 μs. The excess delay can be well fitted by any standard distribution, yet for convenience exponential fits for the over freshwater case and the (2) subset for the over sea case are listed in Table 6.3. Delays in the subset (1) for the over sea case are modeled by a uniform distribution.

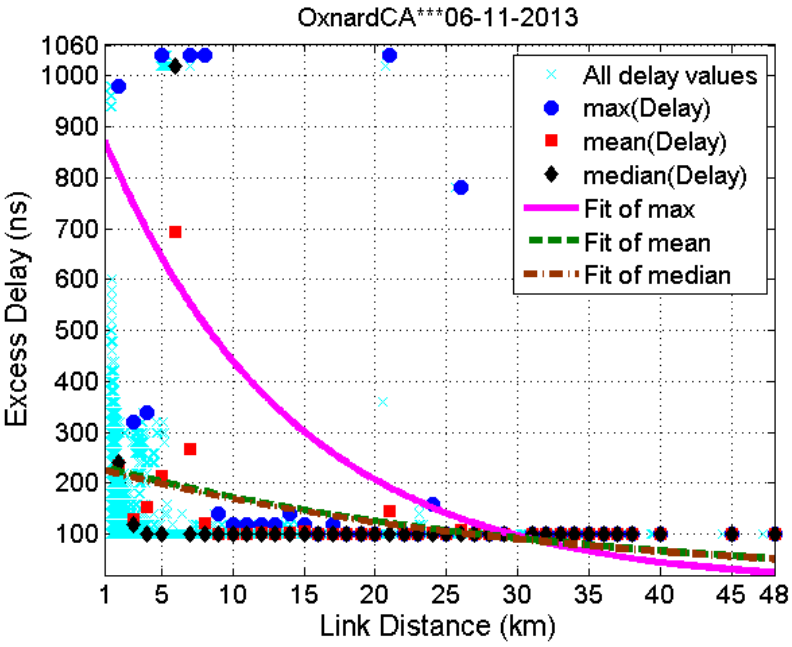

Figure 6.32. Intermittent 3rd ray excess delay vs. link range for over sea environment [58].

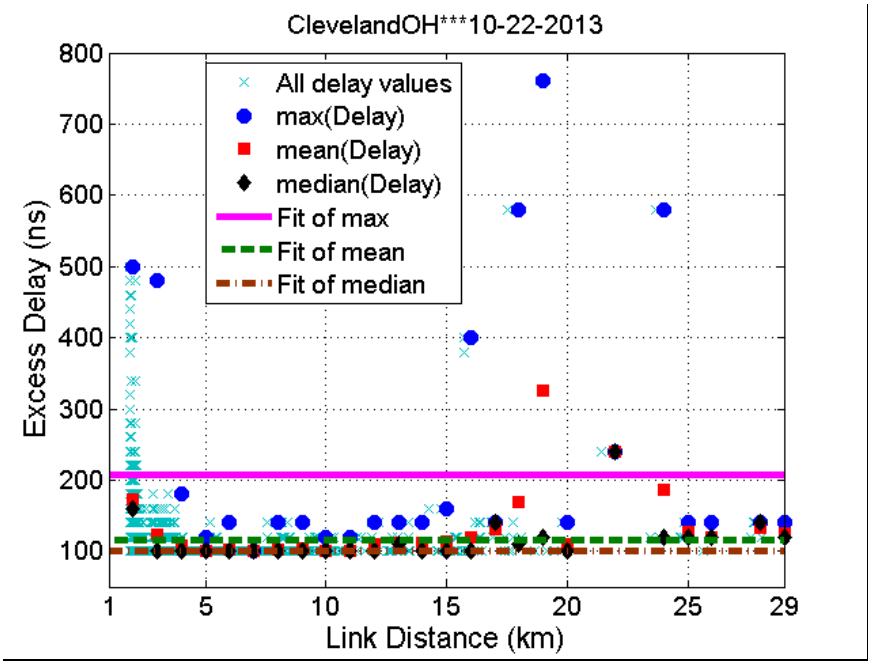

Figure 6.33. Intermittent 3rd ray excess delay vs. link range for over freshwater environment [58].

Table 6.3. Exponential fit parameters for intermittent 3rd ray fractional on probability, duration and excess delay vs. link range [58].

			a	***b***	**RMSE**
Over Sea Oxnard, CA	*On Probability*		0.1672	-0.2474	0.0125
	Duration	Max	12.49	-0.0847	3.254
		Mean	1.141	-0.053	0.3456
		Median	0.4294	-0.0417	0.1854
	Excess Delay	Max	940.4	-0.0759	284.1
		Mean	237.3	-0.0315	91.39
		Median	231.4	-0.0314	144.2
Over Fresh Water Cleveland, OH	*On Probability*		0.0345	-0.1515	0.009
	Duration	Max	15.42	-0.1568	5.063
		Mean	1.122	-0.0967	0.3106
		Median	0.5382	-0.0773	0.1635
	Excess Delay	Max	228	0.0037	191.5
		Mean	108.2	0.0144	50.54
		Median	98.53	0.011	29.25

To implement the TDL model as a function of link range, the following algorithm is provided [58]:

1. For a given value of link range R, implement the CE2R provided in the Section 4.2.

2. From a distribution specified by Figures 6.28 and 6.29 and Table 6.3, generate random variable z_3. If z_3=0, 3rd ray not present, so go to step 1 and increment/change link range R; if z_3=1, go to step 3.

3. From a distribution specified by Figures 6.30 and 6.31 and Table 6.3, generate the 3rd ray's duration D_3. (If needed, convert duration in meters to time or symbol units.)

4. Draw Gaussian random variable with mean μ_3, standard deviation σ_3, to set 3rd ray relative amplitude. Select the 3rd ray phase from a uniform distribution on [0, 2π).

5. From distribution specified by Figures 6.32 and 6.33 and Table 6.3, set the 3rd ray relative delay τ_3.

6. Increment/change range R as desired, update the two-ray model values, and

maintain 3rd ray for duration D_3. After D_3 reached, go to step 1 and continue.

CHAPTER 7

ANTENNA AND FREQUENCY DIVERSITY

Inter-frequency correlation is a measure of mutual influence between signals at different frequencies. Both L-band and C-band will be employed for CNPC links, possibly simultaneously, hence the influence of the channels at the two frequencies is of interest. The desired magnitude of the correlation coefficient is as small (close to zero, uncorrelated) as possible.

Intra-frequency correlation, also known as spatial correlation, quantifies similarity of channels seen by multiple aircraft antennas. Uncorrelated intra-band signals indicate that the channel capacity and/or link reliability can be increased by employing MIMO antennas. For reliability improvements, channel diversity gain can be achieved by MIMO systems if the channels are uncorrelated. However, an LOS component is almost always present in the AG channel, which is strongly similar between different aircraft antennas, hence the signals at different aircraft antennas are generally highly correlated. In this chapter we quantify the correlation coefficient of LOS components.

The correlation computation algorithm is illustrated in Figure 7.1. As noted in Chapter 3.3.3, yellow blocks denote inputs and green blocks denote outputs, *CiLj* denotes the correlation between C-band i^{th} Rx and L-band j^{th} Rx $i,j \in \{1,2\}$, C1C2 and L1L2 denote spatial correlation in C-band and L-band respectively, and *MeasRslt* is a matrix

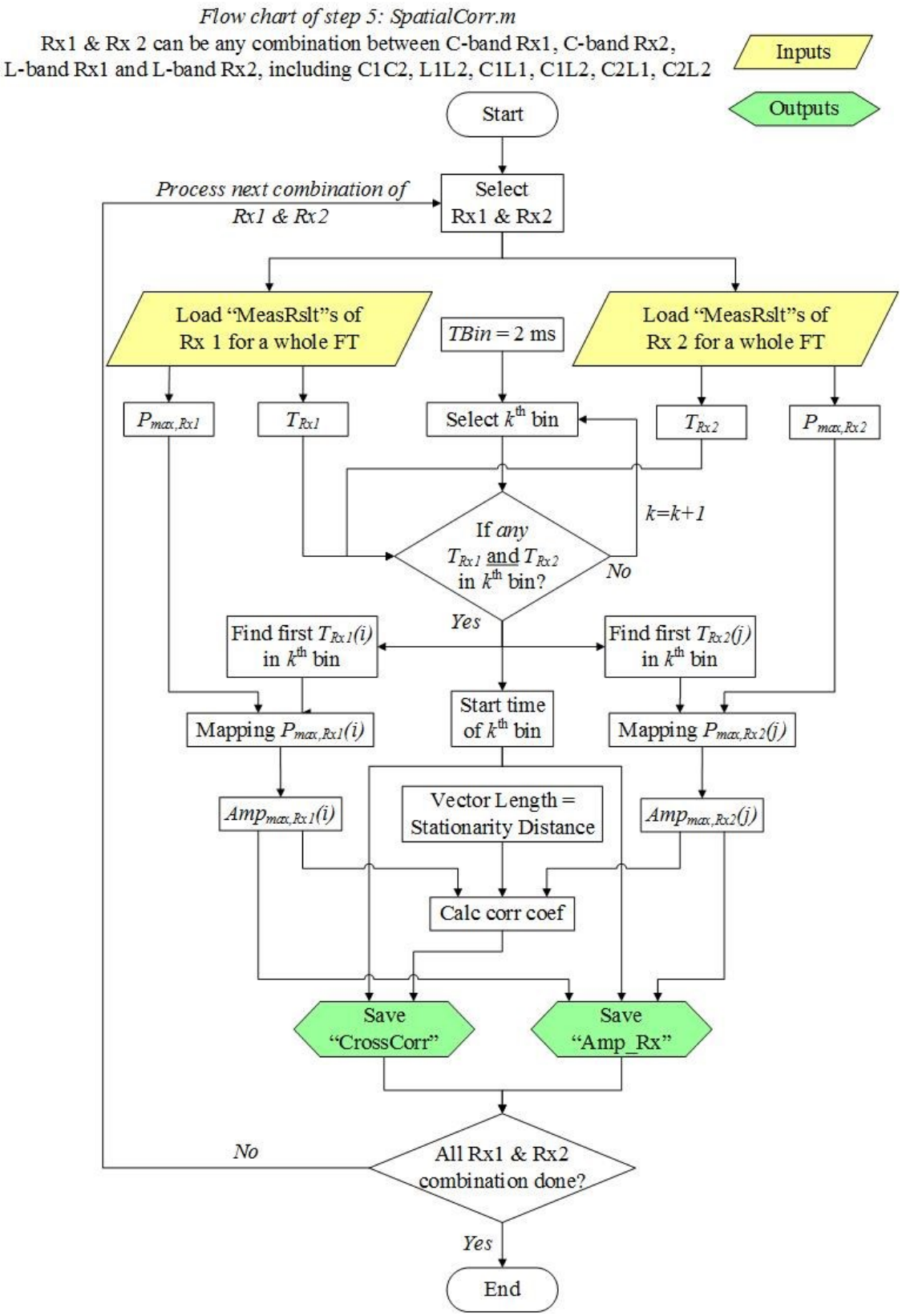

Figure 7.1. Inter-receiver correlation coefficient computation algorithm.

that contains received power. Since the receivers in the different bands have different PDP update rates, we have to synchronize the PDPs used in correlation coefficient calculation (not all PDPs are used) before computing the correlation. One receiver's power value (from a PDP) is selected for each Rx for each time bin *TBin* of 2 ms. These power values are converted to amplitude. The correlation coefficient ρ is given by

$$\rho_{A_1,A_2} = \frac{E[(A_1-\mu_{A_1})(A_2-\mu_{A_2})]}{\sigma_{A_1}\sigma_{A_2}}, \tag{7.1}$$

where E denotes expectation, A_i's denote received amplitude (in linear scale) vectors with length corresponding to the stationarity distance of 15 m, and the μ's and σ's are means and standard deviations of the A_i's. The correlation coefficient ranges between -1 (negatively correlated, channel amplitude from one receiver decreases as the amplitude from the other receiver increases) and 1 (highly correlated, channel amplitudes from one receiver increase as the amplitude from the other receiver increases). A coefficient close to zero indicates the channels for the two receivers are uncorrelated.

7.1 ANALYTICAL SPATIAL CORRELATION

Base on the CE2R model described in Chapter 4.2, signal amplitude is computed numerically with the two aircraft antennas separated by our actual value of 1.24 m. The analysis here is applied to the over freshwater setting. The parameters we use are as follows: aircraft altitude 566.3 m above the GS antenna, average wind speed for Lake Erie on 10 October 2013 of 5 m/s (for water surface roughness which affects the reflection coefficient, as discussed in Chapter 4.3.3) [120], conductivity σ=0.01 S/m, and relative permittivity ε=81 for freshwater [9].

The analytical correlation coefficient versus horizontal distance along the earth surface is shown in Figure 7.2, where the horizontal distance d_{k1} of C-band Rx1 ranges

from 388 m to 30 km. (As described in Chapter 4.2, since some approximations are employed, the CE2R for the over freshwater case is only valid when horizontal distance is greater than 388 m.) As the aircraft is flying away from the GS, the horizontal distance of C-band Rx2 is $d_{k2}+\Delta d$, where the intra-band antenna's spatial separation distance Δd is 1.24 m. The path loss for both receivers can be estimated by the CE2R model, which can be converted to received power, from which the received signal amplitude vector used in Eq. (7.1) is derived. Figure 7.2 contains correlations computed with three different vector (A_i) length values of 5 m (smaller than the SD), 15 m (SD) and 150 m (larger than the SD). The correlation coefficient oscillates from -1 to +1, especially at short distances. Smaller SD values have larger oscillation at larger distances. These oscillations are due to two-ray effects. Figure 7.3 is an enlarged version Figure 7.2 with horizontal distance limited to the short range from 388 m to 5 km. The L-band correlation coefficients versus distance are shown in Figure 7.4; and these contain fewer oscillations than the C-band results, but the oscillation magnitude is the same as in the C-band results.

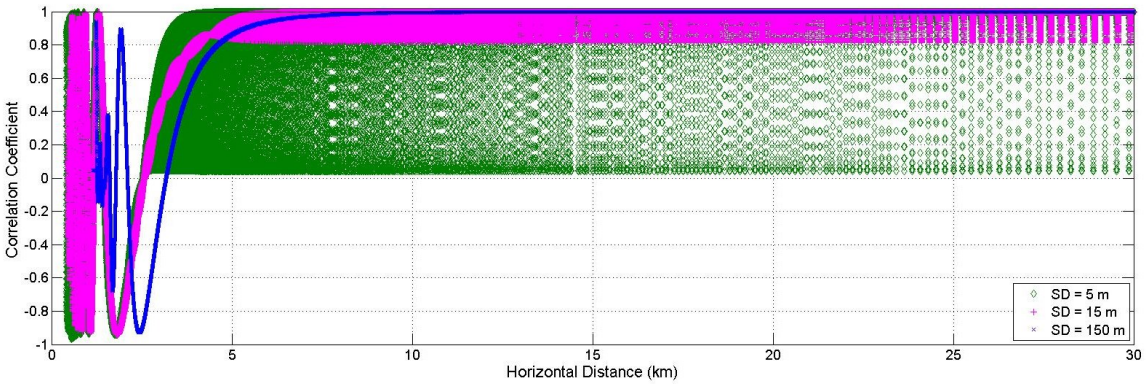

Figure 7.2. Analytical correlation coefficient between two C-band receivers vs. horizontal distance (from 1 m to 30 km) for over freshwater case, based on CE2R without fading.

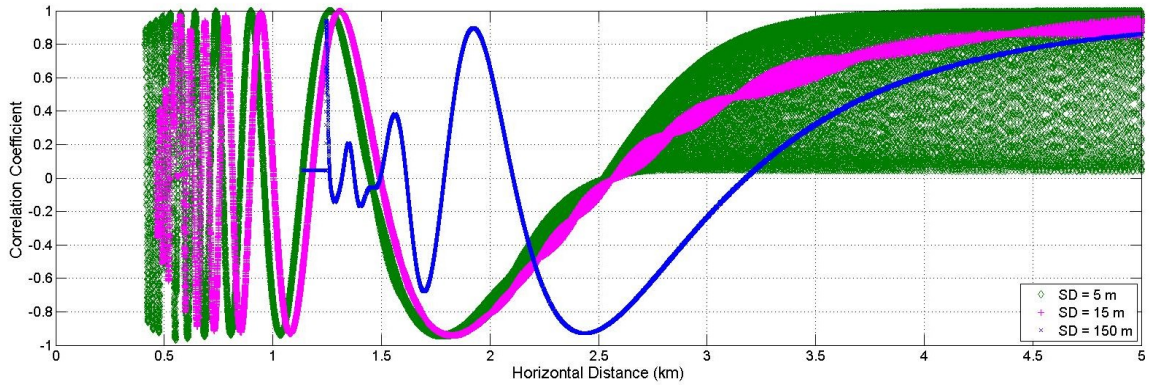

Figure 7.3. Analytical correlation coefficient between two C-band receivers vs. horizontal distance (from 1 m to 5 km) for over freshwater case, based on CE2R without fading.

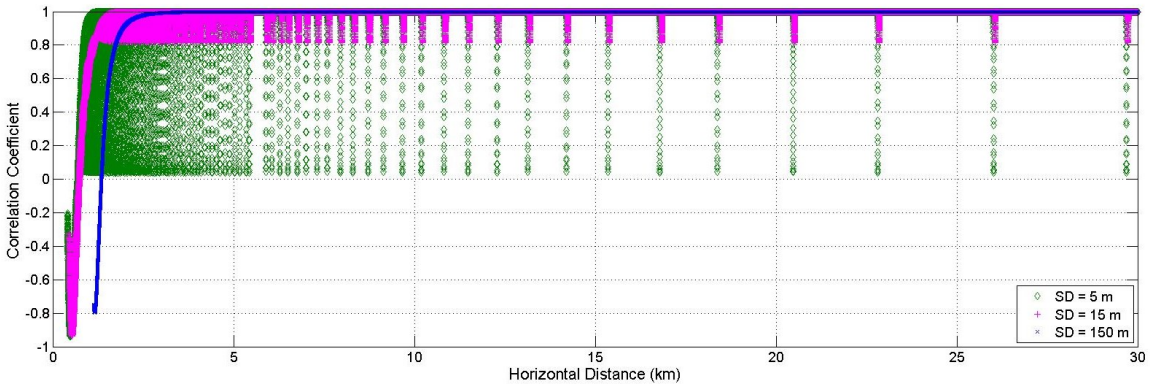

Figure 7.4. Analytical correlation coefficient between two L-band receivers vs. horizontal distance (from 1 m to 30 km) for over freshwater case, based on CE2R without fading.

In Figures 7.5 and 7.6, we incorporate Ricean fading into the signal amplitude computed by the CE2R model. The Ricean K factor employed is 29.9 dB in C-band and 12.8 dB in L-band [58]. The magnitude and duration of the correlation coefficient oscillations become much larger, and as we will show, inclusion of this small-scale fading improves agreement with measured correlations.

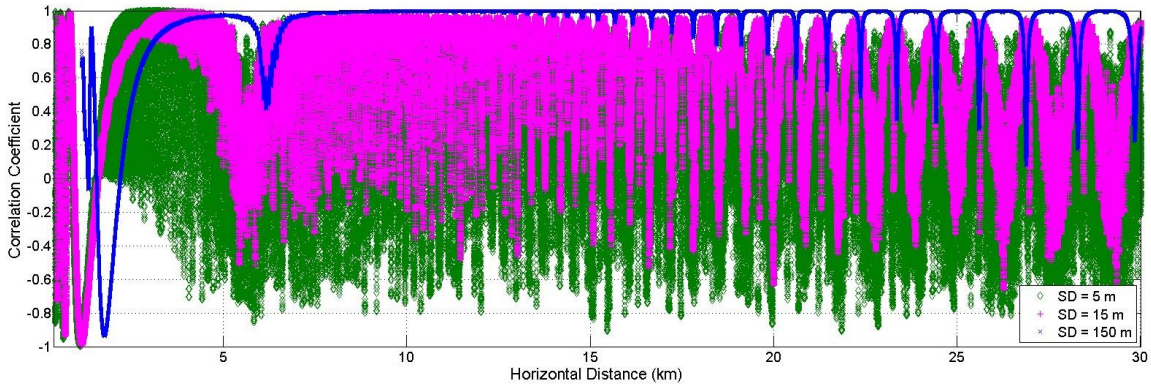

Figure 7.5. Analytical correlation coefficient between two C-band receivers vs. horizontal distance (from 1 m to 30 km) for over freshwater case, based on CE2R plus Ricean fading.

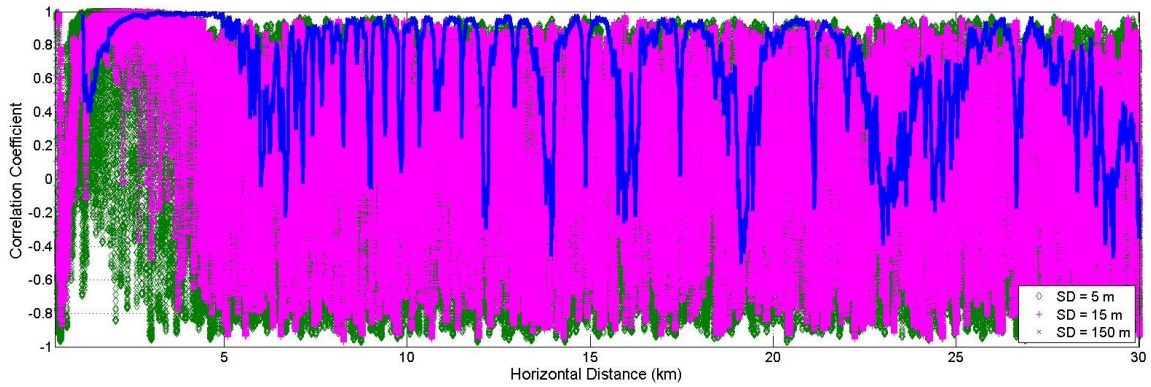

Figure 7.6. Analytical correlation coefficient between two L-band receivers vs. horizontal distance (from 1 m to 30 km) for over freshwater case, based on CE2R plus Ricean fading.

7.2 EMPIRICAL SPATIAL CORRELATION

The example spatial correlation coefficient versus link distance for over freshwater flight track 2 is shown in Figure 7.7 (C-band) and 7.8 (L-band). The empirical results agree with the analytical spatial correlation results shown in Figures 7.5 and 7.6 in terms of the range of values and the oscillatory behavior. The probability density function of spatial correlation for this FT is shown in Figures 7.9 (C-band) and 7.10 (L-band). The

coefficients range from -1 to +1, but most of the values are near +1. The Generalized Pareto distribution fits the PDF well, and this distribution is given by

$$p_\rho(x) = \frac{1}{\sigma}(1 + k\frac{x-\theta}{\sigma})^{-1-\frac{1}{k}}, \quad (7.2)$$

where θ denotes a threshold parameter that is set to the minimum value -1, σ denotes a scale parameter and k is a shape parameter.

Additional empirical spatial correlation coefficients versus link distance for suburban, hilly and mountainous terrains in both C- and L-bands are shown in Figures 11 to 16. The coefficient in Figure 7.13 is relatively small before 10 km. This is due to fact that the aircraft altitude was high for the mountainous terrain FT (approximately 1900 m above the GS antenna), hence the elevation angle at distances less than 10 km was large. The range of distances less than 10 km in Figure 13 is comparable with the range less than 3.5 km in Figure 7.2.

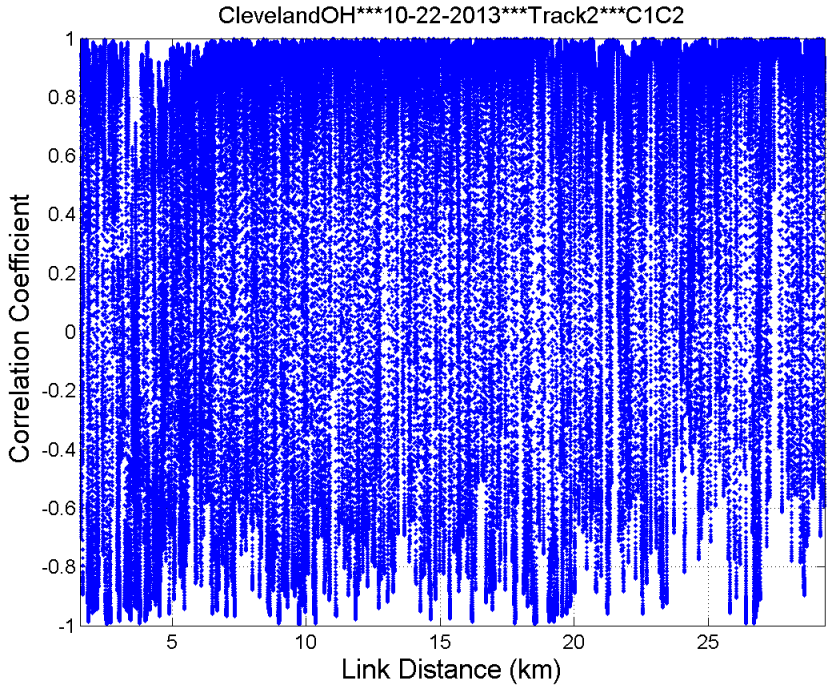

Figure 7.7. C-band spatial correlation vs. link distance for over freshwater FT2.

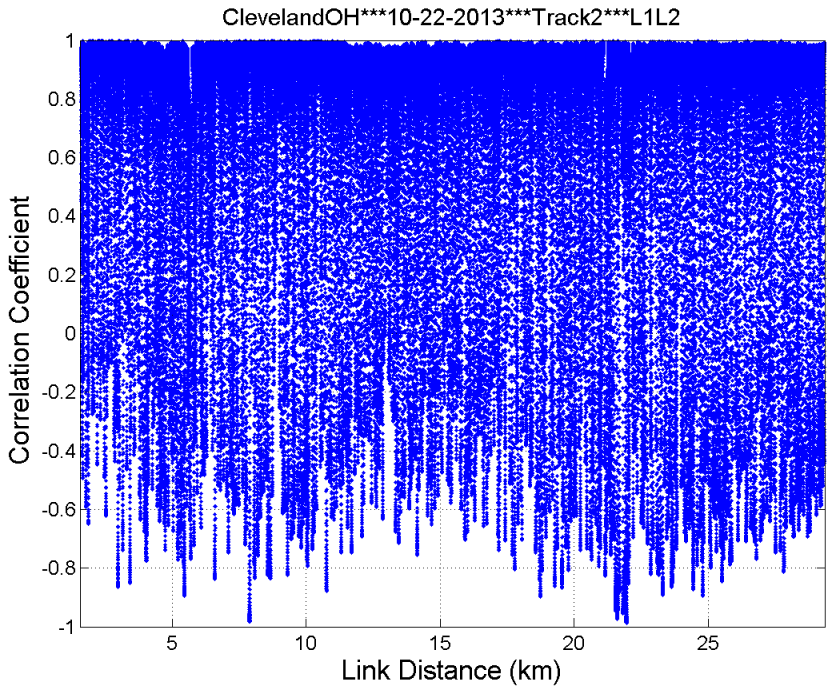

Figure 7.8. L-band spatial correlation vs. link distance for over freshwater FT2.

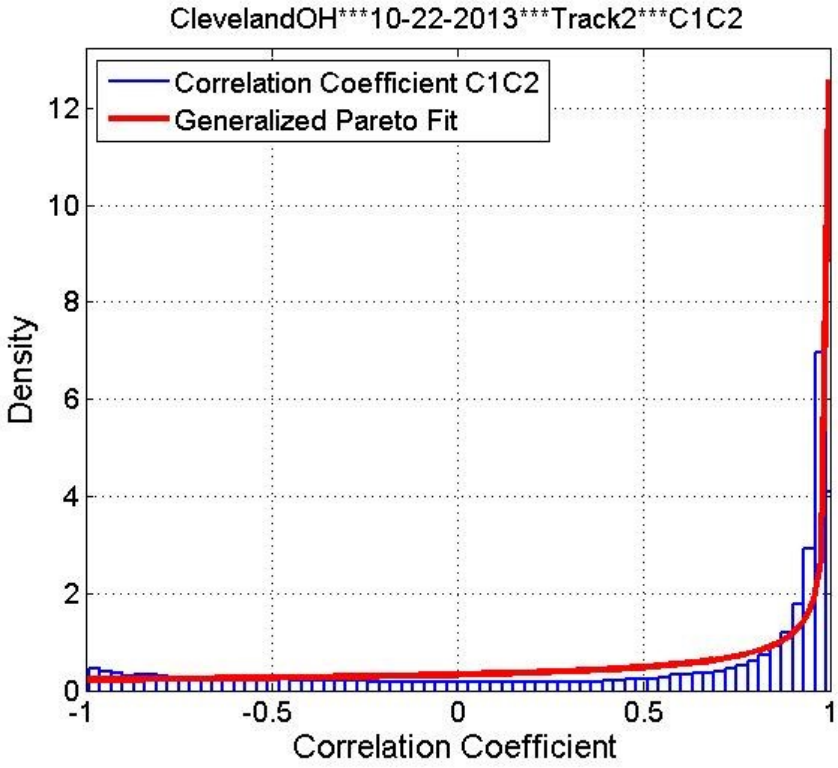

Figure 7.9. PDF of C-band spatial correlation for over freshwater FT2.

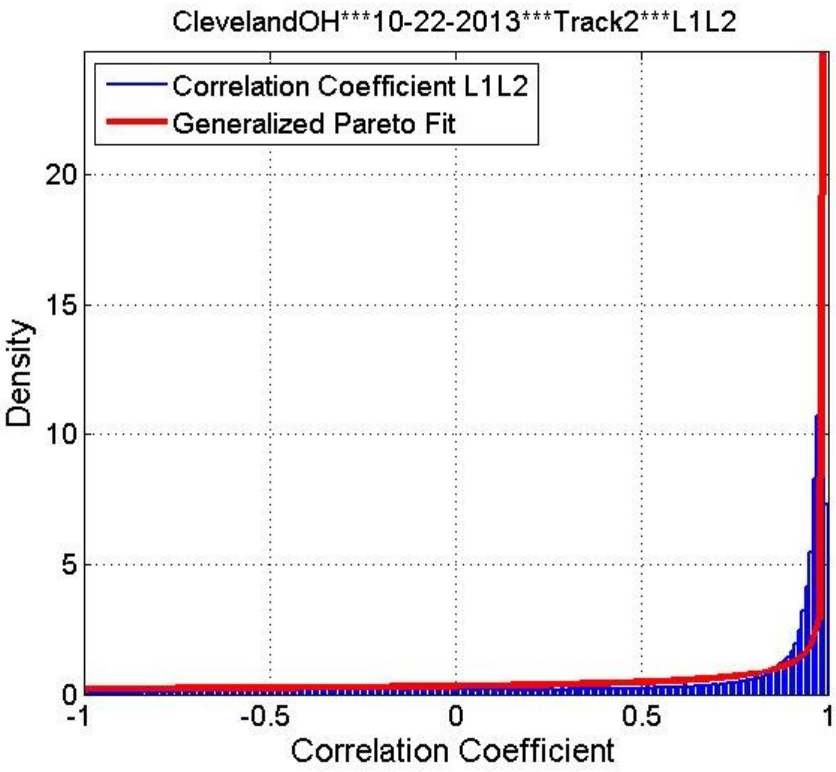

Figure 7.10. PDF of L-band spatial correlation for over freshwater FT2.

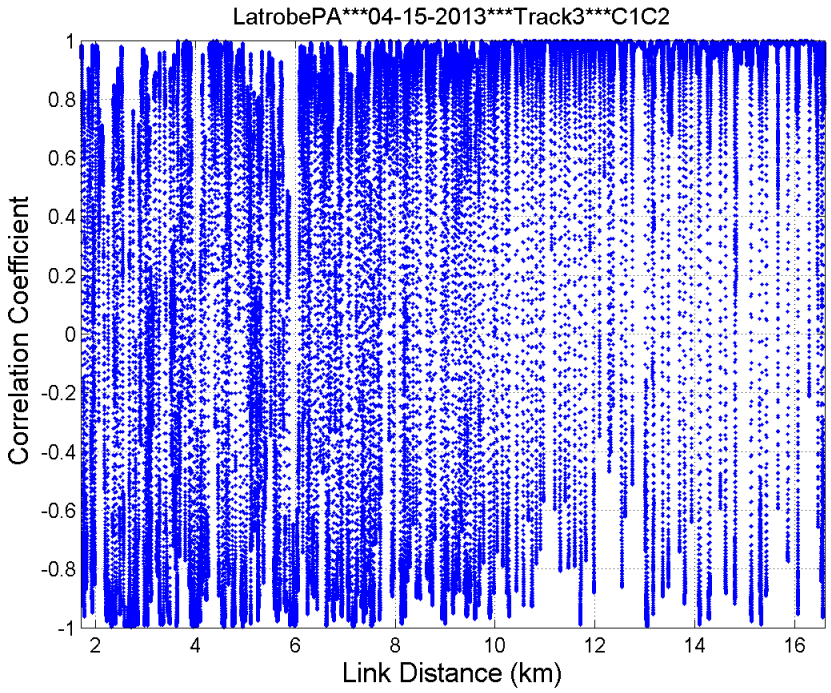

Figure 7.11. C-band spatial correlation vs. link distance for Latrobe suburban FT3.

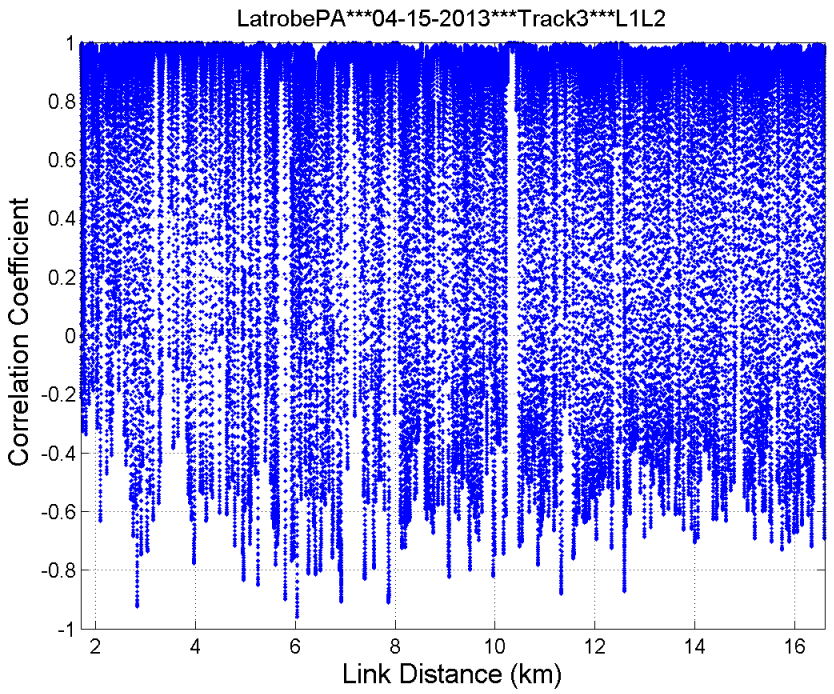

Figure 7.12. L-band spatial correlation vs. link distance for Latrobe suburban FT3.

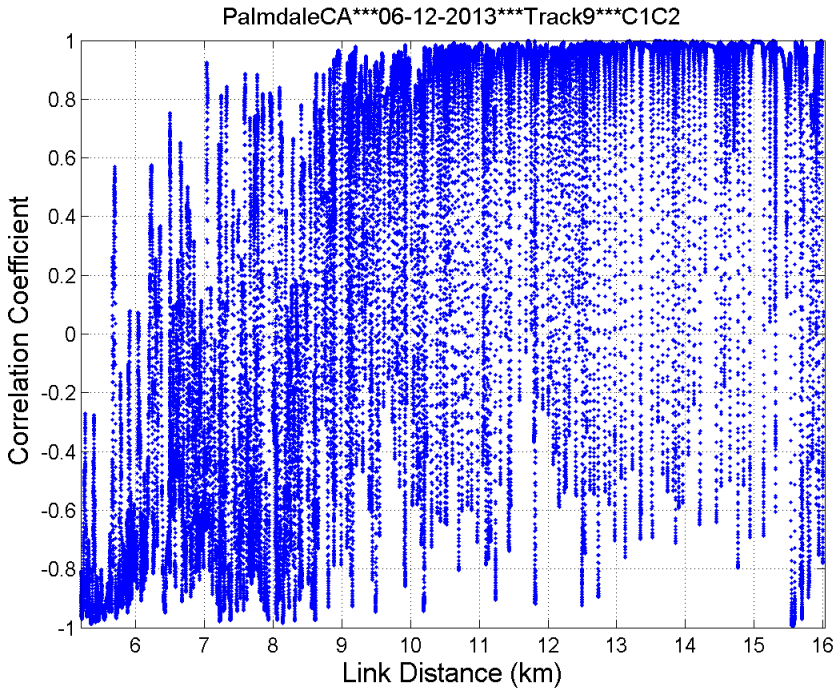

Figure 7.13. C-band spatial correlation vs. link distance for Palmdale hilly FT9.

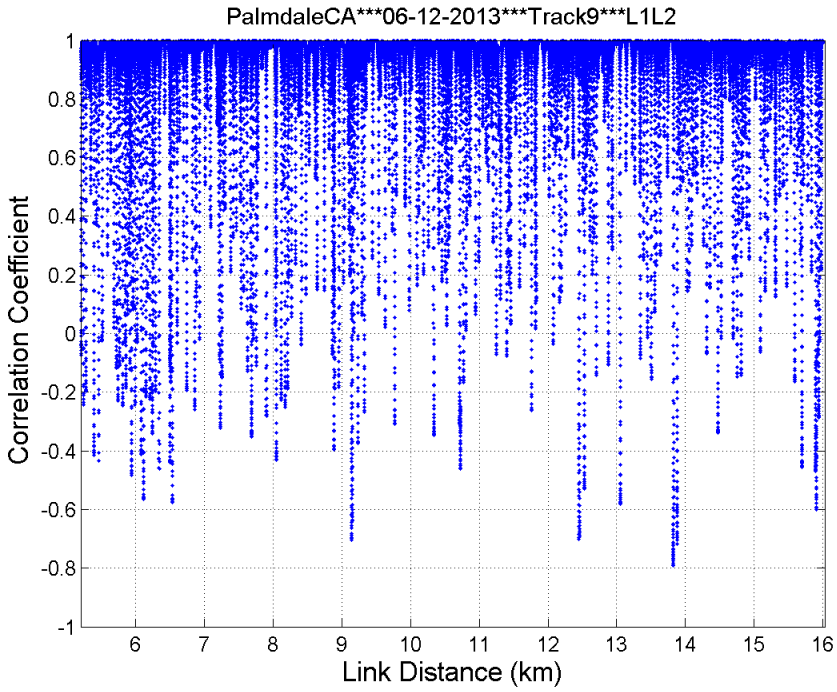

Figure 7.14. L-band spatial correlation vs. link distance for Palmdale hilly FT9.

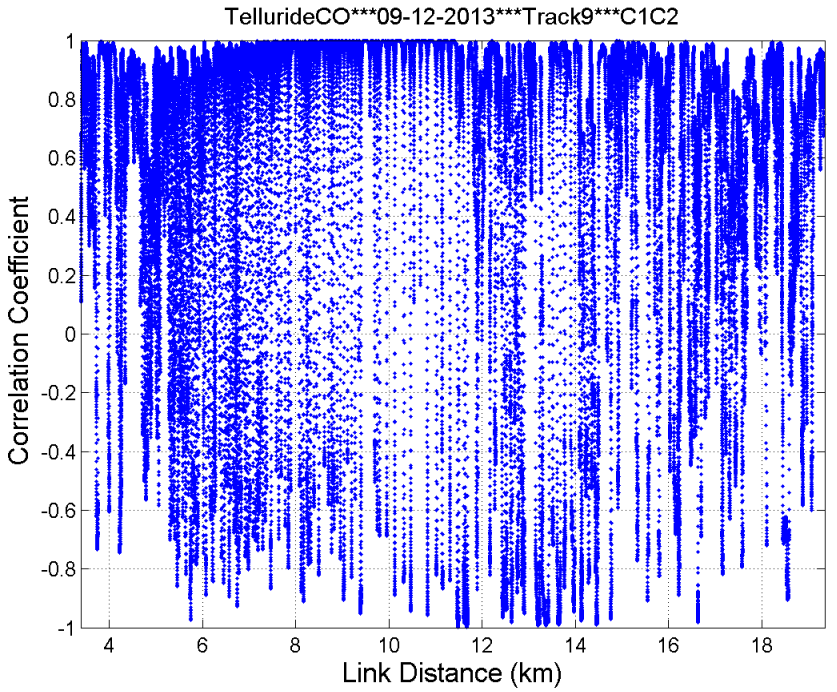

Figure 7.15. C-band spatial correlation vs. link distance for Telluride mountainous FT9.

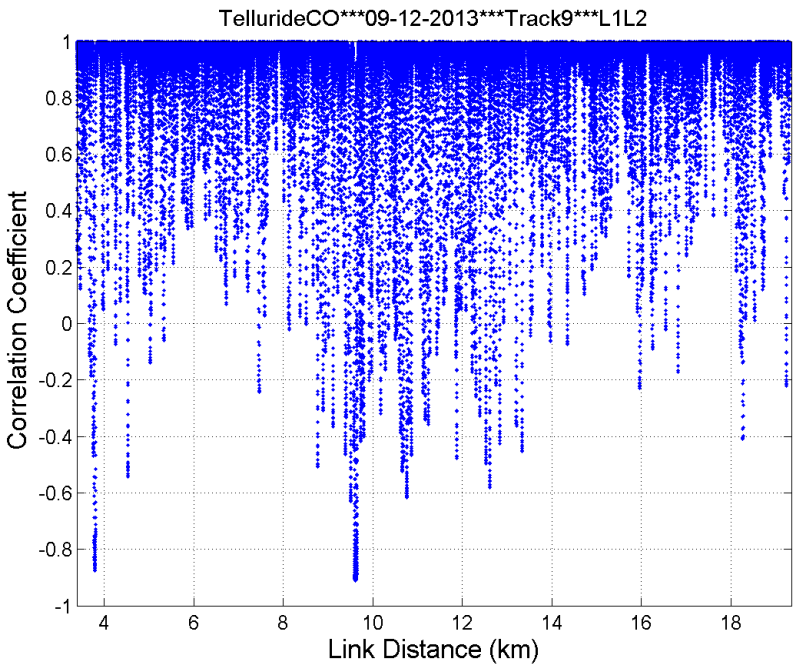

Figure 7.16. L-band spatial correlation vs. link distance for Telluride mountainous FT9.

The statistics of over freshwater spatial correlation are provided in Table 7.1. The median value is approximately 0.9 for both bands, which is much larger than the typically used correlation thresholds of 0.7 or 0.5 [121] and [122], below which the channels are considered approximately uncorrelated. The spatial correlation results in other scenarios have similar values and distributions. Median correlation values for all scenarios are listed in Table 7.2. The L-band correlation coefficient is slightly larger than that for C-band. This can be explained by the analytical spatial correlation shown in Figures 7.2 and 7.4. The L-band spatial correlations have fewer oscillations (which yield the smallest correlation values) than C-band, hence the statistics of the L-band results are slightly larger than those of the C-band results. The intra-band signals are highly correlated, which is because the LOS component is always present and dominant in our AG channel, except where airframe shadowing events occurred (these are reported in Chapter 5.3 and [113]).

Table 7.1. Statistics of spatial correlation for over freshwater FT2.

Cleveland, OH 22Oct2013, FT2			
		C1C2	**L1L2**
Mean		0.50	0.66
Median		0.88	0.93
Max		1.00	1.00
Min		-1.00	-0.99
Generalized Pareto	σ	4.51	4.68
	k	-2.26	-2.34

Table 7.2. Median values of spatial correlation for multiple scenarios.

Median Spatial Correlation		**C-band**	**L-band**
Over freshwater, Cleveland	FT2	0.88	0.93
Over sea, Oxnard	FT2	0.97	0.97
Urban, Cleveland	FT5	0.93	0.94
Suburban, Cleveland	FT2	0.85	0.99
Suburban, Latrobe	FT2	0.87	0.97
Suburban, Palmdale	FT2	0.91	0.98
Hilly, Latrobe	FT9	0.86	0.91
Hilly, Palmdale	FT7	0.90	0.99
Mountainous, Telluride	FT9	0.85	0.99

The spatial correlation in an airframe shadowing event is of interest. The statistics of intra-band correlation coefficients in an example AFS event collected over Lake Erie FT4 is provided in Table 7.3 [113]. The spatial correlation median values decreased from 0.85 or above outside the AFS to approximately 0.6 in the AFS, which is below the typically used threshold of 0.7 for spatial correlation [121].

Table 7.3. Statistics of spatial correlation in an airframe shadowing event [113].

	Whole FT		**Shadowing Area**	
	C-band	**L-band**	**C-band**	**L-band**
Mean	0.42	0.59	0.23	0.26
Median	0.85	0.91	0.56	0.64
Max	1.00	1.00	1.00	1.00
Standard deviation	0.72	0.59	0.77	0.76

7.3 INTER-FREQUENCY CORRELATION

The probability density function of inter-frequency correlation coefficient between C-band Rx1 and L-band Rx1 for over freshwater FT4 is shown in Figure 7.17 [61]. It follows a Gaussian distribution with mean value close to zero. This conclusion pertains for *all* scenarios: this means that the L-band and C-band channels are essentially uncorrelated. Although the physics for both band channels are mostly the same, the reflection coefficients are not, and scattering (small-scale) effects are also different, and this explains the uncorrelatedness of the small scale amplitude fading in the two bands.

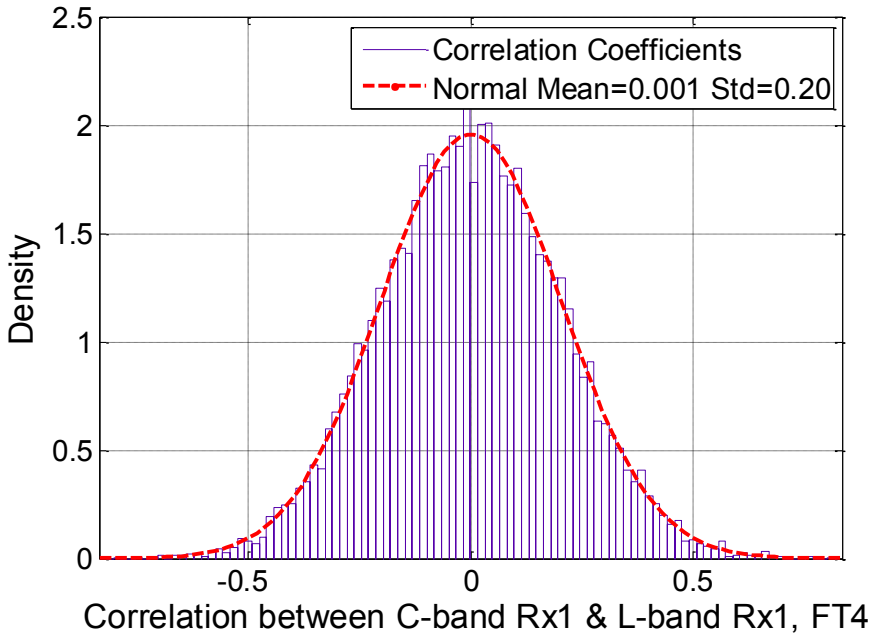

Figure 7.17. PDF of inter-frequency correlation between C-band Rx1 and L-band Rx1 for over freshwater FT4 [61].

CHAPTER 8

CONCLUSIONS AND FUTURE WORK

In this dissertation, we have investigated the topic of dual-band non-stationary channel modeling for the air-ground channel, for two specific frequency bands planned for UAS use. Our investigation employed analysis and empirical results from a large body of data collected from NASA flight tests. In this chapter, the main conclusions and discussion of avenues for future research for academia and industry are presented.

8.1 DISSERTATION CONCLUSIONS

The main objective of our research is to estimate non-stationary air-ground channel characteristics, and from these characteristics develop channel models in both L-band (near 968 MHz) and C-band (near 5060 MHz). A survey of the literature about the AG channel and remaining gaps were provided. Deterministic geometry based stochastic models for the overwater AG channels were provided. Based on experimental data, stationarity distances, over which the channels are considered wide sense stationary, were estimated. We also presented path loss, small scale fading, airframe shadowing, and TDL models for multiple ground station local environments. Multiple aircraft antenna diversity and inter bands correlation were investigated as well, for the specific aircraft and antenna locations used in our flight tests.

We worked on a NASA project entitled “Unmanned Aircraft System Integration in the National Airspace System.” Specifications of the control and non-payload communication (CNPC) link are being designed for UAS in the United States. The AG

channel models we derived in this project provide references for government, industry, academia, and standard bodies who work on the CNPC physical layer design and performance evaluation. Our AG channel models will also be inputs for the ICAO and likely for some ITU contributions. They may also be used for evaluation of proposed aeronautical waveform designs, e.g., the European aeronautical wireless communication system designated LDASC1 and LDASC2.

We developed deterministic geometry based stochastic channel models for overwater environments, and they are also applicable to some terrain channels. Since the LOS is present for almost all the time and the earth surface reflection is present for most GS local terrains, the over water AG channels are modeled by CE2R or FE2R. We made several improvements to the CE2R, including accounting for the earth spherical divergence, atmospheric refraction and earth surface roughness. The limitations and applicable conditions for use of the models were indicated as well. The theoretical intra-band spatial correlation between signals received on two spatially separated aircraft antennas, mounted on the bottom of the aircraft, was also derived from the CE2R. The CE2R and the theoretical intra-band correlation were validated by the measured path loss quite well. Some other effects that may be present in the AG channels were also described, although they were not encountered or were negligible in our measurements; this includes atmospheric gas, hydrometeor attenuation and ducting.

As far as we are aware, NASA Glenn Research Center has conducted the most comprehensive AG channel measurement campaign in history, and this covers all the typical GS local environments, including over sea, over freshwater, suburban, near urban, desert, hilly and mountainous terrains. The measurement system includes an S-3B Viking

aircraft, a transportable GS antenna tower and a dual-band direct sequence spread spectrum channel sounder that contains one transmitter and two receivers in both the C- and L-bands. Approximately 316 million PDPs have been collected over 82 flight tracks.

The stationarity distance is a small range over which channels are wide sense stationary, and knowing this distance is essential for non-stationary channel modeling. One of our main contributions is the estimation of stationarity distance for the AG channels, which has not been investigated before. We employed two measurement based methods: the temporal PDP correlation coefficient and the spatial collinearity (or equivalently, the correlation matrix distance). The results of two methods basically agree with each other. The C-band SD is approximately 15 m (250 wavelengths), which is larger than that in the cellular or vehicle-to-vehicle (V2V) channels since the AG LOS component is generally stronger and more frequently present than in these terrestrial channels. The AG channel MPCs are also more sparse. The L-band SD is expected to be larger than that in C-band because of the larger wavelength, but to be conservative, we employed 15 m as the SD for L-band as well. The SD is used for evaluation of the empirical small scale fading and inter- and intra-band correlations.

The path loss is described by either log-distance or CE2R models along with some corrections such as the adjustments for flight direction. The standard deviations smaller than 4.2 for both bands and for all environments indicates that the log-distance path loss model fit the measured data very well; we note again that for terrestrial path loss models, standard deviations are often 6-12 dB [90]. Since the LOS component is almost always present in the AG channels, the small scale fading is modeled by a Ricean process of unit energy, and is then fully characterized by the Ricean K-factors. The K-factors

estimated by the maximum likelihood method and a moment-based method are essentially the same, and these are approximately 28.7 dB in C-band and 13.1 dB in L-band.

The airframe shadowing is a characteristic that is somewhat unique to the aeronautical channels. It occurs during some specific aircraft maneuvers. Statistics and models of the airframe shadowing duration and loss were computed over 58 S-3B Viking aircraft (wing) shadowing events. The shadowing duration is on average 35 seconds in C-band and 25 seconds in L-band. These durations are longer than expected for practical flights since out flights were purposely designed to fly slowly so that we can capture Doppler. The median shadowing loss is on average 16 dB in C-band and 11 dB in L-band. The maximum loss in L-band is on average 36 dB with the maximum single L-band shadow depth recorded at 47.8 dB. The shadowing loss was found to be independent of the shadow duration, but loss is a function of the aircraft roll angle of the shadowing event. An algorithm to simulate the airframe shadowing loss over time or distance was provided, hence providing models for the narrowband total path loss accounting for distance-dependent path loss, fading, and shadowing.

For the wideband AG channels, C-band RMS-DS, sequences of PDPs and TDL models were presented in this dissertation. In most environments, the RMS-DS was 10 ns for most of time, with numerous bumps with RMS-DS up to 2 microseconds. The CE2R plus intermittent 3^{rd} or 4^{th} or 5^{th} MPCs represent the wideband AG channel very well. The occurrence probability, duration, relative power, phase, and excess delays of the intermittent MPCs for the over water cases were modeled. The algorithm to simulate the

over water TDL model is provided, and models for the other environments will soon be completed.

Based on the correlation between received signal amplitude vectors from two aircraft receivers, the C-band and L-band channels were found to be uncorrelated. The intra-band channels for two Rx antennas with approximately 1.82 m separation distance, mounted on the bottom of the aircraft, were found to be highly correlated except where the airframe shadowing occurred. Therefore, multiple aircraft antennas at larger spatial separations are recommended for the future CNPC link to provide diversity and mitigate the airframe shadowing loss.

8.2 FUTURE WORK

Possible extensions of this dissertation work are listed below:

- Models of the occurrence probability, duration, relative power, phase and excess delays, and Doppler characteristics of the intermittent MPCs, for TDL models applicable for hilly, mountainous, desert, suburban and near urban environments will be generated in the near future and reported in our series of AG channel journal papers.
- L-band wideband models are of interest. These were not developed since our sounder had limited delay resolution (200 ns). Nonetheless, from a physical perspective, MPCs at various delays in C-band are likely to also be present at L-band, albeit with different amplitude characteristics. Thus a basis for wideband L-band models can be constructed from the C-band data, identifying MPC delays and durations. Rough estimates of amplitude characteristics can be obtained via frequency-scaled reflection coefficients,

but translation of scattering and/or diffraction effects is more complex. Hence wideband L-band measurements should be undertaken to identify MPC characteristics in the most dispersive settings.

- The heights of the GS antennas were a constant value of 20 m in our measurement campaign. The CE2R model and characteristics of the diffuse MPCs are expected to change with GS height. The magnitude of the two-ray peaks and nulls are expected to decrease as the GS antenna height decreases, and this can be estimated by theoretical CE2R models. The changes of MPCs characteristics are of most significance for multiple GS heights, especially for urban environments where numerous MPCs are likely present. Multiple other values of the GS antenna heights are thus of interest, such as 1.5 m for a human operating an UAS, 2.5 m for the GS antenna mounted on the roof of a vehicle, and 50 m or larger for the GS antenna mount on an air traffic control tower.
- The aircraft height was between 500 and 2000 m above the earth in our measurement campaign. It would be worthwhile to increase the height to up to 10 km to compare measurements with results from the CE2R model and quantify how (if) the characteristics of the diffuse MPCs change.
- The multiple GS antennas or multiple GSs that are multiple tens of meters, or even kilometers apart, are expected to provide diversity. Therefore, quantitative study of the GS spatial diversity would be useful.
- In our work, the two intra-band aircraft antennas were mounted at fixed locations, relatively close to each other. It would be interesting to compare the

results of spatial correlation and instantaneous diversity gain if the separation distance between antennas and locations of antennas are changed or if more antennas are employed. Determination of how many antennas and where to locate them to mitigate (1) airframe shadowing, and (2) small scale fading (including 2-ray nulls) is of interest.

- The GS was motionless in our measurement campaign. However, it could be moving in practice if the GS antennas were mounted on vehicles or boats, which induces additional time variant factors to the AG channels. Such "doubly-mobile" AG channels should be measured and modeled.
- The aircraft itself is often a large ground plane for the aircraft antennas, and this affects the patterns. However, it's unrealistic to experimentally investigate this effect, especially for a wide variety of aircraft types and sizes. This effect can be studied by ray-tracing and/or full-wave electromagnetics modeling. Moreover, the spatial correlation, instantaneous diversity gain, and airframe shadowing for different numbers of aircraft antennas and different separation distances can be estimated by ray-tracing and compared with any measurements as well.
- Small UAS can fly at very low altitudes on the order of tens of meters, and hence buildings or trees could obstruct the LOS. Investigation of building and/or tree shadowing for small UAS is another topic worthy of investigation.

REFERENCES

[1] International Telecommunications Union (ITU), "Characteristics of Unmanned Aircraft Systems and Spectrum Requirements to Support their Safe Operation in Non-Segregated Airspace," ITU-R M.2171, December 2009.

[2] Radio Technical Commission for Aeronautics, (2015, May 22). [Online]. Available: www.rtca.org

[3] International Civil Aviation Organization, (2015, May 22). [Online]. Available: www.icao.int

[4] International Telecommunications Union, (2015, May 22). [Online]. Available: www.itu.int

[5] K. Shalkhauser, D. W. Matolak, R. Kerczewski, "NASA L-Band and C-Band Air-Ground Channel Measurement and Modeling," *International Civil Aviation Organization (ICAO), Aeronautical Communications Panel, WG-F*, Nairobi, Kenya, 5-12 September 2013.

[6] G. L. Stuber, *Principles of Mobile Communication*, 2nd ed., Kluwer Academic Pub., Boston, MA, 2001.

[7] D. W. Matolak, "Air-Ground Channels & Models: Comprehensive Review and Considerations for Unmanned Aircraft Systems," *in Proc. IEEE Aerospace Conference*, Big Sky, MT, 3-10 March 2012.

[8] D. W. Matolak, R. Sun, "Air-Ground Channel Measurements & Modeling for UAS," *2013 Integrated Communication, Navigation and Surveillance (ICNS) Conference*, pp. 1-

9, Herndon, VA, 22-25 April 2013.

[9] J. D. Parsons, *The Mobile Radio Propagation Channel*, 2nd ed., John Wiley & Sons, New York, NY, 2000.

[10] Wikipedia, "Aircraft Communications Addressing and Reporting System," (2015, June 22). [Online]. Available: en.wikipedia.org/wiki/Aircraft_Communications_Addressing_and_Reporting_System.

[11] Wikipedia, "VHF Data Link," (2015, June 22). [Online]. Available: en.wikipedia.org/wiki/VHF_Data_Link.

[12] European Telecommunications Standards Institute (ETSI), "VHF air-ground Digital Link (VDL) Mode 2; Technical characteristics and methods of measurement for ground-based equipment; Part 1: Physical layer and MAC sub-layer," *ETSI EN 301 841-1 V1.3.1 Final draft*, Jan. 2010.

[13] Broadband VHF, (2015, June 22). [Online]. Available: www.b-vhf.org/.

[14] EUROCONTROL, (2015, June 22). [Online]. Available: www.eurocontrol.int/.

[15] R. Jain, F. Templin, "Requirements, Challenges and Analysis of Alternatives for Wireless Datalinks for Unmanned Aircraft Systems," *IEEE Journal on Selected Areas in Communications*, vol. 30, no. 5, pp. 852–860, June 2012.

[16] G. Dyer, J. Budinger, "FCS Technology Assessment Team: Technology Assessment Phase II – P34 Overview," (2015, June 22). [Online]. Available: www.icao.int/safety/acp/Inactive%20working%20groups%20library/ACP-WG-C-11/ACP-WGC11-WP31-P34_Overview.ppt.

[17] Aeronautical Communications Panel (ACP), "B-AMC — A Promising Future Aeronautical Communications System Based Multi-carrier Technology," (2015, June

22). [Online]. Available: www.icao.int/safety/acp/prl/ACP-1-ENGLISH/ACP.1.IP.008.1.en.doc.

[18] L-DACS1 System Design Proposal: Deliverable D3 - Design Specifications for L-DACS1 Prototype, (2015, June 22). [Online]. Available: www.eurocontrol.int/sites/default/files/article/content/documents/communications/01042009-ldacs1-d3-v10.pdf.

[19] N. Neji, R. de Lacerda, A. Azoulay, T. Letertre, and O. Outtier, "Survey on the Future Aeronautical Communication System and Its Development for Continental Communications," *IEEE Transactions on Vehicular Technology*, vol. 62, no. 1, pp. 182–191, Jan. 2013.

[20] L-DACS2 Transmitter and Receiver prototype equipment specifications: Deliverable D3, (2015, June 22). [Online]. Available: www.eurocontrol.int/sites/default/files/article/content/documents/communications/18062009-ldacs2-design-d3-v1.2.pdf.

[21] Microwave Landing System, (2015, June 22). [Online]. Available: microwave.landingsystem.com.

[22] W. C. Vergara, J. L. Levatich, W. C. Carroll, "VHF Air-Ground Propagation Far Beyond the Horizon and Tropospheric Stability," *IRE Transactions on Antennas & Propagation*, pp. 608-621, September 1962.

[23] K. Chamberlin, "The Effect of Tree Cover on Air-Ground, VHF Propagation Path Loss," *IEEE Transactions on Communications,* vol. COM-34, no. 9, pp. 958-962, September 1986.

[24] S. Elnoubi, “A Simplified Stochastic Model for the Aeronautical Mobile Radio Channel,” in *Proc. IEEE Vehicular Technology Conference*, Denver, CO, 10-13 May 1992.

[25] Aeronautical Mobile Communications Panel (AMCP), Working Group D, “A General Model for VHF Aeronautical Multipath Propagation Channel,” *AMCP/WG-D/WP6*, Honolulu, HI, January 1999.

[26] G. Dyer, T. Gilbert, “Channel Sounding Measurements in the VHF A/G Radio Communications Channel,” *AMCP/WG-D/8-WP/19*, Oberpfaffenhofen, Germany, Dec. 1997.

[27] G. Dyer, T. Gilbert, S. Hendrickson, E. Sayadian, “Mobile Propagation Measurements using CW and Sliding Correlator 16 Techniques,” in *Proc. IEEE Ant. Propagation Symposium*, Atlanta, GA, 1998.

[28] P. Hoeher, E. Haas, “Aeronautical Channel Modeling at VHF Band,” in *Proc. IEEE Vehicular Technology Conference*, Amsterdam, The Netherlands, 19-22 September 1999.

[29] M. Failli (Chairman), “Digital Land Mobile Radio Communications,” *COST 207 final report*, Sept. 1988.

[30] RTCA SC-172, “Signal-in-Space Minimum Aviation System Performance Standards (MASPS) for Advanced VHF Digital Data Communications Including Compatibility with Digital Voice Techniques,” August 2010.

[31] E. Haas, “Aeronautical Channel Modeling,” *IEEE Transactions on Vehicular Technology*, vol. 51, no. 2, pp. 254-264, March 2002.

[32] J. H. Painter, S. C. Gupta, and L. R. Wilson, “Multipath Modeling for Aeronautical Communications,” *IEEE Transactions on Communications*, vol. 21, no. 5, pp. 658–662, 1973.

[33] R. W. Sutton, E. H. Schroeder, A. D. Thompson, and S. G. Wilson, “Satellite-Aircraft Multipath and Ranging Experiment Results at L-Band,” *IEEE Transactions on Communications*, vol. 21, no. 5, pp. 639–647, 1973.

[34] J. R. Child, “Air to Ground Propagation at 900 MHz,” *Proc. in 35th IEEE Vehicular Technology Conference*, pp. 73–80, 1985.

[35] K. Welling, R. Dye, and M. D. Rice, “Narrowband channel model for aeronautical telemetry,” *IEEE Transactions on Aerospace and Electronic Systems*, vol. 36, no. 4, pp. 1371–1376, 2000.

[36] M. Simunek, P. Pechac, and F. Perez-Fontan, “Space diversity analysis for low elevation links in urban areas,” in *Proc. 2012 6th European Conference on Antennas and Propagation (EUCAP)*, 2012, pp. 1165–1168.

[37] M. Simunek, P. Pechac, and F. P. Fontan, “Feasibility of UAV Link Space Diversity in Wooded Areas,” *International Journal on Antennas Propagation*, vol. 2013, pp. 1–5, 2013.

[38] H. T. Kung, C.-K. Lin, T.-H. Lin, S. J. Tarsa, and D. Vlah, “Measuring diversity on a low-altitude UAV in a ground-to-air wireless 802.11 mesh network,” in *Proc. 2010 IEEE GLOBECOM Workshops (GC Wkshps)*, 2010, pp. 1799–1804.

[39] M. D. Rice and A. Davis, “A Multipath Channel Model for Wideband Aeronautical Telemetry,” in *Proc. 2002 IEEE Military Communications Conference (MILCOM 2002)*, vol. 1, pp. 622–626. 2002.

[40] M. D. Rice and M. Jensen, “Multipath propagation for helicopter-to-ground MIMO links,” in *Proc. 2011 IEEE Military Communications Conference (MILCOM 2011)*, 2011, pp. 447–452, 2011.

[41] W. G. Newhall, R. Mostafa, C. Dietrich, C. R. Anderson, K. Dietze, G. Joshi, and J. H. Reed, “Wideband Air-to-Ground Radio Channel Measurements using an Antenna Array at 2 GHz for Low-Altitude Operations,” in *Proc. 2003 IEEE Military Communications Conference (MILCOM 2003)*, vol. 2, pp. 1422–1427, 2003.

[42] A. Al-Hourani, S. Kandeepan, and A. Jamalipour, “Modeling air-to-ground path loss for low altitude platforms in urban environments,” in *Proc. 2014 IEEE Global Communications Conference*, 2014, pp. 2898–2904, 2014.

[43] T. Willink, C. Squires, G. Colman, and M. Muccio, “Measurement and characterization of low altitude air-to-ground MIMO channels,” *IEEE Transactions on Vehicular Technology*, vol. PP, no. 99, pp. 1–1, 2015.

[44] H. D. Tu, S. Shimamoto, and J. Kitaori, “A Proposal of a Wide Band for Air Traffic Control Communications,” in *Proc. 2008 IEEE Wireless Communications and Networking Conference*, 2008, pp. 1950–1955.

[45] Y. H. Lee, Y. S. Meng, and Y. H. Heng, “Experimental Characterizations of an Air to Land Channel over Sea Surface in C Band,” in *Proc. XXIXth International Union of Radio Science General Assembly and Scientific Symposium (URSI GASS)*, pp. 2–5, 2008.

[46] Y. S. Meng and Y. H. Lee, “Study of Shadowing Effect by Aircraft Maneuvering for Air-to-Ground Communication,” *International Journal of Electronic Communications.*, vol. 66, no. 1, pp. 7–11, Jan. 2011.

[47] Y. S. Meng and Y. H. Lee, "Practical Wideband Channel Sounding System for Air-to-Ground Measurements at C Band," in *Proc. 2009 IEEE Instrumentation and Measurement Technology Conference, (I2MTC '09)* , pp. 771–775. 2009.

[48] Y. S. Meng and Y. H. Lee, "Multipath characterization and fade mitigation of air-to-ground propagation channel over tropical sea surface at C band," in *Proc. 2010 IEEE Antennas and Propagation Society International Symposium*, 2010, pp. 1–4.

[49] Y. S. Meng and Y. H. Lee, "Measurements and Characterizations of Air-to-Ground Channel Over Sea Surface at C-Band With Low Airborne Altitudes," *IEEE Transactions on Vehicular Technology*, vol. 60, no. 4, pp. 1943–1948, May 2011.

[50] J. Kunisch, I. de la Torre, A. Winkelmann, M. Eube, and T. Fuss, "Wideband Time-Variant Air-to-Ground Radio Channel Measurements at 5 GHz," in *Proc. 2011 5th European Conference on Antennas and Propagation (EUCAP)*, pp. 1386–1390, 2011.

[51] Q. Lei and M. D. Rice, "Multipath Channel Model for Over-Water Aeronautical Telemetry," *IEEE Transactions on Aerospace and Electronic Systems*, vol. 45, no. 2, pp. 735–742, Apr. 2009.

[52] P. A. Bello, "Aeronautical Channel Characterization," *IEEE Transactions on Communications*, vol. 21, no. 5, pp. 548–563, 1973.

[53] W. G. Newhall and J. H. Reed, "A Geometric Air-to-Ground Radio Channel Model," in *Proc. 2002 IEEE Military Communications Conference (MILCOM 2002)*, pp. 632–636, 2002.

[54] Q. Feng, J. McGeehan, E. K. Tameh, R. R. Nix, J. McGeehan, E. K. Tameh, and A. R. Nix, "Path Loss Models for Air-to-Ground Radio Channels in Urban Environments,"

in *Proc. 2006 IEEE Spring Vehicular Technology Conference (VTC06S)*, vol. 6, pp. 2901–2905, 2006.

[55] D. Hague, H. T. Kung, and B. Suter, "Field Experimentation of Cots-Based UAV Networking," in *Proc. 2006 IEEE Military Communications Conference (MILCOM 2006)*, pp. 1–7, 2006.

[56] M. A. Jensen, M. D. Rice, and A. L. Anderson, "Aeronautical Telemetry using Multiple-Antenna Transmitters," *IEEE Transactions on Aerospace and Electronic Systems*, vol. 43, no. 1, pp. 262 – 272, 2007.

[57] A. I. Alshbatat and L. Dong, "Performance Analysis of Mobile Ad Hoc Unmanned Aerial Vehicle Communication Networks with Directional Antennas," *International Journal of Aerospace. Engineering*, vol. 2010, pp. 1–14, 2010.

[58] D. W. Matolak, R. Sun, "Air-Ground Channel Characterization for Unmanned Aircraft Systems—Part I: Methods, Measurements, and Models for Over-water Settings," *IEEE Transactions on Vehicular Technology*, Submitted, Mar. 2015.

[59] O. Renaudin, V-M Kolmonen, P. Vainikainen, C. Oestges, "Non-Stationary Narrowband MIMO Inter-Vehicle Channel Characterization in the 5 GHz Band," *IEEE Transactions on Vehicular Technology*, vol. 59, no. 4, pp. 2007-2015, May 2010.

[60] R. He, O. Renaudin, V.-M. Kolmonen, K. Haneda, Z. Zhong, B. Ai, and C. Oestges, "Characterization of Quasi-Stationarity Regions for Vehicle-to-Vehicle Radio Channels," *IEEE Transactions Antennas and Propagation*, vol. PP, no. 99, pp. 1–1, 2015.

[61] D. W. Matolak, R. Sun, "Air-Ground Channel Characterization for Unmanned Aircraft Systems: The Over-Freshwater Setting," *2014 Integrated Communications, Navigation and Surveillance (ICNS) Conference*, pp. 1-9, Herndon, VA, 8-10 April 2014.

[62] D. W. Matolak, R. Sun, "Initial Results for Air-Ground Channel Measurements & Modeling for Unmanned Aircraft Systems: Over-Sea," *2014 IEEE Aerospace Conference*, pp. 1-15, Big Sky, MT, 1-8 March 2014. DOI: 10.1109/AERO.2014.6836369.

[63] R. Sun, D. W. Matolak, "Over-Harbor Channel Modeling with Directional Ground Station Antennas for the Air-Ground Channel," *2014 Military Communications Conference (MILCOM 2014)*, pp. 1-6, Baltimore, MD, 6-8 Oct. 2014. DOI: 10.1109/MILCOM.2014.69.

[64] D. W. Matolak, R. Sun, "Antenna and Frequency Diversity in the Unmanned Aircraft Systems Bands for the Over Sea Setting," in *Proc. IEEE/AIAA Digital Avionics Systems Conference*, Colorado Springs, CO, 5-9 October 2014.

[65] D. W. Matolak, R. Sun, "AG Channel Measurement & Modeling Results for Over-Sea Conditions," (Report #6) NASA Grant #NNX12AR56G, 3 December 2013.

[66] D. W. Matolak, R. Sun, "AG Channel Measurement & Modeling Results for Over-Water & Hilly Terrain Conditions," (Report #7) NASA Grant #NNX12AR56G, 26 Sept. 2014.

[67] D. W. Matolak, R. Sun, "Air-Ground Channel Characterization for Unmanned Aircraft Systems: the Near-Urban Environment," *2015 Military Communications Conference (MILCOM 2015)*, Submitted, Tampa, FL, 26-28 Oct. 2015.

[68] D. W. Matolak, R. Sun, "Air-Ground Channel Characterization for Unmanned Aircraft Systems: the Hilly Suburban Environment," *2014 IEEE 80th Vehicular Technology Conference (VTC'14 Fall)*, pp. 1-5, Vancouver, Canada, 14-17 Sept. 2014.

[69] R. Sun, D. W. Matolak, "Air-Ground Channel Characterization for Unmanned

Aircraft Systems: the Mountainous Environment," *2015 IEEE/AIAA 34th Digital Avionics Systems Conference (DASC 2015)*, Accepted, Prague, Czech Republic, 13-17 September 2015.

[70] D. W. Matolak, R. Sun, "AG Channel Measurements & Modeling: Initial Channel Sounder Laboratory & Flight Tests," (Report #3) NASA Grant # NNX12AR56G, 29 January 2013.

[71] Berkeley Varitronics, Inc., (2015, June 22). [Online]. Available: www.bvsystems.com.

[72] Cobham Antenna Systems, (2015, June 22). [Online]. Available: www.european-antennas.co.uk.

[73] Sensor Systems Inc. (2015, June 22). [Online]. Available: www.sensorantennas.com.

[74] A. F. Molisch, *Wireless Communications*, Wiley-IEEE Press, Upper Saddle River, NJ, 2005.

[75] P. Mista, P. Enge, *Global Positioning System Signals, Measurements, and Performance*, 2nd ed., Ganga-Jamuna Press, 2010.

[76] D. W. Matolak, R. Sun, "AG Channel Measurements & Modeling: BVS Channel Sounder Performance: Measurement Stability," (Report #5) NASA Grant #NNX12AR56G, 19 April 2013.

[77] D. W. Matolak, R. Sun, "Air-Ground Channel Measurements and Modeling for UAS," *IEEE A&E Systems Magazine*, vol. 29, no. 11, pp. 30-35, Nov. 2014.

[78] D. W. Matolak, R. Sun, "AG Channel Measurements & Modeling: Initial Channel Sounder Laboratory & Flight Tests - Supplementary Report," (Report #4) NASA Grant #NNX12AR56G, 1 March 2013.

[79] W. C. Lee, “Estimate of local average power of a mobile radio signal,” *IEEE Transactions on Vehicular Technology*, vol. 34, no. 1, pp. 22–27, 1985.

[80] A. Gehring, M. Steinbauer, I. Gaspard, M. Grigat, “Empirical Channel Stationarity in Urban Environments,” in *Proc. 4th European Personal & Mobile Communications Conference (EPMCC 2001)*, Vienna, Austria, 20-22 February 2001.

[81] O. Renaudin, “Experimental Channel Characterization for Vehicle-to-Vehicle Communication Systems,” *Ph.D. Dissertation*, UNIVERSIT´E CATHOLIQUE DE LOUVAIN, 2013.

[82] T. T. Georgiou, “Distances and Riemannian Metrics for Spectral Density Functions,” *IEEE Transactions Signal Processing*, vol. 55, no. 8, pp. 3995-4003, August 2007.

[83] F. Kaltenberger, L. Bernad´o, and T. Zemen, “Characterization of MUMIMO channels using the spectral divergence measure,” *COST 2100, TD (08)*, vol. 640, 2008.

[84] G. Matz, “Characterization and Analysis of Doubly Dispersive MIMO Channels,” in *2006 Fortieth Asilomar Conference on Signals, Systems and Computers*, pp. 946–950, 2006.

[85] L. Bernadó, T. Zemen, A. Paier, G. Matz, J. Karedal, N. Czink, F. Tufvesson, M. Hagenauer, A. F. Molisch, and C. F. Mecklenbr, “Non-WSSUS Vehicular Channel Characterization at 5.2 GHz - Spectral Divergence and Time-Variant Coherence Parameters,” in *Proc. XXIXth International Union of Radio Science General Assembly and Scientific Symposium (URSI GASS)*, pp. 3–6, Aug. 2008.

[86] M. Gudmundson, “Correlation model for shadow fading in mobile radio systems,” *Electronics letters*, vol. 27, no. 23, pp. 2145–2146, 1991.

[87] A. Ispac, C. Schneider, G. Asheid, R. Thoma, "Analysis of the Local Quasi-Stationarity of Measured Dual-Polarized MIMO Channels," *IEEE Transactions on Vehicular Technology*, vol. 63, no. 9, July 2014.

[88] International Telecommunications Union (ITU), "Reflection from the surface of the Earth," Report 1008-1 (Question 1/5), pp. 75-82, 1986-1990.

[89] D. W. Matolak, R. Sun, "AG Channel Measurements & Modeling: Initial Analysis & Flight Test Planning," (Report #2) NASA Grant #NNX12AD53G, 8 June 2012.

[90] T. S. Rappaport, *Wireless Communications: Principles and Practice*, 2nd ed., Prentice Hall, Upper Saddle River, NJ, 2002.

[91] H. V. Hitney, "Refractive Effects from VHF to EHF Part B: Propagation Models," Advisory Group for Aerospace Research and Development (AGARD) Lecture Series, 1994.

[92] E. C. Jordan, K. G. Balmain, *Electromagnetic Waves and Radiating Systems*, 2nd ed., Prentice-Hall, Englewood Cliffs, NJ, 1968.

[93] Earth Fact Sheet (24 June 2015), [online] available: nssdc.gsfc.nasa.gov/planetary/factsheet/earthfact.html.

[94] L. Boithias, *Propagation des ondes radioelectriques dans l'environment terrestre, Collection Technique et Scientifique des Telecommunications*, 2*nd* ed., Dunod, Paris, France, 1984.

[95] International Telecommunications Union (ITU), "Effects of Tropospheric Refraction on Radiowave Propagation," Recommendation ITU-R P.6834-5, July 2005.

[96] A. R. Miller, R. M. Brown, E. Vehg, "New derivation for the rough-surface reflection coefficient and for the distribution of sea-wave elevations," *IEE Proc. H*, vol. 131, no. 2, pp. 114-116, April 1984.

[97] O. M. Philips, *Dynamics of the Upper Ocean*, London, Cambridge Univ. Press, 1966.

[98] International Telecommunications Union (ITU), "Attenuation by atmospheric gases," Recommendation ITU-R P.676-10, September 2013.

[99] C. A. Levis, J. T. Johnson, F. L. Teixeira, *Radiowave Propagation: Physics and Applications*, John Wiley & Sons, Hoboken, NJ, 2010.

[100] International Telecommunications Union (ITU), "Attenuation due to clouds and fog", Recommendation ITU-R P.840-6, September 2013.

[101] International Telecommunications Union (ITU), "Specific attenuation model for rain for use in prediction methods," Recommendation ITU-R P.838-3, March 2005.

[102] E. Dinc and O. Akan, "Beyond-line-of-sight communications with ducting layer," *IEEE Communications Magazine*, vol. 52, no. 10, pp. 37–43, Oct. 2014.

[103] A. L. Martin, "VHF and Microwave Propagation Characteristics of Ducts," Online, pp. 1–11, 2007.

[104] H. V. Hitney and L. R. Hitney, "Frequency diversity effects of evaporation duct propagation," *IEEE Transactions on Antennas and Propagation*, vol. 38, no. 10, pp. 1694–1700, 1990.

[105] H. V. Hitney and R. Vieth, "Statistical assessment of evaporation duct propagation," *IEEE Transactions on Antennas and Propagation*, vol. 38, no. 6, pp. 794–799, Jun. 1990.

[106] H. J. M. Heemskerk and R. B. Boekema, “The influence of evaporation duct on the propagation of electromagnetic waves low above the sea surface at 3-94 GHz,” in *Proc. Eighth International Conference on Antennas and Propagation (Conf. Publ. No.370)*, vol. 1, pp. 348–351, 1993.

[107] International Telecommunications Union (ITU), “The radio refractive index: its formula and refractivity data,” Recommendation ITU-R P.453-10, Feb. 2012.

[108] Y. H. Lee and Y. S. Meng, “Analysis of ducting effects on air-to-ground propagation channel over sea surface at C-band,” in *Proc. Asia-Pacific Microwave Conference*, pp. 1678–1681, 2011.

[109] Y. H. Lee and Y. S. Meng, “Empirical Modeling of Ducting Effects on a Mobile Microwave Link Over a Sea Surface,” *Radioengineering*, vol. 21, no. 4, pp. 1054–1059, Dec. 2012.

[110] P. A. Bello, “Characterization of Randomly Time-Variant Linear Channels,” *IEEE Transactions on Communications Systems*, vol. 11, no. 4, pp. 360–393, 1963.

[111] C. Tepedelenlioglu, A. Abdi, G. B. Giannakis, “The Ricean K factor: estimation and performance analysis," *IEEE Transactions on Wireless Communications*, vol. 2, no. 4, pp. 799-810, July 2003.

[112] D. W. Matolak, R. Sun, “Unmanned Aircraft Systems: Air-Ground Channel Characterization for Future Applications,” *IEEE Vehicular Technology Magazine*, vol. 10, no. 2, pp. 79-85, June. 2015.

[113] R. Sun, D. W. Matolak, “Initial Results for Airframe Shadowing in L- and C-band Air-Ground Channels,” *2015 Integrated Communications, Navigation and Surveillance (ICNS) Conference*, pp. , Herndon, VA, 21-23 April 2015.

[114] R. H. Bartels, J C. Beatty, B. A. Barsky, *An Introduction to Splines for Use in Computer Graphics and Geometric Modelling*, Morgan Kaufmann, San Francisco, CA, 1998.

[115] FAA, "Overview of Small UAS Notice of Proposed Rulemaking," (2015, June 11). [Online]. Available: www.faa.gov/regulations_policies/rulemaking/media/021515_suas_summary.pdf.

[116] International Telecommunications Union (ITU), "Multipath propagation and parameterization of its characteristics," Recommendation ITU-R P.1407-5, September 2013.

[117] J. Chuang, "The Effects of Time Delay Spread on Portable Radio Communications Channels with Digital Modulation," *IEEE Journals on Selected Areas in Communications*, vol. 5, no. 5, pp. 879–889, Jun. 1987.

[118] J. C. I. Chuang, "The effects of delay spread on 2-PSK, 4-PSK, 8-PSK and 16-QAM in a portable radio environment," *IEEE Transactions on Vehicular Technology*, vol. 38, no. 2, pp. 43–45, May 1989.

[119] W. C. Y. Lee, *Mobile Cellular Telecommunications: Analog and Digital Systems*, McGraw-Hill, 1995.

[120] National Climatic Data Center, (2015, June 22). [Online]. Available: www.ncdc.noaa.gov.

[121] A. Chockalingam and B. S. Rajan, *Large MIMO Systems*. Cambridge University Press, 2014.

[122] C. Oestges and B. Clerclx, *MIMO Wireless Communications: From Real-World Propagation to Space-Time Code Design*, 1st Edition, Academic Press, 2007.